ANNUAL REPORT

of

THE INSTITUTE OF PHYSICS

ACADEMIA SINICA

VOLUME 6 DECEMBER 1976

THE INSTITUTE OF PHYSICS, ACADEMIA SINICA

NANKANG, TAIPEI, TAIWAN, REPUBLIC OF CHINA

中央研究院物理研究所集刊

編輯委員會

The Annual Report is published annually by the Institute of Physics, Academia Sinica, Nankang, Taiwan 115, Republic of China. The Annual Report is available on an exchange basis to other scientific, research, and educational institutions.

本集刊每年出版一次

非賣品

中央研究院

物理研究所集刊

第六卷

發行人：王　唯　農

編輯者：中央研究院物理研究所集刊編輯委員會

出版者：中央研究院物理研究所　臺北市南港區

印刷者：崇文企業有限公司

電　話：三七一〇二二〇・三三一二六〇八

中華民國六十五年十二月出版

中央研究院物理研究所集刊

第 六 卷

中央研究院物理研究所印行

CONTENT 目 錄

Part A Physics and Biophysis

ARTICLES

Probability: Its Fundamental Concept and Its Role in Physics ..... Ta-You Wu 1～ 19
Study of the Sequential Process of the $Li^7(d, \alpha)$ $He^5(\alpha)n$ Reaction ..... W. N. Wang, P.S. Song and D. Wang 21～ 29
Elastic Scattering of Protons from ^{12}C and ^{16}O ..... E.K. Lin 31～ 38
Surface Scattering of Optical Waves in Graded Index Waveguides ..... N. T. Liang 39～ 44
The Setup of a Nuclear Lifetime Measurement System on Ge(Li)-NE 102A Detectors··· G.C. Kiang, D. Wang, B. Chen and E.K. Lin 45～ 50
No Conflict between Kondo Effect and Mictomagnetism ··· Y.D. Yao 51～ 58
The Limitation of Two-Current Model in Nickel-Rich Nickel-Chromium Alloys ..... Y. D. Yao 59～ 63
A Model of Perceived Direction of Adapted Motion ··· Chun Chiang 65～ 67
Undampted Sinusoidal Lineal Chemical Reaction System. Chun Chiang 69～ 75
Membrane Patential, Active Transport and Maxwell Demon ..... Wei-Kung Wang, Yuh-Ying L. Wang 77～ 86
The Pentose Cycle in Dorsal Roat Ganglia of Chick···Wei-Kung Wang 87～ 91
Rhodopsin and the Early Receptor Potential ..... Wei-Kung Wang 93～ 99

ABSTRACTS

原子態之組態相互作用 ..... 吳大猷 101
The Time Arrow and the Problem of Macroscopic Irreversibility ··· ..... Ta-You Wu 101
A Nanosecond Associated Particles Time of Flight System for Studying Fast Neutron Scattering ..... W. N. Wang, W.S. Hou, B. Chen and L. P. Liang 102

Study of Energy Levels of ^{117}In from the Beta Decay of ^{117}Cd ..... E. K. Lin, W.N Wang and C. Chou 102
Electronic Conductivity and Percolation Theory in Aggregated Films ..... N. T. Liang 103
Even-Parity Energy Levels of Singly Ionized Magnesium Donors in Silicon ..... L. T. Ho 103
Experimental Methods of Ionizing Impurity Atoms in Semiconductors ..... L. T. Ho 104
Time-Dependent Effect of Donor Lines in Silicon ..... L. T. Ho 104
Electrical Resistivity of Nickel-Rich Nickel-Chromium Alloys Between 4 and 900K Y. D. Yao, Sigurds Arajs, and E. E. Anderson 105
Magnetic Susceptibility of Pd Ce Alloys at Low Temperatures ..... K. V. Rao, S. Arajs and Y.D. Yao 105
Electrical Resistivity of Palladium-Silver Alloys at High Temperatures ... Sigurds Arajs, K.V. Rao, Y. D. Yao, and W. Teoh 106
Electrical Resistivity of Aluminum-Boron Composites Between 78K and 400K ..... D. Abukay, K. V. Rao and S. Arajs and Y. D. Yao 106
Nerve Excitations by the Coupling of the Dipoles and the Membrane Matrix ..... Chyuan-Yih Lee and Chun Chiang 107
A Theory of Ambiguous Pattern Perception ..... Chun Chiang 107
Science, Truth and the Absolute Value ..... Wei-Kung Wang 108

Part B Atmospheric Physics and Fluid Mechanics

ARTICLES

The Effects of Mountains on a Typhoon Vortex as Identified by Laboratory Experiments ..... H. P. Pao, Robert R. Hwang and Jin Jso 109~117
Effect of Barriers on Flows Associated with a Fixed Vortex ..... Robert R. Hwang, H. P. Pao and T. Y. Kou 119~132
Horizontal Diffusion of a Turbulent Sewage Plume ..... Robert Rong-jiann Hwang 133~141
利用風洞實驗探討高速風車性能之研究 ..... 黃榮鑑、簡又新、劉通敏 143~151
A Variational Analysis Scheme Suitable for Operational Use ..... Chung Yi Tseng 153~159
東亞地區天氣資料變分客觀分析之研究 ..... 曾忠一 161~178
The Variational Optimization of Wind Field for the Estimation of Vertical Velocity ..... Wen-Jey Liang 179~198

The Diagnostic Analysis and Modifications of Kuo's Parameterization of Cumulus Convection in Middle Latitutes……Wen Jey Liang 199～230
有限區域原始方程式模式之初步探討……蕭錫璋、汪群從 231～262

ABSTRACTS

Still Water Resistance of a Single-Step Planing Hull……C. T. Wang and C. Y. Lu 263
Experimental Study of a 27800 LTDW Bulk Carrier ……C. T. Wang and C. L. Huang 263
Analytic Solutions of the Falkner-Skan Equation When $\alpha=-1$ and $\gamma=0$ …… H. T. Yang and L. C. Chien 264
Theoretical Study of Two-Dimensional, Incompressible, Turbulent, Curved-Wall Jets……George Mon and Hsien-Ping Pao 264
The Effects of Mountains on a Typhoon Vortex as Identified by Laboratory Experiments …… Hsien-Ping Pao 265
On Vortex Trails Over Ocean Islands …… Hsien-Ping Pao and Timothy W. Kao 266
Hydrodynamic Instability of Stoke's Second Problem……Robert R. Hwang and C. J. Chen 266
二次元紊性熱漬流擴散之分析……黃榮鑑 265
臺中港設置風車之研究……黃榮鑑、簡又新、劉通敏 267

中央研究院物理研究所集刊

第 六 卷

中央研究院物理研究所印行

CONTENT 目 錄

Part A Physics and Biophysis

ARTICLES

Probability: Its Fundamental Concept and Its Role in Physics Ta-You Wu 1～ 19

Study of the Sequential Process of the $Li^7(d, \alpha)$ $He^5(\alpha)n$ Reaction ..... W. N. Wang, P. S. Song and D. Wang 21～ 29

Elastic Scattering of Protons from ^{12}C and ^{16}O ..... E. K. Lin 31～ 38

Surface Scattering of Optical Waves in Graded Index Waveguides ..... N. T. Liang 39～ 44

The Setup of a Nuclear Lifetime Measurement System on Ge(Li)-NE 102A Detectors ..... G. C. Kiang, T. Wang, B. Chen and E. K. Lin 45～ 50

No Conflict between Kondo Effect and Mictomagnetism ..... Y. D. Yao 51～ 58

The Limitation of Two-Current Madel in Nickel-Rich Nickel-Chromium Alloys ..... Y. D. Yao 59～ 63

A Model of Perceived Direction of Adapted Mation ..... Chun Chiang 65～ 67

Undampted Sinusoidal Lineal Chemical Reaction System ..... Chun Chiang 69～ 75

Membrane Potential, Active Transport and Maxwell Demon ..... Wei-Kung Wang, Yuh-Ying L. Wang 77～ 86

The Pontose Cycle in Dorsal Roat Ganglia of Chick ..... Wei-Kung Wang 87～ 91

Rhodopsin and the Early Receptor Potential ..... Wei-Kung Wang 93～ 99

ABSTRACTS ..... 101～108

Part B Atmospheric Physics and Fluid Mechanics

ARTICLES

The Effects of Mountains on a Typhoon Vortex as Identified by Laboratory Experiments ... H. P. Pao, Robert R. Hwang and Jin Jso 109～117

Effect of Barriers on Flows Associated with a Fixed Vortex ..... Robert R. Hwang, H. P. Pao and T. Y. Kou 119～132

Horizontal Diffusion of a Turbulent Sewage Plume ..... Robert Rong-jiann Hwang 133～141

利用風洞實驗探討高速風車性能之研究 ..... 黃榮鑑、簡又新、劉通敏 143～151

A Variational Analysis Scheme Suitable for Operational Use ..... Chung Yi Tseng 153～159

東亞地區天氣資料變分客觀分析之研究 ..... 曾忠一 161～178

The Variational Optimization of Wind Field for the Estimation of Vertical Velocity ..... Wen-Jey Liang 179～198

The Diagnostic Analysis and Modifications of Kuo's Parameterization of Cumulus Convection in Middle Latitudes ..... Wen Jey Liang 199～230

有限區域原始方程式模式之初步探討 ..... 蕭錫璋、汪群從 231～262

ABSTRACTS ..... 263～267

Annual Report of the Institute of Physis, Academia Sinica, Vol. 6, 1976

Probability: Its Fundamental Concept And Its Role in Physics

Ta-You Wu

(*Notes of Lectures delivered at the National Research Council of Canada, Feb.* 1960)

I. INTRODUCTION

The "theory of probability" is a difficult and still developing subject. First of all, it involves such questions as i) the meaning of the word "probability", which is immediately related to ii) the determination of the scope of problems to which the concept of probability so interpreted can be applied, and finally iii) the formulation of a mathematical calculus for dealing with the probability concepts. The subject has a long history, traceable to Aristotle in his work on (biological) heredity, and since the 17th century has been developed by a large number of mathematicians and logicians. There have been many different interpretations given to the concept of probability, and correspondingly many definitions of probability. These many interpretations can now be broadly classified into two categories, namely A) probability as a measure of the degree of confirmation or weight of evidence, and B) probability as a measure of the relative frequency of occurrence of a property in a specified class of elements. This difference is by no means a trivial one, for the attempts to base a clear definition of probability on these interpretations are intimately involved, not only with questions of the internal consistency of their theories, their suitability for various kinds of problems, but also with much deeper questions of the relation of probability theory to inductive logic, many-valued logic. A completely satisfactory interpretation of probability is still being sought. This situation is understandable from the fact that the word "probability" has been used in connection with a great variety of situations, with really different meanings, and unlike pure mathematics, the theory of probability (although the calculus itself has only logical content) must eventually make contact with empirical evidence and cannot ignore the question of what probability is defined to be.

In the present talk, we shall attempt a brief look into the various interpretations of probability and the nature of the difficulties in this subject.

II. EVOLUTION FROM CLASSICAL RATIONALISM TO PROBABILITY CONCEPT

Until very lately, "classical rationalism" predominates the philosophical and scientific thinking of many prominent men. Classical rationalism is the belief that knowledge, or science, should be based on certain exact propositions (or laws) of nature and not on experience (in the sense of observations and experiments). These exact laws are "necessary", "self-evident truths", and "obtainable by the intellect directly". (We might mention that Einstein in his late years believed in the possibility and desirability of such laws of nature.)

The concept of probability was introduced only when man, while still believing in rationalism, was forced to admit man's ignorance or lack of knowledge in certain matters. Hence, in treating situations where there is a lack of our knowledge of the "great laws of nature", the concept of "a priori" probability is maintained which is not to be based on empirical findings but is a "degree of rational belief". This "belief" is to be based on the "Principle of Indifferences" —a negative sort of principle according to which a proposition is made in the absence of knowledge to the contrary. (Example, the probability of any face of a symmetrical dice turning up is $\frac{1}{6}$).

The mathematical development of a theory of probability has its beginning from the problems of the games of chance. The names are: Cardan, Galileo (16th century), Pascal, Fermat (17th century); Huygens, the Bernoulli's, Montmort, De Moivre, and Bayes, and finally Laplace (early in the 19th century). The concept is that of "degree of belief"; the mathematical apparatus is that of combinatorial algebra.

When applied to the systematization of measurements and observations (originally in astronomy and now in all other fields), this forms the "theory of errors". The names are Boscovital, Lambert, Euler, Thomas, Simpson (18th century), Daniel Bernoulli, Legendre, Gauss, Laplace (18-19th century), and Poisson, Pearson, Gram and Charlier.

When applied to social, economic, biological problems, the statistical theory is that of "sampling". The names are: Lexis, Bortkiewicz, Tschuprow, Markoff; R. A. Fisher; Fechner, Bruno, Gallor, Thiele, Pearson, Neyman.

In addition to the above applications leading to the "theory of errors", "theory of sampling", "theory of curve fitting" etc., the theory has its most notable successes in:

1) the the kinetic theory of gases:
   Bernoulli's interpretation of Boyle's law
   Joules' calculation of the average velocities of hydrogen molecules
   Maxwell's velocity distribution
   Boltzmann's statistical interpretation of the Second Law of Thermodynamics
2) the quantum theory of radiation, and eventually,
3) the fundamental, statistical interpretation in quantum mechanics
4) Mendel theory of genetics —R.A. Fisher, J.B.C. Haldane, S. Wright.

The great successes in the development of statistical methods in the kinetic theory of gases towards the end of the 19th century are neither the first serious nor the decisive blows against the philosophy of rationalism. The use of statistical method in the kinetic theory may be regarded as a matter of convenience but not absolute necessity. The first serious challenge to the philosphy that there are absolute, a priori laws comes from the discovery of the non-Euclidian geometries. These show that there are alternative, equally logically consistent, geometries. Eventually, the use of Riemannian geometry in the general theory of relativity.

Then came, towards the end of the 19th century, the positivistic point of view (notably from E. Mach) which is the other extreme of the classical rationalism. Einstein acknowledged the influence of Mach on his early thinking, and his abandonment of the absolute space and time and the introduction of the "operational definition" of space and time measurements, leading to his theory of relativity, are epochs in the history of scientific and philosophy thinking. His theory of photons brings the probability concept in physics to a basic role. However, it was his "operational" point of view, namely, the use of concepts which can be defined by measurements, that sparked the initiation of quantum mechanics by Heisenberg. In the present system of quantum mechanics, the concept of probability becomes a fundamental notion.

We shall also attempt to discuss these developments briefly.

III. INTERPRETATION OF THE PROBABILITY CONCEPT

Before reviewing the various interpretations of the probability concept, let us have a few examples of statements in which the word probability (or probable) is used.

1) Group 1.
   a) The probability of a normal coin turning up a head is $\frac{1}{2}$.

b) The probability that a molecule of a gas having a velocity between v and $v+dv$ is p.
c) The probability of an α-particle being deflected through an angle greater than θ in going through a certain film is p.
d) A snow storm in Ottawa during February is more probable than during November.
e) The probability of a man of age 65 in North America surviving to his 66th birthday is 0.875.

2) Group 2.
a) It is highly improbable that Aristotle composed all the works attributed to him.
b) The theory of evolution has a greater probability than the theory of special creation.
c) It is probable that, had Cleopatra's nose been a half-inch longer, the course of the Roman Empire would have been different.
d) It is probable that the American Indians originally came from Asia.

It is seen that the word probability (or probable) does not all have exactly the same meaning. In fact much of the controversies about the interpretation of probability comes from the attempt to cover the various meanings by one term. Many interpretations have been put forth, but they may be broadly classified into three main groups. We shall not go into the many variants in each group but shall discuss the essential points of the three main interpretations.

In discussing the various interpretations, it is essential to distinguish between two parts in each interpretation, namely, the meaning of the concept in a qualitative form, and the attempt to give this qualitative meaning a precise definition. The two parts are not necessarily bound together and it is possible to modify or sharpen the second part without giving up the general meaning given to the concept. Failure to distinguish between these two parts, called the explicandum and explicatum, has also been the cause of controversy among the proponents of the various interpretations.

1. Classical interpretation (Laplace)

This view has been held since the time of Laplace until comparatively recently. According to Laplace, all our knowledge has a "probable" character simply because we lack the skill and knowledge to know the past accurately. A degree of probability is therefore a measure of the amount of certainty

associated with a belief. According to De Morgan, "probability" means the state of mind with respect to an assertion, a coming event, or any matter, on which absolute knowledge does not exist. Thus a probability statement in this view is a subjective expectation, a degree of belief.

Whenever a number is to be assigned to a probability, it is defined by the ratio of

$$\frac{\text{no. of favorable cases}}{\text{total no. of equiprobable cases}} \qquad (1)$$

This is thus an a priori probability, and has no logical relation to the relative frequency meaning in another view to be discussed in the following.

The question arises as to how does one know certain cases to be equally probable. Doesn't this smell of defining the concept probability in terms of that concept itself? Indeed the judgment of equiprobability depends on the Principle of Indifference (or Principle of Insufficient Reason, or Principle of Equal Distribution of Ignorance). This principle states that two or more properties are assumed to be equally probable if there is no knowledge to the contrary. In the case of the throw of a coin, this a priori probability of a head is $\frac{1}{2}$; in the case of the throw of a dice, the a priori probability of any face turning upward is $\frac{1}{6}$. These seem so obvious that they have caused us to forget that the a priori probabilities so defined have no logical relations with the factual results of an experiment. In these two cases of a coin and a dice, these a priori probabilities agree with the a posteriori probabilities according to the relative-frequency view we are going to discuss. But in other cases, the use of the Principle of Indifference as the basis of the probability can lead to absurd results, as we shall show in Section IV below. This classical interpretation is now regarded as untenable by most leading workers in the field of probability theory. Norman Campbell, in his Elements of Physics, put it very strongly thus: "Insistance on interpreting the probability of an angle θ deflection of an α-particle in going through a foil" in any sense other than that of relative frequency, convinces us of nothing except his ignorance of physics.

2. Logical concept of confirmation

John M. Keynes: A Treatise on Probability, 1921.

H. Jeffreys: Treatise on Probability, 1939

J. Hosiasson-Lindenbaum: "On Confirmation", J. Symbolic Logic, V, 133-148, 1940.

According to this school, a probability proposition is a logical relation

between two other propositions. This relation is not only based on logical (inductive) argument, but is also intuitive and unanalyzable.

Consider the following example. Among 30 observed things with the property M_1, 20 have been found to have the property M_2. Let an individual thing b not belonging to the 30 observed be M_1. The probability that M_1 is M_2 is, according to this concept of degree of confirmation, 2/3. This proposition of probability 2/3 is a logical statement based on the evidence that of 30 M_1, 20 are M_2, and the proposition that b is M_1. The probability is thus not a factual proposition. It is not the limit of a relative frequency, which would call for an infinite (at least a large number) number of samples, not just one sample of 30 things as above.

Consider another example. "On the evidence of meteorological data, the probability of rain tomorrow is 1/5". Again this proposition is a logical relation based on the other propositions (meteorological data), and is

i) not factual
ii) not to be understood as a relative frequency of actual occurrences,
iii) not meant to be verifiable, since the probability 1/5 will not agree with fact no matter whether it rains or does not rain.

The question arises as to what possible content such a probability statement may have, if it is not factual, nor to be verifiable. That this interpretation of probability denies verification from the outset is not a shortcoming in its logical nature, since by construction there is not to be any logical connection between a probability statement (on this view) and empirical result. It is exactly this denial of the possibility of interpreting probability on the empirical, relative frequency view that is the root of this interpretation. It does not follow, however, that such an interpretation of probability is necessarily empty, for while the probability statement is a logical relation, the evidences (the other propositions on which the probability statement is made) usually have factual content (for example, the meteorological data.)

3. Frequency interpretation of probability

This view has been put forth and held by Bolzano, Cournot, Ellis, Venn, Peirce in the 19th century, and most completely developed and advocated more recently by von Mises and Reichenbach. In this view, the degree of probability is a measure of the relative frequency of occurrence of a property (say the ace of a dice) in a specified class of elements (the throws of a dice).

The numerical value to be assigned to the probability is defined as the limit of this relative frequency as the number of elements tends to infinity.

Before answering questions that obviously arise in our mind concerning this concept of a limit in an infinite sequence, we must emphasize a few points that are also the cause of misunderstanding.

i) The probability so interpreted is entirely empirical, or factual; it is a posteriori, unlike the probability in the classical theory (of Laplace) in which it is a priori, for example, the probability of an ace in a throw of dice is $\frac{1}{6}$.

ii) The probability refers to a class, not to an individual. In fact, no meaning can be atatched to a statement that explicitly gives a probability value to a single event.

Thus the statement that "the probability of persons of age 30 in a certain country during the present decade surviving at least to the age 31 is 0.945" has a relative frequency meaning, whereas to tell Mr. Smith whose age is 30 that his probability of living to 31 is 0.945 has no meaning.

Failure to remember this statistical nature of the direct evidence (empirical data) in the definition of probability is the most common source of erroneous understanding. You have likely heard about this joke: a doctor told his patient Mr. A. before an operation that the chance of patients not surviving the operation is 50%, but that since he has already had his 50% of patients dead, Mr. A. shouldn't worry. We all immediately understand the point; but in actual fact, the doctor is not any more stupid or erroneous than the physicist who claims to have determined the lifetime of a particle from the length of the track of one single particle in a cloud chamber or a photographic emulsion.

Passing on to the quantitative (metrical) definition of probability let a class R contain n elements, and let

nu (A and R) = *no.* of elements of R that have the property A and denote the relative frequency

$$\underset{n}{nu}\ (A \text{ and } R) \equiv freq_n(A,R).$$

Then the definition of probability of A in R is

$$p = \lim_{n\to\infty} freq_n(A,R)$$

and we also denote this by prob(A,B).

This definition is convenient for the development of a mathematical calculus of probability, but in dealing with an infinite class instead of a

finite class, it is open to the following objection, namely, that p will forever remain unknown. One may try to defend this definition by the following modifications:

1) One may allow a limit of uncertainty (possible limit of accuracy in factual data) and work with large, but finite, class R.
2) One may relax the above requirement of "limit" and replace it by the "condensation point" of relative frequency, i.e. the value on which the $freq_n$ for large n crowds themselves. (Copeland, Popper).

The trouble is that there might be more than one "condensation points" in the class, and that a "condensation point" exists even though no limit exists.

But deep questions do arise in the definition of probability as a limit. Consider, as an elementary example, the sequence of Head (H) and Tail (T) in the throws of coin,

HHTTTHHTHTTHHTTHHHHTHTHHTTT...

.....HHHHHHHHHHHH.....

The question is this: Let S_n be a subseries (finite, of n elements) and the probability of H in S_n is found to be 0.501. There is a finite, though small, probability that from the $(n+1)$th throw on, a run of m H's takes place. Then the probability of H in S_{n+m} will be >0.501.

Thus the situation seems not to obey the usual definition of the existence of a limit in a series.

This question can be answered in two parts.

1) Many theorems in the theory of probability depend for their validity on the "irregular" or "random" nature of the series. Obviously if R is the sequence

   HTHTHTHTHTHTHTHTHT

   one would get the probability $(H,R)=1/2$. But if one takes the subclass R' consisting only of the odd elements above, then $\text{Prob}(H,R')=1$. Thus one must require the class to have an irregular nature (v. Mises).
2) The occurrence of a long run of H at a certain point in R in a single event, and we must remember that in order to give probability meaning, we have to work with a class, i.e. we have to find the probability of such a long run of H at the $(n+1)$th throw from a class R whose elements are the classes R_{n+m} themselves. That $\text{Prob}(H,R_{n+m}) = p$ and $\text{Prob}(H,R_{n+m}) \neq p$ do not contain any contradiction. The

difficulty is really to choose n. The assumption is made that an n exists such that for any given ϵ,

$|\text{Prob}\ (H,R_{n+m})-\text{Prob}\ (H,R_n)| \leqslant \epsilon$ for all m.

Now comes the question of irregularity mentioned above in 1). It is not an easy matter to give an exact definition of "irregularity" or "randomness", for to be able to do so would involve a self-contradiction. Criticisms and studies have been made of such "irregular" reference classes (Reichenbach, Popper, Copeland, Wald). We shall not be able to go into these. This brief account serves to show the nature of the difficulties involved in the limit definition of probability.

After setting forth the three main interpretations of the concept of probability, let us see whether they are adequate in covering the following categories of statements using the word probability in some sense.

(A) Everyday discourse. Examples:

a) It is probable that he reads it in some book.

b) It is not probable that he could have forgotten me.

c) It is probable that the witness has spoken the truth, and those in Group 2, Section III, above.

(B) Applied statistics and measurements

(C) Physical and biological theories

Examples, b, c, e in Group I, Section III.

(D) "Comparative" probabilities of theories

Examples b, in Group II, Section III.

"It is probable that the probability of getting heads with the throws of a coin is $\frac{1}{2}$."

(E) Calculus of probability

According to the Classical Interpretation, denoted as (α), the statements in (A), (D) are rightly expressions of degrees of belief. (α) is not relevant for (B), (C). The "degree or strength of belief" meaning is not immediately relevant for a mathematical formulation, however, with the probability defined by the ratio (1), the mathematical theory is the combinatorial analysis.

According to the Concept of Degree of Confirmation, denoted as (β), the statements in (A) and (D) are covered by (β) if they are completed by stating some "evidence", such as

(A) a) "on the evidence that he is known to read widely"

b) "on the evidence that he is known to have good memory", etc.

Strictly interpreted, (β) cannot be applied to physics and statistics: for the "logical, unanalyzable relation..." stating the probability calls for an intuitive power which may or may not be there in a given person, and furthermore, the result should not depend on how good or bad his intuitive power is. [Altogether (β) is somewhat illusive, mainly because different proponents of this same view do not make the same statements in their writings.]

According to the Relative Frequency Interpretation, denoted as (γ), some of the examples in (A) and (D) can not be understood on (γ), but some can, after they are amended. Thus (A) c), the statement may be taken to mean that the witness is a church goer, and the relative frequency of a regular church goer lying on important occasions is less than $\frac{1}{2}$.

On the other hand, it is not always possible to give the statement "that theory is probably true" a relative frequency meaning in the sense of the frequency of the affirmative verification of its consequences. Since the total number of deductions of a theory may be infinite, the number of verified consequences has a measure zero.

IV. CALCULUS OF PROBABILITY: BASIC THEOREMS

While there are various different interpretations of the concept of probability, a mathematical theory can be constructed which to certain extent is independent of the interpretation of the meaning of "probability"; instead it starts with certain premises which are of the nature of propositional functions, i.e. statements concerning "probability" as a free variable. For example, one starts with a premise like: "If p, q are the probabilities of two independent variables x and y respectively, then the probability of x or y is $p+q$". Such premises of course prescribe certain properties to the word "probability" (apart from one's interpretation of it, namely, the three different views discussed in the preceding sections); and these properties "define" the mathematical content, but not the empirical content of "probability". The mathematical theory is concerned with the purely logical deductions from, not the empirical content of, the premises.

The most basic properties of the probability in the calculus of probability are contained in the following theorems, some of which may be regarded as postulates.

Let the reference class be R. Let A and B be properties of R.

Probability: Its Fundamental Concept And Its Role in Physics

Probability of A in $R \equiv$Prob (A,R)

Probability of B in class of A and $R \equiv$Prob $(B,$ A and $R)$

Probability of A and B in $R \equiv$Prob $(A$ and $B.$ $R)$.

Theorem I. Prob $(A$ and $B,R) =$Prob $(A,R) \times$ Prob $(B,$ A and $R)$.

[Here the implication is that Prob. $(B,$ A and $R) \neq$Prob (B,R).]

For example R is the class of all people in Canada

A is a physicist

B is a member of the N. R. C.

Prob $(A,R) =$prob. of a physicist in Canada

Prob (B,R) prob. of a N. R. C. member in Canada

Prob $(B,$ A and $R) =$prob. of a physicist in N. R. C.

Prob $(A$ and $B,R) =$prob. of being both a physicist and N. R. C. man in Canada.

Obviously Prob $(B,R) \neq$Prob $(B,$ A and $R)$, since the properties A and B are not independent.

If A and B are independent, then

Theorem II. Prob $(A$ and $B,$ $R) =$Prob $(A,R) \cdot$Prob (B,R)

Theorem III. Prob $(A$ or $B,$ $R) =$Prob $(A,R) +$Prob (B,R)

Theorem IV. Prob $(A$ or not $A,$ $R) = 1$

Theorem V. By III & IV, we get: Prob $(A,R) +$Prob (not $A,R) = 1$

Since Prob $(A$ and $B,R) =$Prob $(A,R) \cdot$Prob $(B,A$ and $R)$

$=$Prob $(B,R) \cdot$Prob $(A,$ B and $R)$

hence

Theorem VI: Prob $(B,$ A and $R) = \dfrac{\text{Prob } (B,R) \cdot (\text{Prob } (A,B \text{ and } R)}{\text{Prob } (A,R)}$

or

Bayes's Th. Prob $(B,$ A and $R) =$

$$\frac{\text{Prob } (B,R) \cdot \text{Prob } (A,\ B \text{ and } R)}{\text{Prob } (B,R) \cdot \text{Prob } (A,\ B \text{ and } R) + \text{Prob } (\text{Not } B,R)\ \text{Prob } (A,\text{Not } B \text{ and } R)}$$

Proof. The denominaotr is, by VI,

$$\text{Prob}(A \text{and} B,R) + \text{Prob}(A \text{ and Not } B,R) \overset{\text{by III}}{=} \text{Prob } (A \text{ and } B \text{ or } A \text{ and Not } B,R) = \text{Prob } (A,R).$$

General form: Let $B_1,\ B_2 \ldots B_n$ be mutually exclusive and exhaustive properties

$$\text{Prob } (B_i\ A \text{ and } R) = \frac{\text{Prob } (B_i,\ R) \cdot \text{Prob } (A,\ B_i \text{ and } R)}{\sum_i \text{Prob } (B_i,R) \cdot \text{Prob } (A,\ B_i \text{ and } R)}$$

Example:

R=shots fired at a target from rifles 1, 2, 3.

A=bull's eye hit

B_1=shot from rifle 1

B_2=shot from rifle 2

B_3=shot from rifle 3

Prob(B_1, R)=$\frac{3}{8}$, Prob(B_2 R)=$\frac{1}{8}$, Prob(B_3, R)=$\frac{4}{8}$

Prob(A, B_1 and R)=$\frac{1}{5}$, Prob(A, B_2 and R)=$\frac{2}{5}$, Prob(A, B_3 and R)=$\frac{1}{5}$

What is Prob(B_2, A and R)? i.e. the prob. that bull's eye hit is from rifle 2?

Prob(B_2, A and R)=$\frac{2}{5}$

Now the probabilities Prob(B_i, R), sometimes called the anticedent probability of the "cause" Prob(B_i, A and R) [A is the "effect"], are, in cases where knowledge is absent, often assumed to be equal to one another, according to the Principle of Indifference. On the basis of Bayes' theorem and this Principle, Laplace deduced the so-called Rule of Succession which for a long time has been accepted as reliable basis for scientific prediction. According to this rule, if n events of a certain kind have been observed in succession, then the probability of its recurrence is $\frac{n+1}{n+2}$. Following Laplace, Quetelet declared that "after having seen the sea rise periodically ten successive times at an interval of about twelve hours and a half, the probability that it will rise again for the eleventh time would be $\frac{11}{12}$". But it also follows from the rule that, if the tide has not bee observed to rise at all, the probability of its rising is $\frac{1}{2}$. This is a reductio of absurdum.

On the relative frequency interpretation, the use of the Principle of Indifference in dealing with probabilities is unjustified and is a serious error.

V. THE ROLE OF PROBABILITY CONCEPT IN CLASSICAL PHYSICS.

We have already mentioned in Secion I that the probability concept has been applied by Bernoulli to the kinetic theory of gases. By ascribing the pressure of a gas to the bombardment of the walls by the gas molecules, it was possible to explain Boyle's law. This forerunner of the kinetic theory of gases is remarkable, not only because the statistical concept was introduced, but because the "reality" of the atoms and molecules was not yet known, and the kinetic theory was then only a model.

The use of statistical method in the kinetic theory of gases was greatly advanced by Maxwell and Boltzmann. First there was the derivation of the Maxwell distribution law of velocities on considerations not depending on the mechanics of the collisions of the molecules. Then on considering the

numbers of ways Nr in which a large number of molecules, called "systems", can distribute themselves over the various possible energy states of a molecule, and on interpreting the equilibrium state as the "most probable" state, namely, the state that can be realized in the largest number Nr of ways, a "statistical theory" of thermodynamics was born. In this statistical theory, it is possible to identify certain parameters and quantities with the thermodynamic concepts and functions such as temperature, entropy, free energy etc. The exceedingly sharp nature of the maximum Nr for the most probable state when the number of molecules involved is large gives a satisfactory of account of all fluctuation phenomena. From the technical point of view, certain approximations, such as the use of Stirlings' formula for the logarithms of the factorials of large numbers, are not very satisfactory. In the later theory of Darwin and Fowler, instead of the "most probable" state, the "average state" is calculated directly without having to use Stirlings' formula. The results obtained, i.e., the statistical interpretation of thermodynamic functions, etc., are the same as with the Maxwell- Boltzmann theory.

We may note that in both of these theories, one deals with an assembly which is made up of a large number of particles. Only a counting of states is involved and no assumptions have been made concerning the dynamics of the particles, except that the particles do not interact with each other. Thus we may call these theories "classical statistics". A union of statistical concepts and dynamics was achieved in the "statistical mechanics" first developed by Gibbs, and just a couple of years later, independently, by Einstein. In this theory, an assembly is an actual physical, macroscopic body, consisting of N particles (called systems), which has the Hamiltonian $H(q_1 \cdots q_n \; p_1 \cdots p_n)$, so that the systems may be independent or may interact with one another. The statistical element is introduced by the construction of an "ensemble" out of a large number of assemblies, each having the same Hamiltonian H and differing from one another only in the "phase" (the initial values of the coordinates and momenta of the systems). Each assembly is represented by a point in the 6N-dimension phase (Γ) space, and the the ensemble is represented by a distribution of a large number of points in this Γ-space. This distribution is described by a function $D(t,q,\cdots\cdots q_n, p,\cdots\cdots p_n) \equiv D(t,q,p)$. Classical dynamics is introduced by Liouville's theorem which states that

$$\frac{\partial D}{\partial t}+\sum_i\left(\frac{\partial D}{\partial q_i}\dot{q}_i+\frac{\partial D}{\partial p_i}\dot{p}_i\right)=0$$

and which follows from the theorem of classical dynamics that during the motion of the systems according to the equations of motion, any volume element in phase space $\Delta\tau=\Delta q_1\cdots\cdots\Delta q_N\ \Delta p_1\cdots\cdots\Delta p_N$ remains unchanged. The postulate in statistical mechanics is then made that the long time average value of any macroscopic property M of an assembly in equilibrium is given by the value of M averaged over the ensemble, i. e.

$$\overline{M^t}=\int\cdots\int MD\ d\tau$$

where, for equilibrium, D does not depend on time explicitly. (On the ergodic hypothesis which is however untenable, this equality can be proved as a consequence.)

In one theory of Gibbs, that of canonical ensemble, the function D is given the form

$$D(q,p)=e^{\frac{\psi-H(q,p)}{\theta}}$$

The parameter θ can be identified with kT on considerations of the results of the theory applied to systems in thermodynamic equilibrium. It is not possible, nor is it the purpose, to go into any of the above theories in the present talk. I shall confine myself to making a few general remarks that are relevant to my main theme, namely, the probability concept and its role in the development of physics.

1. I believe most physicists agree that the meaning of "probability" in statistical mechanics must be that of relative frequency, discussed in Section III.

2. In the Maxwell-Boltzmann and the Darwin-Fowler statistics, the concept of an a priori weight is used, namely, a weight of unity for an elementary state and a weight g for a "degenerate" (g−fold) state.

This postulate about the probability of a state is a basic postulate. Although the weight is usually regarded as "a priori", I believe its ultimate meaning must still be that of "relative frequency", or otherwise one would have to invoke the Principle of Indifference.

3. In the statistical mechanics of Gibbs and Einstein, the corresponding postulate (corresponding to that of equal weights for elementary states) is that of equal probability for equal volume of Γ-phase space. The specific postulate of long-time-average=ensemble-average may be made plausible on the ergodic theorem of poincare according to which the phase point, in the

course of time, will approach any given point (consistent with the constants of motion of the assembly) as close as we please. This makes it plausible that in the course of time, the given assembly spends a time in the neighbourhood of any state (phase point) which is proportional to the volume element $\Delta\tau$. Let us take the microcanconical ensemble of Gibbs. It follows that the long time average of any property of assembly is given by the distribution of the phase points of the ensemble averaged over the whole accessible valume of the phase space (accessible, subject to the constants of motion).

4. We should perhaps emphasize that, statistical theories, while giving an interpretation of thermodynamic functions and the Second Law, do not, by themselves, lead to the absolute increase of entropy, $ds \geq 0$, and therefore do not lead to rigorously irreversible processes. In the theory of Boltzmann (Boltzmann equation of non-equilibrium processes H-theorem), we must note that not only dynamics is used. Both the irreversibility of transport processes (conduction heat, etc.) and the law $ds \geq 0$ comes about from the so-called Stosszahlansatz in the "collision term" of the Boltzmann equation for the distribution function $f(x,v,t)$

$$\frac{\partial f}{\partial t}+\sum_x \frac{\partial f}{\partial x}v_x+\sum_x \frac{\partial f}{\partial v_x}\dot{v}_x=\int d\vec{v_1}\, d\Omega\, g\, \sigma(g,\theta)\,[f(x,v_1',t)f(x,v',t)-f(x,v_1,t)f(x,v,t)]$$

where v, v_1 are the velocities of two colliding particles before collision, v', v_1' those such that after collisions, they go into v, v_1. $g=|v-v_1|=|v'-v_1'|=$the relative velocity, $\sigma(g,\theta)d\Omega$ the differential cross section, and the summations are over x, y, z. It is seen that this equation is not invariant upon time reversal, the left hand side changing sign and the right hand side remaining unchanged upon $t\rightarrow -t$. This Stosszahlansatz is not a consequence of dynamical laws, but is an assumption in Boltzmann's equation. It is from this Stosszahlansatz that the H-theorem and the transport equations that follow from Boltzmann's equation have their origin. Statistical method and (reversible) dynamics alone do not lead to irreversible processes.

5. In the statistical mechanics employing liouville's theorem, there was once the difficulty of an apparent contradiction between the ergodic theorem according to which the phase curve in the course of time will approach as close to the initial point as we please, and the inreversible approach of a non-equilibrium assembly to an equilibrium state. This difficulty is resolved by noting that i) one does not claim "absolute" irreversibility from pure statistical mechanics (i.e., not polluted by additional assumptions such as

Boltzmann's Stosszahlansatz), and ii) the "practical" (or observed) irreversibility is due to the different time scales for a Poincare "cycle" and for our times of observation.

VI. THE ROLE OF PROBABILITY CONCEPT IN QUANTUM PHYSICS.

In classical physics, one may, with Laplace, suppose that statistical methods are introduced only because we lack the knowledge about the positions and velocities of all the particles, that, given this information, a super human intellect can, in principle, calculate the whole history, past and future, of the whole universe. With the advent of the quantum theory and the investigations in the realm of atomic physics, however, this belief has been shown untenable.

The first hint that "probability" plays a more fundamental role than in the sense of Laplace, or even Boltzmann, comes from the discovery, by Rutherford and Soddy, of the law of radioactive decay, namely,

$$-\frac{1}{n}\frac{dn}{dt}=\frac{1}{\tau}, \qquad \tau=\text{constant}.$$

The implication of this law is most profound; it means that the decay of any single radioactive nucleus is governed by an intrinsic probability law. It states that the nucleus, irrespective of how long it has been existing, has a probability of decaying in the time τ. Again, this probability refers to the "class", not to an individual, specific nucleus, as discussed in Section III.

In 1905 Einstein introduced the statistical concept in his theory of photons, and in 1917, introduced the concept of transition probabilities (the A and B coefficients) in deriving Planck's radiation formula. These latter transition probabilities (per unit time) are similar to the probability $\frac{1}{\tau}$ for radioactive decays, and imply that, like radioactive decay, the emission and absorption of radiation by matter are governed by a probability law. This is in fundamental contrast with classical physics in which we think all processes as being governed by deterministic laws (such as classical dynamics and electromagnetism).

But still greater surprise was in store for not only the physicist, but also the philosopher and the scientific thinker. In the short period of a few years, say 1925-30, first the formalisms and later the full physical and philosophical meaning of the present system of quantum mechanics were created, developed and completed. It is a self-consistent system which is entirely satisfactory within a rather large domain--the whole of the physics

of atoms and molecules. Furthermore, it is believed by such profound thinkers as Niels Bohr that the basic concepts of the present system are the only ones that are possible. This view is held by many physicists (of whom, of course, only a few are capable of independent and deep thinking), but many founders of the quantum theory, namely, Planck, Einstein, Schrödinger, de Broglie, have never been willing to accept this philosophy. It is again not possible, in this talk, either to explain the physical and philosophical import of the present system of quantum mechanics, or to discuss the points of controversies among these prominent physicists and philosophers of science. But I shall attempt just a brief resumé of the present situation.

Now quantum mechanics has been formulated in an axiomatic form. The axioms or postulates can be divided into two groups, namely, the "Complementarity Principle" and the "probability postulate". The Complementarity Principle starts by accepting the basic limitations of the nature of our basic concepts and knowledge which are expressed by the wave-particle duality relations of Einstein and de Broglie,

$$E=h\nu\ , \qquad p=\frac{h}{\lambda}$$

The postulates under the second group require physical quantities ("observables") to be represented by linear, hermitian operators, and "states" of a physical system by wave functions (vectors in Hilbert space). As a consequence of the Einstein-de Broglie relations above, the operators representing canonically conjugate observables do not obey the commulative law of multiplication, but in fact, obey the law

$$pq-qp=\frac{h}{2\pi i}$$

The Probability Postulate asserts that if a measurement of an observable A is performed on a system whose state is represented by the function $\psi_m(q)$, the result of the measurement is given by

$$<\mathrm{A}>=\bar{A}\equiv\int\overset{*}{\psi}_m(q)\ A\ \psi_m(q)dq$$

If $\psi_m(q)$ is an eigen state of an observable B, and $\phi_n(q)$ an eigen states of the observable A, i.e.,

$$B\psi_m=b_m\psi_m, \qquad A\phi_n=a_n\phi_n, \qquad b_n,\ a_n=\text{constants},$$

then the value of A above is given by

$$A=\Sigma|\ C_n^m\ |^2a_n\ ,$$

where

$$C_n^m=\int\overset{*}{\psi}_m(q)\phi_n(q)dq,$$

i.e., the theory only gives the probabilities with which the various possible values (the eigen values) of A may come out from the measurement. (This is somewhat similar to the prediction of the various faces of a dice coming up, each with a probability 1/6, but not which face will come up in any single throw). Only in the special cases when the operators A and B above commute, i.e.,

$$AB=BA$$

does the theory predict the outcome of a specific value with probability unity, namely, in this case

$$\psi_m=\phi_m, \qquad C_n^m=0 \qquad \text{unless } m=n,$$

and

$$\overline{A}=\int\overset{*}{\phi}_m A\psi_m dq=a_m.$$

All these results are the consequences of the two groups of fundamental postulates of the theory.

From this, it is seen that in the present quantum mechanics, the probability concept enters at a basic level. In classical physics, one is allowed to think that, in principle, unlimited accuracy in measurements and definite results are possible. In quantum mechanics, these are not possible, not only in practice, but in principle, as well. This impossibility is the consequence of the fundmental postulates of the theory, and these fundamental postulates have their origin in the limitation of the classical nature of the concepts, such as coordinate and momentum, energy and time, particle and waves, each being defined by a prescription of an experimental procedure for its measurement, which is of necessity "classical" in nature. Thus on the views of quantum mechanics, the probability nature of the laws is inseparably connected with the nature of our concepts and, with them the (only) way a theory can be built up. It is clear that the import of this system is most profound and far-reaching indeed.

I have already mentioned that Einstein in spite of his having contributed most to the very spirit that undearlies the present quantum mechanics, namely, the use of concepts that are definable by means of criteria for their measurements, was dissatisfied with the philosophy of the present system of quantum mechanics. He was ready to accept the probability interpretation of $|\psi|^2$, not as basic property for an individual particle, but only in the sense of classical statistical physics. He believed that the laws of nature are deterministic, that the present probabilistic form results ony because of its

being at a higher level, just as classical statistical physics lies above the deeper foundation of exact laws. Many physicists do not agree with Einstein's outlook; some regard Einstein's view with pity and regret; others argue in dogmatic and sarcastic terms; and most argue irrelevently simply on the ground of the self-consistancy of the present system. It is true that no successful alternative system has yet been found; but I believe it is not in accord with the scientific spirit to brush aside skepticisms on the ground of the self-consistency of the present theory. Here the controversy is not merely one of philosophic and scientific outlook; it is of significance for the future development of physical theories.

Annual Report of the Institute of Physics, Academia Sinica, Vol. 6, 1976

Study of the sequential process of the $Li^7(d,\alpha)$ $He^5(\alpha)n$ reaction*

W. N. Wang, P. S. Song** and D. Wang

Institute of Physics Academia Sinica and National Tsing Hua University

Abstract

The reaction $Li^7(d,\alpha)He^5(\alpha)n$ has been studied by alpha alpha coincidences. The measurements were performed at bombarding deuteron energies from 1.0 to 2.8 MeV in steps of 0.2 MeV at $\theta_f=90°$ and $\theta_m=65°$. The angular correlation has been observed at bombarding energy of 1.9 MeV for fixed one detector at $\theta_f=90°$ and moving the other detector from $\theta_m=55°$ to 95° in steps 5°. The final interaction between the α-particle and the neutron is observed mostly in the ground state of He^5. The excitation of the broad first excited state of He^5 is also seen. Special effort has been made for looking this state, the position and width have been estimated. The sequential decay by through $Li^7(d,\alpha)Be^8(\alpha)\alpha$ process in this energy region is observed to be very weak.

I. INTRODUCTION

The study of nuclear reaction with more than two particles in the outgoing channel is of great interest both theoretically and experimentally. Due to an apparent success of cluster model in describing properties of light nuclei[1] and some uncertained value of the energy and width in the excited state of nuclei, the three-body break-up reaction especially through sequential decay process has been studied.

Deuteron bombardment of Li^7 is a very convenient reaction for studying three-body decay process, due to the large positive Q-value to decay into two alpha particles and a neutron. This reaction is also very suitable for studying the particle unstable nuclei He^5 and Be^8 through sequential decay process. Most of the experiments[2-12] on Li^7+d reaction in deutron energy region from 0.1 to 3.0 MeV had been performed "incompletely" by measurement of the energy spectra of only one of the outgoing particles. Their results are inconsist with each other. The Be^8 energy levels are found to be different in different experiments. The position of the first excited state of He^5 has been observed in energy range from 2.5 MeV to 4.6 MeV and the width of that state

* Work supported partially by the physics research center, National Science council.

** Present address: Institute of Nuclear Science, Atomic Energy Commission, Taipei, R. O. C.

has been predicted from 1.5 to 4.0 MeV. The discrepancy between their results is essentially due to measuring only one of the outgoing particles.

Recently, a few "complete" experiments with measuring two outgoing particles in coincidence of the $Li^7+d\rightarrow n+\alpha+\alpha$ reaction has been studied by several authors. At the deuteron energy below 1 MeV region, some authors [13-16] use α-α or α-n coincidence method to study the reaction mechanism. They found that in the Li^7+d reaction, sequential decay through ground and first excited state of He^5 play a important role.

At the deuteron energy from 2.6 to 4.0 MeV region, Valkovic et al[17] found that the ground state of He^5 and ground state, 2.9 MeV, 16.63, 16.92 and 20 MeV states of Be^8 were observed, and the first excited in He^5 and 11.4 MeV state in Be^8 were only weakly excited.

Hofmann et al[18] studied by n-α coincidence at deuteron energy between 0.98 to 1.6 MeV and found that the width of the 11.4 MeV level of Be^8 is 2.8 $\pm$0.2 MeV, but no indication for participation of an excited state of He^5 in the reaction is found. At deuteron energy 2.0 MeV, Flannant et al[19] studied the mechanism of $Li^7+d\rightarrow 2\alpha+n$ through α-α and α-n coincidence and their results express in terms of phase space unit. Wen M. et al[20] studied Li^7 (d,α,α) reaction at deuteron energy of 1.5 MeV.

The aim of the present experiment is to extend the experimental study of the Li^7 (d,α) He^5 (α)n sequential decay by the α-α coincidence method in the deuteron energy range from 1.0 MeV to 2.8 MeV, where no results were reported, and to obtain more information about the first excited state of He^5, especially in the energy-angle regions where the ground state of He^5 is not present.

II. EXPERIMENTAL APPARATUS AND PROCEDURE

The thin Li^7 target ($\sim$200 μg/cm^2) in the form of LiH evaparated on a carbon backing ($\sim$1 μg/cm^2) was bombarded by a deuteron beam provided by the National Tsing Hua University Van De Graaff accelerator. The target was mounted on a target holder, on which three targets can be placed and rotated manually from outside the chamber.

The bombarding deuteron beam were deflected through 25° by the analying magnetic to the 14″ scattering chamber and collimated by two slits to an area of approximately 0.5$\times$2mm^2 on the target. The strength of the magnetic field was measured by the Nuclear Magnetic Resonance method. The deuteron beam was collected by a Faraday cup after passing through the target and deuteron

charge was monitored by a currect integrator. The beam energy was calibrated precisely by the Li^7 (p,n) reaction. The experimental arrangement used for study Li^7 (d,α) He^5 (α)n reaction is shown in figure 1.

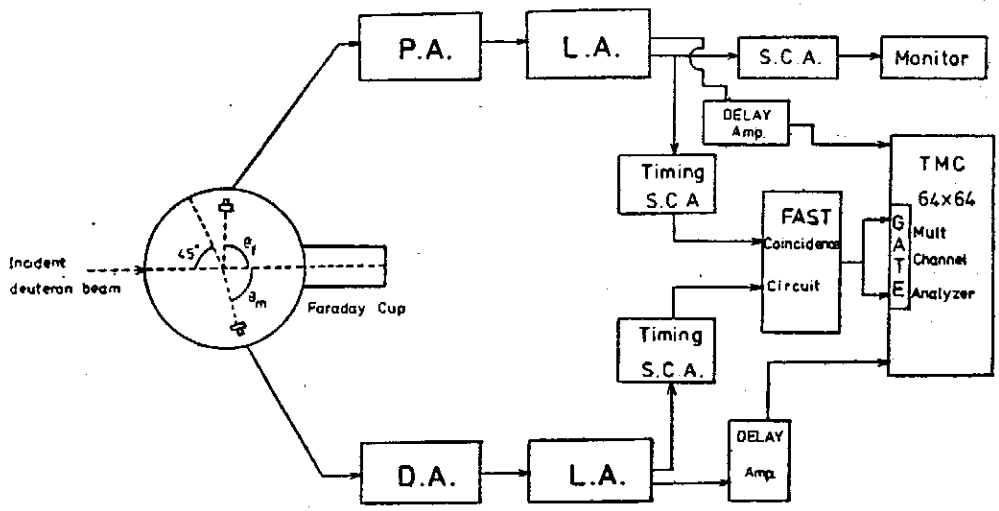

Fig.1

Fig. 1. Block diagram of the circuit used for measurement of the alpha-alpha coincidences.

The two surface barrier α detectors, f and m, are placed at 9.5cm distance from the center of target. The beam, detectors and target were adjusted complanate by a telescope. In order to reduce interference coulomb scattered deuteron, two collimating covers have been placed in front of each detector, those collimating covers have a hole about 2mm diameter.

The energy calibration for both detectors is made with the helps of a P_0^{210} and a A_m^{241} standard source, (wich give the 5.30 MeV and 5.48 MeV alpha-particles, respectively;) and the alpha-particle come from the reaction Al^{27} ($d\alpha$) Mg^{25} reaction and a standard pulse generator. The overall energy resolution was about 180 keV, The relation between energies and channel numbers of two dimensional coincidence spectra was calibrated by using pulse from a standard pulse generator, which was normalized previously.

In order to avoid serious pile-up caused by the elastic scattered deuterons from the target and the backing, the beam current was limited to 0.08 μA and the base line of both single channel analyzers was set to cut off about 2 MeV of alpha-particle signal.

The minotor was use to check the target condition and to normalize the counting rate in angular correlation data.

During present experiment, the energy excitation function were performed at bombarding energies from 1.0 to 2.8 MeV in steps of 0.2 MeV by fixed $\theta_f = 90°$ and $\theta_m = 65°$, the angular correlation was observed by fixed bombarding energy at 1.9 MeV and fixed angle at $\theta_f = 90°$ and the moving angle θ_m moved from 55° to 95° in step of 5° degree, In addition, a few two-dimensional coincidence spectra were observed in the energy-angle regions were ground state of He^5 is not present kinematically,

III. EXPERIMENTAL RESULTS AND DISCUSSION

A typical α-α two dimensional kineratic curve calculated from energy and momentum conservations in the case of direct three-body break-up process [11] at $E_d = 1.5$ MeV, $\theta_m = 60°$, $\theta_f = 105°$ is shown in Fig. 2. The black, x, and Δ points

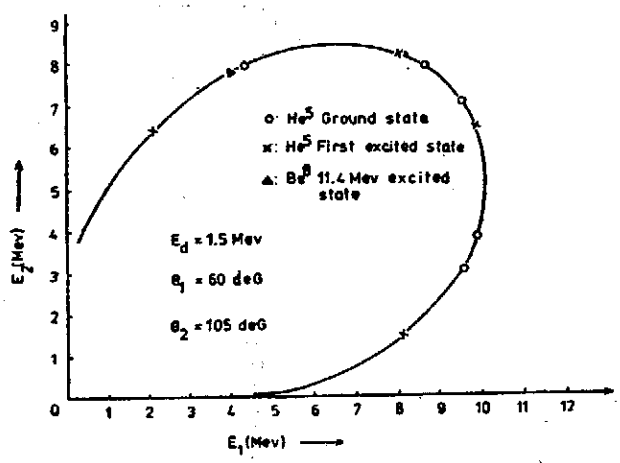

Fig. 2

Fig. 2. The Calculated kinematic locus fdr $E_d = 1.5$ MeV, $\theta_f = 60°$ and $\theta_m = 105°$ in Li^7 $(d.\alpha,\alpha)$ n reaction.

are the calculated positions where the ground state of He^5, the first excited state of He^5 (assuming 3 MeV) and the 11.4 MeV excited state of Be^8 located by assuming a sequential decay process. The α-α coincidence spectum at above energy and angles is shown in Fig. 3. In Fig. 3(a) the experimental coincidence events are shown, the events are all located on the kinematical locus as expected. The data in Fig. 3(b) is presented as projection onto the E_m axis and the data in Fig. 3(c) is presented as projection onto the E_f axis. The projection onto the E_m axis contains only the events above the horizontal dash line, while projection onto the E_f axis contains only the events on the right from the Vertical dash line. The arrows in the Fig. indicate the expected

positions of the ground and first excited state of He^5 and also the 11.4 MeV state of Be^8. Only these state ate kinematcially allowed.

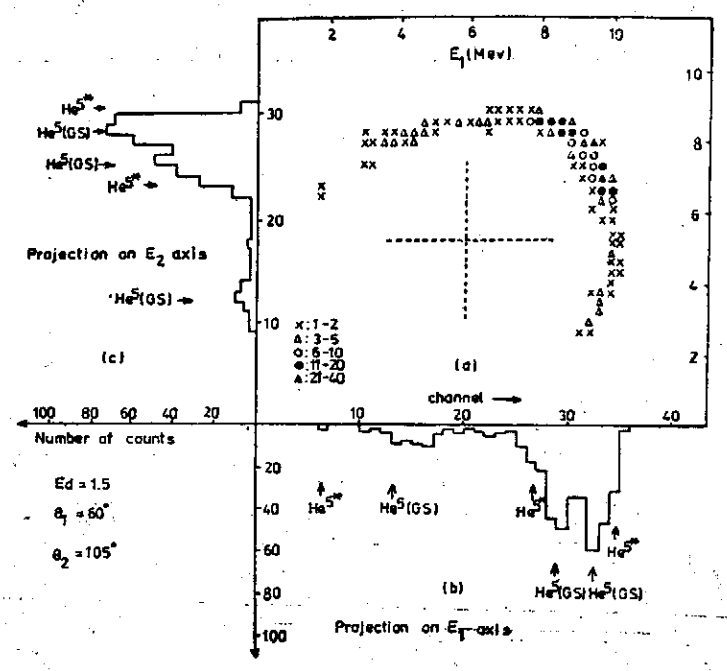

Fig. 3

Fig. 3. The alpha-alpha coincidence spectrum at E_d=1.5 MeV, θ_f=60° and θ_m=105°. The dash lines indicate how the data projection onto the E_f and the E_m axes were made. The projecton onto the E_f axis contains only the events above from the horizontal dash line, while the projection onto E_m axis contains only the events on the right from the vertical dash line.

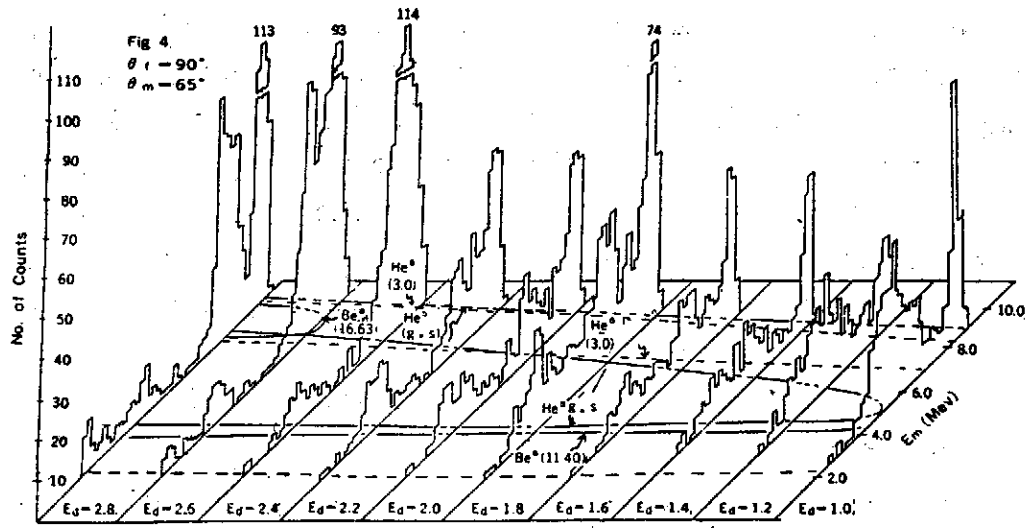

Fig. 4. Projection of the α-α coincidences spectra onto the E_m axis for all bombarding energies at θ_f=90°, θ_m=65°.

α-α Coincidence spectra were measured at bombarding energy from 1.0 to 2.8 MeV in step of 0.2 MeV for $\theta_m^l=65°$ nda $\theta_f^l=90°$, the projections of all measured spectra onto the E_m axis and the E_f axis are shown in figure 4 and figure 5 respectively; where the data are normalized by the current integrator.

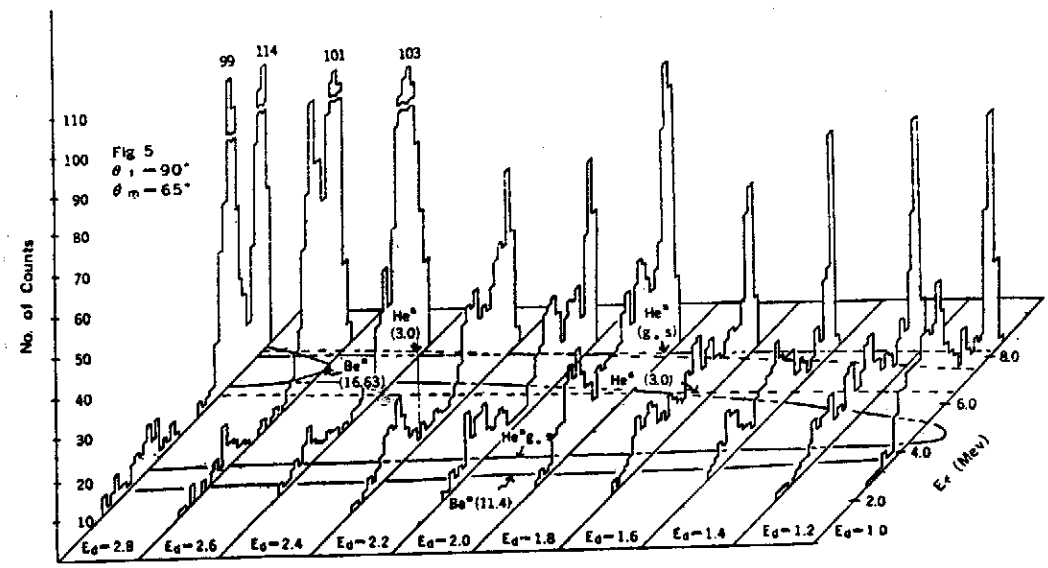

Fig. 5. Projection of the α-α coincidences spectra onto the E_f axis for all bombarding energies at $\theta_f=90°$, $\theta_m=65°$.

The solid lines represent the positions of the ground state in He^5, the 11.4 MeV state and the 16.63 MeV state in Be^8. The dash lines represent the position of the first excited state in He^5 assuming excitation energy at 3 MeV. In the figure 4 or 5, one can see that the contribution of the cross-section is normally increasing with the bombarding energy, and a resonance peak in sequential decay is observed at bombarding energy of 1.8 MeV. The He^5 ground state and He^5 first excited state are excited. The first excited state of He^5 is evident especially in the low energy (1.0~1.4 MeV) range where no other state in the same energy region of the α-spectra is kinematically possible. The Be^8 11.4 MeV state is very weakly excited through the energy range at this fixed angles.

At bombarding energy 2.6 MeV, the contribution of 16.63 MeV state of Be^8 come into the spectrum. This results are consistant with previous report [17] at deuteron energy range from 2.6 to 4.0 MeV, and with the previous "incomple" experiment[12] in the deuteron energy rang from 0.6 to 3.0 MeV.

Another set of α-α coincidence spectra have been observed at bombarding

energy 1.9 MeV for fixed one of detector at θ_f=90° and moving other detector from θ_m=55° to 95° in step of 5°. Figure 6 and figure 7 are shown the results

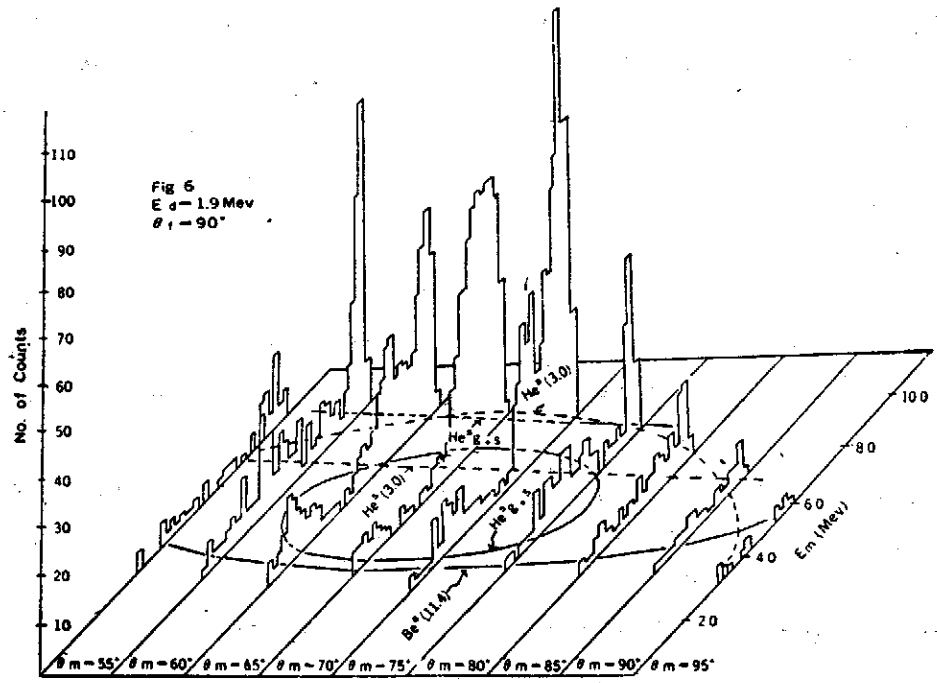

Fig. 6. Projection of the α-α angular correlation coincidences spectra onto the E_m axis at E_d=1.9 MeV, θ_f=90°.

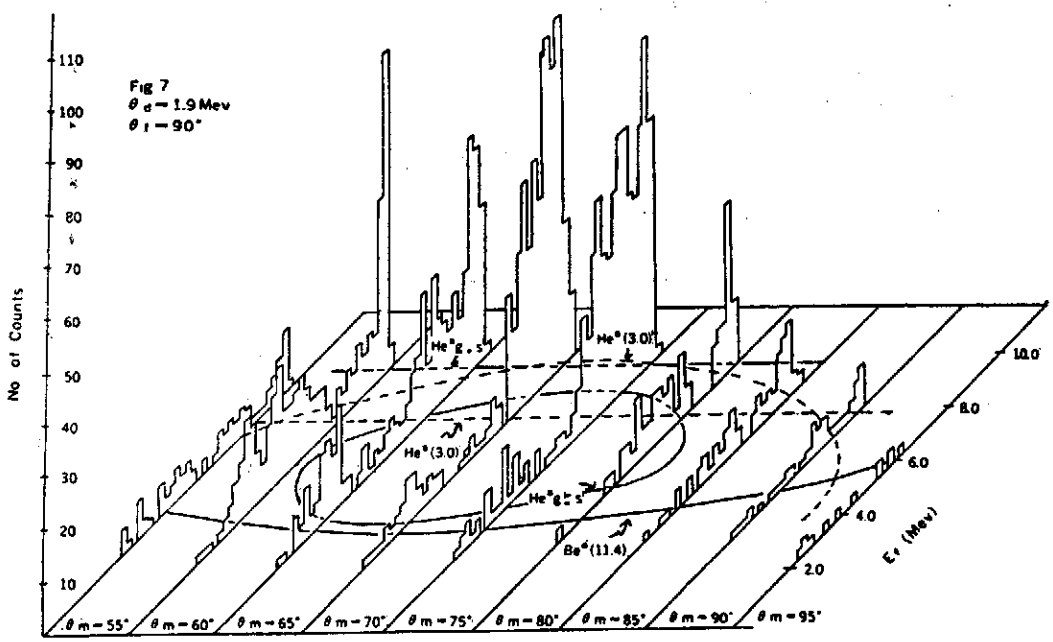

Fig. 7. Projection of the α-α angular correlation coincidences spectra onto the E_m axis at E_d=1.9 MeV, θ_f=90°.

as projection onto the E_m axise and onto the E_f axis respectively. The spectra were normalized to each other by monitoing the alpha particles by the detector at fixed angle $\theta_f=90°$. The solid lines represent the position of ground state of He^5 and 11.4 MeV state of Be^8. The dash lines represent the position of the first excited state of He^5 assuming excited enegy at 3.0 MeV. In the figure 6 or 7, one can see that the ground state of He^5 are existed in a small cone from $\theta_m^i=60°$ to $\theta_m^i=80°$ and the contribution of cross section is maximum near the recoil angle ($\theta_m^i=71.4°$) of the intermediate system as expected. The first excited state of He^5 around 3 MeV is clearly seen especially near the recoil angles ($\theta_m^i=65\sim75°$). The 11.4 Mev state in Be^8 is barely seen.

A few additional α-α coincidence spectra were taken at energy-angle regions where the ground state of He^5 are not present kinematically.

Due to the complication of the decay channels and the measurement of two identical α-particles. We are difficult to analysis those measured spectra directly. A method of analysis[22,23] is considered for fitting the spectra to estimate the positions and widths of the excited states.

The reaction cross section is give[22] for each decay channel

$$\frac{d\sigma_{exp}}{dE_1 d\Omega_1 d\Omega_2}=F\{[C(\theta_2)+\sum_n \frac{\Gamma_n B_n(\theta_2)+(E_x-E_n)A_n(\theta_2)}{(E_x-E_n)^2+\Gamma_n^2/4}]\sigma(E_1)\}$$

where

$$B_n=\sum_i \frac{1}{2}B_{in}P_i(\cos\theta_{RCM})$$

$$A_n=\sum_i \frac{1}{2}A_{in}P_i(\cos\theta_{RCM})$$

θ_{RCM}=recoil system center of mass

$\rho(E_1)$=phase space factor

$F=\frac{1}{\sqrt{2\pi}\Delta E}[\frac{1}{2}\frac{(E-\bar{E}^2)}{(\Delta E)^2}]$ the operation of folding the theoretical curve with the experimental resolution, was taken to have a gaussian form.

A computer fitting program has been written for the above formula. Several spectra with clear first excited state of He^5 have been fitted. The first excited state of He^5 have been estimated to have an excitation energy of 3.0 ± 0.5 MeV and a width of 1.5 ± 0.3 MeV.

IV. LIST OF REFRERENCE

1. Phillips, G.C. and Tombrello, T.A., Nuclear Physics **19** (1960) 555.
2. Ajzenbert-Selove, F. and Lauritsen, T., Nuclear Physics. **11** (1959) 7.

3. Cuer, P. and Jung, J.J., Comput Rend 236, 1253 (1953) Jung, J.J. and Cuer, P. Physics. **22**, 1159 (1956).
4. Riviere, A.C., Nuclear Rhysics **2**, 81 (1956/57).
5. Frye, G.M., Jr. Phys. Rev. **93**, 1086 (1954).
6. Weber, G., Phys. Rev. **110**, 529 (1958).
7. Hannah, B. O., Carter, E. B. and Davis, R.H. Bull. Am. Phys. Soc. **5**, 229 (1960).
8. Friedland, E. Venter, I.E. Phys. (Germany) **284**, 126 (1971).
9. Fressender, Peter and Maxson, D.R., Phys. Rev. Vol. **133** B71 (1964).
10. Johnson, C.H. and Tratl, C.C., Phys. Rev. 153 (64) B1183.
11. Spear, R.H., Australian J. Phys. **11**, 502 (1958).
12. Paul, P. and Kohler, D., Phys. Rev. **129** (63) 2698.
13. Assimakopoulos, P.A., Gangas, N.H. and Kosszonides, S., Nuclear Physics 81 (1966) 305.
14. Milove, C. and Dotenza, R., Nuclear Physics. **84** (1966) 25.
15. Jerremie, H., Martain, Pa. and Calamand, A., Nuclear Physics A**105** (1967) 689.
16. Wise, M.N. Washinton State Unv. Thesis Univ. Microfilms, Ann. Arbor, Mi USA (1968) 65.
17. Vallkovic, V., Jckson, W.R., Chen, Y.S., Emerson, S.T. and Phillips, G.C., Nuclear Physics A**96** 241 (1967).
18. Hofman, G. Zeit-Physik (Germany) Vol. **224**, No. 5 P446-60 (1969).
19. Flannant, Par. Y., Chanut, Y. and Dalline, R. Journal, Le. Physique, De. **28** (1967) 622.
20. Wen M., Wang, W.N. and Wang, D. Ann Rept. Inst. Phys. Acad. Sin. **1973** 23 (1974).
21. Ohlsen, G.G., Nuclear Instruments and Methods **37** 240 (1966).
22. Haase, E.L., Wang, W.N. and Fawze, M.A. Nucl. Phys.A**172** 81 (1971).
23. Haase, E.L., Haqulberg, R. and Wang, W. N. Nucl. Phys. A**188** 89 (1972).

Annual Report of the Institute of Physics, Academia Sinica, Vol. 6, 1976

Elastic Scattering of Protons from ^{12}C and ^{16}O*

E. K. Lin

Academia Sinica and Tsing Hua University, Taiwan, China

and

W. C. Tung

Institute of Nuclear Energy Research, Atomic Energy Council, Taiwan, China

Abstract

The elastic scattering of protons from ^{12}C and ^{16}O has been studied for proton energies from 1.5 to 3.0 MeV. Excitation functions have been obtaind at center-of-mass angles of 84.7°, 104.7°, 133.7° and 152.4° for ^{12}C and of 132.8° and 151.8° for ^{16}O. Angular distributions have been measured at three off-resonance energies, E_p=2.0, 2.5 and 3.0 MeV. The 1.73 MeV anomaly in ^{12}C $(p,p)^{12}C$ and the 2.66 MeV anomaly in $^{16}O(p,p)^{16}O$ were observed. The differential cross sections obtained in the present experiment are in reasonable agreement with existing data. Partial wave analysis was made for the $^{12}C(p,p)^{12}C$ data, and the parameters concerning the resonance level in the compound nucleus ^{13}N were obtained.

I. INTRODUCTION

The elastic scattering of charged particles has been studied rather extensively in the last decade. A large volume of data has been accumulated and analyzed in terms of scattering from a complex potential well on the basis of the optical model. From the results of such analyses considerable information has been accumulated on the parameters obtained by fitting such a well to the experimental data. In particular, experimental investigations of protons elastically scattered by nuclei at various energies have been reported [1-7]. These results at energies above about 10 MeV show the regular behaviour in the angular distributions as a function of both energy and atomic nuclei. The data of the low-energy experiments at energies below 10 MeV show the complicated behaviours and especially for the light and light medium weight nuclei[4-7], they show the anomalies behaviour and some resonance phenomena. For example, the anomalies have been observed in the elastic scattering of protons by ^{12}C and ^{16}O at 1-3 MeV. The anomaly at 1.73 MeV in the elastic scattering of protons from ^{12}C has been determined from a theoretical fit data

* Work supported partially by the physics research center, National Science Council, Taiwan, China.

obtained at several scattering angles to be associated with $5/2^+$ (Γ=74 keV) resonance[8], and the 2.66 MeV anomaly in the elastic scattering of protons from ^{16}O has been adequately explained[9] by the assumption of a single level resonance with $\Gamma=20\pm1$ keV, $J^\pi=1/2^-$.

The present work was undertaken to provide accurate absolute differential cross section measurements of the elastic scattering of protons by ^{12}C and ^{16}O at E_p=1.5−3.0MeV. Such data are of use in the interpretation of the angular distribution of the reaction products to be investigated in this laboratory. Also, an attempt was made to investigate the 1.73 MeV and the 2.66 MeV anomalies in the $^{12}C(p,p)^{12}C$ and $^{16}O(p,p)^{16}O$, respectively. We have calculated the theoretical cross sections using a CDC 3300 computer with parameters which give the best fit to the experimental data.

II EXPERIMENTAL

The Tsing Hua University 3.0 MeV Van de Graaff accelerator was used to accelerate the protons. The experimental equipment used for the measurement of the $^{12}C(p,p)^{12}C$ and $^{16}O(p,p)^{16}O$ absolute cross sections has been described in detail in a previous paper[10] where we reported the elastic scattering of 1.5 −3.0 MeV deuterons by ^{12}C, ^{25}Mg and ^{27}Al. In brief, a magnetically analyzed proton beam from the accelerator bombarded the prepared target contained in a scattering chamber. Two solid state detectors were used to monit the scattering protons. The detection system was adjusted to select and count only the desired elastically scattered protons. The accumulation of beam was performed by using a current integrator and a monitor. The total number of protons scattered elastically at a given angle was averaged over counts from two detectors. The thickness of targets and the geometric factors were determined by normalizing the data to the Rutherford scattering cross section for elastic scattering of protons at 1.0 MeV. From these normalizations the absolute values of the differential cross section were determined. The uncertainties in the obtained absolute cross sections are believed to be approximately within 10%.

III. RESULTS AND DISCUSSION

The data obtained in this measurement for the elastic scattering of protons by ^{12}C and ^{16}O consist of excitation curves measured in the energy range 1.5 to 3.0 MeV and angular distributions measured in the angular range 40° to 140° at an interval of $\Delta\theta=10°$. The center-of-mass angles chosen for the

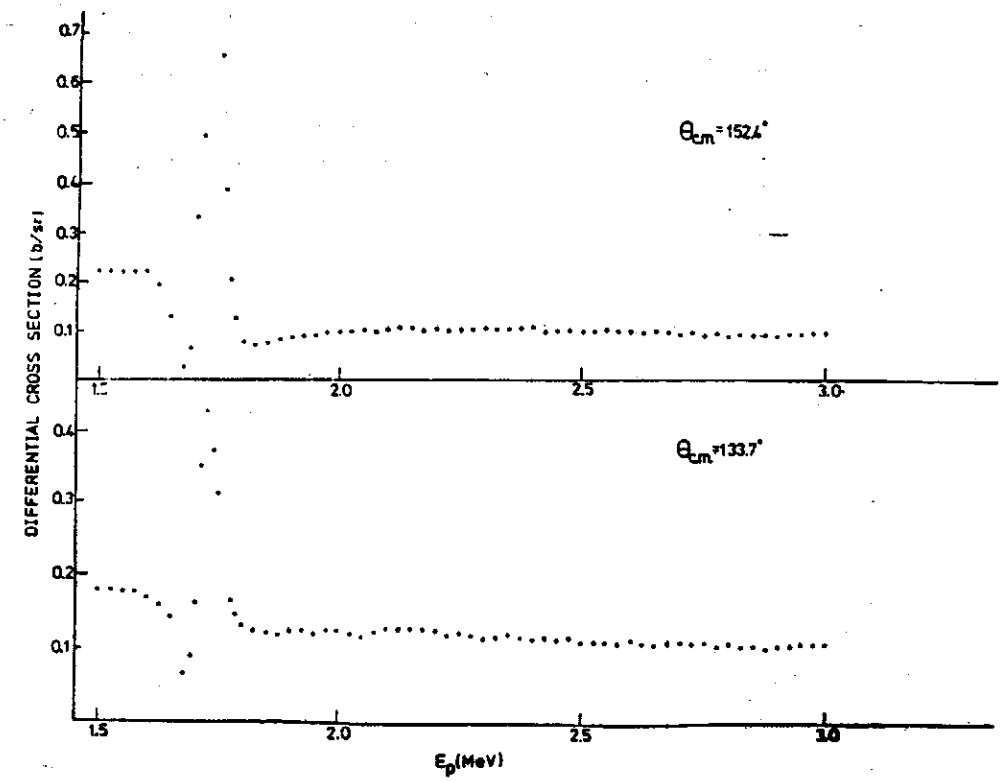

Fig. 1. Differential cross section for elastic scattering of protons from ^{12}C in the incident-proton energy range 1.5 to 3.0 MeV. (a) $\theta_{c.m.}=133.7°$, (b)$\theta_{c.m.}=152.4°$,

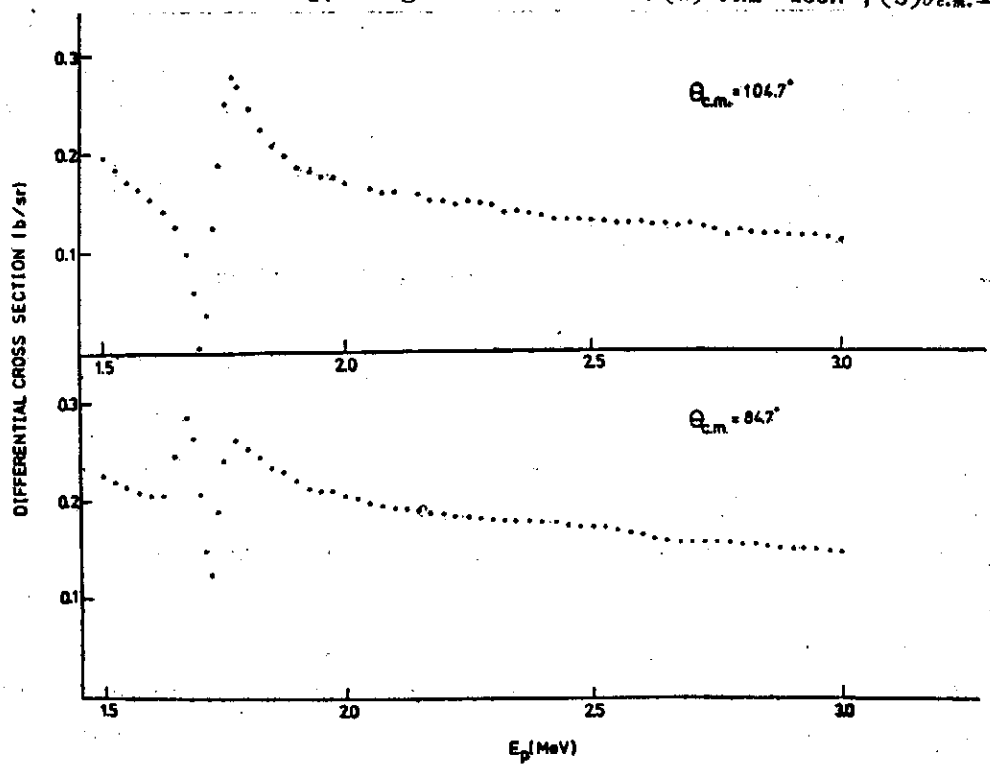

Fig. 2. Differential cross section for elastic scattering of protons from ^{12}C in the incident-proton energy range 1.5 to 3.0 MeV. (a) $\theta_{c.m.}=84.7°$, (b) $\theta_{c.m.}=104.7°$

excitation curves were 84.7°, 104.7°, 133.7° and 152.4° for $^{12}C(p,p)^{12}C$ scattering and 132.8° and 151.8° for $^{16}O(p,p)^{16}O$ scattering. Figs. 1 and 2 show the $^{12}C(p,p)^{12}C$ center-of-mass differential cross section (in barns/steradian) vs bombarding energy at 84.7°, 104.7°, 133.7° and 152.4° and Fig. 3 shows the $^{16}O(p,p)^{16}O$

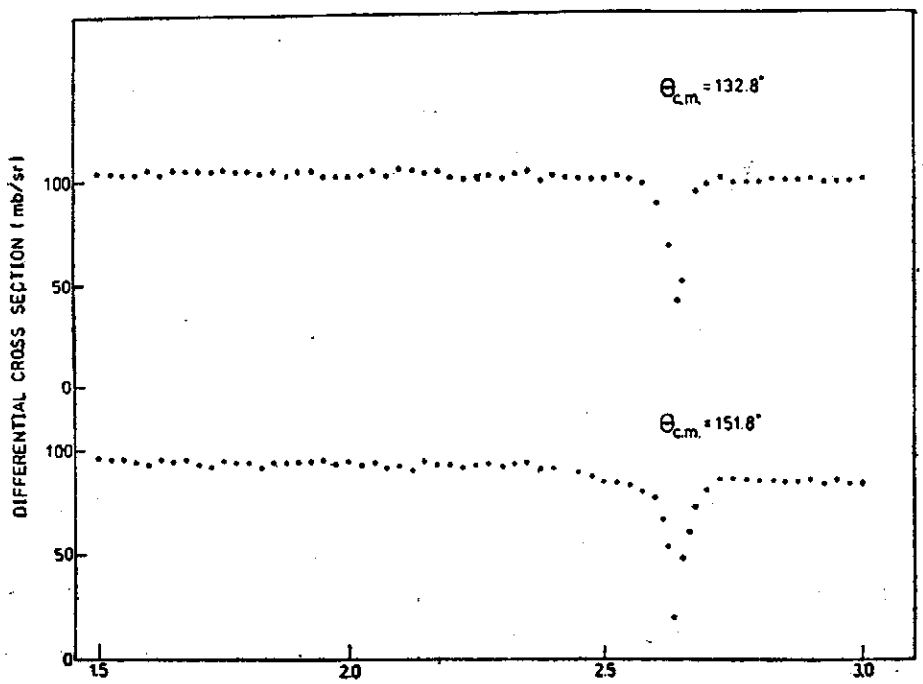

Fig. 3. Diffential cross section for elastic scattering of protons from ^{16}O in the incident-proton energgy range 1.5 to 3.0 MeV. (a) $\theta_{c.m.}=132.8°$, (b)$\theta_{c.m.}=151.8°$

center-of-mass differential cross section vs bombarding energy at 132.8° and 151.8°. The $^{12}C(p,p)^{12}C$ and $^{16}O(p,p)^{16}O$ center-of-mass differential cross sections vs center-of-mass angles at three off-resonance energies (E_p=2.0, 2.5 and 3.0 MeV) are shown in Figs. 4 and 5.

As is clearly seen in Figs. 1-3, the anomaly at 1.73 MeV in the elastic scattering of proton by ^{12}C and the 2.66 MeV anomaly in the elastic scattering of protons by ^{16}O appear at all angles of observation. It was found that for ^{12}C the values of maximum cross section σ_{max} lie between 0.28—0.8 b/sr, and the differential cross sections increase as angle increases. For ^{16}O, the measured differential cross sections appear to be much smaller than those for ^{12}C.

It is noted from the angular distributions as shown in Fig. 4, that the differential cross sections for ^{12}C decrease rapidly at forward angles and become approximately constant at backward angles. The results agree very well with the values previously reported[7,8]. For ^{16}O, the angular distributions as shown in Fig. 5 are presented as the ratio of measured cross section to

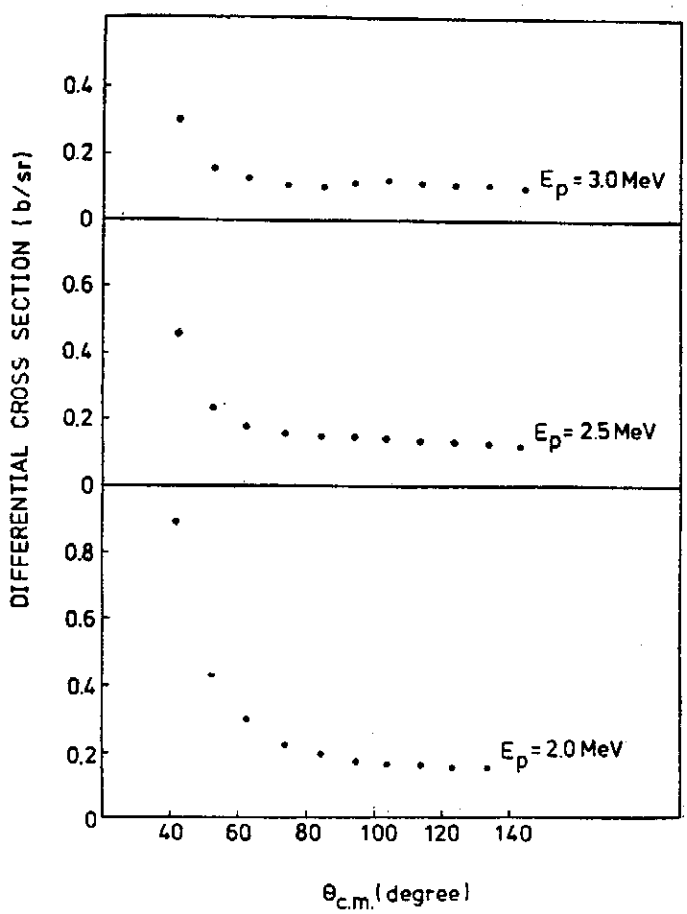

Fig. 4. Angular distributions of elastically scattered protons by ^{12}C at three didfferent energies.

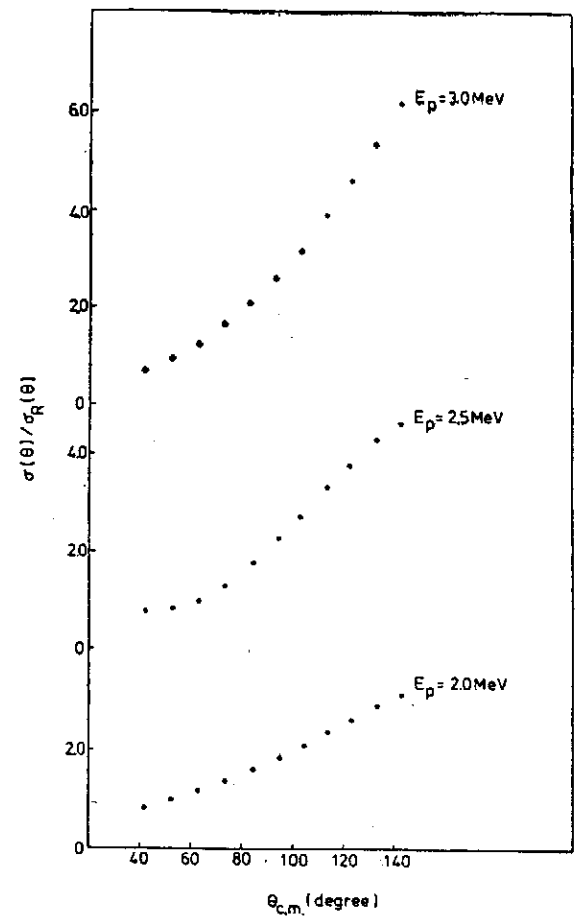

Fig. 5. Angular distributions of elastically scattered protons by ^{16}O at three different energies.

the Rutherford cross section, $\sigma(\theta)/\sigma_R(\theta)$, vs center-of-mass angles. It was intended to compare our results on the differential cross section with previous measurement by V. Gomes et al[9]. The agreement was found to be good within experimental error.

The cross section data of $^{12}C(p,p)$ show an anomaly at 1.73 MeV indicating the presence of a resonance level in the compound nucleus ^{13}N. A partial wave analysis was performed using excitation function data at four angles as the input to the computer programme. The theory formalism used in this analysis and the usual methods of applying it are already described in the literature[11,12]. The 1.73 MeV anomaly is the only resonance which appears in the energy range investigated. The assumption made in the analysis that only one level with angular momentum and parity well defined is involved is valid. The Coulomb wave functions used in the analysis are calculated as shown in the

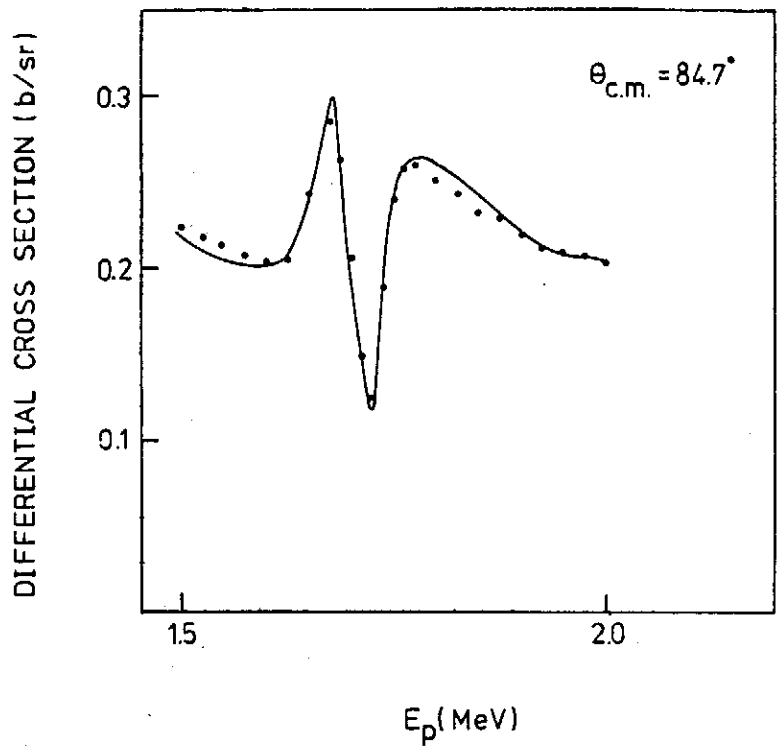

Fig. 6. Typical fit to the excitation function data obtained from ^{12}C $(p,p)^{12}C$ at $\theta_{c.m.}=84.7°$ Experimental results are shown as points and the curves give the results of the analysis.

Appendix[13] by using a CDC 3300 computer. Typical fit obtained to the data at $\theta_{c.m.}=84.7°$ is shown in Fig. 6. The resonance energy, E_p, reduced width, γ^2, the characteristic energy of the resonance, E_i, for the $J^\pi=5/2^+$ level associated with the 1.73 MeV anomaly have been determined from a best fit to the data. The interaction radius, a, was fixed at 4.77F throughout the analysis. The results are as follows:

	Present work	Previous work[8]
E_p(MeV)	1.723	1.734
E_i(MeV)	3.598	3.609
E_R(MeV)	3.536	3.546
γ^2(MeV cm $\times 10^{-13}$)	3.31	3.55
Γ(keV)	70	74

The resulting parameter values are in good agreement with previous work[8] although there is a few keV discrepancy in energy value. More detailed analysis will be given in a next paper.

We wish to thank the members of the Van de Graaff accelerator laboratory at Tsing Hus University for their technical assistance. We are also indebted to C. L. Wang of the Conputer Center of the Instituteof Nuclear Energy Research for aid in the computer programming.

Appendix

Calculation of Coulomb Wave Functions

We have used the numeical treatment of these functions based on the paper of E. C. Froberg.[14] The solutions of the differential equation

$$\frac{d^2Y}{d\rho^2}+\left[i\frac{2\eta}{\rho}-\frac{L(L+1)}{\rho^2}\right]Y=0$$

are encountered as the radial component in the separation of Schrodinger's wave equation for a Coulomb field of force and continuous energy values. They are useful for the calculation of scattering of charged particles from atomic nuclei or their binding by nuclei. From the known theory of the confluent hypergeometric function, it may be shown that the above equation has a regular solution $F_L(\eta,\rho)$ and a irregular solution $G_L(\eta,\rho)$.

Where

ρ=kr, r is the interparticle separation

$k=\sqrt{2\mu E/\hbar^2}=0.2195376\sqrt{\mu E}$ fermi^{-1}

$\mu=m_i m_t/m_i+m_t$, the reduced mass

m_i=mass of incident particle in amu

m_t=mass of target in amu

$\hbar$=Planck's constant/2π

$L\hbar$=angular momentum

$E=\dfrac{m_t}{m_i+m_t}E^{lab}$ in MeV

E^{lab}=Energy of the indicent particle in the laboratory system.

The Coulomb wave functions depend on ρ,η and L. However, by making use of L being an integer, F_{L+1} can be computed if F_L and F_L' are known. Therefore, we compute F_o,F_o', G_o and G_o' first, then using the recurrence formulas to obtain the rest. These functions and their derivatives calculated are tabulated, and for a given L, ρ and η we may obtain F_L, G_L, F_L', G_L' directly from table.

Accordingly we have developed a subroutine for calculation of Coulomb wave functions on a computer of CDC 3300. The results have been checked well with the avaliable data to five figures.

Reference

1. J. Eenmaa, R. K. Cole, C. N. Waddell, H. S. Sandhu, R. R. Dittman, Nucl. Phys. A218, 125 (1974).
2. Y. Oda and M. Murakami, J. Phys. Soc. Japan 30, 1217 (1971).
3. C. Pegel, Proceedings of International Conference on Nuclear Physics, Volume 1, Munich, Germany, 27 Aug. —1 Sept. 1973, p. 334.
4. H. L. Jackson, A. I. Galonsky, F. J. Eppling, R. W. Hill, E. Goldberg, and J. R. Cameron, Phys. Rev. 89, 365 (1952).
5. C. W. Reich, G. C. Phillips, and J. L. Russell, Jr., Phys. Rev. 104, 143 (1956).
6. H. L.Jackson and A. I. Galonsky, Phys. Rev. 89, 370 (1953).
7. A. C. L. Barnard, J. B. Swint, and T. B. Clegg, Nuc. Phys. 86, 130 (1966).
8. J. C. Armstrong, M. J. Baggett, W. R. Harris, and V. A. Latorre, Phys. Rev. 144, 823 (1966).
9. V. Gomes, R. A. Douglas, T. Polga and O. Sala, Nuc. Phys. 68, 417 (1965).
10. W. N. Wang, E. K. Lin, C. C. Hsu, T. Chiao and C. C. Chu, Chin. J. Phys. 5, 1 (1967).
11. R. A. Laubenstein and M. J. W. Laubenstein, Phys. Rev. 84, 18(1951).
12. L. J. Koester, Phys. Rev. 85, 643 (952).
13. W. C. Tung and C. L. Wang, Technical Report, Institute of Nuclear Energy Research, Atomic Energy Council, June, 1971.

Annual Report of the Institute of Physics, Academia Sinica, Vol. 6, 1976

Surface Scattering of Optical Waves in Graded Index Waveguides*

N. T. Liang

Academia Sinica, Instiute of Physics
Nankang, Taiwan, Rep. of China

and

Shou-Yih Wang, Been-Yih Jin, Hwa-Yueh Yang

National Tsing Hua University, Institute of Physics
Hsinchu, Taiwan, Rep. of china

Optical waveguides formed by diffusion processes or ionexchange processes have been reported by many authors[1]. Among a number of advantages of these graded index waveguides over the usual uniform index slab type waveguide low propagation loss would be the most important. Loss of propagation in an optical waveguide usually results from boundary scattering and bulky loss. As bulky loss consists of scatterings and absorptions along an optical path, it depends largely on the optical quality of waveguide material. Besides, it dose not contribute to the overall attenuation as much as the surface scatterings especially in typical slab-type waveguides. Therefore we will discuss boundary scatterings alone. Giallorenzi et al[2]. showed experimentally very low attenuation due to boundary scatterings and claimed inadequacy of a simple formula given for uniform index waveguides by Tien[3]. Rigorouse treatment of boundary scatterings and mode conversions has been done on uniform index symmetrical waveguides by Marcuse[4]. However the simple formula of Tein, which was nicely deduced and shown to be consistent with the formal theory of reference 4, gives clear physical insights. It deserves discussions how the formula is to be applied to graded index waveguides. To

* Sponsored by NSC of ROC,

discuss the matter we imagine a graded index waveguide to be divided into many thin layers each of constant and uniform refractive index, just as that treated by Hocker and Burns[5]. Within each layer of the guide one can use ray optics as is usually used in slab type guides[3]. Clearly the layer involving the upper boundary should contribute most to the surface attenuation. Thus, within the upper layer, the arguments employed in Ref. 3 in deriving the simple formula for surface scattering should still apply to the case of graded index waveguides. In this paper we shall use certain results of Ref. 2 and Ref. 3 and discuss via the simple formula some inherent properties of low surface attenuation in graded index waveguides.

Let the power flux of an optical guided wave propagation along x direction in the waveguide be proportional to an usual exponential function $\exp(-\alpha x)$. α is well known as the attenuation constant characterizing the loss per unit length of optical power while propagating in the waveguide. The simple formula mentioned above for an uniform index waveguides takes the form:

$$\alpha = K^2\left(\frac{1}{2} \cdot \frac{\cos^3\theta}{\sin\theta}\right)/W_{eff} \tag{1}$$

where we have from ref. 3.

$$K^2 = (4\pi/\lambda_1)^2(\sigma_{10}^2+\sigma_{12}^2). \tag{2}$$

The first factor of α, K^2, represents surface roughness of a waveguiding film with σ_{12}^2 and σ_{10}^2 as the variances of the irregularities respectively at the upper and lower Surfaces. λ_1 is the wavelength of light in the waveguide. The second factor of α, $(\cos^3\theta/2\sin\theta)$, depens very sensitively on modal index m for an uniform index waveguide. θ is the incident angle of the the zigzag light ray to the boundary surfaces. The third factor W_{eff} is the effective thickness of a waveguide. It is given as[3]

$$W_{eff} = W+1/P_2+1/P_0 \tag{3}$$

where W is the actual thickness of the wave-guiding film whereas $1/P_2$ and $1/P_0$ are the characteristic depths of the decaying exponential fields of the guided wave extended beyond the upper and lower film boundaries respectively. The dependence of P_2 and P_0 on modal index m would be very much insensitive as compared to that of the second factor.

We combine some results of Tien[3] and Giallorenzi et al[2]. in Fig. 1. As claimed by Tien the attenuation constant for the mode m=3, in a uniform index Ta_2O_5 film is about 14 times larger than that for the mode m=0. This

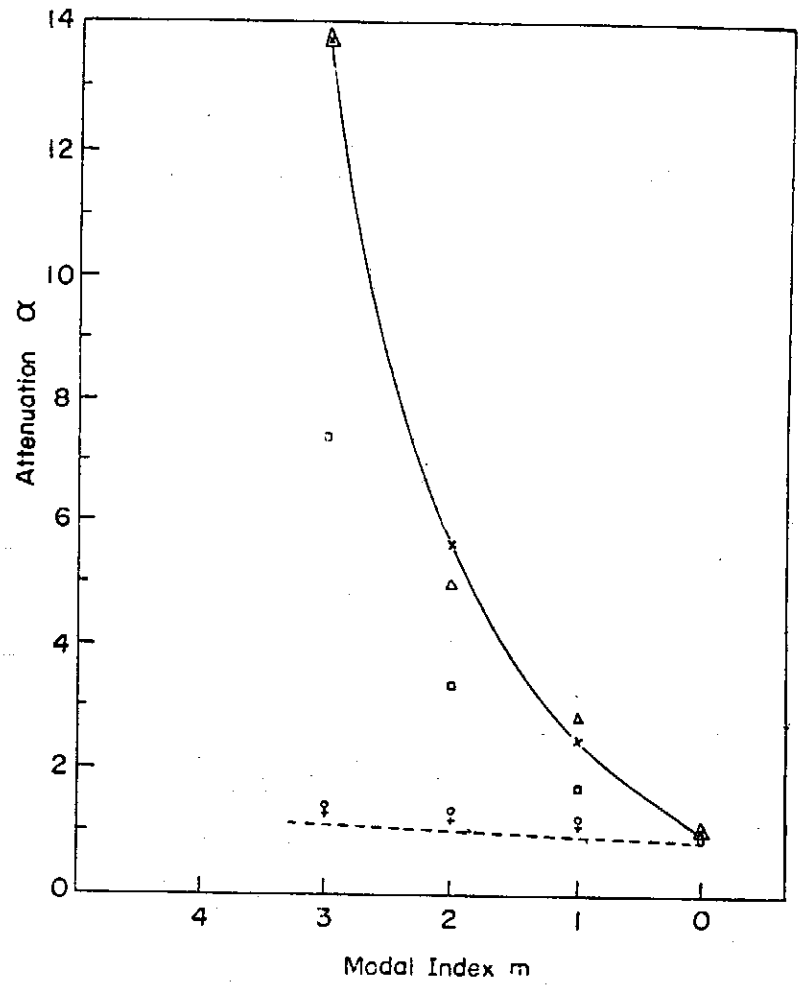

Fig. 1. Comparing and demonstrating various modal dependence of attenuations: ×and △are Tien's theoretical and experimental values respectively in Ref. 3; ○and+are Giallorenzi's stirred and unstirred data respectively in Ref. 2: □are Tien's theoretical values if σ_{10} were assumed zero; dotted line represents the bulk contribution to modal attenuation as that shown in Ref. 3 and 2; all the attenuations for modal $m=0$ are normalized to unity.

strong modal dependence has been successfully explained by Tien using Eq. (1). On the contrary the modal attenuation of guided optical waves in Ag^+ ion-exchanged waveguides has been found very small by Giallorenzi et al[2].. Its negligibly small modal dependence is shown with pluses + for unstirred ion-exchanged processes and circles ○ for stirred processes. To understand the low attenuation of graded index waveguides we will note some inherent properties of these waveguides over the uniform index ones. For an ion-exchanged waveguide or other kinds of graded index the variance of surface

roughness σ_{10}^2 should vanish inherently because of the lack of lower interface. Furthermore, since the authors of Ref. 3 had delibrately treated the surface of ion-exchanged waveguides with fine optical polish, the variance of upper surface σ_{12}^2 could be very small as compared to those without specially treated. This explains partly how they obtained such low surface-loss waveguides as compared to Tien's. Based on the formula for K^2 one could possibly control or make vanishingly small the loss due to surface scattering by controlling the fineness of surfaces. In Tien's results if σ_{10}^2 were set to zero, the attenuation would drop to those denoted by squares □ in Fig. 1. We include these for better comparison and assumed $\sigma_{12}=\sigma_{10}$ in drawing them. Apart from this substantial influence to α the modal dependece is still strikingly small for Giallorenz's o or + as compared to the squares □. This strong modal dependence should stem from the second factor of *Eq.* (1), ($\cos^3\theta/2 \sin\theta$). It is interesting to note that the modal angle θ in graded index waveguide depends on the profile of refractive index n_s at the upper boundary surface of a waveguide. For most cases one would encounter approximately come plementary error functions, Gaussian of exponential profiles. For these types of profiles the graded index has its maximum occuring at the upper surface. As a result, the angle θ near the surface is the smallest of those well below the surface because of the Snell's law:

$$n_s \sin\theta_s = n_i \sin\theta_i \tag{4}$$

where n_s, θ_s and n_i, θ_i are respectively the index and index and incident angle at the surface and in the ith layer of a graded index waveguide when divided into many thin layers as mentioned above. The dependence of θ_s on mode is through the relation:

$$\sin\theta_s = n_{eff}/n_s \tag{5}$$

where n_{eff} is the effective refractive index[5] depending on mode. For higher modal index m, n_{eff} is lower and makes the modal factor ($\frac{1}{2}\cos^3\theta/\sin\theta$) larger. For uniform index slab-type waveguides this factor is very sensitive to the incident angle because change in θ is comparatively much larger. From Ref. 3, we estimate the factor for m=3 to be about 79 times as big as that for m=0. For graded index waveguides this factor is much less sensitive because change in n_{eff} is very small. One can estimate the narrow range of n_{eff} from the following two relations:

$$n_s = n_b + \Delta n, \tag{6}$$

$$n_b < n_{eff} < n_s, \tag{7}$$

where n_b is the refractive index of the bulk substrate and Δn is typically much less than 0.1. This is another inherent property of graded index waveguide which yields very low modal attenuation when compared to uniform index waveguides. The third factor in *Eq.* (1) is the effective thickness W_{eff}. The actual thickness W of an uniform index waveguide would be at least one order of magnitude smaller than the maximum depth W_m of optical ray during propagation in a graded index waveguide if both guides carry the same number of modes of guided wave. W_m can be obtained from $n(W_m)=n_{eff}$ where $n(y)$ is the index profile along the thickness direction y of the guide. To faciltate the comparison one may simply apply a two-mode procedure[6] for slab typ guides to calculate an equivalent refractive index $n_{eq.}$ and an equivalent film thickness $W_{eq.}$ of a graded index waveguide. This procedure, although developed only for uniform index waveguides, is based on measurements of angular positions of all guided modes. The equivalent thickness $W_{eq.}$ computed this way would be much smaller than W_m or even the diffusion depth D of the waveguide. In comparsion to a uniform index waveguide with same number of modes this inherent feature of larger $W_{eff.}$ for graded index waveguides substantially reduces attenuation constant as can be clearly seen from *Eq.* (1). The modal dependence of W_m is again interesting in the sense that higher modes tend to decrease the attenuation. The reason is that as modal index m increases, n_{eff} decreases and the W_m obtained from $n(W_m)=n_{eff}$ should increase. This modal dependence of W_m would greatly reduce that of the second factor of *Eq.* (1) and could practically result in negligibly small modal attenuation as that of Giallorenzi et al.

The effect of stirring during ion-exchange can be visulized again from *Eq.* (1). In Fig. 2b of Ref. (3) when comparison is made to stirred sample the unstirred sample has its peak of Ag^+ concentration profile displaced to about 6 μm from the boundary surface. The corresponding refractive index at surface n_s should be smaller than its peak value at about 6 μm below surface. Consequently the corresponding incident angle θ_s at surface in eq. (4) becomes larger and results in smaller attenuation constant α via *Eq.* (1). Besides, as the profile is displaced inside the surface, the maximum thickness W_m for a given mode m again becomes larger in the unstirred sample. This further decreases α via *Eq.* (1). Thus the remarkably lower attenuation should occur in the unstirred sample than the stirred as shown in Fig. (1). In conclusion, the simple *Eq.* (1) has been applied to describe the attenuation of surface

scatterings in graded index waveguides. Qualitatively, it suffices to account for the striking difference between the results of the uniform index waveguide of Tien's and the graded index ones of Giallorenzi et al.. Detailed and quantitative computation with experimental data on specific sampless can be carried out in a straight forward fashion and would be reported eleswhere.

References

1. R. H. Dovenmus, J. Phys. Chem. 68, p.2212 (1964); Kitano, et al., J. of Japan Society of Applied Physics, 39, p.63 (1970); W. E. Martin, J. Appl. Phys., 44, No. 12, p. 5639 (1973).
2. T. G. Giallorenzi, et al., Applied Optics, 12, No. 6, p. 1240 (1973).
3. P. K. Tien, Applied Optics, 10, No. 11, p. 12 (1971).
4. D. Marcuse, Bell Syst. Tech. J., 48, pp 3187-3215 (1969).
5. G. B. Hocker and W. K. Burns, IEEE Journal of Quantum Electronics QE-11, No. 6, p. 270 (1975).
6. R. Ulrich and R. Torge, Applied Optics, 12, p. 2901, (1973).

Annual Report of the Institute of Physics, Academia Sinica, Vol. 6, 1976

The Setup of a Nuclear Lifetime Measurement System on Ge(Li)-NE 102A Detectors*

G. C. Kiang, D. Wang, B. Chen and E. K. Lin

Institute of Physics, Academia Sinica aod
National Tsing Hua University

Abstract

A nuclear lifetime measurement system of Ge(Li)-Ne 102A spectrometer has been set up. Based on a typical fast/slow coincidence circuit with the Smplitude and rise time compensation method the time resolution for ^{60}Co γ-cascade is 1.84 ns.

I. Introduction

Nuclear states formed after radiactive beta decay are frequently reached a cascade transition of gamma rays through a very short-lived excited states. For understanding the nuclear structure, those foundamental quantities such as the multipolarities of the γ-transitions, branching ratios, spin-parities and the lifetimes of the excited states have to be measured for comparison with the theoretical models. The knowledge of the lifetime of a nuclear state, especially, provides not only the essential informations to obtain the transition matrix elements, but also the means of investigating the nuclear models and wave functions[1-4]. It plays an impartant role in the nuclear spectrocopy.

For the measurement of the timing informations, in the range of $10^{-3}>\tau>10^{-11}$ sec. the most common method is the delayed coincidence technique[2]. The timing resolution is usually dependent on the detector which being used as well as the electronic circuit. Althrough this method has been widely used for many years, and a steady progress has been made in accuracy and time range; however, the tedius adjustment still need some technique in order to have its optimum timing resolution.

Based on the typical Fast/Slow coincidence design, a delayed coincidence spectrometer with Ge(Li)-Plastic scientillator assembly has been set up at the nuclear lab., IPAS. Using an ARC (Amplitude and Rise Time Compensated Timing) unit to eliminate the intrinsic walk effect of the Ge(Li) signal, the timing resolution of 1.84 ns was obtained which is pretty satisfied for the

* Work partially supported by the Physics Research Center, National Science Council, R. O. C..

demaned of lifetime measurements.

II. Apparatus and Experimentals

A 2″×1.5″ NE 102A organic crystal adapted to a 56 AVP photomultiplier with ORTEC 269 tube base was served as one detector. Another detector was a 43 C. C. true coax Ge(Li) detector (FHWM 2.1 keV at 1.33 MeV). In order to minimize the compton γ-rays, the two detectors were arranged perpendicular to each other.

A conventional Fast/Slow coincidence circuit was chosen for the lifetime measurements (see Fig. 1). A home made ^{60}Co point γ-source about 400 μc was used for determining the time resolution of the system. The distance from the point source to both surfaces of the two detectors of Ge(Li) and Ne 102A was kept at 2 cm. Two pieces of 2 mm thick Acrylic plates were used as a β-filter to prevent the β particles for the detectors.

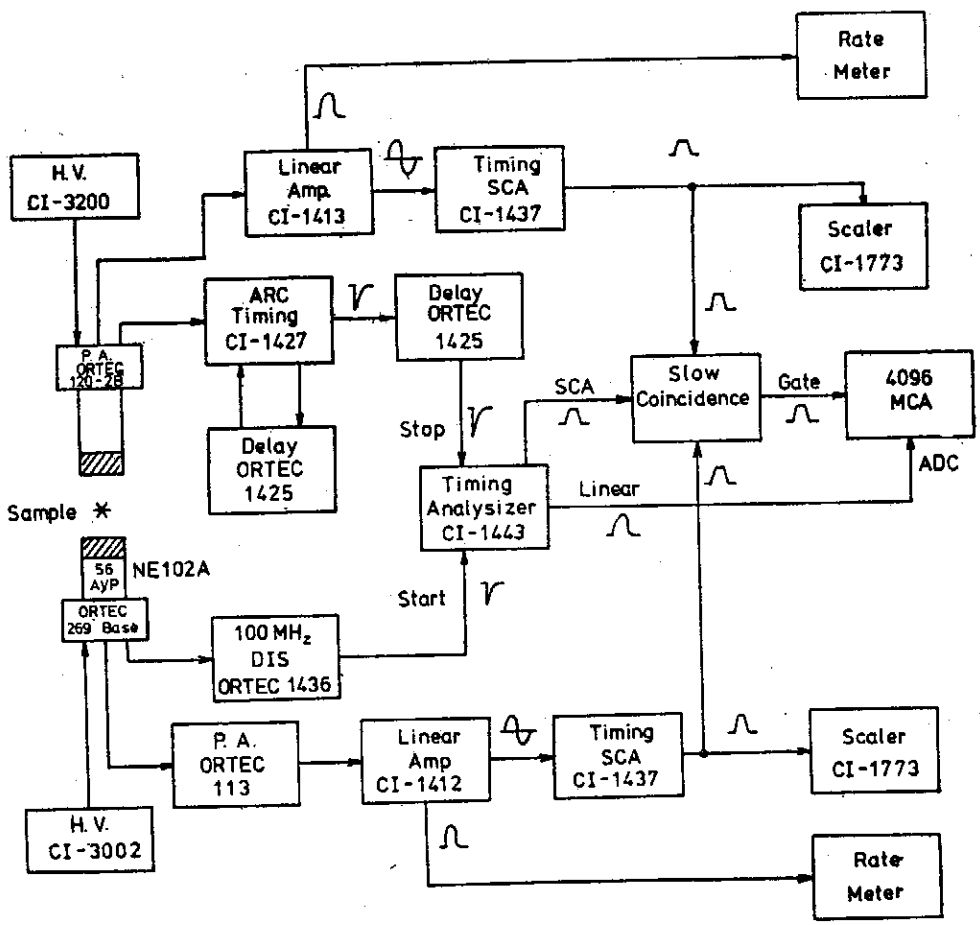

Fig. 1. A system for γ-γ lifetime measurement.

Due to the varying rise time and the intrinsic time jitter of the germanium detector signals, the walk effect was strongly affect the timing resolution. An ARC (Amplitude and Rise Time Compensated Timing) unit of CI-1427 was used to extract the timing information from the Ge(Li) detector via an ORTEC 120-2B Preamplifier. An external Nanosecond Delay of ORTEC 425 instead of the 50 Ω delay line was used to provide the proper delay for the ARC unit. Since the rise time of the pulse from the ORTEC 120-2B is approximately 30 ns at 34 pf. The delay time may be set at 30 ns to obtain the optimum time resolution and to minimize the walk effect. Besides, the gain and Rise Time Reject of the ARC have to be set dependent on the amplitude and noise of the input pulses. Gating the linear signal of the Ge(Li) detector, with the positive out put of the ARC the gain and rise time reject may be set at 9 and 4.65 respectively.

The ORTEC 436-100 MHz Discriminator was used to shape the fast timing signal from the anode output of ORTEC 269 Phototube base, which was coupled with 56 AVP photomultiplier and NE 102A crystal. In order to reduce the low energy noise and unwanted pulses, the Discrimination Level of the ORTEC 436 was set at 1.53 which means the pulse <153 mV were clipped

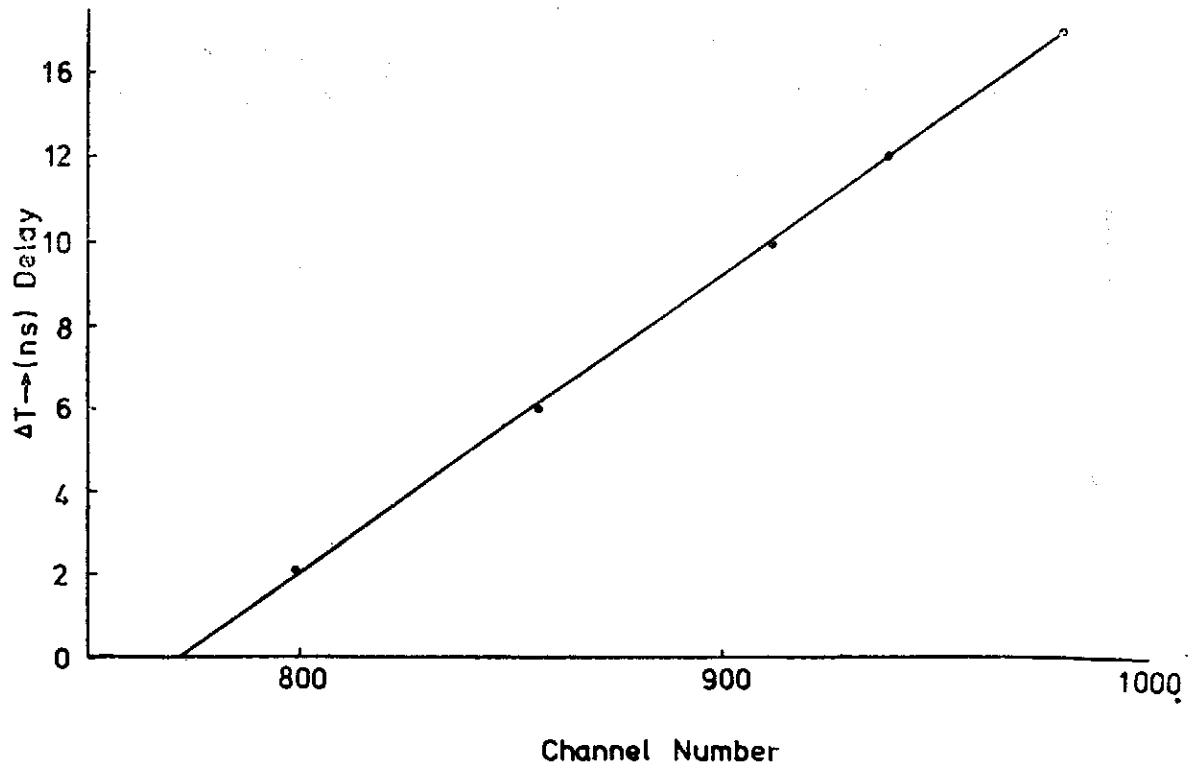

Fig. 2. The calibration of timing resolution.

out. The dynamic range for both fast channels were set~100:1.

The time difference of the fast timing signals were adjusted by a nanosecond delay. A start-stop type time analyzer of CI-1423 (TAC) was used to analyze the time difference of the time signals. The linear output of the TAC has been checked for 24 hrs. No obvious channel sihft was observed. The Time-to-channel ratio was found to be 72 ps/ch., as shown in Fig. 2. The window width of SCA output of the TAC was set 20% for the triple coincidence with the two slow channel outputs.

In the slow branch, the linear signals from both of the detectors were fed into the Timing Single Channel Analyzer (CI-1437) at proper selection of the energy region of interest.. In our case, the Ge(Li) side was windowed at 1332 ±6 keV while in the NE 102A side the window was set in the dynamic range of 50:1; the 1173 keV peak was involved. The dynamic range setting is shown in Fig. 3. The two slow timing signals withthe SCAoutput were fed into a Slow Coincidence Unit of CI-1445. The triple coincidence output served as a gate signal to gate the linear signal of TAC for the timing measurement, and recorded by a 4096 MCA.

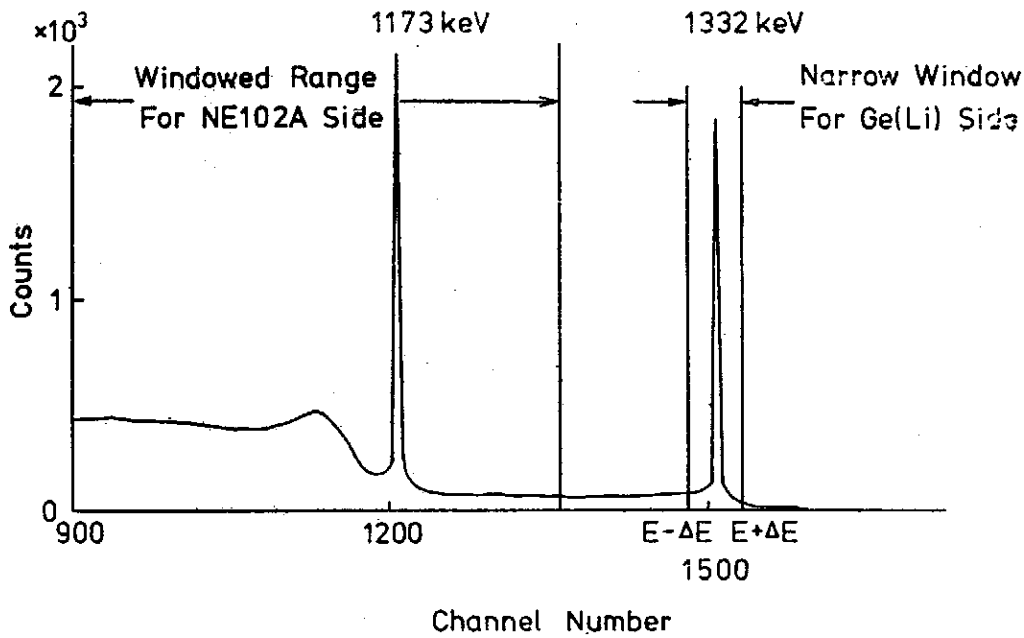

Fig. 3. The energy spectrum of ^{60}Co γ-rays showing the dynam ic range settin$\mathcal{g}$.

III. Resulats nd Discussion Figure Caption

The timing spectrum obtained by the system for ^{60}Co γ-cascade transition

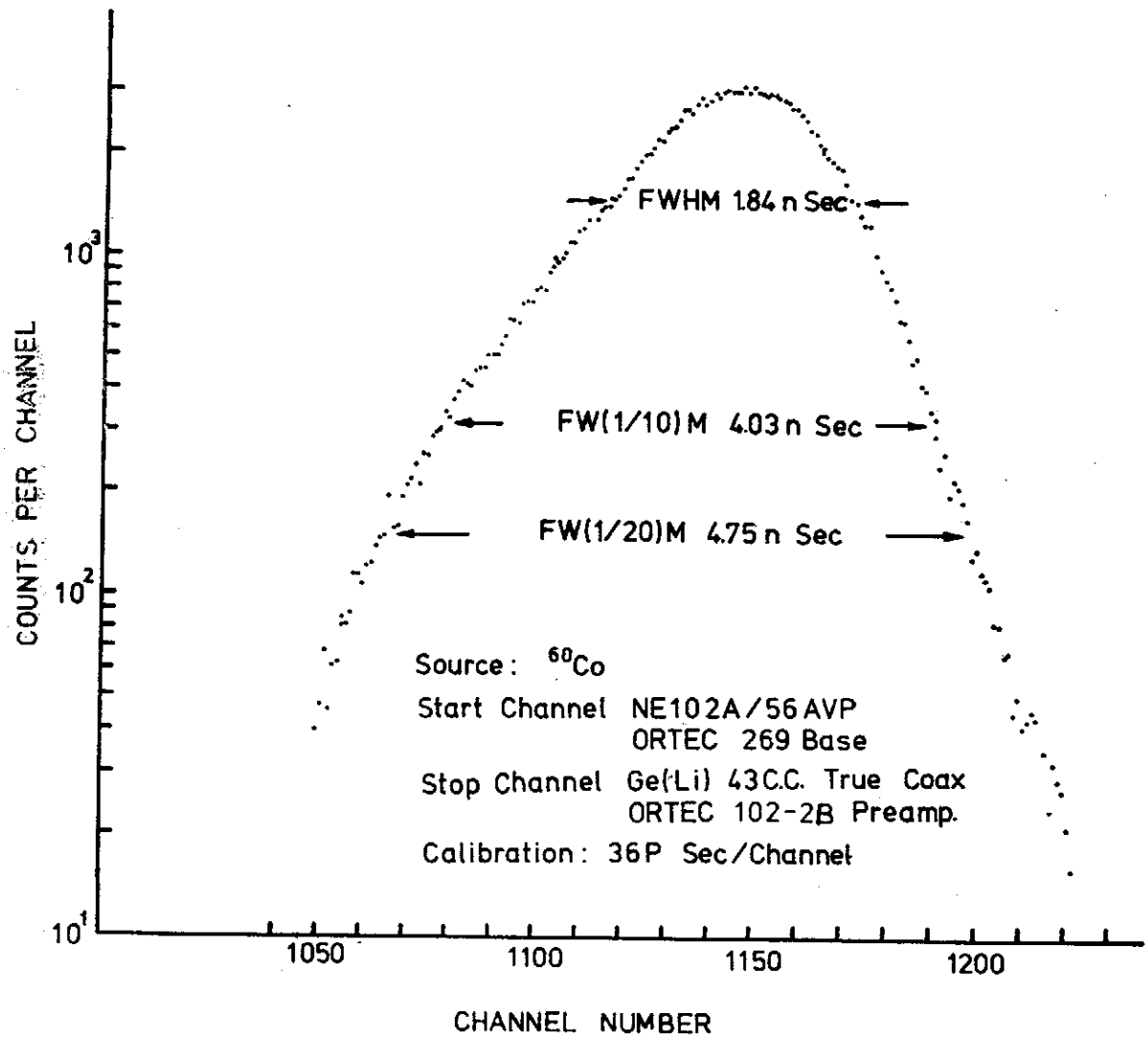

Fig. 4. The timing spectrum of ^{60}Co cascade.

was shown in Fig. 4. The timing resolution (FWHM) and FW($\frac{1}{10}$) M are1.84 $\times 10^{-9}$ sec. and 4.03×10^{-9} sec. respectively. In comparsion with the privious work[6], the present result is satisfied. Due to the amplitude variation of a Ge(Li) detector signals, the serious walk effect strongly affects the timing resolution. It is not suitable to be used for sub-nanosecond timing usage, even the ARC circuit is used. An Nn NE102A-Na(T1) or NE 102A-NE 102A system

may be used instead of the said system in order to measure the very fast events in the pico-second order.

References

(1) S. Devons, in Nuclear Spectroscopy edited by F. Ajzenberg-Selove, p. 512.
(2) A. Z. Sehwarzchied and. E. K. Warburton, Ann. Rev. of Nucl. Phys. Vol. 18, (1968) p. 256
(3) R. E. Bell, R. L. Graham and H. E. Petch, Can. J. of Physics, Vol. 30 (1952) p. 35.
(4) R. E. Bell in α, β, γ-Ray Spectroscopy, edited by K. Siegbahn, North-Holland (1965) p. 905.
(5) S. A. Moszkowski, ibid, p. 863.
(6) AN 31, ORTEC Application Note "Timing with Ge(Li) Detectors" (1970).

Annual Report of the Institute of Physics, Academia Sinica, Vol. 6, 1976

No Conflict between Kondo Effect and Mictomagnetism

By

Y. D. Yao

Institute of Physics
Academia Sinica
Nankang, Taipei, Taiwan
The Republic of China

ABSTRACT

Recently, some experimental reports have shown that Kondo-like electrical resistivity minimum accurs in non-dilute alloys. A self-consistent model for the Kondo effect is developed to explain these experimental results. No conflict between Kondo effect and Mictomagnetism is also demonstrated.

INTRODUCTION:

The well-known electric resistivity minimum phenomenon observed in many dilute alloys[1,2] has been known experimentally for quite a number of years. Around twelve years ago, it was established that the resistivity minimum accurs whenever the impurity atom is magnetic[3]. The weak concentration dependence of the temperature of the resistivity minimum and the scaling of the low temperature with impurity concentration indicates[4,5] that this effect does not arise from impurity-impurity interactions, but is a property of a sea of conduction electrons interacting with isolated magnetic impurities. The first successful theoretical explanation of these resistivity anomalies was made by Kondo[6]. Since 1964 the interest in the dilute magnetic alloy problem commonly referred to as the "Kondo effect" has been steadily rising. The theoretical activity in this field has been quite high, as evident between these review articles in 1968[7] and 1974[8].

In recent years, some experimental reports have shown that the Kondo-like resistivity minimum accurs in some non-dilute alloys containing transition elements, for example, *Pd-Ag*[9,10], *Pd-Cr*[11] and *Cu-Ni*[12,13] systems. Since 1970, there have been quite a few theoretical papers on this topic, as a example, the Kondo Sidebands Model etc.[14-20]. However, the theoretical situation is still not very clear. In this paper, with the concept of Mictomagnetism[21], we would like to present a "dilutionization treatment model" for the accurrence of Kondo effect in both dilute and non-dilute alloy

systems.

ANALYSES:

The experimental data by Clogston et al[22] for the average magnetic moment of dilute **Fe** impurities in 4*d* metals and alloys shows that the effective moment on the **Fe** impurity is changed as the host system is varied across the 4*d* series. Following the concept of Anderson model[23], this means that the gradual development of the impurity **Fe** moment can be interpreted as a continuous change both in the width Δ of the impurity *d* band and its position E with respect to the Fermi level E_F of the system. It has also been shown by Jaccarino and Walker[24] that when a few impurity ions, for example, **Fe** or *Co*, are dissolved in a 4*d* binary alloys, that prabability of the formation of local moments at the impurity ion sites is critically dependent on the number and kind of the nearest neighbors.

Here, we will concentrate upon the binary alloy only. Let the binary alloy system be written as $A_{1-x}B_x$, where A and B represent any pure metal elements, and x represents the atomic concentration of B. Either A or B, or both, belong to the transition metals. In a binary alloy system, if the influence of any atom on its neighbors is ignored that means we ignore that solubility of the two elements, we can assume that the atomic sites are occupied at random. Under this situation, the order parameters which were introduced by Bethe and Cowley etc. vanish[25]. Therefore, each site can be occupied by a B atom with probability x, and by an A atom with probability $(1-x)$. Generally, it is found that small cluster are randomly distributed throughout the material. We will choose a particular B atom, with the i-th nearest-neighbor coordination number N_i, as origin to form any size of cluster. There are three sufficient conditions for a cluster: First, there are at least n_i $(n_i \leqq N_i)$ B-type atoms in the i-th nearest-neighbor shell; second, the largest i (or say k) can be zero or any positive integer (here, zero means the B atom at origin itself); third, outside the cluster, or say in the j-th shell, where $k+1 \leqq j \leqq s$, the number m of the B-type atom should be no more than ℓ_j where ℓ_j can be zero or any positive integer. Let $P^{k,s}(n_i, \ell_j, x)$ be the prabability of this event. We have:

$$P^{k,s}(n_i; \ell_i; x) = \left[\prod_{i=0}^{k} \sum_{n=n_i}^{N_i} C_N^n x^n (1-x)^{N-n}\right]\left[\prod_{j=k+1}^{s} \sum_{m=0}^{\ell_i} C_{n_j}^m x^m (1-x)^{Nj-m}\right]$$

where $C_N^n = N!/n!(N-n)!$

This equation is valid under the assumption that the size of the clusters is much much smaller than the whole binary alloy system. The equation was calculated with the aid of a computer. The detailed analyses and discussions for different types of crystal structures have been carried out and will be reported elsewhere. The property of cluster is sensitive to the local inhomogeneities in the alloy concentration. The most obvious distinction between different clusters is the nature of their local environment in the disordered alloy. In this paper, we would like to mention just its physical concepts by showing below two simplest cases in a arbitrary body center cubic crystal system. In this case, we get $N_0=1$, $N_1=8$, $N_2=6$, $N_3=12$ and so on. Although they seem oversimplified pictures of an alloy, they give an enormous amount of information that helps us to understand more complicated cases.

The probability of finding a single B atom with no other B-type atoms in its first three nearest neighbors is given as:

$$P_{bcc}^{0;3}(1;\ 0,\ 0,\ 0;\ x)=x(1-x)^{26}$$

which is shown by the left solid curve in Fig. 1. It is quite reasonable sufficient case for the theoretical derivation of the Kondo effect in dilute alloys. The probability of finding a B atom with its first nearest neighbor shell having at least seven B-type atoms and its second nearest neighbor shell no more than one B-type atom is

$$P_{bcc}^{1;1}(1,\ 7;\ 1;\ x)=x[x^8+8x^7(1-x)][(1-x)^6+6x(1-5x)^5]$$

which is shown by the right solid curve in Fig. 1. Generally speaking, it occurs in non-dilute regions.

The occurrence of giant moments in some binary alloy system is a direct consequence of exchange enhancement effects in the host's narrow d-band, and its attendant supperssion[26] of RKKY type spin density oscillations to large distance from the cluster. This means that a single B-type cluster in the host may not give rise to a local moment, but the presence of the B-type cluster significantly increases the polarizability of the host in its vicinity. For example, if A and B both belong to transiton elements, the occurrence of the local moments of this binary alloy system can be either due to (1) the virtual bound d (or f) band of the cluster, (2) the polarized virtual bound d (or f) band of the host in the vicinity of the impurity, or (3) the combination of the above two cases.

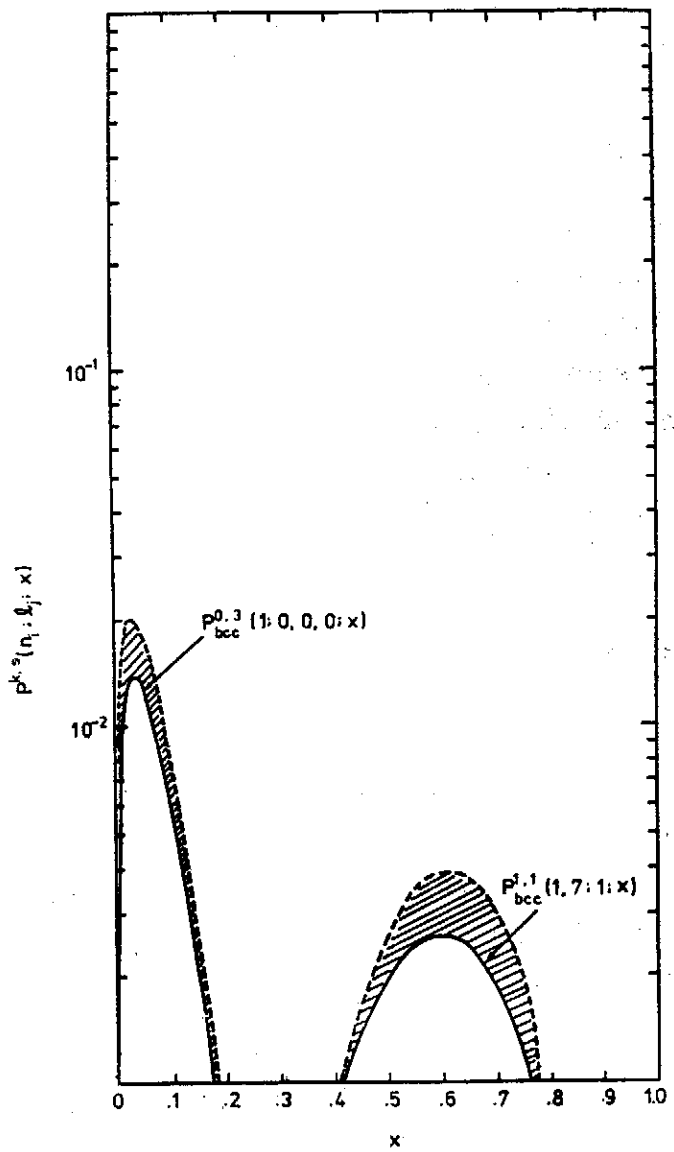

Figure 1: The probability of finding special clusters as a function of the atomic concentration of B in a binary alloy $A_{1-x}B_x$.

An additional probability may be induced by the polarization of the host which is shown by the shaded regions in Fig. 1. The area of this shaded regions will depend on the individual physical situation of various binary alloy systems. In case the Kondo effect exists for several completely different size and shape of clusters for a special concentration, the final results will be the supperposition of these clusters. If we add the influence of the atom on its neighbors, this also means to change the shape and the peak position of the probability curves shown in Fig. 1.

For a critical concentration, x_0, the binary alloy; $A_{1-x_0}Bx_0$, begin to favor

some special size and kind of clusters; and it has a suitable localized energy state theat its width Δ and position E with respect to the Fermi level E_F of the system has the properties of exhibiting the Kondo electrical resistivity minimum phenomenon. Following Kondo's theory[6], we can say that the local moments around these suitable clusters are formed and the antiferromagnetic s-d interaction between the cluster and the conduction electron is occurred. If the Kondo-like behavior is manifest in the concentration range x, where $x_0 \leqq x \leqq x_0 + \Delta x$ and $\Delta x > 0$, we can define this critical concentration alloy, $A_{1-x_0}Bx_0$, to be a new "pure-like" metal. When a small amount of B-type impurities with concentration C is dissolved into this so-called "pure-like" metal, where $C=(x-x_0)/(1-x_0)$, the Kondo-like effect occurs in this "dilutionized" non-dilute alloy. Because the interaction between a cluster and conduction electrons in non-dilute alloy is quite similar to that between a single impurity and conduction electrons in dilute alloy, all the theorems to explain Kondo effect in dilute system should be able to apply to Kondo-like effect in non-dilute binary alloys. It is definitely sure that besides the Kondo-like interaction, some other electron-electron interactions exist in the host metal and the clusters itselves, as well as between the host and the clusters.

Following Anderson's concept[23], we will analysis the occurrence of the Kondo-like behavior in a binary alloy. If the impurity concentration, x, is

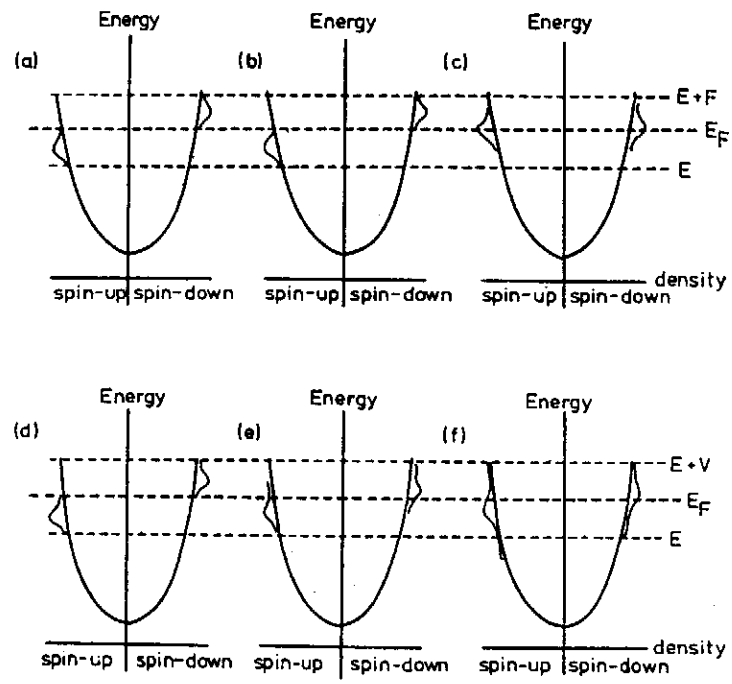

Figure 2. Density of State distribution following the Anderson model.

varied from x_0 to $x_0+\Delta x$, the physical meaning of this process can be represented by a continuous change of the six figures in Fig. 2. according to the following procedures: (a)→(b)→(a),(a)→(b)→(c),(d)→(e)→(f) or (d)→(e)→(d). For a complicated system, the variation process can be any reasonable combination of the above four procedures. In other words, several parameters are usually needed to express this cooperative phenomenon.

In a special temperature range, spins within a given cluster are ordered, whereas ordering between clusters is lacking[27]. If we define an exchange interaction Γ_{dd}, which is described by Heisenberg Hamiltonian, that the local moments mentioned above are formed under this exchange interaction. Here, we can regard the exchange interaction Γ_{dd} as a bounding energy for the local moments around the cluster. For temperatures below Γ_{dd}/k_B and J_{s-d}/k_B, where J_{s-d} is the *s-d* exchange interaction which is also described by Heisenberg Hamiltonian and k_B is the Boltzmann's constant, the Kondo-like effect can occur whether the binary alloy is in the paramagnetic, the weak ferromagnetic, the weak ferrimagnetic or the weak antiferromagnetic regions. However, the Kondo-like behavior can be mashed by phonon interaction or any other interactions, if the order of Kondo-like behavior is small enough comparing to other physical interactions. As the temperature approaches absolute zero, the local moments remain in their ground states, and the *s-d* interaction will die out, *i.e.* the Kondo effect disappear when the temperature approaches absolute zero.

CONCLUSIONS:

Kondo-like electrical resistivity minimum do or do not occur depending on the relations between the local cluster state and the Fermi level of the system. It can occur in the paramagnetic, the weak ferromagnetic, the weak ferrimagnetic or the weak antiferromagnetic alloys. For examples, the *Cu-Ni* alloys, Kondo effect occurs both in the weak ferromagnetic region[13] and in the paramagnetic region[12], the *Pr-Ce*[28] and *Au-Cr*[29] alloys, it occurs in the antiferromagnetic region.

Kondo-like behavior can occur two or more times in a binary alloy of two definite elements but in different concentration regions and temperature ranges. For example[11], the Kondo effect occurs in dilute *Pd-Ce* alloys in the temperature range above 25 *K*, as well as in the non-dilute *Pd-Ce* alloys in the temperature range below 4 *K*. The available data are not enough to allow more demonstration about this model. However, this model can be considered

as a reasonable one to explain the available experimental data.

Finally, with the cluster concept, we have shown no conflict between Kondo effect and Mictomagnetism.

COMMENTS:

This paper has been sent out to C.C.T. Potsdam, N.Y. U.S.A. for asking Prof. Arajs and Prof. Anderson to make some contribution.

REFERENCES:

1. W. Meissner and G. Voigt, Ann. Phys. **7**, 761 and 892 (1930).
2. J. Korringa and A. N. Gerritsen, Physica **19**, 457 (1953).
3. M. P. Sarachik, E. Corenzwit and L. D. Longinotti, Phys. Rev. **135**, A1041 (1964).
4. W. B. Pearson, Phil. Mag. **46**, 911 and 920 (1955).
5. B. Knook, Thesis, Univ. of Leiben (1962).
6. J. Kondo, Progr, Theoret. Phys. **32**, 37 (1964).
7. M. D. Daybell and W. A. Steyert, Rev. Mod. Phys. **40**, 380 (1968).
8. C. Rizzuto, Reports on progress in Phys. **37**, 149 (1974).
9. C. W. Chen, L. R. Edwards and S. Legvold, Phys. Stat. Sol. **26**, 611 (1968).
10. L. R. Edwards, C. W. Chen and S. Legvold, Solid State Commun **8**, 1403 (1970).
11. W. M. Star, E. de vroede and C. van Baarle, Physica **59**, 128 (1972).
12. R. W. Houghton, M. P. Sarachik and J. S. Kouvel, Solid Stare Commun **8**, 943 (1970).
13. J. Crangle and P. J. L. Butcher, Phys. Letters **32A**, 80 (1970).
14. F. E. Maranzana, Phys. Rev. Letters **25**, 239 (1970).
15. B. cornut and B. Caqblin Phys. Rev. **B5**, 4541 (1972).
16. F. E. Maranzana, J. Phys. Chem. Solids **31**, 2245 (1970).
17. M. T. Beal-Monod, Solid Stete Commun. **9**, 401 (1971).
18. R. Hasegawa, Phys. Letters **36A**, 207 (1971).
19. J. Kübler, Z. Physik **254**, 385 (1972).
20. R. N. Silver and T. C. McGill, Phys. Rev. **B9**, 272 (1974).
21. P. A. Beck, J. Less-Common Metals **28**, 193 (1972).
22. A. M. Clogston, B. T. Matthias, M. Peter, H. J. Williams, E. Corenzwit and R. C. Sherwood, Phys. Rev. **125**, 541 (1962).
23. P. W. Anderson, Phys. Rev. **124**, 41 (1961).

24. V. Jaccarino and L. R. Walker, Phys. Rev. Lett. **15**, 258 (1965).
25. L. Guttman, in **Solid State Physics** edited by F. Seitz and D. Turnbull (Academic, New York, 1956) Vol. 3. p. 145.
26. D. J. Kim and B. B. Schwartz, Phys. Rev. Lett. **20**, 201 (1968).
27. K. Levin and D. L. Mills, Phys. Rev. **B9**, 2354 (1974).
28. M. Altunbas, K. N. R. Taylor and G. A. Wilkinson, Phil. Mag. **29**, 349 (1974).
29. Y Shiozaki, Y. Nakai and N. Kunitomi, Solid State Commun. **12**, 429 (1973).

Annual Report of the Institute of Physics, Academia Sinica, Vol. 6, 1976

The Limitation of Two-Current Model in Nickel-Rich Nickel-Chromium Alloys

By

Y. D. Yao

Institute of Physics
Academia Sinica
Nankang, Taipei, Taiwan
The Republic of China

Abstract

It is demonstrated that the two-current model in nickel-rich nickel-chromium alloys is definitely limited. For Ni-Cr alloys with Cr concentration smaller than 5.5 at. %, the deviations from Matthiessen's rule of the resistivity can be explained by a two-current model. However it is not valid for Ni-Cr alloys with Cr concentration larger than 11.3 at.%.

Introduction:

The concept of two-current conduction was first suggested by Mott[1]. It was used to explain the deviations from Matthiessen's rule[2] of the resistivity measurements of dilute iron based alloys by I. A. Campbell et al[3]. Later, Schwerer and Conroy[4] reported that their experimental data of dilute Ni-Cr alloys with Cr concentration smaller than 5 at. % can be analyzed under the two-current model. In this paper, we will combine the experimental data of Ni-Cr alloys reported by Yao et al.[5] and Schwerer et al.[4] to analyze the limitation of the two-current conduction in nickel-rich nickel-chromium alloys.

Under the assumption that there is only one type of current carrier and that the scattering processes which cause resistance are independent, the Matthiessen's rule can be expressed as:

$$\rho_a(C,T)=\rho_p(T)+\rho_0(C) \qquad (1)$$

where $\rho_0(C)$ is the resistivity produced by the impurity at O °K, $\rho_p(T)$ is the resistivity of an ideal pure metal, and $\rho_a(C,T)$ is the resistivity of a dilute alloy containing a concentration C of impurity.

In fact, there are always deviations from Matthiessen's rule. However, in many cases, these deviations are very small, and Matthiessen's rule represents

quite a good approximation to the experimental data. We can always write $\rho_a(C,T)$ exactly as

$$\rho_a(C,T)=\rho_p(T)+\rho_0(C)+\Delta(C,T) \tag{2}$$

Presuming that $\rho_p(T)$, $\rho_a(C,T)$ and $\rho_0(C)$ can be determined experimentally, Equation (2) provides a definition for the quantity $\Delta(C,T)$. We call this experimental value of $\Delta(C,T)$ the "Deviation from Matthiessen's Rule" associated with the concentration C of the given solute in the given solvent. The existence of a non-zero $\Delta(C,T)$ has been known for over 100 years, ever since the original study by Matthiessen and Vogt. However, with the exception of a flurry of interest in the early 1930's, quantitative investigation of the form and magnitude of $\Delta(C,T)$ proceeded rather slowly until quite recently. From the previous work devoted to this topic[6-11], the existence of the deviation from Matthiessen's rule in systems involving defects other than substitutional impurities is demonstrated.

According to the two-current model in which spin-up and spin-down electrons conduct in parallel, the resistivity, $\rho_a(C,T)$, can be represented as follows[3]:

$$\rho_a(C,T)=\frac{[\rho\uparrow(o)+\rho_a\uparrow(T)][\rho\downarrow(o)+\rho_a\downarrow(T)]+\frac{1}{2}\rho\uparrow\downarrow(T)[\rho\uparrow(o)+\rho\downarrow(o)+\rho_a\uparrow(T)+\rho_a\downarrow(T)]}{\rho\uparrow(o)+\rho\downarrow(o)+\rho_a\uparrow(T)+\rho_a\downarrow(T)+2\rho\uparrow\downarrow(T)} \tag{3}$$

where $\rho\uparrow(o)$ and $\rho\downarrow(o)$ are the impurity residual resistivities for the two spin directions, $\rho\uparrow\downarrow(T)$ is the resistivity due to the spin-mixing which is characterized by a relaxation time$\tau\uparrow\downarrow$. $\rho_a\uparrow(T)$ and $\rho_a\downarrow(T)$ are the thermal resistances of the alloy for each spin direction; in general, $\rho_a\uparrow(T)\neq\rho_a\downarrow(T)$. Let $\rho_p\downarrow(T)$ and $\rho_p\uparrow(T)$ be the thermal resistances of the pure host metal for each spin direction, and $\rho_h(T)$ be the resistivity of the pure host metal at temperature T. At low temperatures, both the $\rho_a(T)$ and the $\rho\uparrow\downarrow$ are small. For the simplest case,

$$\rho_a\uparrow(T)=\rho_a\downarrow(T)=\rho_p\uparrow(T)=\rho_p\downarrow(T)\equiv\rho(T),$$

$$\text{and letting}\qquad \rho(o)=\frac{\rho\uparrow(o)\rho\downarrow(o)}{\rho\uparrow(o)+\rho\downarrow(o)} \tag{4}$$

we get for low temperatures:

$$\rho_a(C,T)=\rho(o)+\rho_h(T)+\frac{1}{2}\,\frac{[\rho\uparrow(o)-\rho\downarrow(o)]^2[\rho(T)+\rho\uparrow\downarrow(T)]}{[\rho\uparrow(o)+\rho\downarrow(o)][\rho\uparrow(o)+\rho\downarrow(o)+2\rho(T)+2\rho\uparrow\downarrow(T)]}$$

$$\approx\rho(o)+\rho_h(o)+\frac{1}{2}\left[\frac{\rho\uparrow(o)-\rho\downarrow(o)}{\rho\uparrow(o)+\rho\downarrow(o)}\right]^2[\rho(T)+\rho\uparrow\downarrow(T)] \qquad (5)$$

The third term is the deviation from Matthiessen's rule. For the general case, the deviation does not separate out quite as simply; however, it is always positive. The physical picture is that the electrons in the low resistance spin direction, which carry most of the current at low temperature, are "Braked" as the temperature rises, and they are brought into contact with slower electrons. At high temperatures, the deviation should saturate. We will then have:

$$\rho_a(C,T)=\tfrac{1}{2}[\rho\uparrow(o)+\rho\downarrow(o)+\rho_a\uparrow(T)+\rho_a\downarrow(T)] \qquad (6)$$

Analyses and Discussions:

A detailed list of proposed sources for the deviation from Matthiessen's rule is given in the review article by Bass[11]. In this paper, we only want to show the deviation from Matthiessen's rule of Yao et al's experimental data[5]. Due to the experimental difficulty, we replace $\rho_0(C)$ by the resistivity at 4.2 °K. Also, we will define a deviation parameter $\Delta(C, T)$ by

$$\Delta(C,T)=[\rho_m(T)-\rho_m(4.2)]_{\text{alloy}}-[\rho_m(T)-\rho_m(4.2)]_{\text{pure}}\equiv\Delta\rho(C,T)-\rho_c \qquad (7)$$

where

$$\Delta\rho(C,T)\equiv[\rho_{\text{alloy}}(T)-\rho_{\text{pure}}(T)]_{\text{measured}}$$

$$\equiv[\rho_m(T)]_{\text{alloy}}-[\rho_m(T)]_{\text{pure}} \qquad (8)$$

$$\rho_c\equiv[\rho_m(4.2)]_{\text{alloy}}-[\rho_m(4.2)]_{\text{pure}} \qquad (9)$$

and $\rho_m(T)$ is the measured resistivity at temperature T.

Figure 1 shows the temperature-dependent behavior of $\Delta\rho(C, T)$, which is the difference between the Ni-alloy resistivity and the "pure" Ni sample resistivity. According to this figure, the temperature-dependent behavior of $\Delta\rho(C, T)$ does not agree with the two-current model for Ni-Cr alloys containing Cr in amounts greater than 11.3 at.%. In other words, the two-current model is based on the spin polarization of the conduction electrons due to the ferromagnetic state of the host metal. For high concentration Ni-Cr alloys (say, larger than 11.3 at.% Cr), the alloys do not show strong ferromagnetic ordering in the experimental temperature range; and we can probably say that it is in the weak ferromagnetic state for samples up to around 22 at.% Cr. We suggest that the critical composition for the weak

ferromagnetism is about 22 at. % Cr. We can further suggest that the maximum of the $\Delta\rho(C, T)$ vs T curve could be a functional change of the Curie temperature of the alloys. Since pure Ni is in the ferromagnetic state below 631 °K, the decrease of $\Delta\rho(C, T)$ with increasing temperature could mean that the resistivity of the alloy due to ferromagnetism disappears above a special temperature which is changed according to a special function of the maximum in the $\Delta\rho$ (C, T) curve.

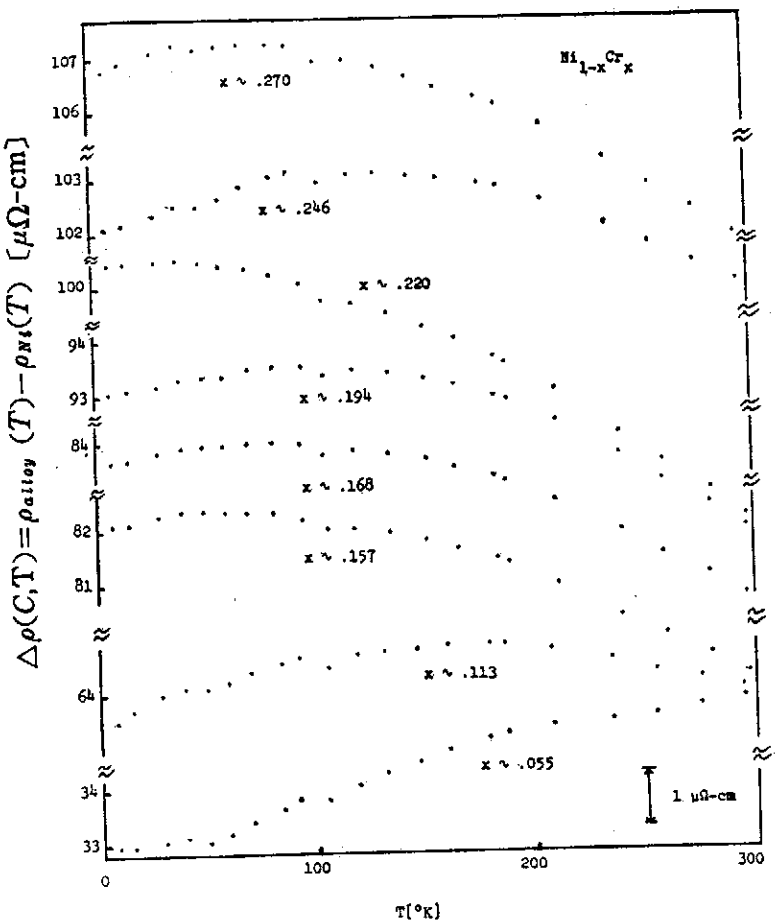

Fig. 1. The difference $\Delta\rho$ (C,T)between the alloy resistivity and the pure Ni sample resistivity for Ni_{1-x} Cr_x

Analyzing the experimental data of the Ni-Cr alloy containing 5.5 at.% Cr, together with the data reported by Schwerer and Conroy[4] for Ni-Cr alloys with Cr concentration smaller than 5 at.%, we conclude that these deviations of Ni-Cr alloys with Cr concentration smaller than 5.5 at.% can be explained by a two-current model in which spin-up and spin-down electrons conduct

in parallel.

However, Figure 1 shows evidently that the two-current model is not valid for Ni-Cr alloys with Cr concentration larger than 11.3 at.%. A further detailed analysis of the proposed sources for the deviation from Matthiessen's rule for the Ni-Cr alloys with Cr concentration larger than 11.3 at.% will be published elsewhere.

Acknowledgments:

The author would like to thank professor Arajs and professor Anderson who gave the opportunity of performing the experiments in their laboratory, and also to the National Science Council of Republic of China for the financial support of this analysis work.

References:

1. N. F. Mott, Proc. R. Soc. **153**, 699 (1936).
2. A. Matthiessen, Ann. Phys. **7**,761, 892 (1864).
3. I. A. Campbell, A. Fert and A. R. Pomeroy, Phil. Mag. **15**, 977 (1967).
4. F. C. Schwerer and J. W. Conroy, J. Phys. F.**1** , 877 (1971).
5. Y. D. Yao, S. Arajs and E. E. Anderson, J. Low Temp. Phys. **21**, 369 (1975).
6. G. Borelius, Handbuch Metall. Physik **1**, 1 (1935).
7. H. Jones, Handbuch der Physik **19**, 227 (1956).
8. D. K. C. MacDonald, Handbuch der Physik **14**, 137 (1956).
9. A. N. Gerritsen, Handbuch der Physik **19**, 137 (1956).
10. F. R. Fickett, Cryogenics **11**, 349 (1971).
11. J. Bass, Adv. Phys. **21**, 431 (1972).

Annual Report of the Institute of Physics, Academia Sinica, Vol. 6, 1976

A model of perceived direction of adapted motion

By

Chun Chiang (蔣忻儒)

Institute of Physics
Academia Sinica
Nankang, Taipei, Taiwan
The Republic of China

ABSTRACT

A model utilizing the concept of relative velocity has been proposed to explain the perceived direction change of an adapted motion. Theoretical calculation agrees with experiment very well.

Recently, experimet[1] shows that prolonged exposure to a field of random dots drifting in one direction selectively elevates the contrast detection threshold for subsequently presented moving test dots. Levinson and Sekuler[2] also show that previous adaptation alters perceived direction of motion. Interesting data have been provided which indicate that the perceived direction always deviated away from previously adapting direction, the deviation is large for adaption direction near the test direction ($\pm 30°$) and decreases as the adapting direction was made less similar to the test direction. This phenomenon is not only interesting but also important in many phases of daily life, thus it is desirable to find out what is the mechanism responsible for this phenomenon.

This letter will propose a model, which can quantitatively calculate the deviation and comparison with the experiment can thus be made.

Let θ, θ_1, θ_2 be the perceived direction, the test direction, and the adapting direction respectively, V the velocity of the stimulus. The component of the adapting velocity along the test direction is

$$rV\cos(\theta_2-\theta_1) \tag{1}$$

where r is a percentage factor indicating the amount of the induced adapting velocity along the test direction. The difference between the test velocity and the adapting velocity along the test direction is

$$V-r\ V\ \cos(\theta_2-\theta_1) \tag{2}$$

Similarly, the component of the adapting velocity perpendicular to the test direction is

$$-r'\ V\ \sin(\theta_2-\theta_1) \tag{3}$$

where r' is another percentage factor indicating the induced adapting velocity perpendicular to the test direction. It is proposed that the perceived direction

θ of a test stimulus will then be

$$\theta-\theta_1=\tan^{-1}\frac{-r'V\sin(\theta_2-\theta_1)}{V-r\ V\cos(\theta_2-\theta_1)} \tag{4}$$

Let $\theta'=\theta_2-\theta_1$ represents the normalized adaption direction, $\psi=\theta-\theta_1$ the deviation of the perceived direction from the test direction, then equation (4) becomes

$$\psi=\tan^{-1}\frac{-r'\ \sin\theta'}{1-r\ \cos\theta'} \tag{5}$$

Equation (5) is ploted in Fig. 1 for $r'=0.033$ and $r=0.866$ together with the data of Levinson and Sekuler (1976), it can be seen that the fit is quite good. If there are two adaptation stimuli, then the perceived direction will be the sum of the individual perceived direction, thus if there are two idential adapting stimuli moving in opposit direction, the resultant perceived direction ψ will be

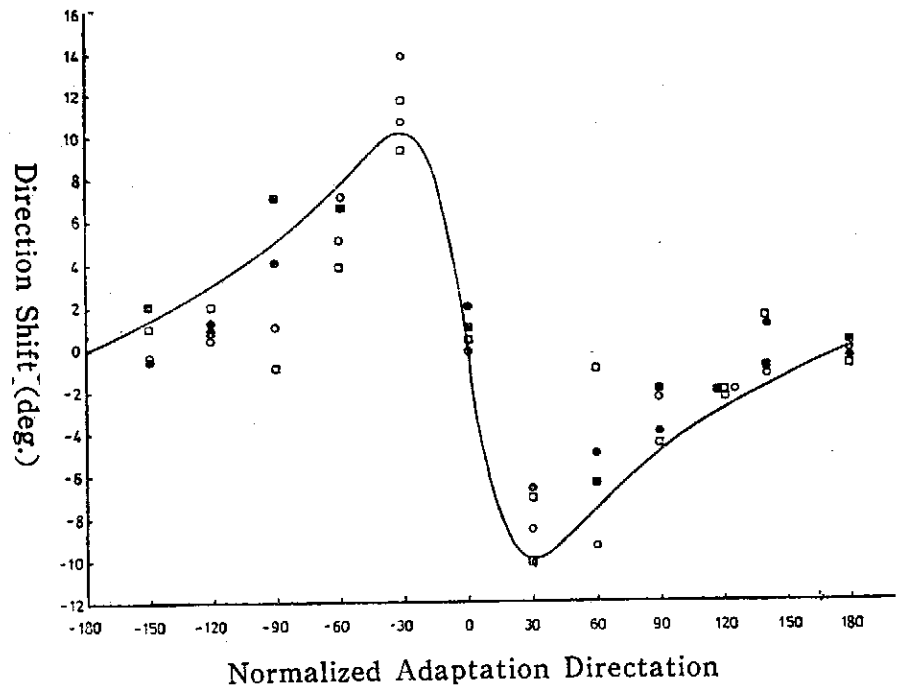

Fig. 1. Plot of Eq-(5). The data are taken from Lievinson & Sckuler (1976)

$$\psi=\tan^{-1}\frac{-r'\ \sin\theta'}{1-r\ \cos\theta'}+\tan^{-1}\frac{-r'\ \sin(\theta'+180°)}{1-r\ \cos(\theta'+180°)} \tag{6}$$

This is a fixed amount as indeed shown by Levinson and Sekuler[2]. A similar additative result has also been reported in motion after effect by

Scott et al[3].

References

1. Levinson E. and Sekuler R. (1974) Direction-specific adaptation in human vision: Measurements using istropic random dot patterns. Presented at the meetings of the Psychonomic Society, Boston.
2. Levinson E. and Sekuler R. (1976) Adaptation alters perceived direction of motion. Vision Res. **16**, 779-781.
3. Scott, T. R., Jordan, A. E. & Powell, D. A. (1963) Does visual after effect of motion add algebraically to objective motion of the test stimulus. J. Exp. Psychol. **66**, 500-505.

Annual Report of the Institute of Physics, Academia Sinica, Vol. 6, 1976

Undamped Sinusoidal Lineal Chemical Reaction System with Enzymes

Chun Chiang (蔣忻儒)

Institute of Physics
Academia Sinica
Nankang, Taipei, Taiwan
The Republic of China

ABSTRACT

A series of enzyme reactions is devised, where the enzymes are continuously produced in one set of enzyme reactions and are continuously consumed by inhibitors in another set of enzyme reactions, the inhibitors being also produced by a set of enzyme reactions. Under the condition that the pool of reactants are large enough such that the rection rate depends only on the enzymes, it shows an undamped pure sinusoidal oscillation.

I. INTRODUCTION

The oscillation phenomena increasingly gain attention in many devergent fields, such as the biological clock, ecology and environmental changes etc. Since many biological and physical processes involve chemical reactions, it would be interesting to know a chemical reaction system which has the property of undamped sinusoidal oscillation. Many authors (Bak, 1963; Lotka 1910; Moore, 1949) have shown a chemical oscillating system; however, it is the nonlinearity of the system which gives rise the oscillation phenomenon. Hyver (1972), Denbigh et al (1948), Hearson (1953) and Meixner (1949) have proved that a linear chemical reaction system under their specified conditions can not have undamped oscillation. However, Seeling (1970) has devised an open system which has the property of undamped sinusoidal oscillation. His system consists of: (1) a chemical reaction whose rate is linearly dependent on the concentration of a catalyst, (2) a series of successive first order reactions with the product of part (1) as input and the catalyst as output,(3) the catalyst is one of the products and is destroyed by a first order reaction in addition to a reaction with constant rate. The purpose of this paper is to show that an enzymatic linear system will also show this undamped sinusoidal oscillaton. Furthermore, unlike Seelig's system being open in flux,

this system can be both open and closed and may have applications in modelling the biological clock or construct the chemical oscillator.

II. THE SYSTEM OF CHEMICAL REACTIONS

Suppose we have following enzyme reactions:

$$E_1(S_1+\cdots\cdots)\xrightarrow{k_1}E_2(P_1+\cdots\cdots) \tag{1}$$

$$E_2(S_2+\cdots\cdots)\xrightarrow{k_2}E_3(P_2+\cdots\cdots) \tag{2}$$

$$E_3(S_3+\cdots\cdots)\xrightarrow{k_3}E_4(P_3+\cdots\cdots) \tag{3}$$

$$E_4(S_4+\cdots\cdots)\xrightarrow{k_4}E_5(P_4+\cdots\cdots) \tag{4}$$

$$E_5(S^5+\cdots\cdots)\xrightarrow{k_5}E_1(P_5+\cdots\cdots) \tag{5}$$

and

$$E_1(S'_1+\cdots\cdots)\xrightarrow{k_5}I_5(P'_5+\cdots\cdots) \tag{6}$$

$$E_2(S'_2+\cdots\cdots)\xrightarrow{k_1}I_1(P'_1+\cdots\cdots) \tag{7}$$

$$E_3(S'_3+\cdots\cdots)\xrightarrow{k_2}I_2(P'_2+\cdots\cdots) \tag{8}$$

$$E_4(S'_4+\cdots\cdots)\xrightarrow{k_3}I_3(P'_3+\cdots\cdots) \tag{9}$$

$$E_5(S'_5+\cdots\cdots)\xrightarrow{k_4}I_4(P'_4+\cdots\cdots) \tag{10}$$

and

$$E_1+I_1\xrightarrow{\text{very fast}}E_1I_1 \tag{11}$$

$$E_2+I_2\xrightarrow{\text{very fast}}E_2I_2 \tag{12}$$

$$E_3+I_3\xrightarrow{\text{very fast}}E_3I_3 \tag{13}$$

$$E_4+I_4\xrightarrow{\text{very fast}}E_4I_4 \tag{14}$$

$$E_5+I_5\xrightarrow{\text{very fast}}E_5I_5 \tag{15}$$

where equation (1) means that the enzyme E_1 catalyzes the substrate S_1 to form enzyme E_2 and product P_1, and equation (2) through (5) have similar meanings. Equation (6) means that the enzyme E_1 catalyzes the substrate S'_1 to form the inhibitor I_5 and product P'_5, and equations (7) through (10)

have similar meanings. Equation (11) means that enzyme E_1 and inhibitor I_1 combine to form E_1I_1 rapidly and the activity of the enzyme is destroyed by the inhibitor I_1, and equations (12) through (15) have similar meaning; k_1, k_2, k_3, k_4 and k_5 are reacton rate constants. The above reactions can be concisely expressed in a diagram in Fig. 1, where→represents the forward reaction and↔represents the combination.

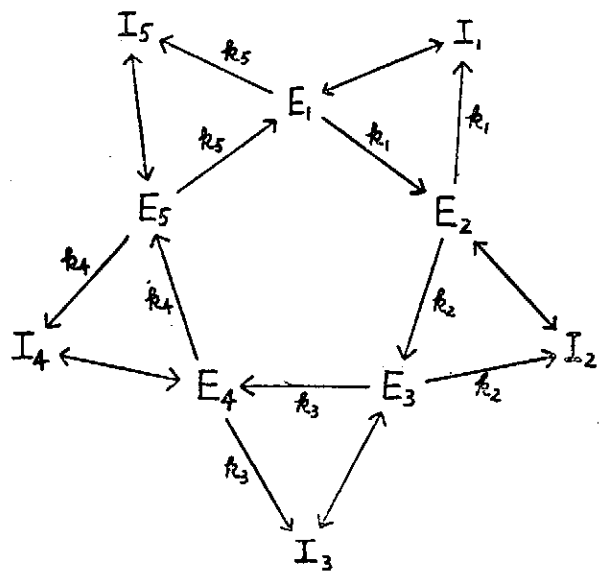

Fig. 1. A dagram showing the relationships among enzymes and inhibitors. →represents the fhe forward reaction and↔represents the combination, k_1……k_5 are rate constants.

III. THE RATE EQUATIONS AND SOLUTIONS

Suppose the concentration of S_1……S_5 and S_1……S'_5 is very large and since the enzymes only catalyze a reaction but retain its concentration in the process, thus the enzymes in the left side of equation (1) through (5) are left unchanged, however the enzymes in the right side of equations (1) through (5) are continuously produced from the pool of reactants S_1…… Also, the concentration of enzymes in equations(6) through (10) is unchanged and the inhibitors I_1……I_5 are continuously produced from the pool of reactants S'_1…… However, the enzymes in equation (11) through (15) are destroyed as soon as the inhibitors are formed, thus the rate of the decreasing of the enzymes is proportional to the rate of producing of the inhibitors. From this argument, the rate equations can be written accrodingly The rate equations of the inhibitors are:

$$\frac{dI_1}{dt}=k_1E_2 \tag{16}$$

$$\frac{dI_2}{dt}=k_2E_3 \tag{17}$$

$$\frac{dI_3}{dt}=k_3E_4 \tag{18}$$

$$\frac{dI_4}{dt}=k_4E_5 \tag{19}$$

$$\frac{dI_5}{dt}=k_5E_1 \tag{20}$$

the rate quations of the enzymes are the combination of two parts, the part of production according to equations (1)~(5) and the part of destruction according to equations (11)~(15), namely,

$$\frac{dE_1}{dt}=k_5E_5-\frac{dI_1}{dt}=k_5E_5-k_1E_2 \tag{21}$$

$$\frac{dE_2}{dt}=k_1E_1-\frac{dI_2}{dt}=k_1E_1-k_2E_3 \tag{22}$$

$$\frac{dE_3}{dt}=k_2E_2-\frac{dI_3}{dt}=k_2E_2-k_3E_4 \tag{23}$$

$$\frac{dE_4}{dt}=k_3E_3-\frac{dI_4}{dt}=k_3E_3-k_4E_5 \tag{24}$$

$$\frac{dE_5}{dt}=k_4E_4-\frac{dI_5}{dt}=k_4E_4-k_5E_1 \tag{25}$$

where equations (16)~(20) have been used.

The simutaneous system differential equations (21) to (25)can be written in a vector form as

$$\frac{dE}{dt}=AE \tag{2 }$$

where E and A are respectively

$$E=\begin{pmatrix} E_1 \\ E_2 \\ E_3 \\ E_4 \\ E_5 \end{pmatrix} \quad \text{and} \quad A=\begin{pmatrix} 0 & -k_1 & 0 & 0 & k_5 \\ k_1 & 0 & -k_2 & 0 & 0 \\ 0 & k_2 & 0 & -k_3 & 0 \\ 0 & 0 & k_3 & 0 & -k_4 \\ -k_5 & 0 & 0 & k_4 & 0 \end{pmatrix}$$

Undamped Sinusoidal Lineal Chemical Reaction System with Enzymes

The differential equation (26) can be solved by finding the eigenvalue (λ) of A, namely finding the λ in the following equation:

$$\begin{vmatrix} -\lambda & -k_1 & 0 & 0 & k_5 \\ k_1 & -\lambda & -k_2 & 0 & 0 \\ 0 & k_2 & -\lambda & -k_3 & 0 \\ 0 & 0 & k_3 & -\lambda & -k_4 \\ -k_5 & 0 & 0 & k_4 & -\lambda \end{vmatrix} = 0 \qquad (27)$$

λ in eqution (27) has five roots and can be found to be

$\lambda_1 = 0$

$$\lambda_{2,3,4,5} = \pm \frac{1}{\sqrt{2}} \sqrt{(k_1^2+k_2^2+k_3^2+k_4^2+k_5^2) \pm \sqrt{(k_1^2+k_2^2+k_3^2+k_4^2+k_5^2)^2 - 4(k_1^2k_3^2+k_2^2k_4^2+k_3^2k_5^2+k_4^2k_1^2+k_5^2k_2^2)}\, i}$$

The solution of (28) can be shown (Duff and Naylor, 1966) to be

$$E(t) = C_1X_1e^{\lambda_1 t} + C_2X_2e^{\lambda_2 t} + C_3X_3e^{\lambda_3 t} + C_4X_4e^{\lambda_4 t} + C_5X_5e^{\lambda_5 t} \qquad (28)$$

where $X_1, X_2, \cdots\cdots X_5$ are eigenvectors corresponding to the eigenvalue $\lambda_1, \lambda_2, \cdots\cdots \lambda_5$, and $C_1, C_2 \cdots\cdots C_5$ are constants which can be determined by the intitial conditions. The eigenvectors can also be obtained from equation (27) to be

$$X = \begin{pmatrix} 1+2\lambda+\lambda^3 \\ 1-\lambda-\lambda^2 \\ 1+\lambda+\lambda^2 \\ 1-2\lambda-\lambda_3 \\ 1+3\lambda^2+\lambda_4 \end{pmatrix} \qquad (29)$$

Since λ has five distinct values, there are five different eigenvectors, furthermore, since λ is either zero or pure immaginary, equation (28) is a pure sinusoidal equation.

IV. NUMERICAL CALCULATIONS

For a numerical calculation, we let $k_1 = k_2 = k_3 = k_4 = k_5 = 1.000$ and choose the initial conditions as $E_1(0) = 9.077$, $E_2(0) = 4.284$, $E_3(0) = 0.480$, $E_4(0) = 3.923$, $E_5(0) = 8.236$. λ thus can calculate to be

$$\lambda_1=0,\ \lambda_2=0,\ \lambda_2=\sqrt{\frac{5+\sqrt{5}}{2}},\ \lambda_3=-\sqrt{\frac{5+\sqrt{5}}{2}},\ \lambda_4=\sqrt{\frac{5-\sqrt{5}}{2}},\ \lambda_5=-\sqrt{\frac{5-\sqrt{6}}{2}}$$

Utilizing equation (29), equation (28) can transform to be

$$\begin{aligned} E_1&=5+4.576\ \cos(0.605t+0.350)\pi \\ E_2&=5+4.5t6\ \cos(0.605t+1.950)\pi \\ E_3&=5+4.576\ \cos(0.605t+1.451)\pi \\ E_4&=5+4.576\ \cos(0.605t+1.150)\pi \\ E_5&=5+4.576\ \cos(0.605t+0.750)\pi \end{aligned} \tag{30}$$

The above calculation is tedious, but straighfoward. Equation (30) shows that every enzyme is pure sinusoidal and with a fixed phase shift, however the amplitude is all the same.

V. DISCUSSIONS

In the above reaction system, the concentration of the enzymes shows an undamped oscillation. Unlike the open system devised by Seelig, this system exhibits the oscillation property regardless whether the mass flux is open or close, as long as the reactants are sufficiently large such that the reaction rate depends solely on the enzymes as shown in equations (16) through (25). Furthermore, equation (1) shows that the production of product P_1 is proportional to E_1; now suppose there is a proper constant leakage J_{P1} for P_1 or suppose P_1 involves in another chemical reaction, then the rate equation for P_1 is respectively

$$\frac{dP_1}{dt}=E_1-J_{P1} \text{ or } \frac{dP_1}{dt}=E_1-P_1 \tag{31}$$

In these two cases, P_1 would also be sinusoidal. Thus, not only the enzymes are sinusoidal, other properly related chemicals also would show an undamped sinusoidal oscillation. This enzyme reaction system may be used as a basis for modelling the biological clock or the chemical oscillator.

Acknowledgement

The author is greatful to Drs. R. R. Hwang and Y. D. Yao for their help with calculations.

REFERENCES

Bak, T. A. (1963) "Contribution to the theory of chemical kinetics". New York: W. A. Benjamin, Inc.

Denbigh, K. G., Kicks, M & Page, F. M. (1948). Trans Faraday Soc. 44, 479.

Hearon, J. Z. (1953) Bull. Math. Biophys. 15, 121.

Hyver, C. (1972) J. Theor. Biol. 36, 133.

Lotka, A.J. (1910) J. Phys. Chem. Ithaca 14, 271.

Meixner J. (1949) Z. Naturf. 4a 594.

Moore, M. J. (1959) Trans. Faraday Soc. 43, 1088.

Seelig, F.F. (1970) J. Theor. Biol. 27, 197.

Annual Report of the Institute of Physics, Academia Sinica, Vol. 6, 1976

Membrane Potential, Active Transport and Maxwell Demon

Wei-Kung Wang

Biophysics Lab. Institute of Physics Academia Sinica Taipei

Yuh-Ying L. Wang

Dept. of Physics National Taiwan Normal Univ.
Taipei Taiwan Rep. of China

Abstract

A membrane potential stabilizing mechanism is proposed. The permeability is suggested to be controlled by a potential sensor, while the active transport system is suggested to be a Maxwell demon which has the ability to recognize different ions to let some ion go into the cell and some go out of the cell. The idea that information is equivalent to entropy is used to construct the model of the active transport system. The non-steady ionic state of muscle cell is deduced, ionic concentration may determine the condition of the muscle is also suggested.

Introduction

Membrane potential and ionic concentration gradient which exist in most living cells are related to signal transmission, energy regulation, transportation, differentiation, circadian rhythm and other mechanisms. With the existence of membrane potential and the well regulated ionic concentrations in and out of a cell membrane, questions naturatly be raised on whether they are related to each other, or they are regulated by each other. It is known that ionic concentration may be changed by the alternation of permeability which followed the variation of the membrane potential, while the ionic concentration together with permeability may decide the membrane potential. Thus what does the membrane "see"? The ionic concentration or the membrane potential?

In the past, numerous investigators have given their proposals on the passive transport (permeability), the active transport and the membrane potential[1] [2] [3] [4] [5]. Even before our knowledge on the generation of membrane potential, the idea of an active transport in the nervous system had been suggested by Dean and Davison in 1944.[6] Recently it is confirmed that the active transport can be electrogenic as well as neutral[7] [8] and the system of transportation travels against the gradient of electrical and

chemical potential. The problem is then further complicated. The electrogenic pump may first change membrane potential, and through the change of electric field and permeability to produce the ionic concentration gradient.

It is natural to ask, what does the membrane "see"? How can the membrane "see" the things he want to see? And by what ways the membrane manage to have every thing corrected after understanding their situations. Presently, based on physics we try to explain how membrane "sees" the electric potential, find out the ionic concentration and control it to be right. A few applications of this idea are also suggested.

Permeability

Although the mechanism which regulates permeability is still unknown. To regulate the permeability of a membrane is known as one of the fastest ways to modify the membrane potential. By changing the permeability to have the right membrane potential, the simple way is to variate b value of the following equation according to V_m, where b is the relative permeability of Na^+ and K^+, V_m is the membrane potential, R is the gas constant (8.314 joules degree^{-1} mole^{-1}), T is the absolute temperature, $[K]_o$ and $[Na]_o$ are the potassium and sodium concentrations at outside of the membrane, $[K]_i$ and $[Na]_i$ are the potassium and sodium concentrations inside of the membrane.

$$V_m=\frac{RT}{F}\ell n\frac{[K]_o+b[N_a]_o+\cdots}{[K[_i+b[N_a]_i+\cdots}$$

The membrane potential depends on the b, so long as the permeabilities of other ions are negligibly small compare to that of potassium and sodium (or the permeabilities of other ions are constant).

That means $b=f\ (1/V)+g\ (V)$ (for this simplified derivation, we neglect the effect of time t, for more detail of the effect of t, please see Wei et a 1973)[9], for b is larger with smaller V, we then may have

$$b=f(1/V)=K_0+K_1V^{-1}+K_2V^{-2}+K_3V^{-3}+\cdots$$

If we assume that coefficient K_2, K_3,···and all higher terms of V are negligiblly small, we have $f\ (1/V)\simeq K_0+K_1V^{-1}$, this may explain the electrical excitation process which increase the b by increasing the sodium permeability. This simplified relationship may also explain the increase of potassium permeability by hyperpolarizing the membrane[8].

For a normal neuron or muscle

$$V=\frac{RT}{F}\ell n\frac{[K]_o+b[Na]_o+\cdots}{[K]_i+b[\mathrm{N}a]_i+\cdots}\text{Since } b\ll 1,$$

V depends mostly on the correct potassium concentration. The $[K]_o$, $[Na]_o$ are constant at most of the time (in extracellular medium with enormous volume kept almost constant composition). Therefore, there must be a sensor for the variation of potassium concentration inside the cell. Since $V\simeq\frac{RT}{F}\ell\mathrm{n}\frac{K_o}{K_i}$, $V\simeq\frac{RT}{F}(\ell nK_o-\ell nK_i)$, where R, T, F, K_o, are all constants, we may know K_i from V. The simplest sensor for K_i will be the same dipole sensor for the V.

Now the question turn to "How a sodium concentration sensor can be built?".

The simplest way is through a chemical equilibrium

$$\alpha+Na^+\rightleftarrows[\alpha]_{Na+} \qquad \alpha \text{ is the sensor.}$$

If there is too much $[\alpha]_{Na}$ in the membrane, it indicates that Na^+ is too high. If there is much α, it indicates that Na^+ is too low. The α may be related to the active transport. In the later sections, a discussion concerned with this problem will be offered.

Is the active transport system a Maxwell demon

It is known that active transport system can recognize, transfer and move ions or molecules against their own chemical gradient. In the past, we have the famous paradox, the Maxwell demon (e. g. Pierce, 1961)[10], that challenged the basic law in thermodynamics. This demon can recognize N_2 and O_2 to let them go in and out of a cell, therefore, the demon seems to have an infinite power to reduce entropy without consuming any energy. Now similar question may be asked, *i.e.*, is the active transport system a Maxwell demon? Has it the ability to recognize the K^+ ion and Na^+ ion so that it will allow Na^+ to go out of the cell, and let the K^+ go into the cell?

In muscle cell and neuron, it is believed that ATP is used to pump sodium ions out of the cell and potassium ions into the cell. However the energy come from splitting the ATP molecule is limited. How the active transport system gain the power to move ions against their chemical gradient? Is there a limitation on the active transport pump? Where does the limitation come? By answering these questions, we will be able to establish some basic principles of active transport system.

The pradox of Maxwell demon can be solved by information theory[10][11]. Information is equivalent to entropy, if the demon wants to know which molecule is which, he has to do something (for example, to use light or to use a spring) to gain this information, this information gathering process will increase the entropy or supply energy to the system, therefore at the time when the demon knows that it is a nitrogen molecule, there is already an energy supply or an entropy increase.

Now we have a similar situation, how does the active transport system know that it is a potassium ion or a sodium ion, where is this information from? How the information is gained? An ion or molecule moves against its chemical gradient and the entropy is reduced, there must be an energy supply. Thermodynamics required that the reduced entropy multiplies temperature be smaller than or equal to the energy supply.

In last section we have propsed a simple sensor for sodium ion, a simlar sensor may be built for any ion or molecules, a sensor must be specific for one ion (or molecule) to be a part of the active transport system. The simplest way to built a sensor is through a chemical reaction and the most economic way will be that the sensor itself is also the carrier.[12]

The chemical reaction

$S+I\underset{}{\overset{K_1}{\rightleftarrows}}[S]_I$ happens at the low concentration side of the membrane

S: the sensor or the carrier, I: any specific ion or molecule

$[S]_I$ will diffuse down the concentration gradient, at the same time it carries the I uphill. S has high affinity for I at the low concentration side. Before it diffuse across the membrane, it must reduce its affinity to I to release the I at the high concentration side. After the S cross the membrane, the conformation of S has shifted to S' which has no specific perference to any ion or molecule. Here the information is lost, this is necessary for energy conservation. Then $S'+I\underset{K_2}{\overset{}{\rightleftarrows}}[S_I]_I$, $K_1 \gg K_2$. Then by supplying some energy, S' is converted to S again. This reaction will complete the whole cycle. For S and $[S]_I$ to diffuse across the membrane, there needs no energy. because there is a coneentration gradient. To change its conformation from S' to S, the carrier changes its conformation from having an non-specific binding site (low affinity fo I) to a highly specific binding site (high affinity for I). This procedure is equivalent to an information gathering process, because the S will, therefore, regain the ability to recognize the I ion. This is the entropy reducing process, this will also be the energy consuming process. The

limitation of the uphill transportation is determined by the affinity ratio, $\frac{K_1}{K_2}$. The supplied energy is used to convert the conformation from S' to S, the higher is the affinity of S to I, the larger is the energy consumed (Wang & Wang)[12].

The sodium and potassium exchange pump

Now, based on what has been discussed in last paragraph, we will study a coupled active transport, the K^+ and Na^+ exchange system in neuron and muscle cell.

Suppose the carrier E_k that has high affinity for potassium ion exists at outside of the cell membrane. The following reaction will happen.

$$E+XK^+ \rightarrow [E]_k$$

X is a natural number and $X=2$ is suggested by most investigators

After $[E]_k$ is diffused across the membrane, $[E]_k \rightarrow E'+XK^+$, it is changed to a conformation of E' with low affinity for potassium and high affinity for sodium and release the XK^+, then $E'+Y\ Na^+ \rightarrow [E']_{Na}$ after it is moved back to the other side of the membrane,

$$[E']_{Na} \rightarrow E+Y\ Na^+$$

Y is another natural number and $Y=3$ is suggested by most investigators

Then the E will bind XK^+, the whole cycle is started again.

Now, the question is, where the information is gained? Both the steps

$$E \rightarrow E' \text{ and } E' \rightarrow E$$

can be looked as an information gaining and losing process. We may treat this question by assuming a third conformation E_0, which has no general preference. Then both $E_0 \rightarrow E'$ and $E_0 \rightarrow E$ can be looked as an information gaining process, $E' \rightarrow E$ can be subdivided into

$$E' \rightarrow E_0 \rightarrow E$$

From $E' \rightarrow E_0$ we lose some information, this is something necessary to complete the cycle and by this way the energy is balanced. All information-gaining steps need energy supply, therefore from $E' \rightarrow E$ and $E \rightarrow E'$ may need energy supply. The energy is supplied by the form of ATP. The ATP may modify the E' to change it's conformation to E, by phosphorylate the E', by ATP binding or by the energy supplied from the ATP splitting (for more details of these possibilities, please see (Garrahan & Glynn, 1967)[13]. Then

from $E' \rightarrow E$ the effect of ATP is removed. No matter which way is followed, we may simplify these as two steps (1) ATP joins the reaction, (2) removal of the effect from ATP, we may also simplify this as the release of Z.
The whole scheme may be simplified as shown in Fig. 1.
or in a kinetic form as shown in Fig. 2.

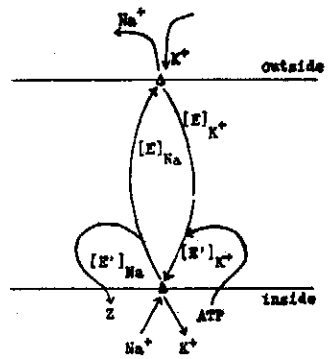

Fig. 1

Fig. 1. Ashematic drawing of the active transport system. Δ is the E binding site that exists at the ontside membrane. At the Δ site, the Na^+ is released and K^+ is binded to E. Δ is the E' binding site that exists at the inside membrane. At ▲ site, K^+ is released and Na^+ is binded to E' The ATP binding and Z releasing both may be happened at or near the ▲site.

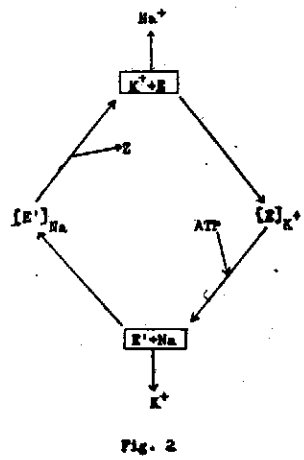

Fig. 2

Fig. 2. A kinetic drawing of the Fig. 1. It is a cyclic reaction similar to an engine or a pump. The fuel is the ATP.

The direction of this pump may depend on the free energy (Garrahan & Glynn, 1967)[13] (The detail of the energy balance and its relation to the direction of pump are discussed eleswhere (Wang & Wang))[12]. In this scheme, there are eight steps to complete a cycle: (1). $[E]_{Na}$ releases Na^+,(2). E binds K^+ to form $[E]_{K+}$, (3). $[E]_{K+}$ diffuses across the membrane, (4). ATP binds $[E]_{K+}$ and shifts the conformation to $[E']_{K+}$, (5). $[E']_{K+}$ releases K^+, (6). E' binds Na^+ to form $[E']_{Na}$, (7). $[E']_{Na}$ releases Z to shift the conformation to $[E]_{Na}$, (8). $[E]_{Na}$ diffuses across the membrane. Step (1), (5), (7) are spontaneous reactions, it should not take any time. Both steps (3) and (8) are the diffusion process which happened in a hundred $A°$ thick membrane, both processes will depend on the concentration gradients of $[E']_{Na}$ and $[E]_K$, that means the speed of these two steps depends on the speed of the step (2) and (6) (Wang & Wang)[12]. If the amount of ATP is adequate, step (4) should not be a variable and will not control the rate.

Now there are two steps left

$E'+Na \rightarrow [E']_{Na}$ at the inside of the membrane

$E+K^+ \rightarrow [E]_K$ at the outside of the membrane

Since the ionic condition of the extracellular medium is constant, it is reasonable to guess that only the reaction $E'+Na^+ \rightarrow [E']_{Na}$ is the rate-limiting step and indeed this is the case. Skou (1975)[14] found that the apparent affinity for potassium relative to sodium at outside membrane is several hundred to one, while the apparent affinity for sodium at inside of the membrane is only several times that of potassium. Although the apparent affinity found by Skou may involve some non-specific binding that will reduce the ratio of binding, it does show that the ratio at the outside of the membrane is much higher than the ratio at the inside of the membrane. This indicates that the reaction rate of $E+K^+ \rightarrow [E]_K$ at the outside of the membrane will be much faster than the reaction $E'+Na^+ \rightarrow [E']_{Na}$ at the inside of the membrane. This will leave the rate limiting step of the cycle to the $E'+Na^+ \rightarrow [E']_{Na}$ and the speed of the pump $\nu = K \cdot [E']_{Na}$, K is a constant. For adequate supply of ATP, concentration of E' is constant we have $\nu \propto \{[Na^+]_i - [Na^+]_c\}$, $[Na^+]_c$ is a constant, when $[Na^+]_i$ is below $[Na^+]_c$, the pump will be stopped.

This is exactly the experimental result of Thomas. (1972[8].)

Can a normal cell be in true steady state

The permeability is a passive transport which reduced the ionic

concentration gradient, while the active transport increases the ionic concentration gradient. In the traditional derivation, most of the authors used the steady state[15] [16] [17] [21] [22] [23]. In other word, they assumed the passive transport is completely compensated by active transport. In a dynamic equilibrium state, the cell membrane potential and the ionic concentration are not a function of time in a macroscopic sense.

Let us concentrate on Na^+ and K^+ ions, most of the data indicate that the transportation of Na^+ and K^+ are directly coupled, when the Y ions of Na^+ moved out of the cell, there are XK^+ ions move into the cell. For muscle cells, most of the investigators suggests that two K^+ ions move in, there are alway three Na^+ moving out. For a muscle at rest the membrane potential is inside negative. Because the potassium permeability is the highest, the K^+ ion is therefore leaking out constantly at a higher rate. To compensate the K^+ loss, the active transport system must pump in more K^+, but at the same time, it must extrude even more sodium ions, because every two K^+ are moved in, three Na^+ are moved out. Therefore if the K^+ is in a dynamic equilibrium state, the Na^+ inside the cell will continuously decrease. In otherword, the cell can not be in a steady state with respect to both potassium and sodium ions. If there is no external distrubance such as the end plate potential or the miniature end plate potential, the cell membrane potential should not be a constant. It should decrease with time, because the Na^+ inside the cell become smaller and smaller. Though the permeability of Na^+ is much smaller, it still should reduce the membrane potential and it may also increase the amplitude of the m. e. p. p. (Lomo & Rosenthal, 1972)[18].

This non-steady state may make the muscle depends on the e. p. p. and m. e. p. p., to maintain the normal membrane potential as well as the ionic condition which may then determine the condition of the muscle. This may be the cause for the hypersensitivity of denervated muscle and the muscle with Ach receptor blocked by some drugs [18] [19] [20].

References

1. Martrosov, V. M. and Mikayelyan (1970) Ion excharge in electrogenic active transport of ions. Biophysics 15, 104.
2. Bonting, S. L., (1970): "Membranes and ion transport" (Bitter E. ed) Vol. 1. John Wiley and Sons Ltd.
3. Kaback, H. R., (1972) "Current topics in membrane and transport" Vol. 2, Academic Press.

4. Moreton, R. B., (1969) An investigation of the electrogenic sodium pump in snail neuron using the constant field theory. J. Exptl. Biol. **51**, 181.
5. Wilbrant, W. (1975) Recent treads in membrane transport research. Life science **16**, 201.
6. Davison, H. (1944) Cold Spring Harbor Symp. Ouant. Biol 8., 255.
7. Thomas, R. C., (1969) "Membrane current and intracellular sodium changes in a snail neuron during extrution of injected sodium" J. Physiol. **151**, 598.
8. Thomas, R. C., (1972) Intracellular sodium activity and the sodium pump in snail neurones. J. Physiol. **220**, 55-71.
9. Wei, L. Y., (1973) Quantum theory of time-varying stimulation in nerve Bull. Math. Biophysics 35, 359-374.
10. Pierce, J. R., (1961) "Symbols signals and noise" (Newman, J. R. ed) Harper & Brother N. Y.
11. Brillouin, L., (1963) "Science and information theory" A. P.
12. Wang, Y. Y. L. and Wang, W. K. (1976) Is active transport in contradiction to second law of thermodynamics. Chinese Journal of Physics. **14**, 89-92
13. Garrahan, P. J. and Glynn, I. M. (1967) The incorporation of inorganic phosphate into adenosine triphosphate by reversal of the sodium pump. J. Physiol. **192**,237-256.
14. Skou, J. C. (1975) Abstract 5th international Biophysics Congress p. 15 S. 3.
15. Mullin, L. J. and Noda, K. (1963) The influence of sodium free solutions on the membrane potential of frog muscle fibres. J. Gen. Physiol. **47**, 117.
16. Schwartz, T. L., (1971) "Direct effect on the membrane potential due to "pump" that transfer no net charge" Biophysics J. **11**, 944-960.
17. Sandblom, J. P., and Eisenman, C. Membrane potential at zero current: The significante of a constant ionic permeability ratio (1967) Biophysics J. 7, 217.
18. Lomo, T. and Rosenthal J., (1972) Control of Ach sensitivity by muscle activity in the rat. J. Physiol. **221**, 493.
19. Thesleff, S., (1960) Supersensitivity of skeletal muscle produced by botulinum toxin J. Physiol **151**, 598.
20. Chang, C. C., Chen, T. F. and Chuang, S. T. (1973) Influence of chronic neostigmine treatment on the number of acetyl choline recpetors and the release of acetylcholine from the rat diaphragm J. Physiol **230**, 613-618.
21. Cross, S. B. Keyes, R. D. and Renata Rylova (1965) The coupling of sodium efflux and potassium influx in the frog muscle J. Physiol. 18, 865-

880.

22. Rapoport, S. I. (1970) The sodium potassium exchange pump I. Theory Biophysics J. **10**, 246.
23. Rapoport, S. I. (1971) The sodium potassium exchange pump II. Analysis of Na^+ loaded frog sartorius muscle. Biophysics J. **11** 631.

Annual Report of the Institute of Physics, Academia Sinica, Vol. 6, 1976

The Pentose Cycle in Dorsal Root Ganglia of Chick*

Wei-Kung Wang

Biophysics Lab. Institute of Physics
Academia Sinica, Nankang, Taipei, Taiwan

Abstract

Dorsal root ganglia of 14 day's chick were incubated in Mccoy 5A medium with (6—^{14}C) glucose, usually it takes more than 18 hr for $^{14}CO_2$ to reach maximum. The pre-incubation will greatly reduce the time needed for $^{14}CO_2$ to reach maximum, For 17 hours of pre-incubation, $^{14}CO_2$ reach maximum in less than 4 hours of incubation. The labelled Fructose 1.6 diphosphate is found to be about 0.2μ mole/g tissue. These results indicate that the C—6 of glucose may go through this F-1.6 dip pool in pentose cycle several times before being liberated as CO_2.

1. Introduction

The glucose is the most essential substract for nervous system, it has gong been an important research subject. However, it is still not clear how tlucose is used in a system. From the enzymatic study, we understand that lhere are three different pathways to metabolize glucose, the glycolysis, citric acid cycle and hexose monophosphate shunt, in a animal. Usually we use the amount of lactate production as the indicator of the activity of glycolysis, and use the ratio $\frac{CO_2(C-1)}{CO_2(C-6)}$ to distinguish the activity of citric acid cycle and hexose monophosphate shunt. The difficulty of such a assumption is that, the ratio $\frac{CO_2(C-1)}{CO_2(C-6)}$ must be a constant to make the traditional theory applicable.

Recently, we use a specially designed respirometer to measure the CO_2 output at different time[1] and find that the CO_2 output is a variable that depends on how long the sample is been incubated, if we pre-incubate the sample, the time course of CO_2 output is significantly changed.

2. Material and Method

Fertile eggs were obtained from near-by farm, a few eggs is put into

* Work Supported by National Science Council, Rep. of China

the incubator every day. Age was defined as the number of days of incubation at 37°C, usually it takes 21 days for an egg to hatch. The weight of embryo is also checked as an additional control of stage.[2] For all healthy embryo the developmental stage according to weight are very close to the incubation time.

Ringer's solution was prepared with 8.39 g of Nacl, 0.44 g of kcl and and 1.26 ml of 2 molor $CaCl_2$ mode up to 1 litter with distilled water. Mccoy's 5A modified medium and antibiotic-antimyotic solution (100 x; 10,000 unit/ml penicillin, 10,000 mcg/ml streptomycin and 25 mcg/ml fungizone) were obtained from Grand Island Biological Company Grand Island, N. Y., Labelled glucose was obtained from New England Nuclear, Boston Massachusetts. The dorsal root ganglia 25-29 was removed from the spinal column in a small petric dish. After the ganglia were picked out, the surrounding membrane and associated sciatic nerve were cut as close to the ganglion as possible, the whole process takes about 20-30 min in cold ringer's solution.

The prepared ganglia were pre-incubated for 6-24 hrs in 100-300 ul bath medium. The volumn was chosen according to the period of pre-incubation to keep the depletion of the glucose less than 10%. The 95% O_2—5% CO_2 gas were flow over the bath medium as was done during the incubation. Afte^r the preincubation, the ganglia were fastly transferred to another incubation chamble that contain 50-100 ul medium with ^{14}C-labelled glucose. Instruments were arranged as shown in Fig. 1. The time constant for CO_2 measurement in this arrangement is less than 10 minutes. The carrier gas 95% O_2—5% CO_2 were flow over a large volumn (100ul-800ul) of bath medium before being

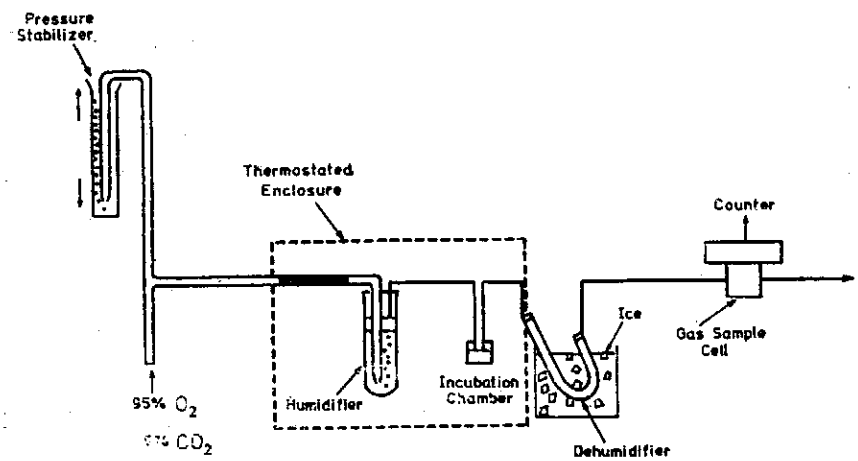

Fig. 1. The respirometer used to measure $^{14}CO_2$ output continuously.

passed over the incubation solution. The flow rate of the carrier gas was set to about 1 ml/min, labelled CO_2 was counted with low background α and β counting system supplied by Canberra Industries, Meriden Connecticut.

The phosphorylated compounds are separated by a procedure modified from Gerlach (1955).[3] The ganglia after incubation is first extracted with 10% trichloroacetic acid. The mixture is centrifuged and 25% barium acetate is added to the supernatant. This bariums acetate precipitate is washed with 25% barium acetate several times before N formic acid is added to extract the soluble fraction which contain 2 and 3 phosphoglyceric acid and hexose 1.6 diphosphate. The soluble fraction is therefore counted with packard liquid scintillation counter model 3375. Each liter of scintillation fluid is consist of Toluene 667 ml, Trition x-100 333 ml PPO 5.5 gm POPOP 0.07 gm.

3. Result:

Figure 2 are the summary of the experimental result. The $^{14}CO_2$ output

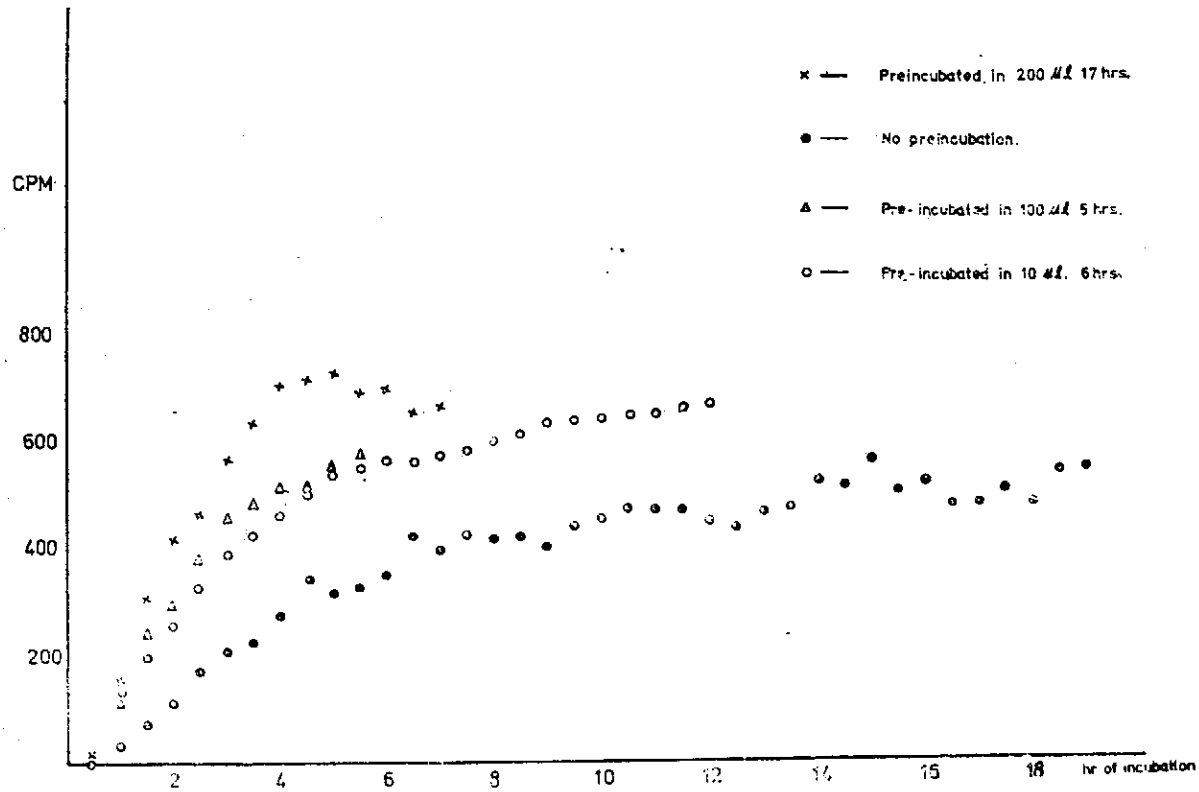

Fig. 2. Time course of $^{14}CO_2$ output from 14 day's dorsal root ganglia (25-29). The importance of this result is that after pre-incubation the liberation of $^{14}CO_2$ for 6—C of glucose is significantly faster.

14 day's ganglia incubated in medium with (6-^{14}C)glucose continuously increase for about 18 hrs of incubation and the largest amount is very close to that from (1-^{14}C) glucose, this result is very confusing, because the tranditional model of using the ratio $\frac{CO_2\ (C-1)}{CO_2\ (C-6)}$ can not be applied. The CO_2 from $C-6$ of glucose is a function of time.

If we pre-incubate the sample is medium without labelled glucose for several hours than transfer it into medium with (6-^{14}C)glucose, the time need for $^{14}CO_2$ output to reach maximum in greatly reduced. For 6-hours of pre-incubation, the CO_2 output reach maximum in about 10 hours of incubation; for 17 hours of pre-incubation, the CO_2 output reach maximum in about 4 hours of incubation.

For ganglia around 10 day's of age, the pre-incubation does not have significant effect on the $^{14}CO_2$ output.[1] The ^{14}C-labelled fraction I of the phosphorylated compound which contains mainly the ^{14}C-labelled fructose 1.6 diphosphate is found to be about 0.2μ mole/g tissue for long time incubation ($^{14}CO_2$ output reach maximum) and less than 0.1μ mole/g tissue for short time incubation (4-6 hrs).

4. Discussion

The slow increase of $^{14}CO_2$ from (6-^{14}C) glucose was interpreted by two possible reasons.[1] (1) There is a large pool in pentose cycle, the carbon atom pass through this pool will have a very large time constant. Therefore, the $^{14}CO_2$ output takes a long time to reach the maximum. (2) The activity of the some pathway is slowly activated. At the beginning of the incubation, there are several transitions, from low temperature to warm temperature, from ringer's solution to McCoy's medium, and from in vivo to in vitro. The cells can not adjust to the suddenly changed environment, therefore, some metabolic pathways may be slow down or even stopped. It may takes a long time before they may be activated again.

The first possibility has been thoroughly discussed. Here, a more detailed discussion is given to the second possibility. During dissection, the ganglia is in cold ringer's solution for about 20-30 minutes, then the ganglia is transferred to warm McCoy's medium. There are several factors may effect the metabolic pathway.

(a) Temperature: The low temperature will reduce the metabolic rate. The slow down effect may be different for different pathway, and some metabolic pathway may even be shut down. When the cell is

warmed up again, it may take a long time for it to recover.

(b) Substract: The ringer's solution is only a salt balanced solution, the leak of nutrient may shift the metabolism of the cell into a new direction. The stop of blood supply may also reduce the oxygen partial pressure which will also have significant effect on the metabolic pathway.

(c) Hormone or Hormone-like substances: In ringer's solution some hormone, or hormone-like substance (Insulin, Thyroxin; etc.) may be washed away, and the cells respond to these with an altered metabolic pathway.

From the result of pre-incubation, we see that, after a long time pre-incubation, the time need for $^{14}CO_2$ from (6-^{14}C)glucose to reach maximum is greatly reduced. This means that the process of dissection do have great effect on the slowly increased fraction of $^{14}CO_2$. However, after even 17 hr of pre-incubation the $^{14}CO_2$ still takes about 4 hours to reach maximum. This indicate the possibilities (1) do play some roll in the slow increasing of CO_2 output.

The pool size of labelled fructore 1.6 diphosphate from (6$-^{14}C$) glucose is found to be about 0.2μ mole/g tissue. If the $C-6$ of glucose but not $C-1$ or $C-2$ has to go through this extra pool for several times before it may be liberated as CO_2 from pentose cycle, it may still takes a few hours to reach maximum. To check for this, it is better to use (4$-^{14}C$)glucose or (5$-^{14}C$)glucose to study the $^{14}CO_2$ output time course and compare it to (3$-^{14}C$)glucose or (2$-^{14}C$)glucose in some carefully pre-incubated ganglia and to do some careful study comparing the labelled F. 1.6 dip. at different incubation time with different labelled glucose. We will then be able to give definite prove that the slowly increasing fraction is from the recycling of carbon in pentose cycle, although we may not be able to exclude the possibility that the slow increase of $^{14}CO_2$ from (6$-^{14}C$)glucose is activated by the artificial incubation medium due to prolonged incubation.

References

1. Wang, W. K. (1973) Glucose metabolism in developing nervous system, Ph. D. Thesis, Johns Hopkins U.
2. Ramanoff, A. L. (1960): "The avian embryo" Macmillam Co.
3. Gerlach (1955): Quoted from "Paper chromatography and paper electrophoresis" R. J. Block, E. L. Durrum, G. Zweig A. P. 1958 N. Y.

Annual Report of the Institute of Physics, Academia Sinica, Vol. 6, 1976

Rhodopsin and the Early Receptor Potential

By

Wei-Kung Wang

Biophysics Lab.
Institute of Physics
Academia Sinica
Nankang, Taipei, Taiwan
The Republic of China

Abstract

A charge separation and subsequent charge spreading model is used to explain the generating mechanism of early receptor potential. The charge separation is produced during the breaking of the S-H bonds and sebsequent chromophore isomerization that change it configuration from a resonanced 11-cis retinal with the order of double bond and single bond interchanged to a 11-trans configuration. The relation between the chemical transition and the correspondent electrical signal are thoroughly discussed.

Introduction

The rhodopsin of vertebrate shares a common chemistry. After the trigger of a photon, rhodopsin goes through a few intermediates before it is decomposed into retinal and opsin[1]. The intermediates of bleach are determined from the change of λ max. During the rhodopsin goes through these intermediates, the electrical events——the early receptor potentials cau also be measured.[2]

Recently, I have discussed both the structure of the these bleaching intermediates[3] and the generating mechanism of the early receptor potentials.[4] In the present paper, a relationship between the chemical process and the electrical events is given. From these relationships, we may understand the process of the visual excitation.

The early receptor potential

The property of early receptor potential is most thoroughly reviewed by Cone (1969).[2] In addition to the R_1 and R_2 responses, there are R_A, R_B and R_C and it is supposed that each corresponds to its own chemical transition.

It is known that the outer segment is composed of double membrane disks (Fig.1a). We may assume it is a short cylinder of cytoplasm that is a good conductor (Fig. 1c), the upper and lower side of the cylinder are covered

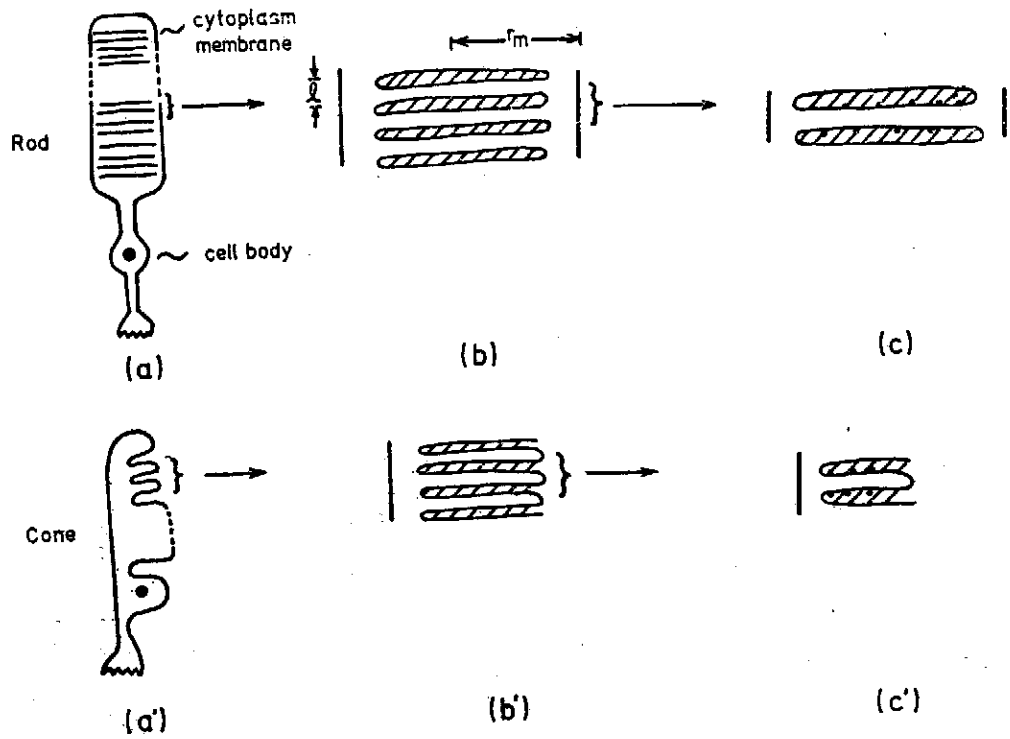

(Fig. 1.)

Fig. 1(a) (a')Sketch of the outer segment.
(b) and (b') Enlargement of a short piece of the outer Segment, $r_m \simeq \mu$ and $\ell \approx 100A°$.
(c) and (c') Unit outer segment

with a double-membrane insulator. A cylinder of this structure is repeated several thousand times in the outer segment of Cone and Rod, and we will call such a cylinder "The unit outer segment". The height of the unit outer segment is about a hundred $A°$, the radius of the cylinder is of the order of μ, (Nilson, 1965;[5] Cohen, 1968[6]).

The early receptor potential is suggested to be from charges released or absorbed from the rhodopsin and the double membrane disk.

The photon excitation causes a sudden introduction of charge q into the unit outer segment, it may be approximated as a charge q in the center of a cylindrical conductor. There will be some induced charges on the membrane' according to the method of image, the charge $q_m \simeq -q\frac{\varepsilon_2-\varepsilon_1}{\varepsilon_2+\varepsilon_1}$ will be induced on each side, ε_1 is the dielectric constant of the cytoplasm and ε_2 is the dielectric constant of the membrane. The total effective charge is q', $q' \simeq q + 2q_m \simeq (1-2\frac{\varepsilon_2-\varepsilon_1}{\varepsilon_2+\varepsilon_1})q = \alpha q$,

the electric field E at r for $r \gg \ell$ will be

$$\vec{E}=(q'/2\pi r^2 \ell \varepsilon_1)\vec{r}, \tag{1}$$

the voltage between point r_1 and r_m is

$$V_{1m}=(q'/2\pi\ell\varepsilon^1)\ \ln\ (r_m/r_1) \tag{2}$$

the current density J is given by

$$\vec{J}=k\vec{E} \tag{3}$$

where k is the conductivity of the cytoplasm.

The current will be $I=-\frac{dq}{dt}=\vec{J}\cdot 2\pi r\vec{\ell}=k\vec{E}\cdot 2\pi r\vec{\ell}$ (4)

substituting eq. (1) into eq. (4), we get

$2\pi r\vec{\ell}k\cdot(q'/2\pi r^2\ell\varepsilon_1)\vec{r}=-\frac{dq}{dt}$; and $q'=\alpha q$

$$q=q_0\ \exp[(-\alpha k/\varepsilon_1)t] \tag{5}$$

Substituting eq. (5) into eq. (2), we have

$$V_{1m}=\alpha q_0\ \exp[(-\alpha k/\varepsilon_1)t]/2\pi r\ell\varepsilon_1\ \ln(r_m/r_1) \tag{6}$$

This process does not depends on the diffusion process of the ions, however it does depend on the how fast the charge is introduced into the cytoplasm and the dielectric constant, conductivity of the cytoplasm. A calculation[4] has shown that the rotation of 11-cis→all-trans retinal needs at least 10^{-9} sec. While in the most recent measurement, R_1 appears less than 10^{-8} sec after the light flash.

The other possible mechanism to produce electric events is ion absorption and subsequent ion migration, this produce a diffused electrical double layers. For the production of R_2 as well as R_A,R_B and R_C we see that hydrogen ion is probably the most important ions that is absorpted and migrate.[4]

The migration of hydrogen ions follow the eqn.

$$\frac{\partial\rho_h}{\partial t}=\frac{D_h}{A}\left[\frac{\partial^2\rho_h}{\partial x^2}-\frac{e^2\rho_h}{KT}\ \frac{4\pi}{\varepsilon}(\rho_h-\rho_{oh})\right] \tag{6}$$

ρ_h: hydrogen ion concentration.

ρ_{oh}: hydrogen ion concentration before photo-excitation.

k: Boltzman constant. T: absolute temperature. ε:dielectric constant

The boundary conditions are

$$\rho_h(o,\ x)=0 \text{ at } x<\zeta, \qquad \rho_h(o,\ x)=\rho_{oh} \text{ at } x>\zeta$$

where ζ is the initial thickness of the double layers and

$$\rho_h(\infty,x)=\rho_{oh}\exp\lfloor eV\exp(-Kx/kT)\rfloor$$
$$K^2=(4\pi e^2/\varepsilon kT)\Sigma\rho_{oi}Zi^2$$

we may approximate both cases by the following equivalent circuits

Equivalent Circuit

It has been shown that the plasma membrane acts as a high capacitance element.[7] Let the capacitance be C_m, the total charge on it is $Q_m=C_mV_m$. No matter what is between the outer segment and the outside world, we may assume it is equivalent to a resistance R_e. We have

$$\frac{d}{dt}(C_mV_m)\cong\frac{d}{dt}(Q_m)\cong I\cong V_e/R_e$$

where V_e is the potential measured extra-cellularly. The equivalent circuit for the $R1$ is shown in fig. 2a.

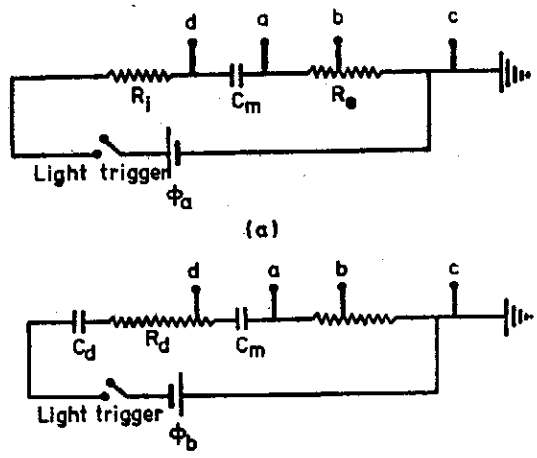

(Fig. 2.)

Fig. 2 Equivalent circuit: C_d is the capacitance of diffused double layer of charges, R_i is the resistance inside the cytoplasma membrane, R_d is the equivalent resistance of the diffused double layer and the C_m is the capacitance of the cyoplasma membrane, R_e is the resistance outside the cytoplasma membrane. The light excitation triggers the circuit, the voltage ϕ of the battery is porportional to the number of absorbed photons.

A diffused double layer has an equivalent capacitance C_d,[8]

$$C_d = -\frac{d}{dx}(Q_s) = (Z\varepsilon A/kT)\ \cosh(Z\varepsilon\zeta/2kT).$$

For low ionic concentration and small ζ, C_d will be a few $\mu f/cm^2$. Therefore the equivalent circuit for the $R2$ is in fig. 2b.

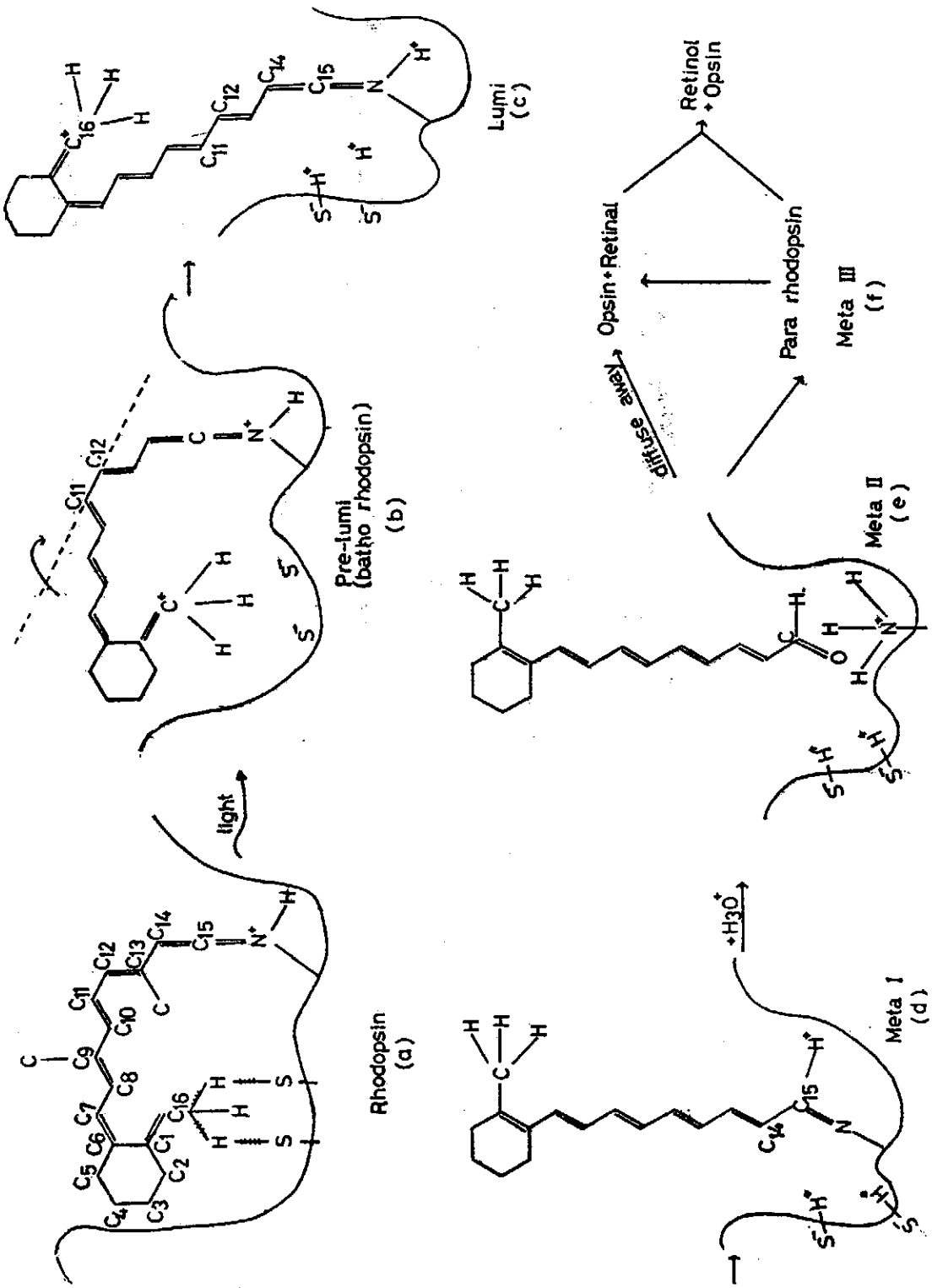

Fig. 3 Proposed molecular configurations. Its E.R.P. correspondences[2] can be easily found from the charge it picks up or releases. (see text)

The potential V_{ab}, V_{bc} and V_{ac} are of the same polarity but of different magnitudes. When the reference electrode is far away, an electrode near d gives an intracellular E. R. P., and an electrode near a and b, gives an extracellular E.R.P. and we have

$$\frac{d}{dt}(\text{E.R.P.})_{intra}=(C_mR)_c^{-1}(\text{E.R.P.})_{extra}$$

The point b can be far away from the retinal providing that the reference electrode at point c is well grounded.[9]

Relation between bleaching intermediates and early receptor potential

The structure of the bleaching intermediates is suggested by Wang[3], here a summary is gives in Fig. III.

From this figure, it is easy to see that, from rhodopsin to lumi, a positive charge is introduced into the cytoplasm. This is most probably correspond to R_1. The S^- picks up hydrogen ion during the transition to lumi and meta I, the corresponding electrical signal will be R_2. The para-rhodopsin is supposed to have retinal bind to a lipid or another amino acid of opsin with a Schiff-base linkage,[3] therefore the electrical signal of transition from meta II→para-rhodopsin should be similar to the reversed signal of meta I→meta II. Because a hydrogen ion is released, the R_B should be a positive signal as was measured by Cone.[2] While the electrical signal (R_C) of the transition from para-rhodopsin to retinal and opsin should be similar to that of meta I→meta II(R_A), a negative one.

Thus we see that the proposed bleaching intermediates will not only fit the chemical properties of the photo-excitation process,[3] but also give the correct electrical signal that corresponds to each transition.

References

1. Wald, G. (1968) The molecular basis of visual excitation, Nature (London) **219**, 800.
2. Cone, R. A. (1969) The early receptor potential. Proceedings of the international school of physics "Enrics Fermi" Ocurse XL111 N. Y. A. P. 1969.
   Cone, R. A. Cobbs, W. H. III (1968) Rhodopsin cycle in the living eye of the rat, nature **221**, 818.

3. Wang, W. K. (1976) A model of rhodopsin and visual excitation in vertebrate. Chinese Biosience. **10**, 42.
4. Wang, W. K. (1975) Early re'ceptor potential generating mechanism in vertebrate retina. Bull. Inst. Zool. Academia Sinica **14**(1) 19.
5. Nilsson, E. G. (1965) The ultrastructure of the receptor outer segment in the retina of the leopord frog. J. Ultrastructure Res. **12**. 207.
6. Cohen, A. I. (1968) New evidence supporting the linkage to extracellular space of outer segment saccules of cones but not rods. J. Cell. Biol. **37**, 424.
7. Murakami, M. and Pak, W. L. (1970) Intracellularly recorded early receptor potential of the vertebrate photoreceptors. Vision Research **10**, 965.
8. Grahame, D. C. (1949) Theory electrocapillarity. Chemical Review **41**, 441.
9. Brown, K. T. (1965) Discussion about E.R.P. cold Spr. Harb. Symp. Quant. **30**, 483.

Annual Report of the Institute of Physics, Academia Sinica, Vol. 6, 1976

原子態之組態相互作用

Ta-You Wu (吳大猷)

Department of Physics, State University of New York at Buffalo, U.S.A.

中文摘要

本文對原子能態問題中各種組態相互作用的情形，作一總合簡論，如(1) Rydberg 系的異常，(2)自電離的現象及其理論的困難，(3)電子組態的能項，(4)某些鹼金屬原子雙重態的倒置，(5)某些鹼金原子主系線強度的異常等。繼對原子光譜中 BeI, CI 等電子數序之 $2p^2$, 2p3p, 2p4p; Si I 序之 $3p^2$,3p4p; Ge I 序之 $4p^2$; Sr I 序之 $5p^2$;Ba I 序之 $6p^2$;BI 序之 $2s2p^2$; Al I 序之 3s $3p^2$; CI 序之 2s $2p^3$;Si I 序之 3s $3p^3$; OI 序之 $2p^4$; SI 序之 $3p^4$; Se I 序之 $4p^4$; NI 序之 $3p^3$; PI 序之 $3p^3$; As I 之 $4p^3$；等能態作一檢討。

The Time Arrow and the Problem of Macroscopic Irreversibility*

Ta-You Wu

Department of Physics, State University of New York at Buffalo. U.S.A.

Abstract

The present article is a brief review, from the view point of a physicist, of the many aspects of the problems connected with the time, the time arrow, the reversibility of basic laws in microscopic physics, the irreversibility of macroscopic phenomena and the relation between the last two groups of phenomena and their theories. It is pointed out that according to the operational definition of time and the principle of relativity, for events that are not causally related, there is no absolute or universal time arrow; each individual inertial frame has its own time sequence of events. It is also pointed out that there is no fundamental contradiction between the reversibility of basic laws of microscopic physics and the irreversibility of macroscopic systems, the latter being of probabilistic, or statistical, origin. There are many ways to build irreversible theories on the basic of reversible ones by a mathematical device or a probabilistic assumption, but in each case, there is a crucial step that must be clearly recognized.

*This paper has been appeared in Memorial Volume to President Chian2 Kai-Shek,Academia Sinica, Taipei, Taiwan, ROC, April 1976.

Annual Report of the Institute of Physics, Academia Sinica, Vol. 6, 1976

A Nanosecond Associated Particles Time of Flight System for Studying Fast Neutron Scattering*

W. N. Wang, W. S. Hou, B. Chen and L. P. Liang

Institute of Physics, Academia Sinica and National Tsing Hua University, Taiwan, ROC

Abstract

A nanosecond associated particles time of flight system is set up in connection with the 14.1 MeV neutron generator. The details of the neutron target and shielding assembly, the associated α particle detector and the electronics for the detecting system are described. Characteristic time resolution, detection efficiency and background are presented. The capabilities of the system is shown.

* Work supported partially by Physics Research Center.

This paper has been appeared in Memorial Volume to President Chiang Kai-Shek, Academia Sinica, Taipei, Taiwan, ROC, April 1976.

Study of Energy Levels of ^{117}In from the Beta Decay of ^{117}Cd*

E. K. Lin, W. N. Wang & C. Chou

Academia Sinica and Tsing Hua University, Taiwan, Republic of China

Abstract

Thermal neutron capture gamma rays from ^{116}Cd have been measured by using a 43 cm^3 $Ge(Li)$ detector and a $NaI(Tl)$ scintillator. From single gamma-ray and gamma-gamma coincidence measurement, a total of 41 gamma rays has been identified belonging to the energy levels in ^{117}In populated in the beta decay of ^{117}Cd from thermal neutron capture in ^{116}Cd. A detailed decay scheme of ^{117}In was constructed. The results are compared with the work by Pandharipande et al.

* This paper has been appeared in Memorial Volume to President Chiang Kai-Shek, Academia Sinica, Taipei, Taiwan, ROC, April 1976.

Annual Report of the Institute of Physics, Academia Sinica, Vol. 6, 1976

Electronic Conductivity and Percolation Theory in Aggregated Films*

N. T. Liang

Institute of Physics, Academia Sinica
Nankang, Taipei, Republic of China

and

Yueh Shan and Shou-yih Wang

Department of Physics
National Tsing Hua University
Hsinchu, Taiwan, Republic of China

Abstract

The resistivity of an ultra thin bismuth film has been observed and analyzed according to a 2 dimensional continuum percolation model. This novel approach has produced interesting results such as critical area fraction $x_c=0.67$, critical exponent $\alpha=1.15$ and other features consistent with the 2 dimensional continuum model of percolation.

* Work supported by the National Science Council of the Republic of China.
This paper has been appeared in Physical Review Letters, Vol. 37, No. 9, p. 526, 30 August 1976.

Even-Parity Energy Levels of Singly Ionized Magnesium Donors in Silicon*

L. T. Ho

Insitute of Physics, Academia Sinica, Taiwan, ROC

Abstract

Three absorption lines observed at 238.66, 239.60 and 241.26 meV in the excitation spectrum of singly ionized magnesium donor impurities in silicon are suggested to belong to the 3s(E), 3s(A_1) and $3d_0$ energy levels, respectively. Observed photoexcitation to these even-parity levels in violation of electric-dipole transition selection rule is attributed to effects of polarization of the donor by other defects and to breakdown of the effective-mass approximation.

* Work supported in part by the National Science Council, Republic of China.
This paper has been appeared in Memorial Volume to President Chiang Kai-Shek, Academia Sinica, Taipei, Taiwan, ROC, April 1976.

Annual Report of the Institute of Physics, Academia Sinica, Vol. 6, 1976

Experimental Methods of Ionizing Impurity Atoms in Semiconductors*

By

L. T. Ho

Abstract

In order to study the behavior of ionized impurity states in semiconductors, it is found that the impurity atoms can be ionized by thermally ionizing neutral atoms, by compensating with other impurities, or by electron irradiation. These experimental methods of producing ionized impurities are discussed and compared using the case of magnesium impurity in silicon as an example.

* Work supported in part by the National Science Council, ROC. This paper has been published in Soochow Journal of Mathematical & Natural Sciences, Vol. 1, Dec. 1975.

Time-Dependent Effect of Donor Lines in Silicon*

L. T. Ho

Institute of Physics, Academia Sinica

Abstract

The photoexcitation spectrum of neutral magnesium donors in silicon is studied. The intensity of the excitation lines is observed to decrease with time. The positions of the excitation lines, however, remain to be the same indicating that the time has no effect on the ground state. The absorption coefficient of the excitation lines is found to depend on the sample age following the relation $\alpha(t) = \alpha_0 e^{-0.04t}$, where t is in month. This time dependence can be partially accounted for by precipitation of magnesium at room temperature. Since the sample contains large amount of oxygen, a magnesium-oxygen interaction may also be one of the reasons for the time-dependent effect of neutral magnesium donor lines in silicon.

* This paper has been published in Proceedings of the National Sciedce Council, No. 9, part 1, may 1976

Annual Report of the Institute of Physics, Academia Sinica, Vol. 6, 1976

Electrical Resistivity of Nickel-Rich Nickel-Chromium Alloys Between 4 and 300K*

Y. D. Yao, Sigurds Arajs, and E. E. Anderson

Department of Physics, Clarkson College of Technology, Potsdam, New York
(Received April 18, 1975)

Abstract

Electrical resistivity ρ of *Ni-Cr* alloys containing 5.5, 11.3, 15.7, 16.8, 19.4, 22.0, 24.6, and 27.0 at *% Cr* has been measured as a function of the absolute temperature T between 4 and 300 *K*. The sample with the *Cr* content of 22.0 at% exhibits a small ρ minimum at about 10*K*. No minimum has been observed in any other of the above samples, although an anomalous T dependence has been found in alloys containing 15.7, 16.8, and 19.4 at% *Cr*. The ρ minimum has been discussed from the viewpoint of the Béal-Monod theory for the Kondo effect in concentrated systems and the mechanism by Greig and Rowlands based on a T-dependent decrease of the impurity electrical resistivity. It is concluded that the ρ minimum in the *Ni-Cr* system is still a phenomenon which is not well understood at the present time.

* This paper has been published in Journal of Low Temperature Physics Vol. 21 p.369 (1975).

Magnetic Susceptibility of PdCe Alloys at Low Temperatures*

By

K. V. Rao, S. Arajs and Y. D. Yao

C. C. T., Potsdam, N. Y. U. S. A.

And

L. Hedman, Ch. Johannesson and H. U. Åström

KTH, Stockholm, SWEDEN

Abstract

Magnetic susceptibility (X) has been measured as a function of temperature (T) between 1.5 and 340*K* on *Pd-Ce* alloys containing 0.0, 0.4, 0.9 and 1.4 at% *Ce*. Clearly, additions of *Ce* considerably lower the X values of *Pd* above 10*K*. Our X results support the previous conclusions that *Ce* enters a *Pd* matrix essentially as a non-magnetic 4^+ ion at least above 20*K*. We find that X of *Pd* and *Pd-Ce* alloys can be described by the equation $X=A+C/(T-\theta)$, where A, C and θ are constants and T is the absolute temperature.

* This paper has been published in Proc. Int. Conf. LT14 Vol. 3 p. 398 (1975).

Electrical Resistivity of Palladium-Silver Alloys at High Temperatures**

By

Sigurds Arajs, K.V. Rao, Y.D. Yao*, and W. Teoh

Department of Physics
Clarkson College of Technology
Potsdam, New York 13676

Abstract

Electrical resistivity (ρ) has been measured as a function of temperature (T) between 300 and 900K on *Pd-Ag* alloys containing 30.0, 34.8, 40.0, 44.3 and 49.9 at.% *Ag*. All the ρ vs. T curves are monotonic with respect to T. We do not confirm the minimum at about 700K in the ρ vs. T curves observed by Ahmad and Greig. We suggest that the anomalous behaviour of ρ results from strain effects and thus is not an intrinsic property of the *Pd-Ag* system.

* Present address: Institute of Physics, Academia Sinica
Nankang, Taipei, Taiwan 115
The Republic of China

** This paper has been accepted by Physical Review.

Electrical Resistivity of Aluminum-Boron Composites Between 78K and 400K+

D. Abukay, K. V. Rao and S. Arajs

Department of Physics
Clarkson College of Technology
Potsdam, N.Y. 13676
U. S. A.

and

Y. D. Yao

Institute of Physics
Academia Sinica
Nankang, Taipei, Taiwan 115
Republic of China

Abstract

The electrical resistivity (ρ) of composites of commercial *Al*(6061)-*B** containing 60 volume % *B* fibers of diameter of 0.008 in., have been studied as a function of temperature (T) between 78 and 400K. The slope of ρ vs T curve is considerably large for the transverse (*B* fibers perpendicular to the electric current) than for longitudinal case. The results will be discussed from the viewpoint of existing theories for electrical conduction processes in composite materials.

+ It will be sent to Journal of Composite Materials.

* Materials obtained from Commonwealth Scientific Corporation, Alexandria, Va., U.S.A.

Annual Report of the Institute of Physics, Academia Sinica, Vol. 6, 1976

Nerve Excitations by the Coupling of the Dipoles and the Membrane Matrix*

Chyuan-Yih Lee†

Department of Physics,
Tamkang College of Arts and Sciences,
Tamsuei, Taiwan, R.O.C.

Chun Chiang

Institute of Physics,
Academia Sinica,
Nankang, Taiwan, R.O.C.

Abstract

Based on Wei's dipole flip-flop model and with the assumption that the dipole is coupled to the membrane matrix, the cathode-make-excitation. the anode-break-excitation and the cathode-gap-excitation can be explained in a systematic way. The strength-duration relations for these three processes are derived.

† Present address: Department of Physics, University of Delaware, Newark, DE 19711, U.S.A.
* This paper has been appeared in Bull. Math. Biol. 38, 1976

A Theory of Ambiguous Pattern Perception*

Chun Chiang

Institute of Physics
Academia Sinica
Nankang,Taipei, Taiwan
The Republic of China

Abstract

A theory of ambiguous pattern perception is formulated. This theory proposes a feature selector (field of attention) based on the time-sequential discrete property of the attention, a short-term memory for storage of the selected features, and a synthesizer (perception) to synthesize the consecuitvely stored features. Since the selected features keep comming in and since the features can only be stored in the short-term memory for a short period, the features which can be synthesized in the synthesizer vary with time. When all the essential features belonging to one pattern happen to be in the synthesizer, the picture is perceived to be that pattern; when all the essential features belonging to another pattern happen to be in the synthesizer, then the picture is perceived to be the other pattern. Thus the picture appears to oscillate between two patterns.

* This paper has been appeared in Bull. Math. Biol. 38, No. 5, 1976

Annual Report of the Institute of Physics, Academia Sinica, Vol. 6, 1976

Science, Truth and the Absolute Value*

Wei-Kung Wang

Institute of Physics, Academia Sinica, Taiwan, ROC

Abstract

From the similarity in all sciences, we know that each branch of science has its not compatible pair. In physics the momentum and position, in mathematics consistancy and completeness, in philosophy reality and Certainty, in political science the freedom and equality, are the not compatible pair. What the science can reach is to optimize the not compatible pair. These best pairs do not uniquely exist, therefore the truth may not uniquely exist.

If truth exist not uniquely, how do we define "value", contribution"? From the idea of entropy in thermodynamics, if we believe that human is able to make a reasonable choice for himself, then to increase the option is a great contribution to all mankind.

* Some of this work was presented in the 4th International Conference on the Unity of Science, New York City, Nevember' 1975.
This paper has been appeared in Memorial Volume to President Chiang Kai-Shek, Academia Sinica, Taiwan, Taipei, ROC, April, 1976.

Annual Report of the Institute of Physics, Academia Sinica, Vol .6, 1976

The Effects of Mountains on A Typhoon Vortex As Identified By Laboratory Experiments

PART II. THREE-DIMENSIONAL BARRIERS

By

H. P. Pao, Robert R. Hwang and Jin Jso

Institute of Physics
Academia Sinica
Nankang, Taipei, Taiwan

ABSTRACT

This paper continues the former study of the experimental performed series for investigating the interaction between the typhoon vortex and Taiwan island. An essentially two-dimensional free vortex in an otherwise uniform flow past a three-dimensional barrier is studied and three different three-dimensional symmetrical models resembling the general shape of Taiwan are used. Results show that the phenomena of blocking and deflecting, and its moving path of the free vortex are similar for these three barriers. -The vortex movement seems to be strongly dependent on the approaching path way of the vortex relative to the barrier. Comparisons are also made between the experimental results and field data. It is found that the flow patterns and the moving paths of the free vortex are reasonably similar to the actual track of typhoon vortex. This suggests that the laboratory Modeling may be a reasonable tool to predict the movement of typhoon vortex when it is in the vicinity of the island.

I. Introduction

In this study, we continue the experimental performation for investigating the interaction between the typhoon vortex and Taiwan island. Three-dimensional symmetrical barriers resembling the general shape of Taiwan island are used to replace the previous study of a two-dimensional elliptical barrier. Owing to its strong two dimensional characters, the typhoon was simulated as before by an essentially two-dimensional concentrated vortex in a flume. Various cases for different shapes of barrier, approaching paths of vortex, and angles of incidence were investigated. All these barriers symmetric with respect to some plain are short and can be immersed in the flume water. So not only the de-flecting but also the climbing phenomena of the typhoon vortex can be observed in the laboratory.

The basic objectives are still to find (a) the general flow pattern of the

typhoon vortex when interacting with the barriers, (b) the moving paths of the typhoon vortex (c) the sensivity of the typhoon vortex to the shapes of the barriers, and (d) the influence of approaching paths and angles of incidences of typhoon vortex on the interation.

After the comparison with the actual field data, we believe that for the problems converned, the laboratory modeling is certainly a valuable research tool, although the neglection of the latent heat and the Coriolis had set some limits to it.

II. Experimental Set-up and Procedures

The experiments were carried out in the same flume as mentioned in the previous study. The two-dimensional concentrated vortex was effectively created by suddenly moving an airfoil at an angle of attack. A vortex was shed instantly off the trailing edge of the airfoil, while another vortex of opposite sense was also shed as soon as the airfoil was brought from motion to rest. In order to dislodge the opposite sense vortex, the airfoil was kept moving for a considerable distance before it was brought gradually to rest; thus the second vortex was far apart from the first one and was also very much weakened and diffused.

A Nikon F 2 camera of 50 mm lens with MD-2 motor drive was used to record the development of the flow field. The flow was made visible bya suspension of small (0.1~0.5 mm) Pliolite S-5 beads which was illuminated by a horizontal sheath of light from two sides. Two light boxes were used for illumination; each one has horizontal openings at three levels, two inches apart, which permit observations of the flow pattern at any of these three le vels. The Pliolite particles having a specific gravity of about 1.05, sinking slowly in a uniform cloud. To give particle streaks of a convenient length, and to show the flow pattern effectively, the shutter time was set at 1/4 sec. It was found that good quality streakline pictures can be obtained at f. 1.4 with a film speed of ASA 400 (Kodak Tri × Pan).Since the MD-2 motor drive was used, the firing speed controlled by the MD-2 motor was set as one film per 1.3 sec constantly.

For facilitating the picture taken and visual observations a large mirror was mounted on top of the flume, inclined at an angle of 45°. Therefore, the camera set in front of the inclined mirror can see a top view of the flow field in the mirror. A two-dimensional airfoil at an angle of attack of about 25° was set in a sudden motion, thus creating a concentrated vortex behind

its trailing edge. The uniform flow in the flume acts as the steering flow for the vortex. Top view pictures of different shapes of barriers, approaching paths, and angles of incidence were then taken successively.

III. Experimental Results and Comparisions with Field Date

In this study, a series runs of experiments for different shapes, angles of incidence and layers of light sheet were performed for the case of free vortex interacted with three-dimensional barriers. The top-view pictures shown in figures 1, 2 and 3 are from the representative experiments for a free vortex approaching and passing over barriers of elliptical cylinder, ellipsoid and rhombus in the same height respectively. The free vortex approaches the barrier at an angle of 45° to the major axis of the elliptical barrier and 90° for both ellipsoid and rhombus in the corresponding figures. When meeting the barrier, t he vortex was blocked for some while with the velocity apparently decelerated, and then soon accelerated and passed over the barrier. The time interval between successive pictures is 1.3 sec. From figures 1b-1c, it can been seen that an eddy is being formed at the tip on the lee side of the barrier when the vortex is in the vicinity of the barrier. However, the eddy induced is relatively weak and of small strength as compared with the former experiment. The induced eddy is significant in the lower layer but vague on the upper layer. It can be stated that for a two-dimensional vortex associated with a three-dimensional barrier the induced eddy is three-dimensional. As the main vortex is passing over the barried, the induced eddy is also drifting away from the barrier, but it is quickly overtaken by the main vortex in the moving downstream. This can be noted from figures le through lg and figures 2e to 2g clearly. The sequential location of the center of the free vortex can be connected to get its moving path as shown in figure 1h. It is noted that the main vortex, as mentioned in the previous study, has the tendency to be veering to the right as it approaches a barrier. This leads to the fact that the passing path is firstly deflected upward and then downward as passing over the barrier. Several representative path lines are also obtained and plotted as solid lines in figure 4 and figure 5 for both of climbing and deflecting cases respectively. Eight climbing typhoon tracks and six deflecting typhoon tracks are selected and plotted as dotted lines in the same figure as the mountain barrier interacts the typhoon vortex. It is seen that the agreement between the laboratory results and the field data is very good for both casses.

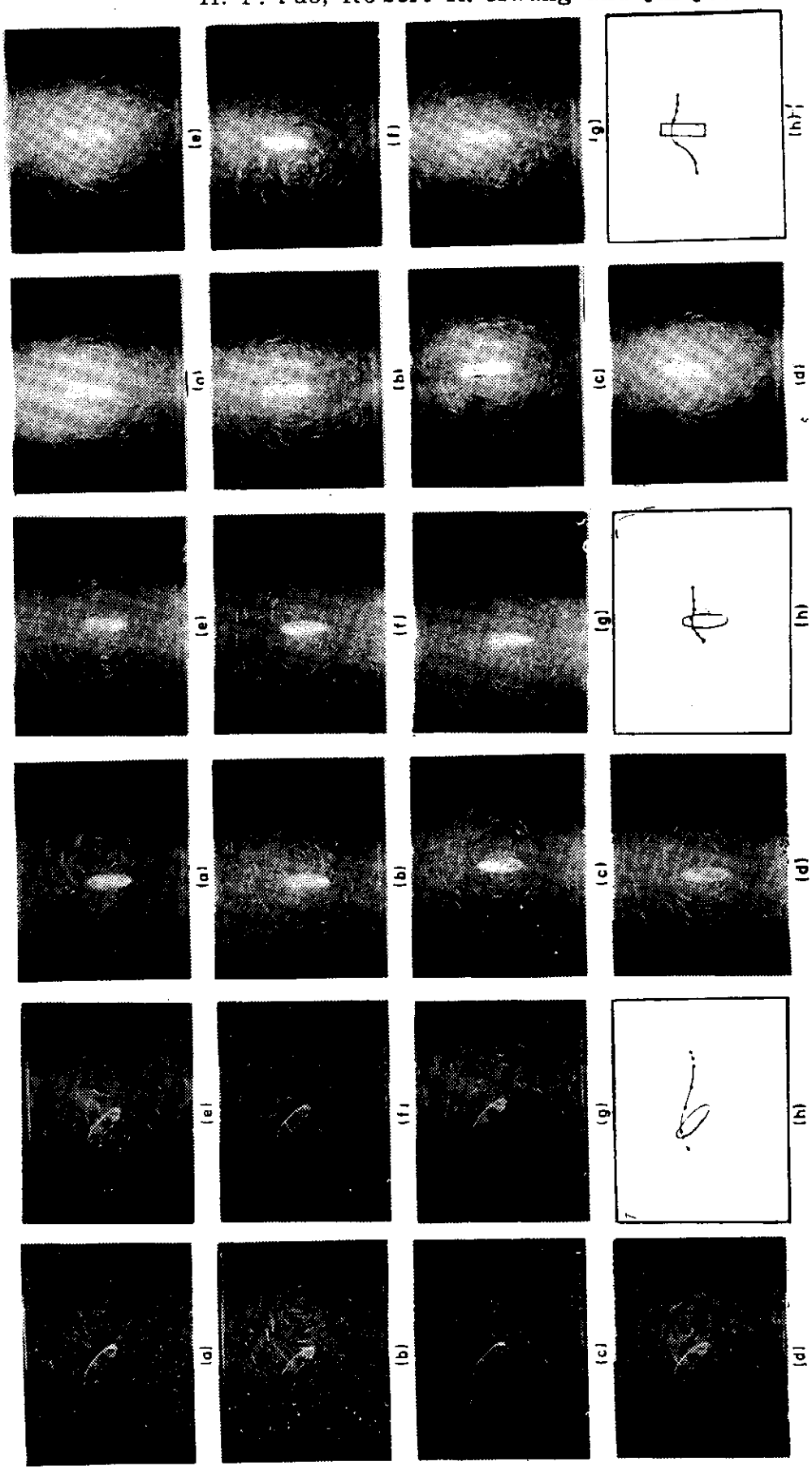

Fig. 1. Laboratory experiment of a free vortex past over an elliptical barrier. Angle of approach $\alpha=45°$, U=1.9 cm/sec.

Fig. 2. Laboratory experiment of a free vortex past over an ellipsoid. Angle of approach $\alpha=90°$, U=1.9 cm/sec.

Fig. 3. Laboratory experiment of a free vortex past over a rhombus. Angle of approach $\alpha=90°$, U=1.9 cm/sec.

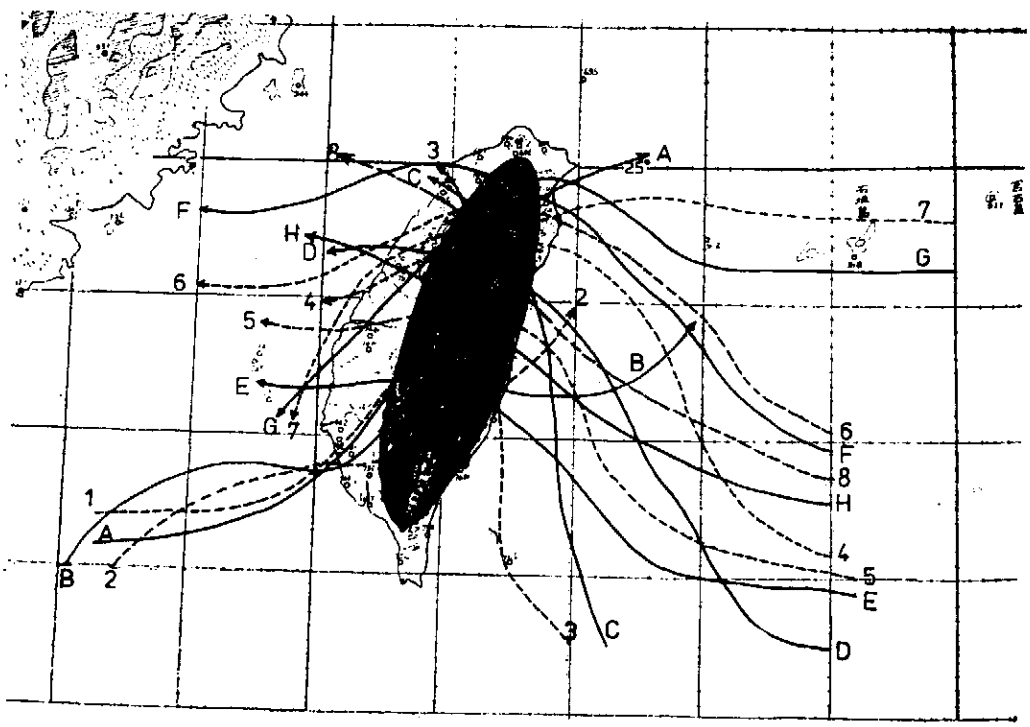

Fig. 4. Comparison of eight typhoon tracks with the pathlines of a free vortex obtained from the experiments for pass over case. The number of each typhoon track corresponds to the following typhoons: 1. Nadine, 27-28 July 1968. 2. Judy, 30-31 May 1966. 3. June 5,-7 Aug. 1961. 4. Amy, 3-6 Sept. 1962. 5. Winnie, 14-16 July 1978. 6. Freda, 14-17 Sept. 1956. 7. Agnes, 13-15 Aug. 1960. 8. Typhoon 091, 9-10 Sept. 1952. ····· typhoon track; ———experimental path line.

In comparison the results with different shapes of barriers, the phenomena of blocking and deflecting, and its moving path as exemplified in figure 6, are similar. Solid lines indicate the moving paths of vortex for elliptical barrier, the dotted lines are for the shape of ellipsoid and the others for rhombic barrier. The height of these barriers used in this study is the same. This seems to indicate that the path of vortex is not sensitive to the shapes of barriers which have the same height. But it must be noted here that all the barriers are three-dimensional and symetric with respect to some plane axis. This, in fact, has defined the major behavior of the free vortex when interacted with the barrier. So only to this extent, we can state that the sensitivity to the shapes is not high. Even so, from photos of different shapes, we found that the local random degree of the vortex just over the barrier has some relationship to the curvature of barrier surface. To those of larger curvature, the random degree of the flow pattern seems

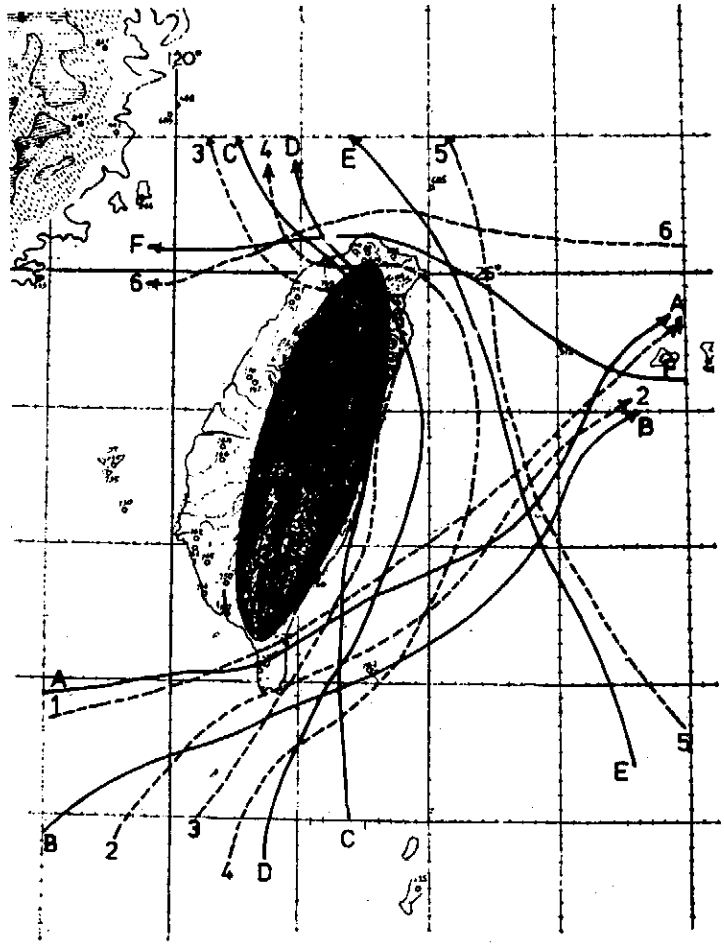

Fig. 5. Comparison of six typhoon tracks with the pathlines of a free vortex obtained from the experiments for deflection case. The number of each trphoon track corresponds to the following typhoons: 1. Elsie, 15–17 Sept. 1966. 2. Thelma, 22–24 April 1956. 3. Ka5e, 21–23 July 1962. 4. Wendy, 26–29 Sept. 1974. 5. Typhoon 084, 16–17 Aug. 1955 6. Trix, 7–8 Aug.1960.

larger, Of course, it also depends on the strength of the free vortex.

From results of photos, the resemblence of behavior and the moving paths at different layers can be noticed except when the free vortex is just over the barrier. Figure 7 shows the time development of the induced eddy at the tip on the lee side and the movement of the free vortex at the lower layer for associated with an elliptical barrier. An eddy is being formed at the tip on the lee side as the main vortex is approaching the barrier. As the vortex climbing over the barrier at the upper layer, the vortex is deflected around the barrier at the lower layer. As the main vortex is passing around the tip, the induced eddy is also drifting away from the barrier for a while

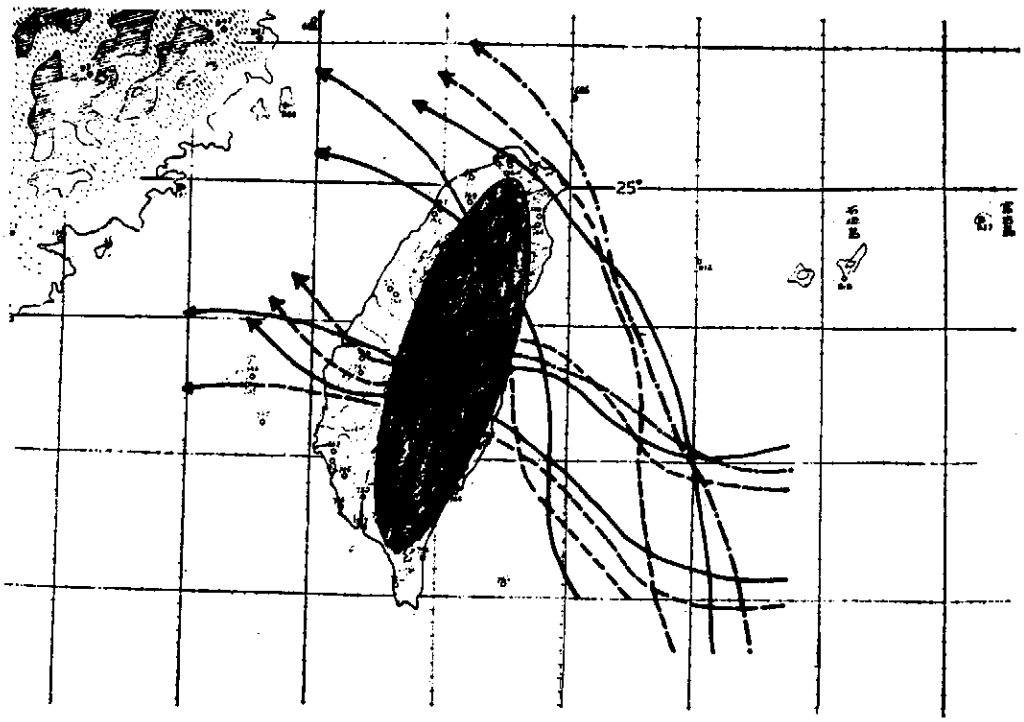

Fig. 6. Comparison of the pathlines of a free vortex obtained from the experiments for the interaction with different barriers. ——— elliptical barrier;····· elliposoid; ——•——•——rhombus.

and then quickly overtaken by the main vortex in the moving downstream. As compared figure 7 with firures 2 and 3, it can be noted that the significance of the induced eddy is strongly dependent on the surface condition of barriers. For instance, elliptical and rhombic barriers have stronger induced eddies on the lee side than ellipsoid can have. In this experiment, we also tried to study the effect due to different paths. The relative position of different paths as shown in figure 8 is always found to be kept in their development.

IV. Concluding Remarks

In this laboratory study, the effect due to the Coriollis force, latent heat, second flow and vertical structure of vortex as mentioned in the former study are apparently neglected. The free vortex once created is assumed to be a mature typhoon vortex that no further growth will happen along the moving path, only subject to decaying. However, since the agreement between field data and experimental results is good, we believe that, to the present stage without concerning the maintenance and structure of a mature typhoon,

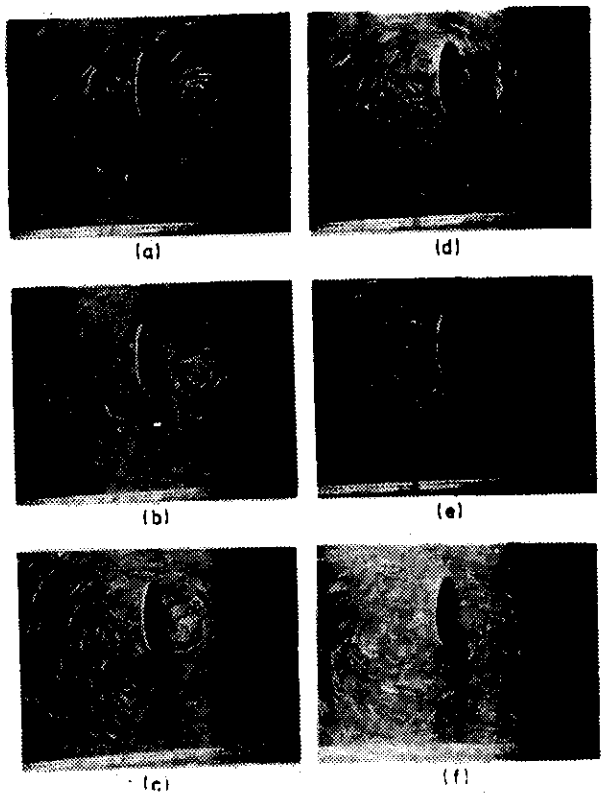

Fig. 7. Photo at lower for the laboratory experiment of a free vortex past an elliptical barrier.

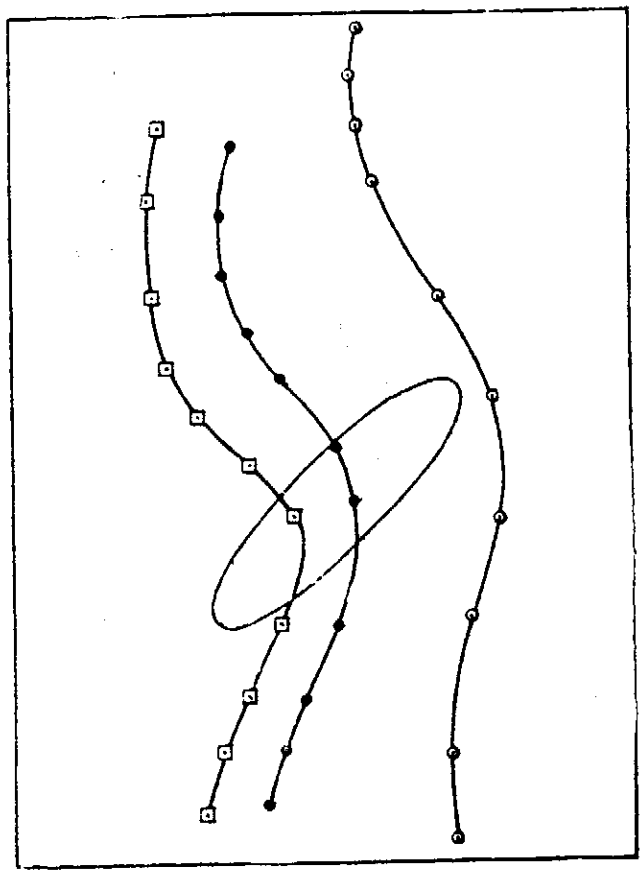

Fig. 8. Free vortex passing an elliptical barrier at different locations. Angle of approach α=135°, U=1.9 cm/sec.

and the precipitation distributin etc., all of these effects upon interaction can be taken as of secondary importance.

In the case of deflected free vortex, the interacttion seems to be not too sensitive to the vortex strength, while in its passing over, it is not so certain. The induced eddy at the tip on the lee side of barrier is strongly affected by the surface of the barrier. The eddy induced for a two-dimensional free vortex interacted with a three-dimensional barrier is three-dimensional.

Acknowledgments: The authors wish to express their gratitute to Dr. Chun-Tasung Wang for his encouragement, to Col. K. C. Chu and Col. Shih-Ting Wang for providing the analyzed typhoon data, to Mr. C. F. Chen for helping some experiments and drawning the moving paths of the vortex motion. This work was partially supported by the National Science Council of ROC.

1. Batchelor, G. K., 1967: An Introduction to Fluid Mechanics. London, Cambridge University Press.
2. Brand, S., and J. W. Blelloch, 1974: Changes in characteristics of typhoons crossing the island of Taiwan, Mon. Wea. Rev., **102**, 708-713.
3. Greenspan, H. P., 1969: The Theory of Rotating Fluids, London, Cambridge University Press.
4. Hsu, Y. C., and S. T. Wang, 1960: On the problem of prediction of typhoons in the vicinity of Taiwan. Weather Forecasting and Analysis, Quarterly, No. 2, Weather Central. CAF. (in Chinese)
5. Lamb., H., 1932: Hydrodynamics. New. York, Dover.
6. Lin, T. M., K. C. Chu, C. C. Yu, and Others, 1972, 1973 & 1974: On the wind force of typhoons affecting Taiwan. Research Reports of Weather Central, CAF, No. 004, No. 005, No. 006. (in Chinese)
7. Pao, H. P., 1976: The effects of mountains on a typhoon vortex as identified by laboratory experiment. Atmospheric Science, Vol. **3**, pp. 55-66.
8. Wang, S. T., 1954: On typhoons passing over the central mountain of Taiwan. Weather Analysis of China, Monthly, Vol. 4, No. 10, Weather Central, CAF. (in Chinese)
9. Wang, S. T., 1963: Topographic effect on typhoons moving along the central mountain of Taiwan. Weather Forecasting and Analysis, Quarterly, No. 14, Weather Central, CAF. (in Chinese)
10. Yanai, M., 1964: Formation of tropical cyclones. Reviews Geophys., **2**,367-414.

Annual Report of the Institute of Physics, Academia Sinica, Vol. 6, 1976

Effect of Barriers on Flows Associated with a Fixed Vortex

By

Robert R. Hwang, H. P. Pao and T. Y. Kou

Institute of Physics
Academia Sinica
Nankang, Taipei, Taiwan

Abstract

Effect of mountain barrier on the typhoon vortex is studied theoretically in terms of the understanding of the dynamical events associated with its blocking phenomena. Utilizing a numerical scheme, this paper studies the flow patterns for various angles attack associated with a fixed concentrated vortex in the presence of a two-dimensional barrier. Numerical model is done on an initial-value problem based on the stream-function/vorticity formulation. The general behavior and the feature of flows when interacting with the barrier have found to depend on angle attack, velocity of uniform flow, the circulation and location of vortex. The agreement of flow patterns between the laboratory experiment and the numerical solution is reasonable

I. INTRODUCTION

The importance of topographic effects on the atmospheric flow have led to numerous studies and investigations by many scientists throughout the world in recent years. It has been recognized that mountain ranges have strong interaction with and influence over typhoons. The mountain effect usually manifests itself in the form of floods and disasters for certain areas. In order to reduce human and economic losses resulting from typhoons, it is important to understand the phenomena and mechanism of the blocking effect when a typphoon vortex is in the vicinity of mountain barriers. But the problem of studying the dynamics of a typhoon vortex in the presence of barriers seems to have not been very well investigated. With the strong two dimensional characters assured by its high rotational itensity, typhoon can be treated as a quasi-two-dimensional rotationally constrained fluid and considered as a two-dimensional concentrated vortex. This paper is then to study the flow pattern of a uniform flow associated with a fixed vortex in the presence of a barrier.

The literature on the flow past obstacles is extensive. The survey papers by Morkovin (1964), Krzywoblocki (1966) and Berger & Wille (1972)should

be mentioned. They studied the onset and the process of vortex shedding behind bodies which are positioned symmetrically relative to the main flow. Recently, Lugt & Haussling (1974) investigated theoretically the process of generation and shedding of the initial vortex for laminar incompressible fluid flows past an abruptly started elliptic cylinder at 45° incidence for Reynolds number from 30 to 300. However, the form and the onset of induced vortex behind barriers in the combinations of uniform flow and a fixed vortex for both symetric and asymetric flows are not well understood. In this paper time-dependent laminar flow associated with a fixed vortex in the upstream of a two-dimensional elliptical barrier for two cases of vortex located are considered. A numerical finite-differce scheme for the stream-function/ vorticity formulation is used to study the dynamic behavior of such flow conditions. Comparisions of the flow patterns are also made between the numerical solutions and the laboratory experiments.

II. THE FLOW PROBLEM

The developing flow due to a uniform flow associated with a fixed vortex in the upstream of a two-dimensional elliptical barrier in an

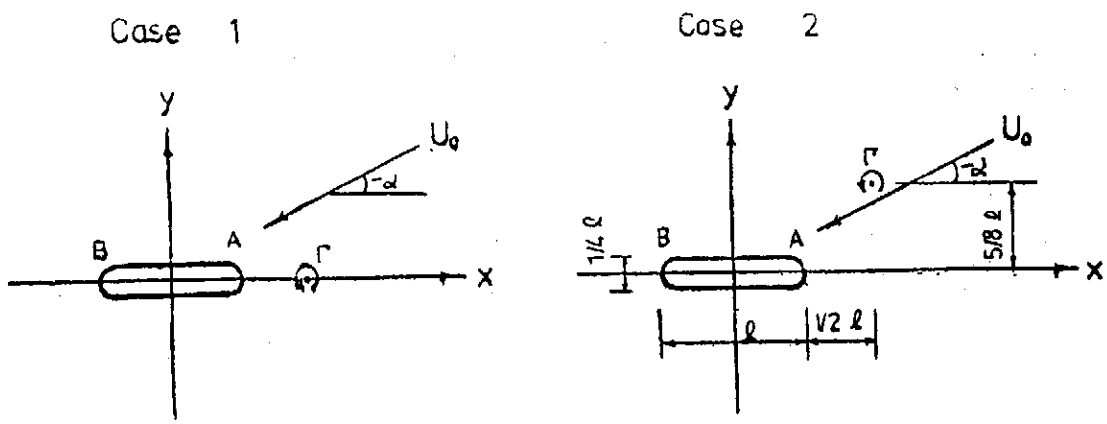

Figure 1. Schematic diagram of flow problems.

open incompressible fluid is considered and shown in figure 1. Mathematically an initial/boundary-value problem for the two-dimensional Navier-Stokes equations with appropriate initial and boundary conditions, must be solved to the flow problem. Thes equations are conveniently carried out in the dimensionless form. In order to non-dimensionalize the variables, we introduce the characteristic length, time and velocity to be ℓ, ℓ^2/Γ and Γ/ℓ

respectively, where ℓ is the length of the elliptical cylinder and Γ the circulation of the fixed vortex. The dimensionless variables are then defined as

$$u^*=u/(\Gamma/\ell),\ v^*=v/(\Gamma/\ell),\ x^*=x/\ell,\ y^*=y^*/\ell$$
$$t^*=t/(\ell^2/\Gamma),\ \phi^*=\phi/\Gamma,\ \zeta^*=\zeta/(\Gamma/\ell^2) \tag{1}$$

In terms of these and neglecting the asterisk symbol on the superscript of variables, the equations of motion are formulated in forms of the dimensionless stream function ϕ and ζ, the dimensionless vorticity component normal to the x-y plane:

$$\frac{\partial\zeta}{\partial t}+u\frac{\partial\zeta}{\partial x}+v\frac{\partial\zeta}{\partial y}=\frac{1}{Re}\nabla^2\zeta \tag{2}$$

$$\nabla^2\phi=\zeta \tag{3}$$

in which $Re=\Gamma/\nu\equiv$Reynolds number, ν, the kinematic viscosity and ∇^2 denotes the Laplace operator in x- and y-directions.

The contour of the barrier in this study is considered as an elliptical cylinder with length of the major axis ℓ. On this surface, boundary conditions are prescribed, according to the no-slip requirement, such that the velocity vector is zero. The dimensionless velocity components u and v are related to ϕ by the equations

$$u=\frac{\partial\phi}{\partial y},\quad v=-\frac{\partial\phi}{\partial x} \tag{4}$$

Thus, at the body surface the boundary conditions are

$$u=\frac{\partial\phi}{\partial y}=0,\ v=-\frac{\partial\phi}{\partial x}=0 \tag{5}$$

While at the unbounded region, the flow field is assumed to be not influenced by the interaction of the elliptical barriers, so the stream function ϕ and the vorticity ζ remain invariant. The initial condition is obtained from the statement that the impulsive start of the development of flow past an obstacle can be treated as potential flow (see, for example, Batchelor 1967). The initial stream function is, therefore set as

$$\phi=\frac{U_0\ell}{\Gamma}(y\cos\alpha-x\sin\alpha)-\ell nr \tag{6}$$

where $r=|(\sqrt{x^2+y^2-a})|$, α is the angle of incidence of uniform flow

relative to the x-axis. and a, the location of the stationary vortex.

III. NUMERICAL ANALYSIS

The infinite domain of integration in the x, y plane is replaced by a finite network of points. The differential equations are replaced by difference equations involving the values of the variables at these grid points. The computation domain is divided into 31×31 square meshes with mesh size $d\times d$, where $d=\ell/m$, m is the number of meshes occupied by the major axis of the elliptical barrier. Grid cells are half size denser near the barrier and the fixed vortex in order to resolve the higher vorticity and stream function gradients. Equation(2) yields, when solved for $\zeta_{i,j}$ at the $(n+1)$th time step, the system of finite difference equations

$$\zeta_{i,j}^{n+1}=\zeta_{i,j}^{n}-\Delta t(ZUC_{i,j}+ZVC_{i,j})+\frac{\Delta t}{R_e d^2}(\zeta_{i+1,j}^{n}+\zeta_{i-1,j}^{n}+\zeta_{i,j+1}^{n}+\zeta_{i,j-1}^{n}-4\zeta_{i,j}^{n}) \tag{7}$$

where the terms of ZUC and ZVC correspond to the convective terms $\partial(u\zeta)/\partial x$ and $\partial(v\zeta)/\partial y$ respectively in equation (2).

To preserve the stability of the numerical scheme in the calculation of the convection terms $\partial(u\zeta)/\partial x$ and $\partial(v\zeta)/\partial y$ for larger Reynolds number, the non-linear space derivatives are approximated with special three point non-central differences (Torrance & Rockett 1969). The special forms are

$$\frac{\partial(u\zeta)}{\partial x}_{i,j}=ZUC_{i,j}=\frac{1}{d}\left(\frac{u_{i+1,j}+u_{i,j}}{2}\zeta_{i,j}-\frac{u_{i,j}+u_{i-1,j}}{2}\zeta_{i-1,j}\right) \tag{8a}$$

when the coefficients $-\frac{1}{2}(u_{i+1,j}+u_{i,j})$ and $\frac{1}{2}(u_{i,j}+u_{i-1,i})$ are positive and

$$\frac{\partial(u\zeta)}{\partial x}_{i,j}=ZUC_{i,j}=\frac{1}{d}\left(\frac{u_{i+1,j}+u_{i,j}}{2}\zeta_{i+1,j}-\frac{u_{i,j}+u_{i-1,j}}{2}\zeta_{i,j}\right) \tag{8b}$$

when the coefficients are negative. When mean velocities $\frac{1}{2}(u_{i+1,j}+u_{i,j})$ and $\frac{1}{2}(u_{i,j}+u_{i-1,j})$ are of different sign, a mixed expression is required which contains one term from each of equations (8), as appropriate. A similar procedure is used to approximate $\partial(v\zeta)/\partial y$ according to the sign of $\frac{1}{2}(v_{i,j+1}$

$+v_{i,j})$ and $\frac{1}{2}(v_{i,j}+v_{i,j-1})$. The velocity components $u_{i,j}$ and $v_{i,j}$, using central difference, are

$$u_{i,j}=\frac{1}{2d}(\psi_{i,j+1}-\psi_{i,j-1}),\ v_{i,j}=\frac{-1}{2d}(\psi_{i+1,j}\mid\psi_{i-1,j}) \tag{9}$$

Equation (3) is approximated by a five-point formula which yields for $\psi_{i,j}$

$$\psi_{i,j}=\frac{1}{4}(\psi_{i+1,j}+\psi_{i-1,j}+\psi_{i,j+1}+\psi_{i,j-1}-d^2\zeta_{i,j}(\tag{10}$$

The system of algebraic equations(10) is solved by the method of sequential relaxation with an over-relaxation factor, $E=1.4$. The iteration process is halted after the kth iteratation if

$$|\nabla^2\psi^k-\zeta^k|<\varepsilon \tag{11}$$

at each grid point, where ε is of order 10^{-3}. The number of iterations depends on the nature of the flow field.

The wall vorticity is an extremely important evaluation. The vorticity transport equation (2) for $\partial\zeta/\partial t$ determines how ζ is advected and diffused, but the total ζ is conserved at interior points. At the body surface a one-sided difference scheme must be used in order to calculate the vorticity ζ_b. Using the Taylor series expansions with the no-slip conditions and regardless of the wall orientation or boundary value of ψ, we can write the first-order approximation as

$$\zeta_b=\frac{2(\psi_{b+1}-\psi_b)}{\Delta h^2}+0(\Delta h) \tag{12}$$

where Δh is the distance from $(b+1)$ to (b), normal to the wall. For ψ_b, the stream function around the elliptical barrier is determined from the average of the initial values of ψ evaluated from equation (6) on the grid points in which the barrier is to be occupied. At the outer boundaries, the following prescribing conditions as mentioned previously are specified as

$$\partial\zeta/\partial x=0 \tag{13a}$$

on vertical outer boundaries,

$$\partial\zeta/\partial y=0 \tag{13b}$$

on horizontal outerboundaries and

$$\frac{\partial \psi}{\partial t}=0 \text{ on outer boundaries.} \tag{14}$$

The integration process is carried out in the following way. The flow is considered to be started impulsively within an infinitesimal time interval. Thus at $t=0$, the motion is assumed irrotational except at the center of the vortex. The initial flow is then obtained from the calculation of ψ_0 and appropriate boundary conditions incorporated in solving the Laplace equation $\nabla^2\psi=0$. The vorticity $\zeta_{i,j}^{n+1}$ for the advanced time step $n+1$ is computed at the interior points according to equation (7). $\psi_{i,j}^{n+1}$is then calculated with the aid of equation (10), The cycle concludes with the calculation of ζ_b^{n+1} from equation (12).

Computations were carried out in single precision on a CDC-CYBER-72 computer. The graphic display of streamlines was produced with a CNTR 2 subroutine.

IV. RESULTS AND DISCUSSION

The flow problem of a uniform flow associated with a fixed vortex in the upstream of a two-dimensional elliptical barrier has been studied numerically. The numerical results show that both of the uniform flow and the fixed vortex play important roles on the effect of flow features. The dimensionless velocity of uniform flow, $\frac{U_0\ell}{\Gamma}$, is incorporated with the Reynolds number, $\frac{\Gamma}{\nu}$, to study the flow problem. As the value of $\frac{U_0\ell}{\Gamma}$ is small (say, 0.5 for example), the combinated flow acts as a fixed vortex in the interaction with a barrier. Otherwise (say, $\frac{U_0\ell}{\Gamma}=1.5$ for example), the steering flow plays an important role in studying the interaction characteristics. Based on the position of fixed vortex and the angle of incidence as sketched in figure 1, the results are presented as follows.

1. Case 1—fixed vortex located on x-axis.

To study the flow patterns associated with a fixed vortex in this location, Reynolds number, $\frac{\Gamma}{\nu}$, in a range of 10^2 to 10^4 was investigated in a

sequence calculations. For $\frac{U_0\ell}{\Gamma}=0$ and $R_e=100$; the flow around the elliptical barrier due to the fixed vortex is weak. The result shows that the streamline pattern has reached a almost steady state solution at $t=0.4864$. The flow pattern shown in figure 2 is quite similar to the case of Stokes flow. Figure 3 is the flow pattern for R_e increasing to 500. It can be seen that as the fluid

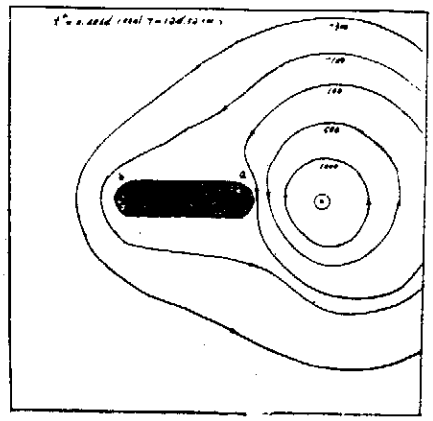

Fig. 2. Streamlines around the barrier in a fixed vortex flow for $R_e=100$ at t=0.4864 (125sec).

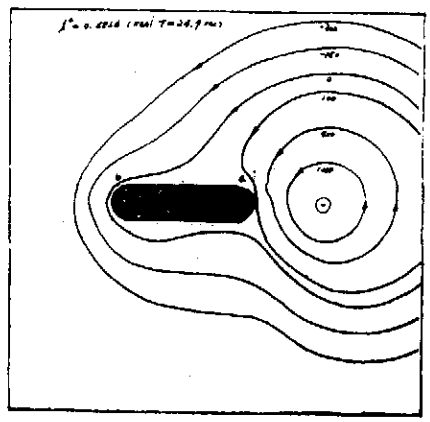

Fig. 3. Streamlines around the barrier in a fixed vortex flow for $R_e=500$ at t= 0.4864 (25sec).

flow of the fixed vortex becomes faster, it migrates the stagnation point of the lower one from the midway toward the edge A of the barrier and the flow has a tendency to be seperated at that tip. When the Reynolds number is increased to 10^4, the fluid of the fixed vortex flow around the barrier becomes fast and flow seperation occurs at both tips of the barrier. An induced eddy is formed observably first at the edge B and grows with time. As this eddy grows, it tends to shed away from the barrier. This can be seen from figure 4. When the first eddy at edge B is shedding, a second eddy is starting to form near the edge A. The eddy near the edge A has a tendency to grow in size and to shed away from the tip. This fact was confirmed in the experimental observation as shown in Fig. 5. When the second eddy of edge A has been shed, the eddy near edge B has closed the shedding and become full-grown, and tends to shed away again. This completes a full cycle of which commences with the shedding of eddy from the edge B and ends with the shedding of the next time at this same edge. The alternate shedding process approaches a steady state at $t=6$ and has a

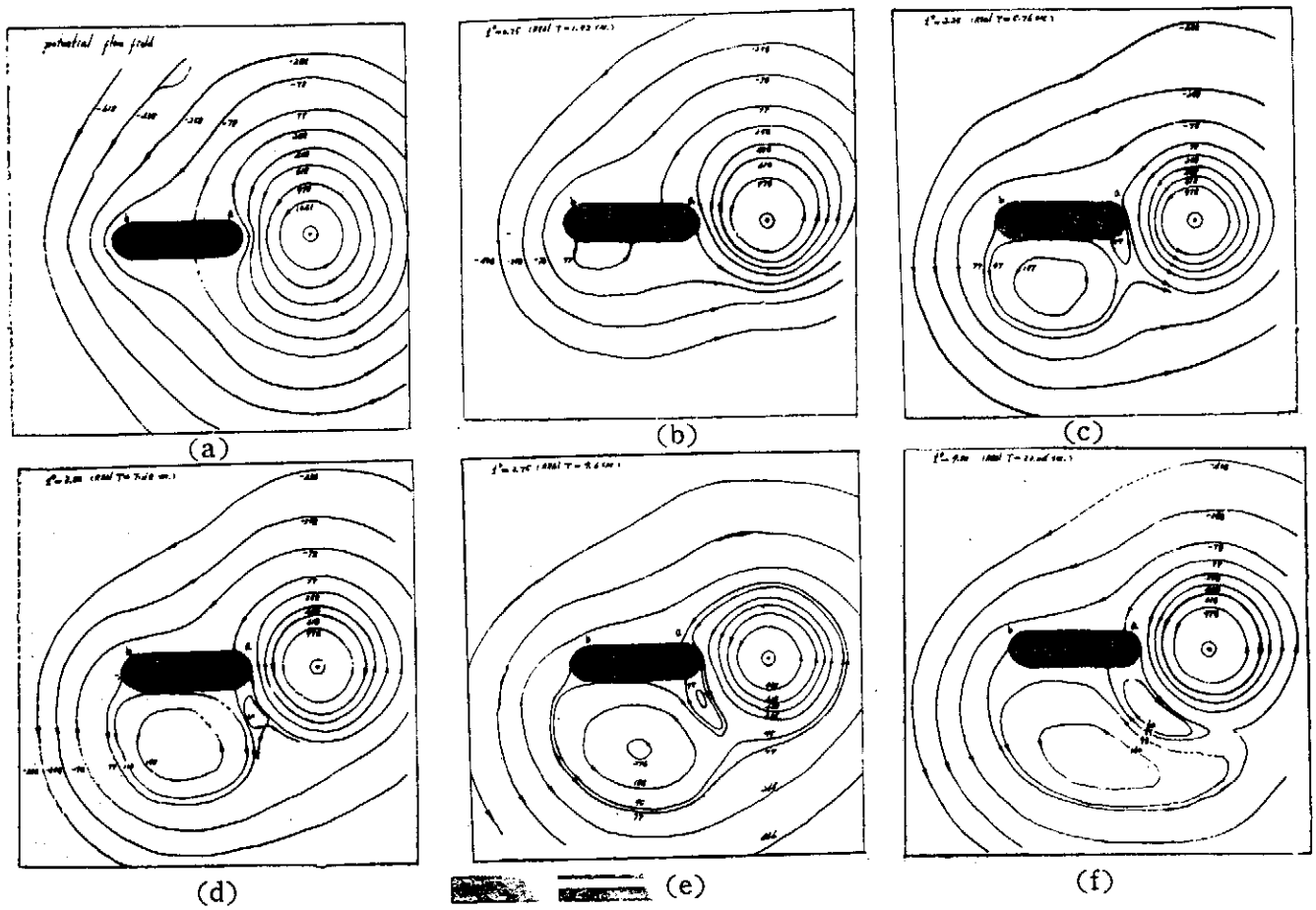

Fig. 4. Some patterns of streamlines for $R_e=10^4$ at various times. Potential flow at t=0

(a) (b) (c) (d) (e) (f) (g)

t 0 0.75 2.25 3.00 3.75 9.0 9.75

time interval of 1.5 between two successive cycles.

For the flow of $\frac{U_0 \ell}{\Gamma}=1.5$, $\alpha=0°$ and $R_e=5\times10^3$, the flow pattern in the interaction with a barrier is quite different from the flow described above. Owing to the effect of steering flow, an induced eddy is formed firstly at the edge A and grows with time. While the eddy is shedding, a second eddy is starting to form near the edge B. At dimensionless time $t=1.8$, both of eddies at edges A and B are shedding and growing in size. A sequence of

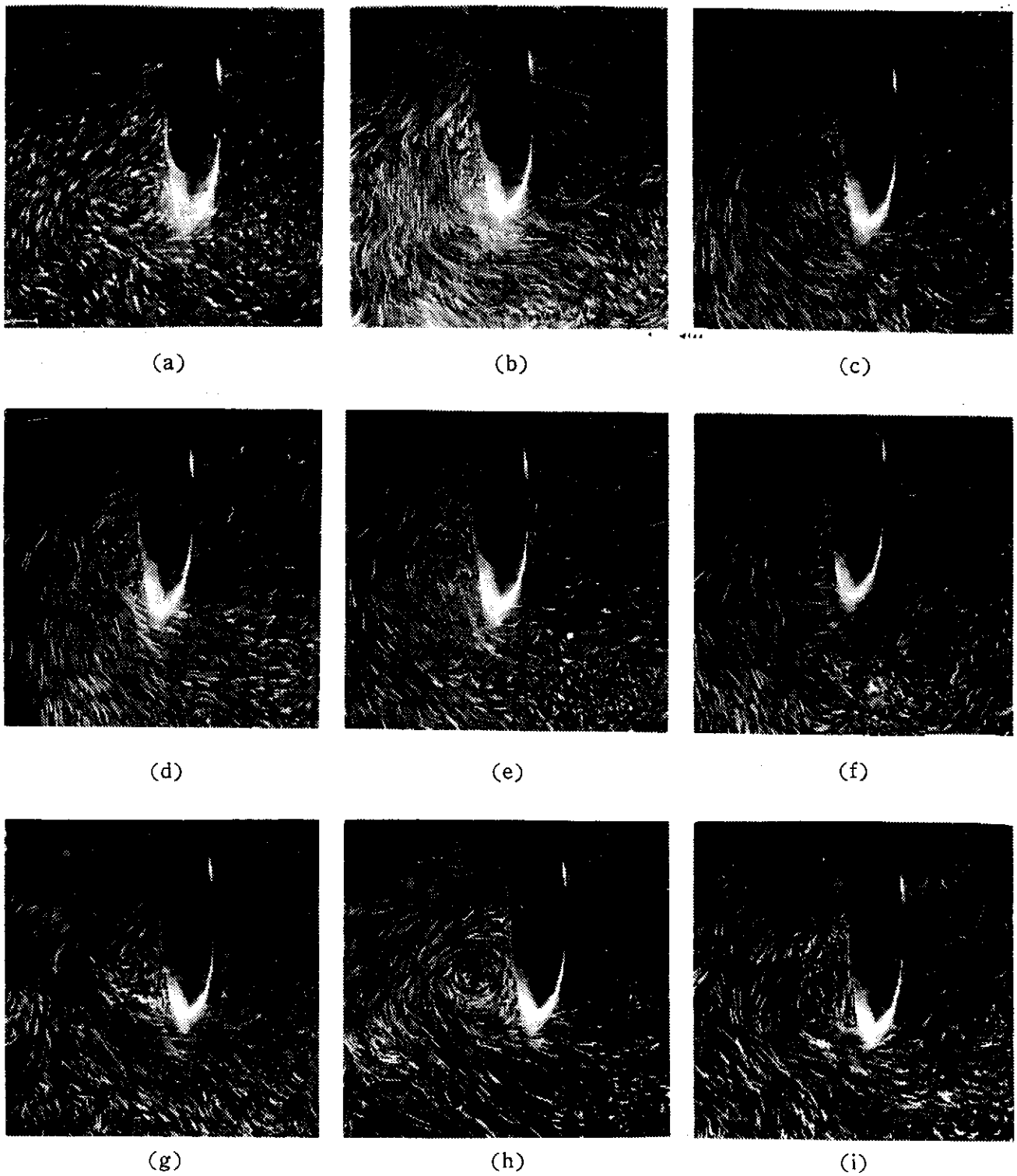

(a) (b) (c)

(d) (e) (f)

(g) (h) (i)

Fig. 5. Sequences of streamline pictures showing the flow pattern of the fixed vortex in the presence of an elliptical barrier. Experimental conditions: Ω=16.4 rad/sec; U=0; r_0=17 cm; flow development at t.

(a) t_0+3sec (b) t_0+5sec (c) t_0+7sec (d) t_0+9sec (e) t_0+11sec (f) t_0+13sec (g) t_0+15sec (h) t_0+17sec (i) t_0+19sec

streamlines for this flow condition can be seen in figure 6. In figure 7 the sequence of streamlines is shown for the same flow conditions except angle of incidec e $\alpha=30°$.

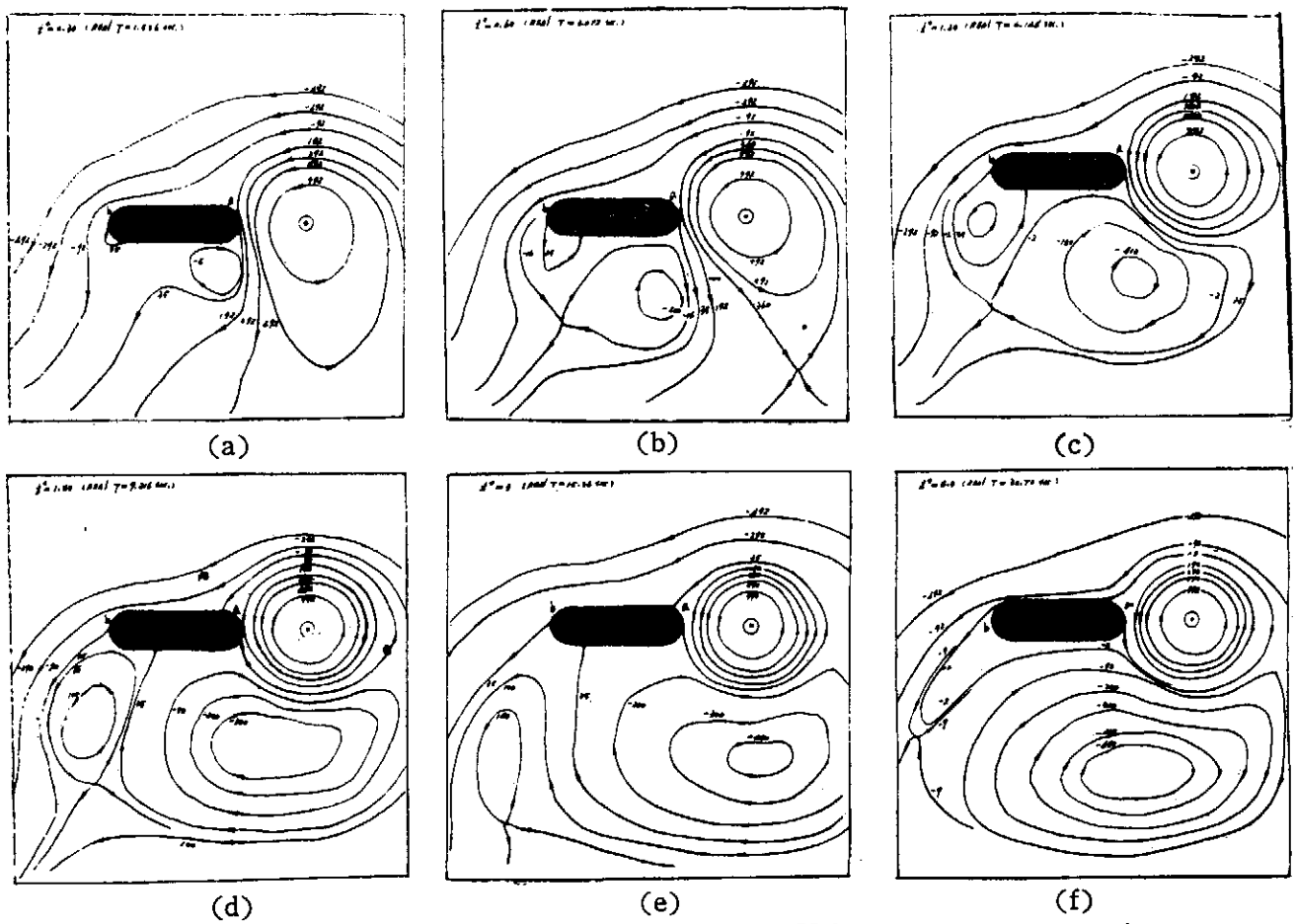

Fig. 6. Sequence of streamlines for $R_e=5\times10^3$, $U_0\ell/\Gamma=1.5$, $\alpha=0^0$ at various times. Potential flow at t=0

	(a)	(b)	(c)	(d)	(e)	(f)
t	0.3	0.6	1.2	1.8	0.6	3.0

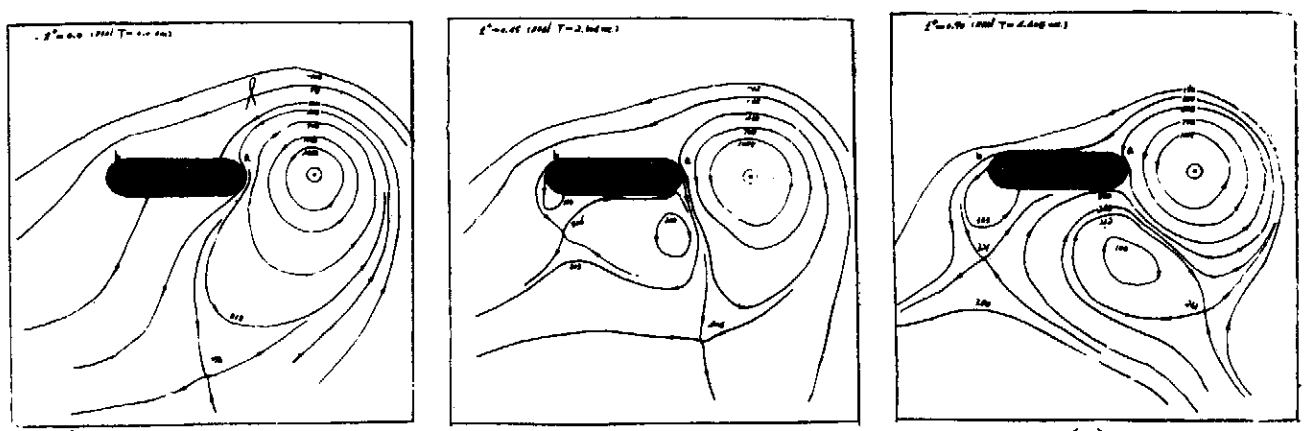

Fig. 7. Some patterns of streamlines $R_e=5\times10^3$, $U_0\ell/\Gamma=1.5$, $\alpha=30^0$ at various times. Potential flow at t=0

(a)	(b)	(c)
0	0.45	0.9

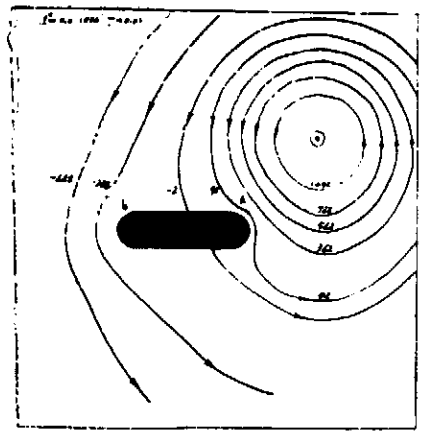

(a)

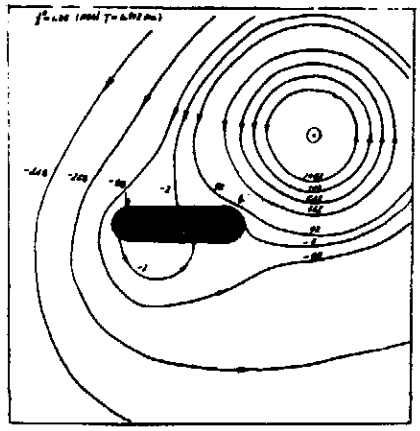

(b)

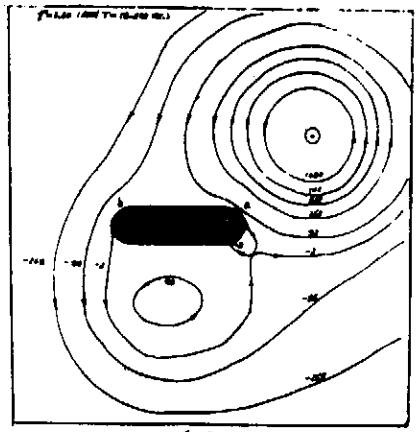

(c)

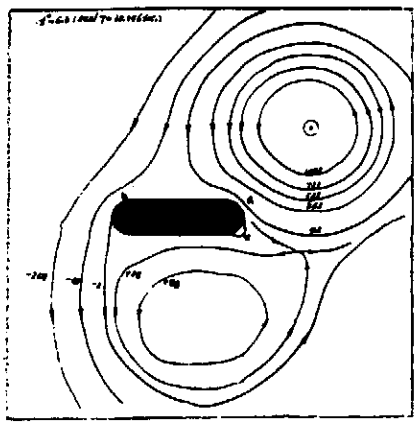

(d)

Fig. 8. Sequence of streamlines for $R_e=5\times10^3$ $U_0\ell/\Gamma$-0.5, $\alpha=0^0$, fixed vortex located at position 2 at various times. Potential flow at t=0

	(a)	(b)	(c)	(d)
t	0	1.35	3.6	6.3

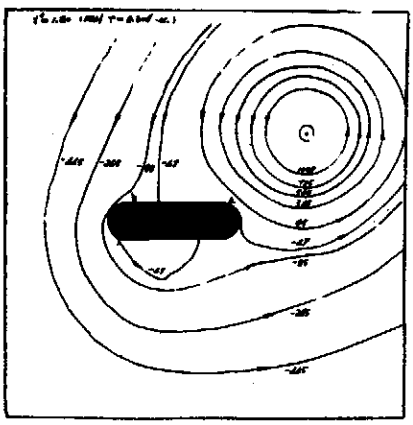

(a)

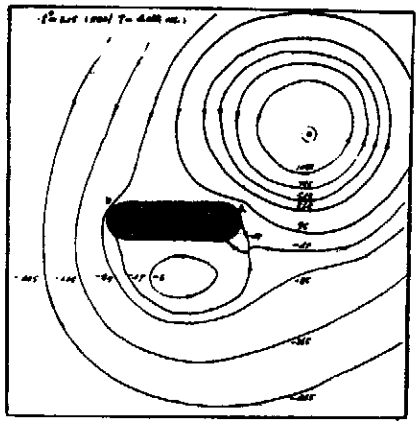

(b)

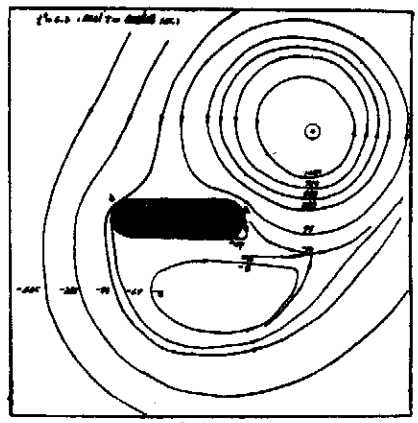

(c)

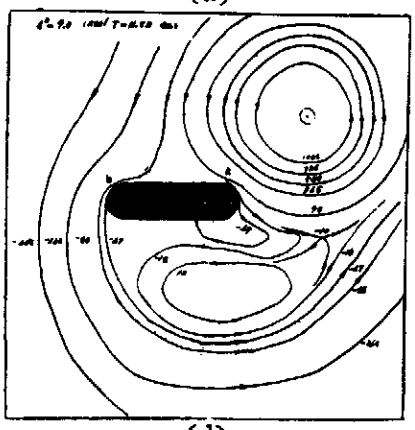

(d)

Fig. 9. Sequence of streamlines for $R_e=2\times10^4$, $U^0\ell/\Gamma=0.2$, $\alpha=30^0$, fixed vortex located at position 2 at various time. Prtential flow at t=0

	(a)	(b)	(c)	(d)
t	1.8	3.15	6.3	9.0

2. Case 2—fixed vortex located on position 2.

For flow of $\frac{U_0\ell}{\Gamma}=0.5$, $\alpha=0°$ and $R_e=5\times10^3$, since the steering flow is comparatively small with respect to the vortex flow, the flow feature is dominated by the effect of the fixed vortex. As shown in figure 8, an induced eddy is formed at first near edge B and grows with time. A second eddy is starting to form at tip A when the eddy of edge B is shedding. These two eddies are growing in size in the transient phase. The alternate phenomena of the formation and shedding of eddies at both tips is not observable in this flow condition. Figure 9 shows the similar flow feature for the case of $R_e=2\times10^4$, $\frac{U_0\ell}{\Gamma}=0.2$ and $\alpha=30°$. These transient developments of flows can be confirmed from the pictures of experimental performation shown in figure 10. Figure 11 shows the flow development for the case of $\frac{U_0\ell}{\Gamma}=1.5$, $\alpha=0°$ and $R_e=5\times10^3$. This flow feature is similar to the flow pattern as shown in figure 6, an eddy is formed firstly at edge A. As the eddy is shedding a

(a) (b) (c)

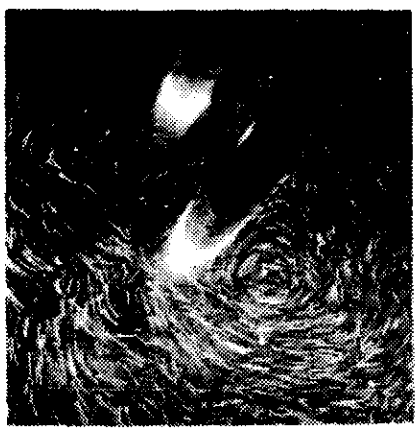

(d)

Fig. 10. Sequence of streamline pictures of laboratory experiment. Same experimental conditions as Fig. 5 except fixed vortex located at position 2.

	(a)	(b)	(c)	(d)
t	t_0	t_0+4sec	t_0+8sec	t_0+12sec

second eddy is starting to formed near edgə B. These two eddies are then kept growing with time.

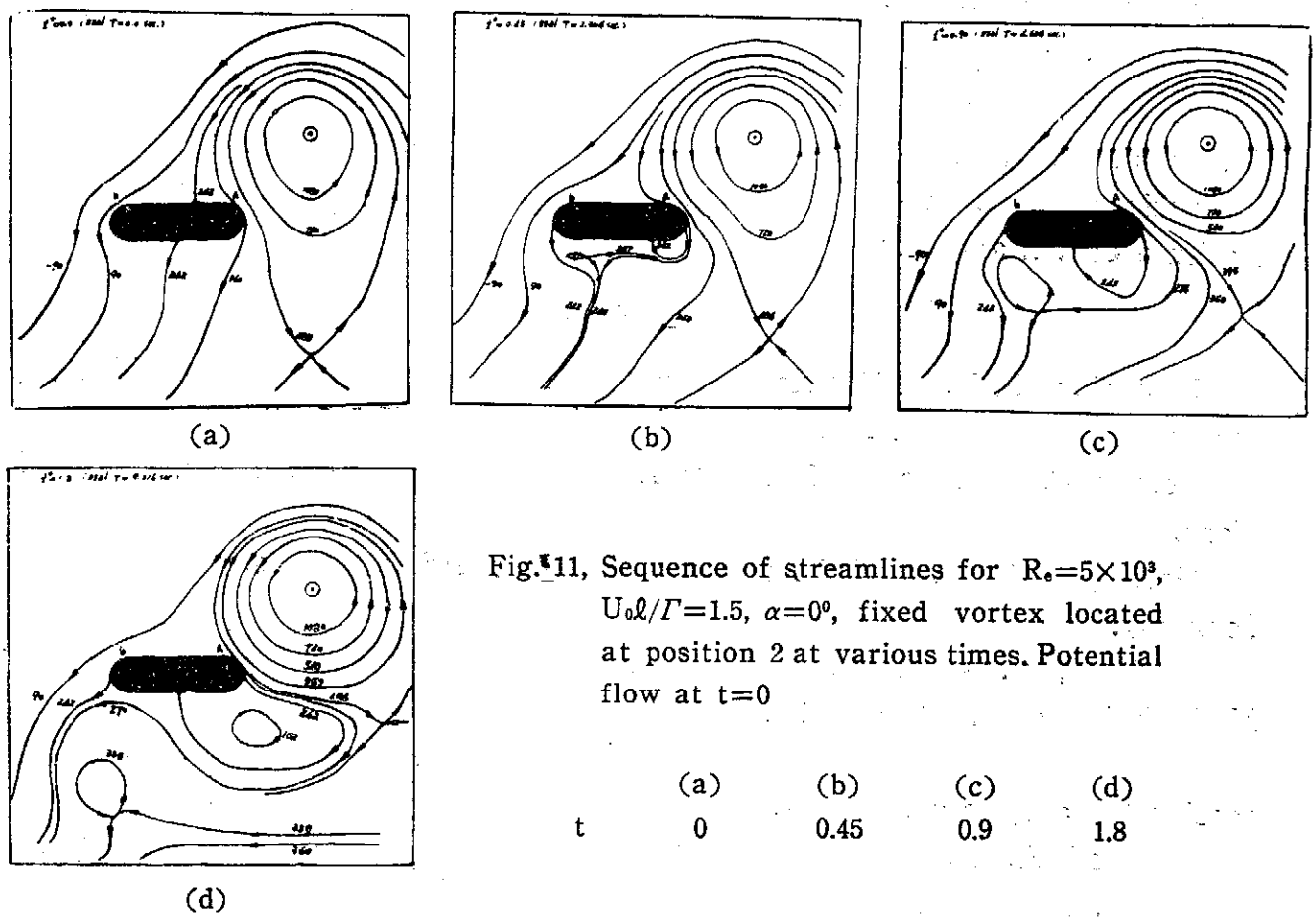

(a) (b) (c)

(d)

Fig. 11, Sequence of streamlines for $R_e=5\times10^3$, $U_0\ell/\Gamma=1.5$, $\alpha=0^0$, fixed vortex located at position 2 at various times. Potential flow at t=0

	(a)	(b)	(c)	(d)
t	0	0.45	0.9	1.8

V. CONCLUSION

In the present study, a numerical scheme is used to analyze the flow feature of a uniform flow associated with a fixed vortex in the interaction of a two-dimensional elliptical barrier. With the numerical calculation for several flow conditions, we now make the following tentative conclusions:

(1) Induce eddies are occurred in the wake region behind the barrier. When the fluid of the vortex flow around the barrier is small, the flow is similar to Stokes flow.

(2) When the steering flow is relatively small in the combinated flow field of uniform flow and fixed vortex, an induced eddy is formed observably at first near edge B. Otherwise, the induced enddy will be formed near edge A. Both of induced eddies are growing in size and shedding away in the sense of transient development.

(3) For the flow of a fixed vortex, two induced eddies behind barrier

will be formed and shed in an alternate development. This exchange process will be approached to a steady situation.

(4) Even the induced eddy is shedding, there will be existed stagnation point in the flow field.

Acknowledgments: This work was supported by the National Science Council of ROC and the Institute of Physics, Academia Sinica. The computer calculations were carried out on the CDC-CYBER-72 computer of Chung-Shan Institute of Sc. and Tech.

VI. REFERENCES

Batchelor, G. K., 1967: An Introduction to Fluid Mechanics. London, Cambridge University Press.

Berger, E. & Wille, R., 1972: Periodic flow phenomena. Ann. Rev. Fluid Mech. 4, 313.

Gerald, D., 1972: Applied Numerical Analysis. Addison Wesley Publishing Company.

Hockney, R. W., 1970: The potential calculation and some applications. Methods in Comp. Phys. 9, 135.

Lugt, H. J. & Haussling, H. J., 1974: Laminar flow past an abruptly accelerated elliptic cylinder. J. Fluid Mech., Vol. 65, 711.

Mitchell, A. R., 1971: Computational Methods in Partial Differential Equations. The Univ. of Dundee, Scotland.

Pao, H. P., 1976: The effects of mountains on a typhoon vortex as identified by laboratory experiment. Atmospheric Science, Vol. 3, 55.

Smith, G. D., 1971: Numerical Solution of Partial Differential Equations. Brunel College of Advanced Technology, London.

Torrance, K. E. & Rockeet, J. A., 1969: Numerical study of natural convection in an enclosure with localized heating from below. J. Fluid Mech., Vol. 36, 33.

Annual Report of the Institute of Physis, Academia Sinica, 1976

Horizontal Diffusion of a Turbulent Sewage Plume

Robert Rong-jiann Hwang

July, 1976

Institute of Physics
Academia Sinica
Nankang, Taipei, Taiwan
Republic of China

Abstract

This paper presents and tests a mathematical model for the prediction on horizontal diffusion of a turbulent sewage plume in stagnant environments. The model is based on the time-average partial differential equations governing the transfer of mass and momentum. The turbulent momentum and mass fluxes appearing in these equations are determined from the Boussinesq approximation in which the turbulent mass transfer coefficient is related to eddy diffusivity by introducing a turbulent Schmidt number. The expression of turbulent viscosity relates the fluxes to the kinetic energy and a length-scale of turbulence. A two-equation model of differential transport equations is employed to determine such turbulence quantities. The results are compared with available experimental data and are found to be in reasonable agreement.

1. Introduction

Disposal of sewage into the ocean and lakes has been practiced by many coastal cities throughout the world. The enormous quantities of waste often creats serious environmental problems for the coastal areas with inadequate dispersal of the pollutants. In order to reduce the detrimental effects of such emissions, it is important to understand the mechanism and to predict the dispersion of pollutants for any given discharge configurations.

The usual method of oceanic disposal of sewage or of sluge is to convey the liquid waste through a submarine pipe to a point some distance offshore in a large lake, sea or ocean and release it there through a system of diffuser ports. The effluent is forced through diffuser ports forming a number of jets which mix with the ambient fluid. In the near-field, differences in velocity and volume flux between the effluent and the ambient flow produce mixing due to the instability of the interface and due to the turbulent energy contained in the jet. The initial sewage field is thus fairly large horizontally and

is well mixed from surface to bottom. The depth of the sewage plume is then assumed to remain constant and its further dilution is caused by lateral diffusion alone.

At present, there exist several prediction methods, depending on the center-line trajectory to analyze the flows of turbulent jets. The method of Rouse, Yih and Humphreys (1952) and Schmit (1957), based on integral equations, predict the devleopment of vertically discharge buoyant jets in uniform surroundings. Using integral forms of the equations governing the mean quantities as the work of Morton, Taylor and Turner (1956), Fan (1967), Fan and Brooks (1969), and Brooks and Koh (1975) obtained a series of numerical solutions to predict the ambient water quality from effluent characteristics in various water environments by the assumption of similarity for jet trajectory, widths, and dilution ratios. In order to close the problem' they introduced a coefficient of entrainment and a spreading ratio which are assumed to be universal constants and to be determined empirically. Many subsequent studies were carries out involving the entrainment concept. Some of them (e.g. Sneck and Brown (1974)) have shown that the entrainment coefficient is not a universal constant but depends on the details of the flow such as the mean velocity profile, the turbulence level etc.. In the present study, a mathematical model is presented for the prediction of horizontal diffusion of a turbulent sewage plume which is not based on the entrainment concept but solved from transport equations for turbulence quantities. A two-equation model of turbulence developed by Launder and Spalding (1972) is used to describe the turbulence behaviour at each point in the flow.

2. Formulation of Problem

Basic equations

Consider a horizontal sewage plume of width 2b, as shown in figure 1, discharging into the stagnent environment with u and v denoting

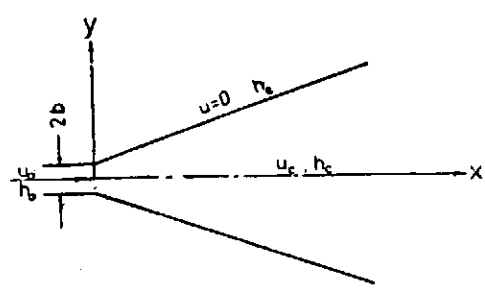

Fig. 1. Schematic Diagram of sewage jet problem studied.

the mean velocity components in the x- and y-direction respectively, where x is longitudinal and y is lateral. The flow is assumed to be steady of the boundary-larer type of turbulent flow ($v \ll u$, $\partial/\partial x \ll \partial/\partial y$), and without swirl. The diffusing substances in the sewage plume are considered to be conservative substances, i.e., no decay, no change of phase and no chemical reactions occurred during the transport in fluid. The equations governing u, v and the mass concentration h are:

contiunity equation

$$\partial u/\partial x+\partial v/\partial y=0 \tag{1}$$

momentum equation

$$\rho u\frac{\partial u}{\partial x}+\rho v\frac{\partial u}{\partial y}=\frac{\partial}{\partial y}\left(\mu\frac{\partial u}{\partial y}-\rho\overline{u'v'}\right) \tag{2}$$

mass diffusion equation

$$\rho u\frac{\partial h}{\partial x}+\rho v\frac{\partial h}{\partial y}=+\frac{\partial}{\partial y}\left(\rho\epsilon_m\frac{\partial h}{\partial y}-\rho\overline{h'v'}\right) \tag{3}$$

Quantities u' and v' are respectively the fluctuating velocity components in the x- and y-direction and h' is the fluctuating concentration. The correlation $\overline{u'v'}$ represents the turbulent momentum flux (shear stress) and $\overline{h'v'}$ the turbulent mass flux in y-direction. With the Boussinesq approximation in $\overline{u'v'}$ and $\overline{h'v'}$ terms, equations (2) and (3) are written as

$$\rho u\frac{\partial u}{\partial x}+\rho v\frac{\partial u}{\partial y}=\frac{\partial}{\partial y}\left(\mu_{eff}\frac{\partial u}{\partial y}\right) \tag{4}$$

$$\rho u\frac{\partial h}{\partial x}+\rho v\frac{\partial h}{\partial y}=\frac{\partial}{\partial y}\left(\frac{\mu_{eff}}{\sigma_t}\frac{\partial h}{\partial y}\right) \tag{5}$$

where μ_{eff} is the effective viscosity, or $\mu_{eff}=\mu+\mu_t$, σ_t is the turbulent Schmidt number, and $\sigma_t=\frac{\mu_{eff}}{\rho}/\epsilon_t$, ϵ_t is the turbulent diffusivity.

Equations (1), (4) and (5) are the differential transport equations governing the mean quantities u, v and h.

Turbulence model

The main problem in solving equations (1), (4) and (5) is to determine the turbulent flux. With the suggestion of Boussinesq, the turbulent shear stress could be replaced by the product of the mean velocity gradient and a quantity termed the turbulent viscosity, and expressed the turbulent viscosity in terms of known or calculable quantities. The turbulence model used in the present study is a two-equation model of turbulence proposed by Spalding

(1970). The turbulent viscosity is determined from the product of the turbulence length-scale and the square root of the turbulence kinetic energy both are obtained from the solutions of two convective transport equations. That is

$$\mu_t=\rho k^{\frac{1}{2}}\ell \tag{6}$$

and

$$w=k\ell^{-2} \tag{7}$$

The turbulence energy k and the length-scale of turbulence w are determined from the following transport equations for these quantities:

$$\rho u\frac{\partial k}{\partial x}+\rho v\frac{\partial k}{\partial y}=\frac{\partial}{\partial y}\left(\frac{\mu_t}{\sigma_k}\frac{\partial k}{\partial y}\right)+k\left[\frac{\mu_t}{k}\left(\frac{\partial u}{\partial y}\right)^2-C_D\frac{\rho^2 k}{\mu_t}\right] \tag{8}$$

$$\rho u\frac{\partial w}{\partial x}+\rho v\frac{\partial w}{\partial y}=\frac{\partial}{\partial w}\left(\frac{\mu_t}{\sigma_w}\frac{\partial w}{\partial y}\right)+w\left[C_1\frac{\mu_t}{k}\left(\frac{\partial u}{\partial y}\right)^2-C_2\frac{\rho^2 k}{\mu_t}\right]+C_3\mu_t\left(\frac{\partial^2 u}{\partial y^2}\right) \tag{9}$$

Equations (1), (4), (5), (6), (7), (8) and (9) form a closed set containing 7 empirical constants for solving unknowns u, v, h, μ_t, w, k and ℓ. For free turbulent flows, these constant values have shown experimentally and theoretically to be

σ_t	σ_k	σ_w	C_D	C_1	C_2	C_3
0.85	0.9	0.9	0.09	1.04	0.17	3.5

Transformation of differential equations

Equations (4), (5) (8) and (9) have the similarity form with different dependent variables. With the von Mises coordinate transformation, the $x\sim y$ system of equations can be written in the $x\sim\phi$ coordinates and be expressed in the following general form:

$$\frac{\partial\phi}{\partial x}=-\frac{\partial}{\partial\phi}\left(\rho u\frac{\mu_t}{\sigma_\phi}\frac{\partial\phi}{\partial\phi}\right)+\frac{1}{\rho u}S_\phi \tag{10}$$

where ϕ stands for any of the quantities u, h, k and w and S_ϕ stands for the corresponding source term. The differences between those equations are then mainly concentrated in the source terms.

As the convience for solving the differential equations, we transform the general form of equation (10) to the Patankar-Spalding coordinate system by defining

$$\omega\equiv(\phi-\phi_I)/(\phi_E-\phi_I) \tag{11}$$

where ϕ_I and ϕ_E are the values of stream function at jet center trajectory and external boundary respectively, and are functions of x. All variations in

dependent variables then take place at ω values between zero and unity. The change of any variable along a stream line in $x\sim\omega$ system has the relation:

$$(\frac{\partial}{\partial x})_\phi=(\frac{\partial}{\partial x})_\omega+(\frac{\partial}{\partial \omega})_x(\frac{\partial \omega}{\partial x})_\phi \tag{12}$$

By differentiating the definition of equations (11) with respect to x and inserting into equation (12), we have the result:

$$(\frac{\partial}{\partial x})_\phi=(\frac{\partial}{\partial x})_\omega+(a+b\omega)(\frac{\partial}{\partial \omega})_x \tag{13}$$

where $a=\dfrac{-1}{(\phi_E-\phi_I)}\dfrac{d\phi_I}{dx}$, $b=\dfrac{-1}{(\phi_E-\phi_I)}\dfrac{d}{dx}(\phi_E-\phi_I)$.

Further, differentiating of equation (11) for constant x yields:

$$(\frac{\partial}{\partial \phi})_x=\frac{-1}{(\phi_E-\phi_I)}(\frac{\partial}{\partial \omega})_x \tag{14}$$

Appling the formulae of equations (13) and (14) to equation (10), the general form of equation (10) is obtained in the $x\sim\omega$ coordinate system as:

$$\frac{\partial \phi}{\partial x}+(a+b\omega)\frac{\partial \phi}{\partial \omega}=\frac{\partial}{\partial \omega}(c\frac{\partial \phi}{\partial \omega})+d \tag{15}$$

where

$$c=\frac{\rho u}{(\phi_E-\phi_I)^2}\frac{\mu_t}{\sigma_\phi} \qquad \text{and } d=\frac{S_\phi}{\rho u}$$

To solve the parabolic differential equations of the mathematical model to predict the horizontal diffusion of turbulent sewage plume, we employ the finite difference procedure of Patankar and Spalding (1970), and incorporate the $k\ell$ model of turbulence into the Patankar-Spalding boundary-layer program. For each problem, boundary conditions have to be specified at the edge of the jet (e.g. $h=he$, the local concentration of the environment outside the jet, $u=k=w=0$). Also, profiles for u, h, k and w are required as starting conditions at an initial cross section of jet.

3. Results and Discussions

The mean velocity and concentration profiles for the turbulent sewage plume have been obtained through the calculation. The dimensionless profiles of mean velocity and concentration against $y/y_{\frac{1}{2}}$, as shown in figure 2, can hardly be distinguished. $y_{\frac{1}{2}}$ is the distance from the symmetry plane at which velocity assumes to be half of its maximum value. In order to test the

validity of the model, the predictions are compard with the experimental data of Yang (1976) and it shows the agreement between experiment and prediction. In figure 3, the profiles of turbulent kinetic energy k and shear stress $-\overline{u'v'}$ are also calculated and plotted. The maximum turblent kinetic energy obtained across the jet is not occurred at the center trajectory but a distance off from the center. The rate of spread of velocity is also compared with the experimental value of Rodi (1972). The experimental rate of spread, $dy_{\frac{1}{2}}/dx$, is 0.11, while the prediction value, as shown in figure 4, of this study is 0.1095. The agreement is quite satisfactory.

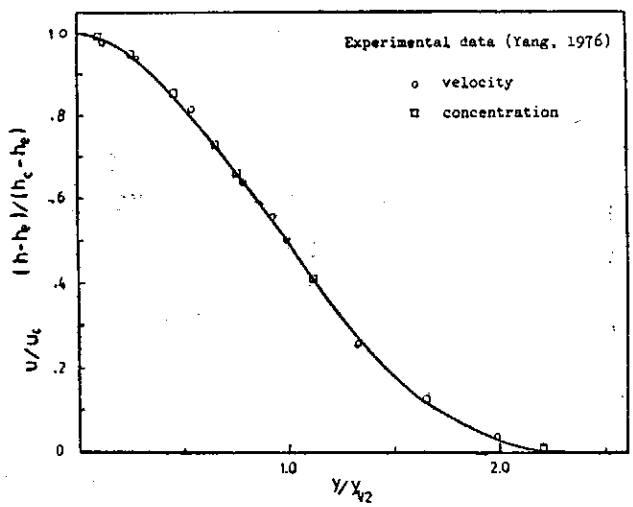

Fig. 2. Profiles of velocity and concentration.

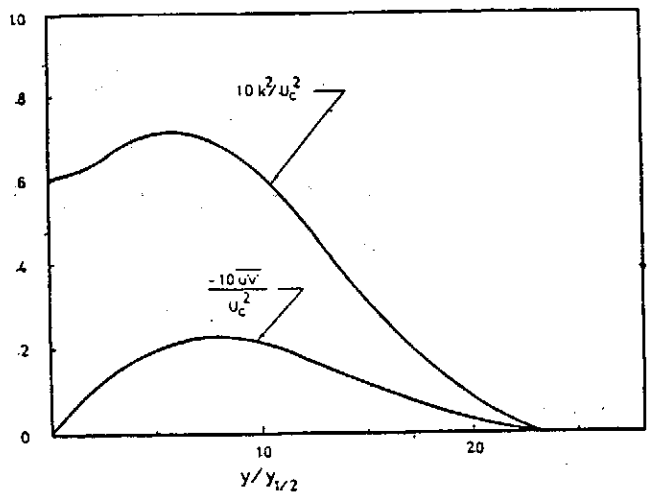

Fig. 3. Profiles of turbulent kinetic energy and shear stress.

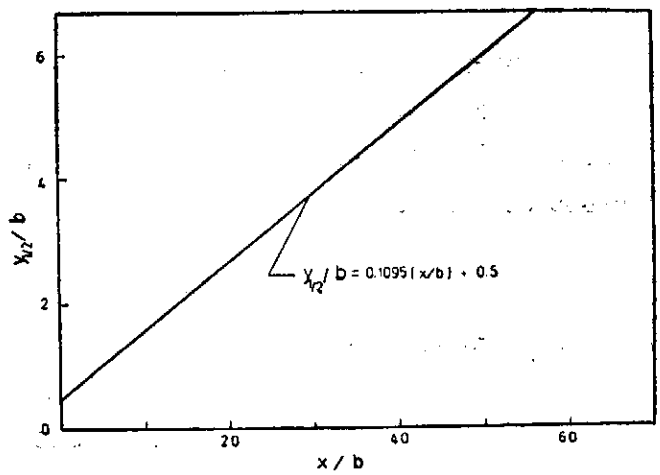

Fig. 4. Horizontal spread of sewage plume.

Variations of concentration profiles on lateral direction at several locations along downstream are presented in figure 5. The concentration of sewage plume at lateral position lowers for the increasing distance in the downstreamwise direction. This is due to the mixing of the plume with the ambient fluid and causes the sewage plume grown laterally and diluted longitudinally. The decay of maximum concentration with distance is also obtained. The peak concentration remains equal to the initial value until a distance downstream of $x/b=5.0$ is reached. At rather larger distances ($x/b>60$) the dilution of the plume behaves as a point-source cloud, the maximum concentration in which decreases as x^{-1}. This is illustrated in figure 6.

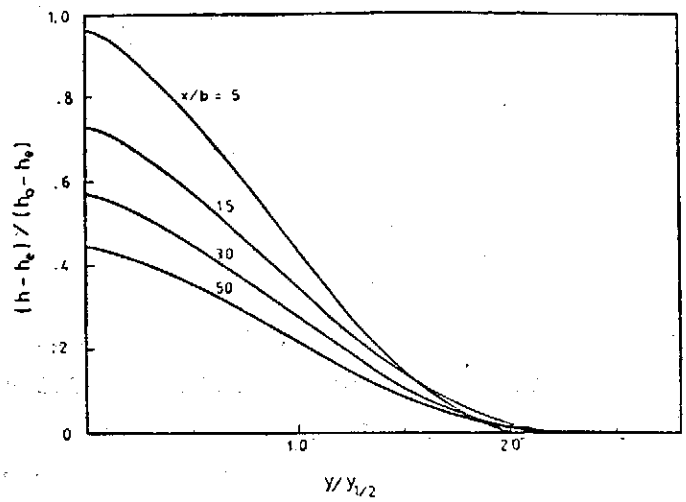

Fig. 5. Variation profiles of concentration along the flow.

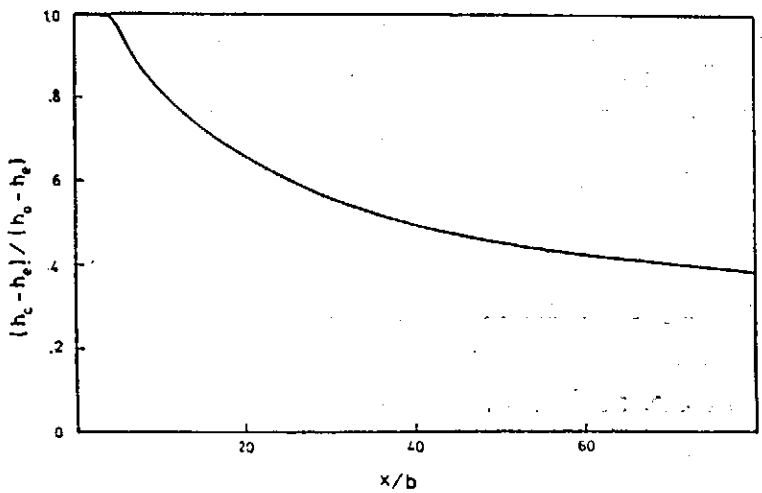

Fig. 6. Decay of maximum concentration with distance.

4. Concluding Remarks

The mathematical model described in section 2 has been shown satisfactoriy with the comparison of some experiments to predict the feature of flows. The model allows a theoretical study of the turbulence quantities of a sewage plume and thus may help to understand and, in the end, to control the sewage disposals. A more detailed comparision with experiments has yet to be carried out; however this is made difficult by the lack of reliable data. Also, the model has to be tested for a wide range flows, and in the course of this, it may prove necessary to refine the model by accounting for the convective and diffusive transport of turbulent momentum and mass fluxes.

Acknowledgment. The research reported in the paper was sponsored by National Science Council of contract No. NSC-64M-0204 and by the Institute of Physics, Academia Sinica. The computer calculations were carried out on the CDC-CYBER-72 computer of Chung-Shan Institute of Science and Technology.

References

Abraham, D., 1970: The Flow of round buoyant jets issuing vertically into ambient fluid flowing in a horizontal direction. Proceeding of the 5 th Conference in Water Pollution Research.

Brooks, N. H. and Koh, R. C. Y., 1975: Fluid mechanics of waste-water disposal in the ocean. Annual Review of Fluid Mechanics, Vol. 7.

Csanady, G. T., 1973: Turbulent Diffusion in the Environment, D. Reidel Publishing Company.

Eckert, E. R. G. and Drake, R. M., 1972: Analysis of Heat and Mass Transfer, McGraw-Hill Book Company.

Fan, L. N. and Brooks, N. H., 1969: Numerical solutions of turbulent buoyant jet problems, W. M. Keck Lab. of Hydraulics and Water Resources, CIT, Rep. No. KH-R-18.

Hwang, R. R., 1975: The mixing characteristics of turbulent buoyant jets in ambient receiving environments. Annual Report of the Institute of Physics, Academia Sinica.

Launder, B. E. and Sp. alding D. B, 1972: Mathematical Models of Turbulence, Academic Press.

Morton, B. R., Taylor, G. I. and Turner, J. S., 1956: Turbulent gravitational convection from maintained and instantaneous sources. Proc. Roy. Soc.,

A234, pp. 1-23.

Patanker, S. V. and Spalding, D. B., 1970: Heat and Mass Transfer in Boundary Layers, Intertest Education and Publishers.

Rouse, H., Yih, C. S. and Humphreys, H. W., 1952: Gravitational convection from a boundary source. Tellus, **4**, pp. 201-210.

Rodi, W., 1972: The prediction on free turbulent boundary layers by use of a two-equation model of turbulence. Ph. D. dissertation, University of London.

Sneck, H. J. and Brown, D. H., 1974: Plume rise from large thermal sources such as cooling tower. ASME, J. of Heat Transfer, **96**, pp. 232-238.

Schmidt, F. H., 1957: On the diffusion of heated jets. Tellus, Ix, Vol. **3**, pp. 378-383.

Tsai, Y. J. and Chang, Y. C., 1974: Two dimensional transient hydr-thermal mathematical model. Proc. of the lst world congress on water resources.

Yang, Y. C. and Hwang, R. R., 1976: Laboratory experimental Study of heated-jet flows. Annual report of the Institute of Physics, Academia Sinica.

Annual Report of the Institute of Physis, Academia Sinica, Vol. 6, 1976

利用風洞實驗探討高速風車性能之研究

黃榮鑑　簡又新　劉通敏

摘　要

根據 Glauert 氏的風車設計理論，採用波音公司 FX 60—126 型翼形剖面，變化四個影響性能的參數——設計翼端速度比，葉片數目，疏密度（或弦長比）及葉片形狀，製成一系列不同的風車模型利用風洞作實驗分析，以對風車的性能特性係數即功率，矩扭及阻力作一連貫的探討，尋找出其高效率的模式，以供大型風車設計時的參考。

一、前　言：

風車之運轉，不需燃料亦不污染環境，為一良好的動力來源，其構想及利用遠在公元前已經開始，十九世紀中在歐洲受到廣泛的注意與研究，其後因各種新能源例如石源、核能等的發展而逐漸末落。近年來由於能源危機的發生，風車又成為先進國家積極研究的對象之一。復且空氣動力學及飛機工業的快速發展，現代的風車，無論是性能或建造比之往昔都有長足的進步。風車依其運動原理，可分為低速及高速兩種，低速風車乃利用阻力設計以迎風轉動，其翼端速度比（tip speed ratio）較低約在零與 2 之間，效率較低；高速風車則利用升力設計，其翼端速度比較高約在 2.5 與 10 之間，效率也高，故為目前各國致力研究之對象。

風車理論係出於飛機的螺旋槳理論，最早由 Glauert 氏提出，利用動量理論、渦旋理論與葉片單元理論，對於風車的設計與性能分析有很完全的探討。但其性能分析僅止於性質上的討論與實際上所量得的數據比較，頗有出入。1973 年 Wiesner 氏利用直昇機葉片理論，分析風車的性能，將風車之輸出功率以風車承受阻力的函數表示，並且對翼端速度比、疏密度、扭角及風的攻角等因素對風車的性能影響，作一系列的探討。他發現採用攻角為 14° 疏密度為 0.2 到 0.4，風車可以獲得最佳的功率輸出。

有關風車的實驗研究發表的較多，但着眼點在於對使用中的各型風車作性能的研究。最早在德國的 Gottingen 曾利用風洞作風車的模型試驗，然所得數據並不適合與理論比較。1953 年 Iwasaki 氏以 Gottingen 623 型葉片製成風車，在風洞中探討葉片扭角由 10° 改變到 80° 時，風車性能的變化，對扭角的效應而言是為一十分詳盡的研究，惟其葉片幾何形狀僅有一種且對葉片疏密度與風車的性能關係沒有加以探討。

1970 年後，美加兩國均致力於打蛋器直立軸高速風車的研究，先後有 South 氏，Templin 氏及 Blackwell 氏等發表了一系列的研究報告，對該型風車的外型設計、理論分析以及模型、原型風車的性能分析有一很完整的結果。惟僅能適合於中小型的製造而無法作大型的建造。1973 年迄今，美國普林斯頓大學對風帆翼型（Sailwing）高速風車進行吉普車上與風洞中的模型試驗。在 Sweeney、Nixon、Maughmer 與 Blaha 四氏所發表的研究報告中，他們並把風車中心體與轉子直徑比對風車效率影響作一系統的實驗分析，結果顯示其影響不大，但其比值在 0.2 時為最佳。

由上述的文獻看來，風車不管在理論分析與實驗的探討均不太完整，並由 1975 年出版的「風能」（Wind energy）一該書對古今中外風車有詳細的目錄收集，即為明證。因此本文最主要的動機，一方面利用 Glauert 氏的風車設計理論，採用波音公司 FX 60—126 型翼形剖面，變化四個性能影響參數—設計翼端速度比、葉片數、疏密度（或疏長比），製成各型風車在風洞中對風車性能特性係數即功率、扭矩

及阻力，作一整套的分析，尋找出其高效率的模式，以供大型風車設計時的參考；另一方面由有系統的變化風車的設計參數，實驗其對風車性能的影響，以供對改進風車理論時的依據。

二、理論分析：

高速風車的性能可利用 Betz 氏的動量理論、Drzwieck 葉片單元理論及渦旋理論等之結合予以探討。

根據動量理論（momentum theory），將葉片轉子視爲一無限薄片之驅動圓碟（actuator disc），當風經過風車時其流場情況可由下圖表示：

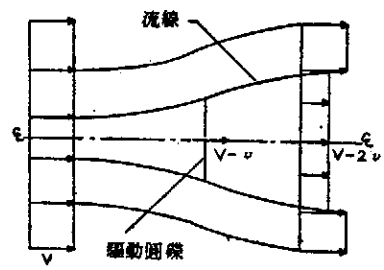

圖 1.　風經過驅動圓碟時的流場情況

圖中V代表自由風速，v 代表軸向誘導速度（induced velocity），由渦旋理論（vortex theory）在葉片轉子後面因自由渦流之影響，在風車翼面產生一誘導速度，其軸向分量爲 v，切線分量爲$r\omega$，而一般常以軸向干涉因素 a（axial interference factor），旋轉干涉因素a（rotational interfence factor）來表示該誘導效應的大小，其定義如下：

$$a \equiv v/V \tag{1}$$

$$a' \equiv \frac{r\omega}{r\Omega} = \frac{\omega}{\Omega} \tag{2}$$

式中，Ω爲葉片轉子的轉速，ω爲葉片轉子授予流經其上之流體的角速度。

由於動量理論並沒有計及葉片幾何形狀及空氣動力（aerodynamic force）之作用，故必須再考慮葉片單元理論（葉片及葉片之間的干涉效應略去不計），葉片單元所受空氣動力及風速情形如圖 2 所示。由

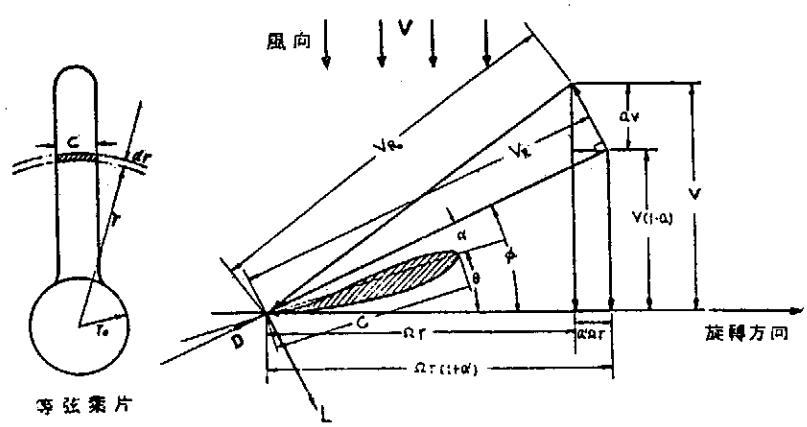

圖 2　在亞向距離 r 處之葉片單元速度及受力圖

圖 2 的幾何關係可得

$$\frac{V_R}{V}=\frac{1-a}{\sin\phi} \tag{3}$$

$$\tan\phi=\frac{1-a}{1+a'}\cdot\frac{V}{r\Omega}=\frac{1-a}{1+a'}\cdot\frac{1}{x} \tag{4}$$

式中 $x\equiv\frac{r\Omega}{V}$，爲局部翼端速度比 (local tip speed ratio) 。綜合上述三個理論以及考慮能量平衡，Glauert 氏理論爲在某一翼端速度比下，欲獲得最大功率輸出時，下列諸式必須予以滿足：

$$a'=\frac{1-3a}{4a-1} \tag{5}$$

$$a'x^2=(1-a)(4a-1) \tag{6}$$

$$x=X\cdot\frac{r}{R} \tag{7}$$

換言之，在翼端速度比 X 固定時，x，a 及 a' 之關係亘爲一定。而局部翼端速度比 x，局部疏密度 (local solidity) σ，疏密度 σ_0，風的相對入射角 ϕ 及葉片翼形剖面升力係數 C_l 與設計參數也必須滿足：

$$x=\frac{\sin\phi(2\cos\phi-1)}{(1+2\cos\phi)(1-\cos\phi)}$$

即

$$\phi=g(x)=g\left(\frac{r}{R}\right) \tag{8}$$

$$\sigma xC_l=\frac{BC\Omega C_l}{2\pi V}=\frac{4\sin\phi(2\cos\phi-1)}{1+2\cos\phi} \tag{9}$$

$$\sigma_0\equiv\frac{\text{葉片總面積}}{\text{葉片圓盤面積}}=\frac{\int_0^R BCdr}{\pi R^2} \tag{10}$$

及

$$\theta=\phi-\alpha \tag{11}$$

方程式(9)提供了弦長及葉片剖面升力係數乘積的關係，因此如風車葉片的弦長 C 爲常數，則由公式(8)至(10)可得

$$\sigma_0=\frac{BC}{\pi R} \tag{12}$$

$$C_l=\frac{2\cdot f(x)}{\frac{BC}{\pi R}\cdot X_D} \tag{13}$$

$$f(x)=f(r/R)=\frac{BC\Omega C_l}{2\pi V} \tag{14}$$

由公式(12)至(14)可知對於等弦風車影響其性能的設計參數爲：設計翼端速度比 X_D，疏密度 σ_0，葉片數目 B 及葉片翼形剖面。由於考慮風車弦長爲一定，故爲設計方便起見，將其疏密度 σ_0 以參數 C/R 表示之，因此影響等弦風車設計的參數爲 X_D，C/R，B 及葉片翼形剖面。

三、模型設計：

由方程式(8)及(9)可得局部翼端速度比 x，相對入射角 ϕ 與 $\frac{BC\Omega C_l}{2\pi V}$ 之關係曲線或數據表，並利用程式將其貯存於電子計算機中以供設計運算之用，其設計步驟概述如下：

1.決定風車直徑（本實驗所使用風車葉片其直徑爲 0.8 公尺）。

2.選定葉片翼形剖面，本文所採用之葉片爲FX 60—126型，其特性曲線如圖 3 之方程式可求之如下：

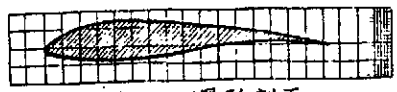

Fx60-126翼形剖面

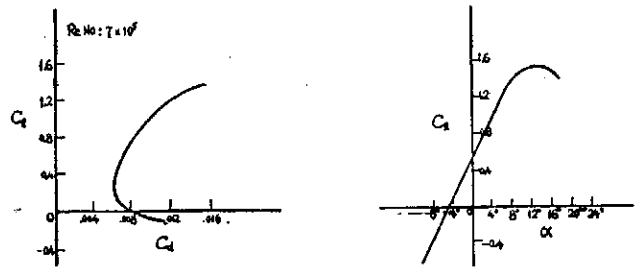

升力係數與阻力係數關係　　升力係數與攻角關係

圖 3　FX60—126 型翼形剖面特性曲線

分兩段近似求 C_l

$$C_l=0.1084\alpha+0.52 \text{ ，當 } \alpha\leq 6^\circ \text{ 時}$$
$$C_l=0.11+0.22875\alpha-0.0090625\alpha^2 \text{，當 } \alpha>6^\circ \text{ 時} \qquad (15)$$

分三段近似求 C_d

$$C_d=0.00833-0.0277C_l+0.09C_l^2 \text{，當 } C_l\leq 0.2 \text{ 時}$$
$$C_d=0.00647-0.00124C_l+0.0044583C_l^2 \text{，當 } 0.2<C_l<0.8 \qquad (16)$$
$$C_d=0.01804-0.026625C_l+0.01804C_l^2 \text{，當 } C_l>0.8$$

3.設定設計參數 X_D，B 及 C/R（或 σ_0）

4.將葉片沿徑向分成十段，依公式(13)及(14)求得各段剖面所對應之升力係數 C_l。

5.利用步驟(2)的公式及步驟(4)的升力係數，求得葉片上各段的攻角 α。

6.由設定的翼端速度比與公式(8)，求得各段的相對風速入射角 ϕ。

7.由公式(1)與步驟(5)及(6)所得結果，即可決定葉片上各段的扭角。

8.設定輪轂、鼻錐尺寸及外形。

由以上各步驟，風車葉片之幾何形狀即可完全決定經由模型製造出各相對應設計參數之葉片模型。（本實驗所採用之葉片爲以鋁合金爲材料鑄造而成。）

四、儀器裝置及實驗方法：

本文實驗利用淡江文理學院航空系之低速風洞進行探討，該風洞屬開放型（Open type），其試驗段斷面爲1.2公尺×1.0公尺，最大風速可達每秒 25公尺，爲使實驗容易控制及進行均定風速每秒 15公尺，其詳細的裝置如圖 4 所示。

1.扭矩及功率的測量

(1)速度：速度的測量利用皮托管（Pitot tube）與傾斜式微分壓力計相連以量取自由風速，風車後面之風速則由皮托管配合U型壓力計來測量。

(2)負荷：爲測量風車在不同的翼端速度比下的功率輸出，本文利用剎車系統來替代所施加的負荷，如圖中所示之剎車裝置，係採用摩托車輪之剎車，利用螺絲與螺母相配合，慢慢均勻的扳動剎車桿以改變

對轉軸負荷而變化風車之轉速。

(3)轉速：如圖 4 所示，在直立傳動軸上貼有反光膠帶，利用同步原理以光學轉速計照射，直接讀取風車之轉速。

所用扭矩儀（torque meter）爲TP—5KMA型，最大容量5kg—m，能承受之最高轉速7000rpm，扭矩儀之安排係透過放大器將訊號放大後送至數字電壓計（digital voltage meter）直接讀出，利用校準曲線（calibration curve）以得出所受扭矩及功率大小。

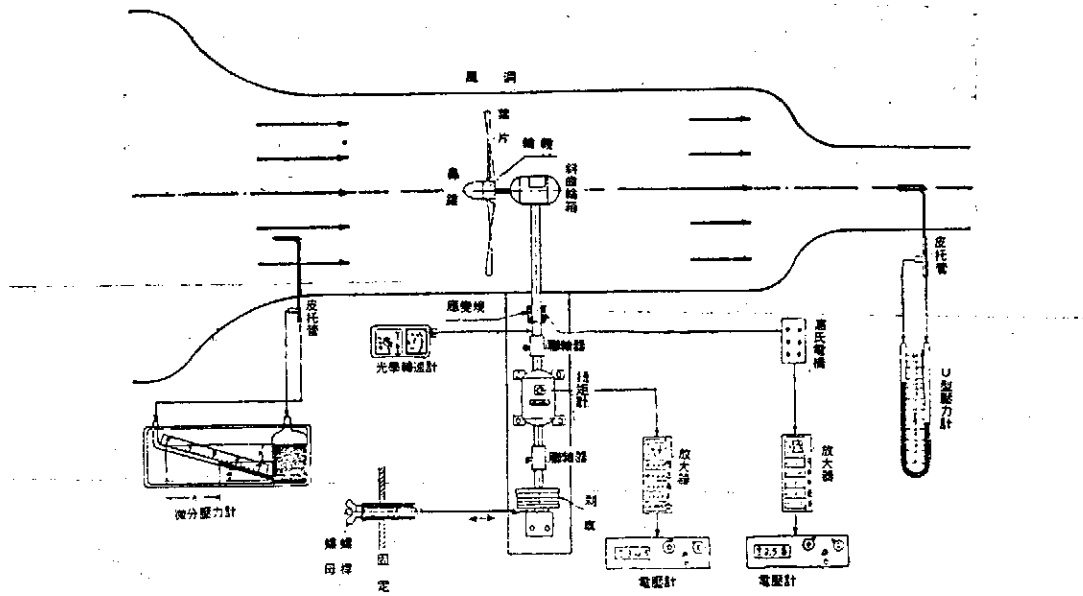

圖 4　實驗系統示意圖：風速、轉速、扭矩、功率及阻力之測量

2.阻力之測量：

在直立傳動軸上迎風及背風兩面各貼有應變規（strain gage），其計器因素（gage factor）爲 1.96±1%，當風車各個葉片所受風的阻力，經由轉軸，作用於直立傳動軸使其發生彎曲時，應變規之電阻隨即發生變化，此電阻變化經由惠氏電橋將訊號由放大器放大後，從數字伏特器讀出伏特數。上述過程所量得之阻力亦包括齒輪箱及直立傳動軸之阻力，故必須將葉片轉子取下後再量取一次阻力值，兩者相減始爲葉片轉子所受眞正阻力，利用校準曲線即可得出所受阻力大小。

五、實驗結果及討論：

由於影響風車性能的設計參數有翼端速度比、疏密度（或弦長比）、葉片數、葉片翼形剖面及葉片形狀等。若將這些參數逐一的自由組合、改變，以求其對風車性能的影響，則因所需製造的模型過多，不管是時間或財力上，均非本文能力所及。故本文以直接尋找出最佳功率的風車爲前題，作實驗分析。

首先固定影響風車性能之其他參數，僅變化設計翼端速度比 X_D，來尋求最大功率輸出時的 X_D；其次以所得的最佳 X_D，變化疏密度 σ_0，實驗求出最佳的 σ_0；再次採取所得的最佳 X_D、σ_0，以實驗葉片數的效應，從而得出最佳功率輸出的風車模式。

整個程序可分下列幾點來說明：

㈠設計參數對風車性能的影響

1.設計翼端速度比的影響—將葉片數與弦長比維持一定，變化設計翼端速度比 X_D。

在設計運算時，發現當 X_D 值的變化由 3 至 6 ，四種等弦風車的外形幾乎完全相同，僅其徑向扭角有少許變化，尤其以一般高速風車所在之 X_D 等於 4 與 5 間，兩者相差只有一度左右，在製造上無法區分，故本文不予探討。

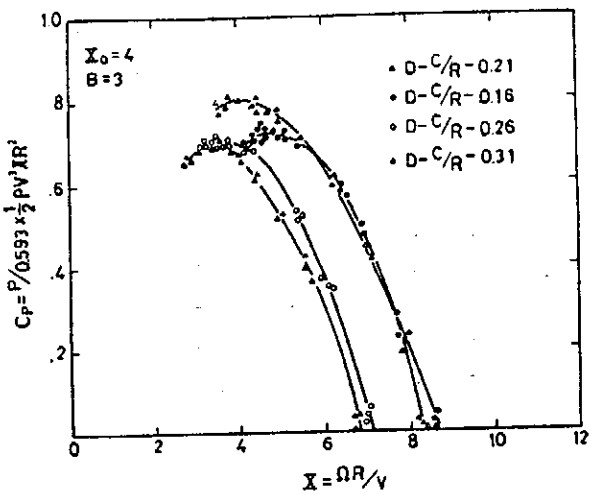

圖 5　弦長比對等弦風車功率輸出的影響

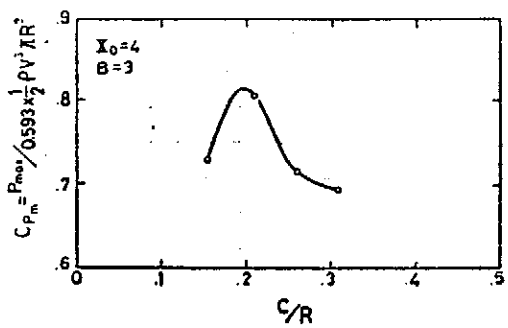

圖 6　等弦風車的弦長比與其最大功率輸出係數間之關係

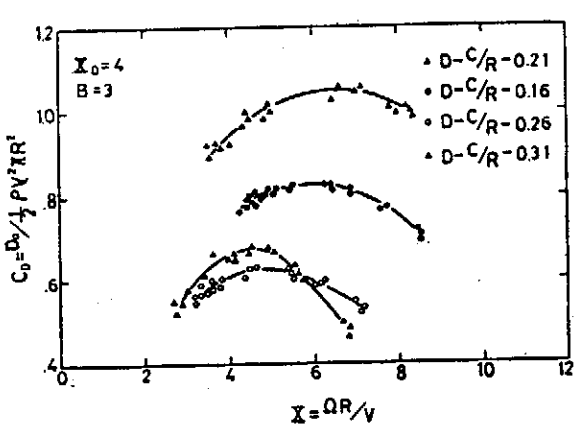

圖 7　弦比對等弦用車阻力的影響

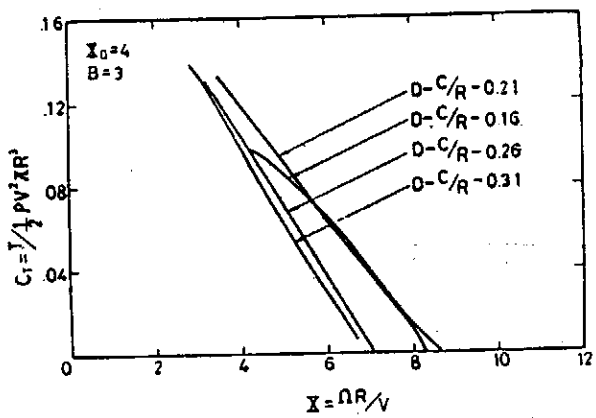

圖 8　弦長比對等弦風車扭矩輸出的影響

2.弦長比的影響—將葉片數與設計翼端速度比維持一定，變化 C/R。

如圖 5 至 8 所示，C/R 的變化對風車的性能有很大的影響，在 C/R 小於 0.21 時，其最大的輸出功率係數 C_{pm}，阻力係數 C_D 及扭矩係數 C_T 均隨 C/R 值的增加而增大，但在 C/R 大於 0.21時，却大抵隨 C/R 的增大而減小，當 C/R 等於 0.21 時得最大值。很顯然地，最大的輸出功率與弦長比存在有一定的關係，如圖 6 所示，以 Lagrange 插值法求出當 C/R 爲 0.19 時，可得最佳功率輸出。又由圖 5 及 7 中亦可看出，當負荷一定時，弦長比大時，則葉片的轉速慢（翼端速度比小）；相反地，在弦長比小時，葉片轉速則快。這個現象與 Glauert 氏理論結果相符合。同時由圖 8 中可得知，輸出扭矩的大小與翼端速度比大約成反向線性關係。

3.葉片數目的影響—將弦長比 C/R 與設計翼端速度比保持一定，變化葉片數目。

葉片數目的多寡，對於風車的性能也有相當大的影響，由圖 9 至12 可大抵看出，當負荷一定，葉片數少的風車轉速高；相反地，葉片數多的風車轉速低。在葉片數爲 3 與 4 可獲得最大的功率輸出，

增減葉片數，其輸出功率都相對地降低。三片及四片風車，其功率輸出相差無幾，但四片却有相當大的阻力，因此對於等弦風車的設計，三葉片型爲最佳。

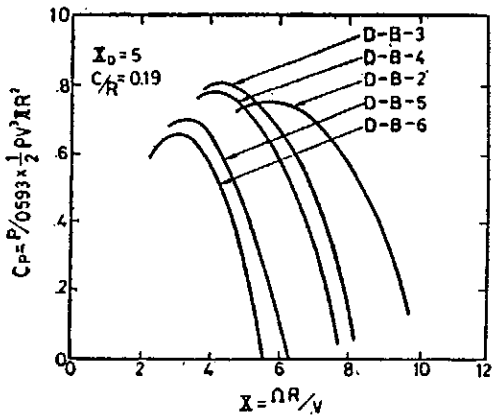

圖 9　葉片數對等弦風車功率輸出的影響

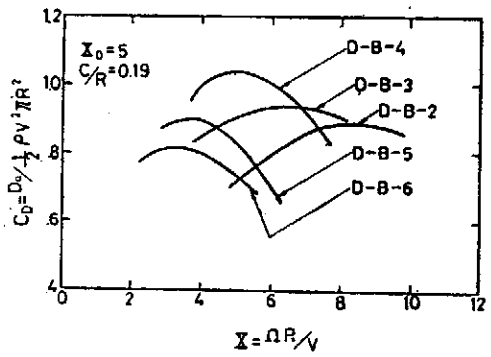

圖10　葉片數對等弦風車阻力的影響

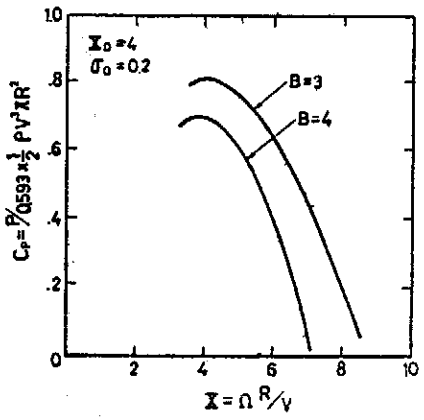

圖11　當設計翼端速度比及疏密度維一持定時，葉片數對等弦風車輸出功率的影響。

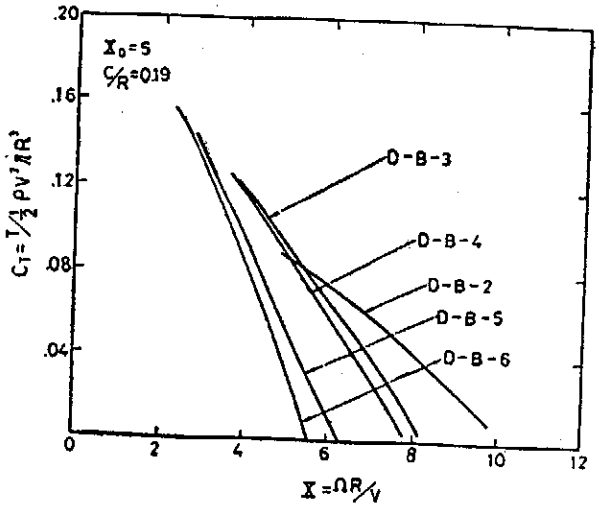

圖12　葉片數對等弦風車扭矩輸出的影響

㈡設計與操作翼端速度比的關係

由圖 5 及10顯示，各個風車在功率輸出爲最大時的翼端速度比（即操作翼端速度比 X_m）與設計翼端速度比 X_D 並不相合——此現象亦發生於螺旋推進器等的設計。這點在本文開始時，即說明是因爲 Glauert 氏的風車設計理論並不十分的完善。至於兩者間之詳細關係，因牽涉太多，非本文所能解決在此提出以供有興趣者繼續研究。將以上各圖的操作翼端速度比與最大功率輸出值 C_{pm} 搜集繪於圖 13 及 14，在這些圖中，每一設計翼端速度比均有一相對應之操作翼端速度比，可供風車設計時的參考。

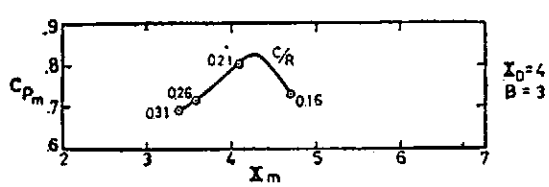

圖13　等弦風車操作與設計翼端速度比、最大功率係數及弦長比間之關係

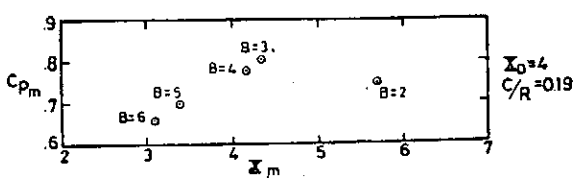

圖14　等弦風車操作與設計翼端速度比、最大功率係數及葉片數間之關係

㈢疏密度與操作翼端速度比的關係

如圖10及15所示，等弦風車之疏密度（$\sigma_0 = \frac{B}{\pi} \cdot \frac{C}{R}$）與操作翼端速度比成反比關係，當風車疏密度 σ_0 大時，其所對應的操作翼端速度比 X_m小；減小 σ_0，其相對應之 X_m 隨之增大，此一現象與 Glauert 氏的理論結果相符合。

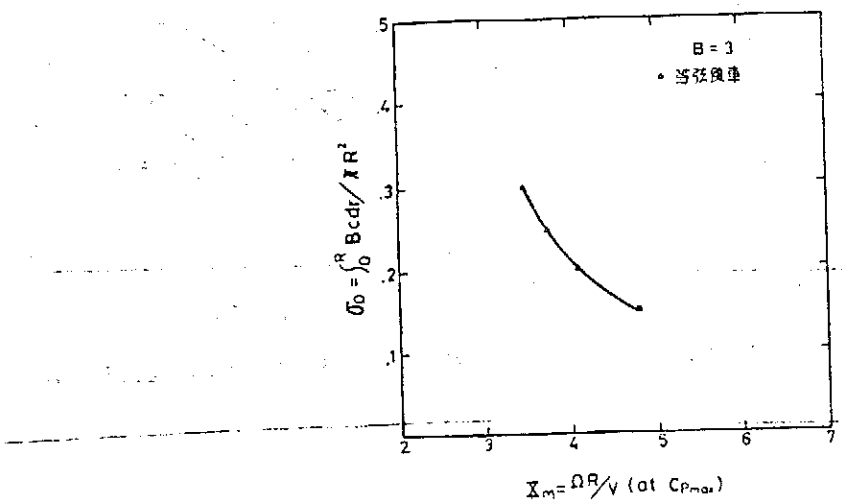

圖15　等弦風車之疏密度與其操作翼端速度比關係

㈣最佳功率輸出風車的選擇：

由於 X_D 的改變，對於整個等弦風車形狀而言，變化甚微，僅在扭角方面有一度左右之差，以致模型製造上無法分辨而放棄實驗。然而從圖13及14可看出在B爲 3，X_D 等於 4 與 5 的幾個例子中，X_m 大致均爲 4 左右，X_m 與 X_D 兩者之值相差無幾，這與一般的等弦風車均在 X_m 等於 4 與 5 之間的運轉相合，也可見 X_D 等於 4 或 5（其他參數固定）時，性能曲線之特性很接近。開始以改變三葉片風車的弦長比，求得當弦長比爲 0.19 時，輸出功率爲最佳；然後以此弦長比反過來查驗三葉片型是否爲最佳形式，結果屬實。亦即當 X_D 在 4 與 5 之間，以B等於 3 及弦長比爲 0.19 時之風車，可獲得最佳功率輸出。

六、結　　論：

依照 Glauert 氏風車設計理論，採用波音公司 FX 60—126 型翼形剖面，變化四個設計參數—設計翼端速度比，葉片數，疏密度（或弦長比）及葉片形狀，製造出一系列風車模型，在風洞中完成實驗，獲得下列幾點結論：

1.本文所得最佳功率輸出模式，其條件爲設計翼端速度比 X_D 等於 4 與 5 之間，弦長比爲 0.19，葉片數B爲 3。

2.設計上的翼端速度比 X_D 與實驗上的操作翼端速度比 X_m（對應於最大功率輸出）無法相合；在葉片數爲 3 時，等弦風車的 X_D 與 X_m 較爲接近。至於 X_D 與 X_m 間之詳細關係有待進一步的探討。

3.在風洞實驗中，發現二葉片型的風車轉子最難平衡。

4.在相同設計翼端速度比及疏密度下（本文實驗中分別爲 4 及 0.2），葉片數對風車性能有相當大的影響。

5.當風車葉片之疏密度增大時，所對應之操作翼端速度比皆隨之降低，即兩者成反比關係。

6.風車的輸出扭矩與翼端速度比大約成反向線性關係，翼端速度比小時，所獲得的扭矩大。

本文爲接受臺中港務局委託研究完成的論文之一，進行實驗所使用的風洞爲淡江文理學院航空系之開放式風洞，中央研究院物理研究所提供儀器及資料，謹此一併致謝。

七、參考資料

"A Synopsis of Energy Research", 1960-1974, Engineering Energy Lab., Oklahoma State University, Stillwater 74074.

Abbott, I.H. and Von Doenhoff, A.E., "Theory of Wing Sections", Dover Publication, Inc. New York, 1959.

Abe, S., "On the Theory of Windmills", Reports of the Institute of High Speed Mechanics, Tohoku University, Japan, No. 67, July 1956.

Blackwell, B.F. and Reis, G.E., "Blade Shape for a Troposkien Type of Vertical Axis Wind Turfine", SLA-74-0154, Sandia Lab., April 1974.

Cermak, J.E., "Applications of Fluid Mechanics to Wind Engineering", A Freeman Scholar Lecture, 1974, New York.

Dommasch, D.O., Sherby, S.S. and Connolly, T.F., "Airplane Aerodynamics", by pitman publishing Corporation, 1967, pp. 211-243.

Gessow, A. and Meyers Jr, G.C., "Aerodynamics of the Helicopter", 1972.

Glauert, H., in "Aerodynamic Theory", Vol. IV, ed. by W.F. Durand, Dover Publ., N.Y 1963, pp. 169-360.

Iwasaki, M., "The Experimental and Theoretical Investigation of Windmills", Reports of Research Institute for Applied Mechanics Vol. II, No. 8, Dec. 1953.

Pope, A. and Harper, J.J., "Low-Speed Wind Tunnel Testing", John Wiley and Sons Inc., New York London Sydney, 1970.

Riegels, F.W., "Aerofoil Sections", Translated from German by D.G. Randell, Butterworths, London, 1961.

South, P. and Rangi, R. S., "A Wind Tunnel Investigation of a 14 Ft. Diameter Vertical-Axis Windmill", National Research Council of Canada, LTR-LA-105, Sep. 1972.

Steyn, R.V., "Wind Energy, A Bibliography with Abstracts and Keywords", Part 1: Alphabetical List, Part 2: Keyword Selection, Dept. of Physics-Wind Energy Group, Eindhoven University of Technology, Eindhoven, The Netherlands, July 1975.

Sweeney, T.E., Nixon, W.B., Maughmer, M.D. and Blaha, R., "Sailwing Windmill Characteristics and Related Topics". AMS Report No. 1240.

Templin, R.J., "Aerodynamic Performance Theory for the NRC Vertical-Axis Wind Turbine", National Research Council of Canada, LTR-LA-160, June 1974.

Vargo, J.D., "Wind Energy Developments in the 20th century", NASA TMX-71634, Technical Paper, Lewis Research center, Cleveland, Ohio 44135 Sep. 1974.

Wilson, R.E. and Lissaman, P.B.S., "Applied Aerodynamics of Wind Power Machines", Report No. NSF-RA-74-113, Oregon State University, July 1974.

"Wind Energy Conversion Systems", Workshop Proceedings, NSF/RA/W-73-006, Dec. 1973.

劉遹敏；「高速風車之性能研究」，臺灣大學機械工程研究所碩士論文，1976.

黃秉鑑，簡又新，劉遹敏；「臺中港設置風車之研究」，中央研究院物理研究所研究報告，1976.

Annual Report of the Institute of Physics, Academia Sinica, Vol. 6, 1976

A Variational Analysis Scheme Suitable for Operational Use

Chung Yi Tseng

Institute of Physics, Academia Sinica and
Department of Atmospheric Sciences, National Taiwan University
Taipei, Taiwan, Republic of China

Abstract

An objective upper-air analysis of height, temperature and wind based on variational method is proposed for operationl use. The analyzed fields by successive corrections method are used as input data to perform the variational optimization analysis. The hydrostatic equation and the horizontal momentum equations are employed as dynamic constraints to maintain the internal consistency. The governing analysis equation for the geopotential is elliptic and amenable to solution by relaxation method. A case study has been made to investigate the applicability of the proposed scheme to synoptic data in East Asia area.

I. INTRODUCTION

The objective analysis of meteorological fields is one of the most basic tools used in meteorology today. Objective analysis is the process of interpolating observations, obtained at irregularly spaced points into data at the points of a regularly arranged grid. An objective analysis scheme must perform several functions, namely, interpolation, removal of data errors, smoothing, and, if its product is used as an initial field in a prediction framework, should insure internal consistency between the analysis and the dynamic prediction model.

Although many attemps have been made to solve the problem of the internal consistency, it was not until 1958 that a reasonable solution was introduced. Sasaki (1958) proposed a theoretical basis for an objective analysis scheme based on the calculus of variations. This scheme was very generalized, permitting a broad spectrum of constraints, such as observational, statistical, dynamical and empirical, into an optimization process to obtain internal consistency. This technique became known as the Numerical Variational Analysis (NVA) or Variational Optimization Analysis.

The purpose of this study is to use the variational method in analyzing the wind, temperature and height fields, using the dynamic equations governing the atmospheric motions as constraints to insure the internal

consistency. In this study variational analysis scheme is proposed to adjust simultaneously the wind, temperature and height fields.

II. VARIATIONAL FORMULATION AND ANALYSIS EQUATION

The method of variational optimization used in this study is based on the principle of variational analysis proposed in Sasaki's previous papers (1958, 1969, 1970). The variational formalism is given as follows:

$$\delta J \equiv \delta \int\int\int \{[\tilde{\alpha}(fu-f\tilde{u})^2+\tilde{\alpha}(fv-f\tilde{v})+\tilde{\beta}(RT-R\tilde{T})^2+\tilde{\gamma}(\phi-\tilde{\phi})^2] + [\alpha\left(\frac{\partial u}{\partial t}\right)^2+\alpha\left(\frac{\partial v}{\partial t}\right)^2]\} J\left(\frac{x_e, y_e}{x,y}\right) dx\ dy\ d\sigma = 0$$

where

δ : variational operator

$\tilde{\alpha}$: observational weight for wind

$\tilde{\beta}$: observational weight for temperature

$\tilde{\gamma}$: observational weight for geopotential

α : dynamic weight

x_e : east-west coordinate on earth

y_e : north-south coordinate on earth

x,y : map coordinates

f : Coriolis parameter

R : gas constant for dry air

u,v : horizontal velocity components

T : temperature

ϕ : geopotential

$(\tilde{})$: analysis resulting from conventional objective method (e. g. successive corrections method)

$J\left(\frac{x_e, y_e}{x, y}\right)$: Jacobian of transformation from earth to map coordinates.

σ : $-\ln(p/p_0)$

p : pressure

p_0 : reference pressure

Equation (1) implies that equal weight is given to equal earth area, not equal map area. This formulation is called the timewise localized version of the variational optimization analysis (Sasaki 1970). The first set of bracked terms forces the analysis u, v, T, ϕ toward the input field $\tilde{u}$, $\tilde{v}$, $\tilde{T}$, $\tilde{\phi}$ in direct proportion to the observational weights on wind, temperature and geopotential, $\tilde{\alpha}$, $\tilde{\beta}$, $\tilde{\gamma}$ respectively. The observationl weights in this study depend, in part, on the accuracy of the observed values. These weights are specified in advance and are not determined as a result of the variational analysis. The second set of terms takes the dynamics into consideration and controls the degrees of steadiness in direct proportion to the dynamic weight α, again specified in advance. The weight α can be interpreted as a measure of the steadiness of the atmospheric motions. Thus the high frequency component may be suppressed by this quasi-steadiness condition.

The dynamic constraints used in this study are the hydrostatic equation and the horizontal momentum equations. The nonlinear advection terms create complications in the numerical solutions as well as the variational formalism. For simplicity, following Lewis (1972), the velocity components in them are approximated by the input values during the variational operation. Thus the dynamic constraints are written as

$$\frac{\partial u}{\partial t}=-\tilde{A}+fv-m\frac{\partial \phi}{\partial x}$$

$$\frac{\partial v}{\partial t}=-\tilde{B}-fu-m\frac{\partial \phi}{\partial y} \qquad (2)$$

$$\frac{\partial \phi}{\partial \sigma}=RT$$

where $A=\tilde{u}\frac{\partial \tilde{u}}{\partial x}+\tilde{v}\frac{\partial \tilde{u}}{\partial y}$ and $\tilde{B}=\tilde{u}\frac{\partial \tilde{v}}{\partial x}+\tilde{v}\frac{\partial \tilde{v}}{\partial y}$ denote the nonlinear advection terms which represent the ageostrophic effects, and m is the image scale factor.

Substituting the above dynamic constraints into (1), and recalling that the Jacobian of transformation is equal to $1/m^2$, we obtain

$$\delta\int\int\int[\tilde{\alpha}(fu-f\tilde{u})^2+\tilde{\alpha}(fv-f\tilde{v})^2+\tilde{\beta}\left(\frac{\partial\phi}{\partial\sigma}-R\tilde{T}\right)^2$$

$$+\tilde{\gamma}(\phi-\tilde{\phi})^2+\alpha\left(-\tilde{A}+fv-m\frac{\partial\phi}{\partial x}\right)^2$$

$$+\alpha\left(-\tilde{B}-fu-m\frac{\partial\phi}{\partial y}\right)^2]\,dx\,dy\,d\sigma/m^2=0$$

The resulting Euler-Lagrange equations for our particular variational formalism are as follows

$$\tilde{\alpha}(fu-f\tilde{u})+\alpha\left(\tilde{B}+fu+m\frac{\partial\phi}{\partial y}\right)=0 \tag{3}$$

$$\tilde{\alpha}(fv-f\tilde{v})-\alpha\left(\tilde{A}-fv+m\frac{\partial\phi}{\partial y}\right)=0 \tag{4}$$

$$\frac{\partial}{\partial x}\left[\frac{\alpha}{m}\left(\tilde{A}-fv+m\frac{\partial\phi}{\partial x}\right)\right]+\frac{\partial}{\partial y}\left[\frac{\alpha}{m}\left(\tilde{B}+fu+m\frac{\partial\phi}{\partial y}\right)\right]$$

$$+\frac{\partial}{\partial\sigma}\left[\frac{\tilde{\beta}}{m^2}\left(\frac{\partial\phi}{\partial\sigma}-R\tilde{T}\right)\right]-\frac{\tilde{\gamma}}{m^2}(\phi-\tilde{\phi})=0 \tag{5}$$

Equations (3) and (4) can be solved for u and v as functions of ϕ, respectively. These expressions are then substituted into (5) and we get the following analysis equation for the geopotential ϕ

$$r\left(\frac{\partial^2\phi}{\partial x^2}+\frac{\partial^2\phi}{\partial y^2}\right)+\tilde{\beta}\frac{\partial^2\phi}{\partial\sigma^2}-\tilde{\gamma}\,\phi+r\frac{\partial}{\partial x}\left(\frac{\tilde{A}-f\tilde{v}}{m}\right)$$

$$+r\frac{\partial}{\partial y}\left(\frac{\tilde{B}+f\tilde{u}}{m}\right)+\tilde{\beta}\frac{\partial RT}{\partial\sigma}+\tilde{\gamma}\,\tilde{\phi}= \tag{6}$$

where

$$r=\tilde{\alpha}\alpha m^2/(\tilde{\alpha}+\alpha)$$

This analysis equation is an elliptic differential equation of Helmholtz type. It is instructive to note that the wind information appears only with the weight r, which is the combination of the observational weight $\tilde{\alpha}$ and the dynamic weight α. If either α or $\tilde{\alpha}$ increases while the other remains

constant, r will always increase. This implies that an increased confidence in the input winds (increased $\tilde{\alpha}$) or increasing steadiness of the wind field (increased α) incorporates more wind information into the geopotential analysis. The critical ratio for the solution of (6) is obviously r: $\tilde{\beta}$: $\tilde{\gamma}$. If r is large relative to $\tilde{\beta}$ and $\tilde{\gamma}$, the adjusted geopotential ϕ is driven to the wind information, as discussed above. If $\tilde{\beta}$ is large relative to r and $\tilde{\gamma}$, the adjusted geopotential is determined largely by the temperature information through the hydrostatic equation. Finally if $\tilde{\gamma}$ is large relative to r and $\tilde{\beta}$, the adjusted geopotential is forced toward the input geopotential.

Once the solution for (6) is found for the geopotential, the u and v may easily be found from (3) and (4) and T, from the hydrostatic equation. It is instructive to write (3) and (4) in the form

$$fu=\tilde{\alpha}f\tilde{u}/(\tilde{\alpha}+\alpha)-\alpha(\tilde{B}-m\frac{\partial\phi}{\partial y})/(\tilde{\alpha}+\alpha)$$

$$fv=\tilde{\alpha}f\tilde{u}/(\tilde{\alpha}+\alpha)+\alpha(\tilde{A}+m\frac{\partial\phi}{\partial x})/(\tilde{\alpha}+\alpha)$$

It is interesting to note that the adjusted wind is a weighted mean of the input wind, geostrophic wind and the wind due to ageostrophic effects. It is evident that as α is small relative to $\tilde{\alpha}$, wind input has greater reliability relative to the dynamic constraints, the adjusted wind approaches the input wind as expected. On the contrary if $\tilde{\alpha}$ is small relative to α, the adjusted wind is determined solely by the dynamic constraints.

The natural boundary conditions accompany all the variational problems. For our particular formalisms, we require the geopotential to be equal to the input values at the boundaries. Thus the analysis equation is an elliptic differential equation subject to Dirichlet boundary conditions and amenable to solution by relaxation method. The method of solution and determination of the weight factors is similar to those presented by Lewis (1972).

The input fields are those analyzed by the successive corrections method (SCM). Inman's version (Inman 1971) of SCM has been used in this study to incorporate observed wind into the analysis of the height. The SCM has

Annual Report of the Institute of Physis, Academia Sinica, Vol. 6, 1976

東亞地區天氣資料變分客觀分析之研究

Variational Objective Analysis of Meteorological Fields in East Asia Area

曾 忠 一

中央研究院物理研究所

摘 要

本研究利用變分原理進行東亞天氣資料的高度場，溫度場與風場的分析。首先進行九個定壓層的逐次校正法客觀分析，然後以動量方程式和靜水方程式爲動力條件進行變分分析，以校正這些氣象變數值，使這些變數值能維持內部一致，亦即能代表大氣大規模運動的特性。由變分原理所得的分析方程式是二階的偏微分方程式，可用緩和法來求解。分析方程式的穩定解可由事先假設的權重來研究解出。本研究分析去年颱風貝蒂的天氣資料來考察校正後氣象變數的內部一致問題。研究成果對改進數值預報的精度甚有幫助

§1. 導 言

用客觀的數值方法來從事氣象變數的分析是近年氣象學上最常使用的方法。客觀分析就是把分佈不規則的測站上所測得的氣象變數值內插到規則的網格點上，以作爲數值天氣預報的起始值或分析大氣現象之用。在作爲前者使用之時，必須注意到分析場必須和使用的預報模式一致，假如這種內部一致的條件沒有獲得滿足，高頻雜波就會出現在預報模式裏面。因此一個完善的客觀分析法通常必須具備下列條件：1.內插 2.除錯 3.修勻 4.內部一致。一般的客觀分析法只能達到前三項要求，只有變分客觀分析能從事內部一致的分析。其他各種客觀分析法本文不加敍述，現在只回顧逐次校正法與變分分析。

最早 Bergthorssen與 Döös (1955) 建立了客觀分析法的基本概念。他們先從網格點周圍測站上的變數值做加權平均以求得網格點上之值。使用最初估計值減少了許多資料缺乏地區的分析問題。同樣的，同時使用觀測風以地轉風的關係作爲高度的傾斜率，對分析高度也有很大的助益。Bushby 與 Huckle (1956) 進一步把預報值當做初次估計值。Shuman (1957)使用濾波器減少了分析場上的短波。Cressman (1959) 年設計了一種權重，已被美國氣象中心 (NMC) 使用於日常的天氣分析 (McDonell 1962)。Inman (1970) 修改 Cressman 的權重，考慮到測站上觀測風速不同而引起的權重的不同。Barnes (1973) 利用指數的權重來分析中規模的大氣現象，並且指出這種權重的優點。McFarland (1975) 吸收了 Inman 權重和 Barnes 權重的優點，設計一種非均質性，非等向性的權重來分析暴風環境。

雖然很多研究客觀分析的學者一再强調內部一致的問題，可是直到 1958 年才獲得合理的解決。Sasaki (1958) 提出用變分原理來從事客觀分析的理論基礎，他的方法用途非常廣泛，能利用各種動力條件來維持分析場的內部一致，這個方法後來被稱爲數值變分分析 (Numerical Variational Analysis, NVA)，或者是變分客觀分析 (Variational Objective Analysis)，又叫變分最佳分析 (Variational Optimization Analysis)。這種方法能將動力的，能量的甚至統計的或經驗的條件納入一個望佳止步的過程中，以從事氣象或海洋變數的分析。可是這種方法在其後十年間並無多大進展。直到 1969 年，Sasaki (1969 a, b) 指出這個方法的特點，動力條件的功能以及濾波器的特性。1970年 Sasaki 又連續發表三篇文章，奠定了變分分析的理論基礎以及從事天氣分析的可行性。此後許多學者從事變分分析的研究

與應用。其中較值得注意的是下列四個人的研究成果。Stephens (1970) 利用平衡方程式作爲動力條件研究數值預報的初期狀態問題。Lewis (1972) 用廣義溫度風的關係式和靜水方程式作爲動力條件分析地面和高空的溫度與風。Sheets (1973 a, b) 用梯度風的關係式來分析颱風資料。Groll (1975) 利用 Lewis 的模式來分析歐洲的天氣，並且發現利用動力條件確能濾除短波。

最近變分分析獲得更進一步的發展。Sasaki (1976) 利用能量守恒的積分條件來控制數值預報積分過程中產生的截斷誤差，因此能避免短波和高離雜波的形成，因此變分分析除了能達成客觀分析的任務外，更能用來設計有限差分程式。

近年來觀測儀器的進步甚爲迅速，要如何把人造衛星測得的溫度和風等非定時資料納入數值預報模式中，產生了四維資料同化的問題。變分分析也可從事四維資料同化問題的研究。Ritchie (1975) 利用線型平衡方程式與連續方程式來從事四維資料同化的實驗。

§2. 研究目的

本文之目的在於設計一個高空天氣資料的客觀分析程式，以作爲研究天氣現象的起始值之用，除了把氣象變數自測站內插到網格點上之外，更進一步以原始方程式爲邊界條件，利用變分學的原理，校正網格點上氣象變數值，使其能在力學上能一致，也就是說使這些變數能代表大氣眞正的運動。我國從事數值天氣預報的研究已有數年的歷史，但絕大部份用主觀分析來求得網格點上的氣象變數值。本文在於發展一種能實際使用的客觀分析程式，以便改進數值預報的精度。本文儘量使用各種觀測資料，諸如高度，溫度與風。利用所有的觀測值加以校正原則上比只利用高度來求得其他變數值較爲優良。完全不用觀測的風和溫度，只利用高度，經由靜水方程式求得溫度，再經由平衡方程式求得非發散風，再由 ω 方程式和連續方程式求得無旋風，是一般數值天氣預報模式中決定初期狀態值時經常使用的方法。假如高度值有誤差，這種誤差立刻會在溫度場和風場中出現。本文所使用的變分分析法能解決這個缺點，儘量利用各種的觀測值使其滿足動力條件，來互相校正，最後使修正值在水平方向與垂直方向在力學上均能一致。

國內已發表的有限的客觀分析研究論文中均未提及觀測風，在一些預報模式中也未用觀測風。事實上風代表高度的梯度。假如觀測站爲等距離，這些測站所能測得的最短波長爲兩倍於測站的間距，根據抽樣定理 (Sampling Theorem) (Stephens 1971)，假如在測站上也測得某一變數的梯度，則這些測站能測得的最短波長減小了，也就是說可定義幅度 (definable scale) 減小，因此更能代表實際的資料。雖然氣象測站分佈不均勻，用抽樣定理來討論比較困難，但其原理仍是一樣，同時使用高度與風，會使其資料更具代表性，尤其是在資料缺乏地區爲然。事實上風速與風向也是從事主觀分析時很重要的資料。此外Bleck (1975) 分析北美地區等熵面的 Montgomery potential 時也發現若只利用由隨機抽出的十個測站上的 Montegomery potential 和風時，則分析結果與採用所有測站上的資料來分析的結果大致相似。若只用 Montgomery potential 而不用風，則由這十個測站所分析得到的 Montgomery potential 場完全與原來的不一樣，每個測站都變成了低壓中心。若只用高度而不用風來分析高度場會產生低壓不够低高壓不够高的情形。因此本研究儘量使用觀測風來分析高度場。溫度在分析高度時地位也和風一樣，是代表高度在垂直方向的梯度。

§3. 研究方法

進行這項研究時，首先將天氣資料打在卡片，再直接由計算機進行譯碼的工作。然後定地圖坐標，同時也把測站的坐標求出。此時卽可進行逐次校正法的客觀分析把測站上的高度溫度與風內插到網格點上，最後利用變分原理以原始方程式爲動力條件校正這些氣象變數，使其能在力學上一致，以下討論本研究所使用的逐次校正法與變分分析程式。

一、逐次校正法 (Successive Corections Method, SCM)

本研究採用 Inman (1970) 的分析程式，但爲分析西太平洋與東南亞資料缺乏地區的天氣資料，分析程式稍爲修改。

基本分析法：假設 $D_k^{\mu-1}$ 是測站上觀測值與第 μ-1 次分析值之差，某一網格點的校正值可由影響半徑內各測站的 $D_k^{\mu-1}$值加權平均得到

$$C_{ij}^{\mu}=\frac{\sum_{k=1}^{N} W_k D_k^{\mu-1}}{\sum_{k=1}^{N} W_k}$$

其中 W_k 是 Cressman 權重函數 (Cressman 1959)，與測站到某一網格點的距離有關

$$W_k=\frac{R^2-d_k^2}{R^2+d_k^2} \qquad d_k<R$$
$$=0 \qquad d_k>R \qquad (1)$$

其中 R 是影響半徑，d_k 是某一網格到第 k 個測站的距離，在某一網格點上的新的分析值爲

$$Z_{ij}^{\mu}=Z_{ij}^{\mu-1}+C_{ij}^{\mu} \qquad (2)$$

在進行下次掃描之前，測站上的分析值必先加估計，在考察範圍內測站上的分析值可用下列線型內插法（圖 1）

$$Z_s^{\mu}=Z_1^{\mu}+(Z_4^{\mu}-Z_1^{\mu})\frac{\Delta x}{\Delta}+(Z_2^{\mu}-Z_1^{\mu})\frac{\Delta y}{\Delta}-(Z_2^{\mu}-Z_3^{\mu}+Z_4^{\mu}-Z_1^{\mu})\frac{\Delta x\Delta y}{\Delta^2}$$

其中 Δ 是格子長度。觀測值的誤差可以比較測站上的觀測值與分析而檢查出來。假如其差的絕對值大於某一最大容許值，我們就可判斷這測站上的觀測值有錯，即當

$$|D_{\mu}^{k}|>\varepsilon^{\mu}$$

時，觀測值有錯，事實上進行主觀分析時也經常用這種方法除錯。本研究在進行這項分析時事先並未進行極端值檢定與靜水檢定，所有資料的錯誤均由這個方法除去。

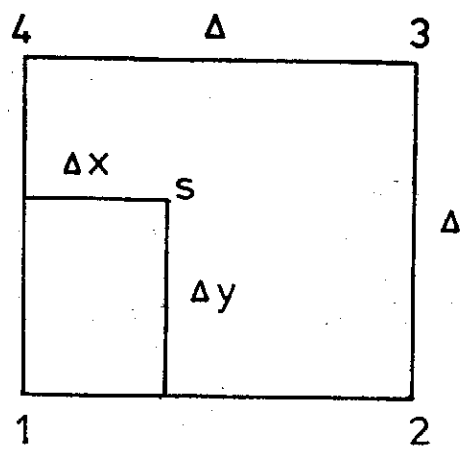

圖 1

初次估計值：初次估計值即(2)式中的 Z_{ij}^{0}，本研究中初次估計值溫度高度均爲零，風的初次估計值爲地轉風。本研究曾首先使用零的風估計值，但發現用這種初次估計值所得到的風的分析非常不良，甚至不能收斂，後來改用地轉風得到較佳的結果。初次估計值也可使用 12 小時前的分析或是當時預報值，但本研究無這兩種估計值，故未使用。

高度場分析程式：除了高度場分析之外，其他變數的分析都是用上面敍述的方法。高度場的分析考慮到觀測風的作用，也就是說觀測風代表高度場的梯度。

假如測站上只有高度觀測值，則

$$D_{1k}=z_k-z_s$$

其中 z_k 是觀測值，z_s 是分析值。假如測站兼有高度與風的觀測值，則

$$D_{2k}=z_k+\left(\Delta x\frac{\partial z}{\partial x}+\Delta y\frac{\partial z}{\partial y}\right)_k-z_{s,j}$$

高度的梯度可用地轉風的關係得到，即

$$\left(\frac{\partial z}{\partial x}\right)_k=\frac{1.08f}{m\sigma g}v_k$$

$$\left(\frac{\partial z}{\partial y}\right)_k=-\frac{1.08f}{m\sigma g}u_k \tag{3}$$

其中 u_k 與 v_k 分別爲測站上 x 方向與 y 方向的風速分量，m 是比例尺，σ 是 image scale factor. (3)式中所代表的意義是網格點間隔是在地圖上量的。

由以上所敍述的方法可以得到網格點上的分析值，掃描的次數大致四五次，每次都把影響半徑 R 縮小，以便使較短波能重現在分析場上，爲了除去短波每次掃描後都使用修勻的方法。之後開始進行變分分析，重新校正網格點上的氣象變數值，使其能滿足控制大氣運動的流體力學方程式，維持這些變數的內部一致。本研究儘量使用觀測值，雖然有些變數的觀測值在某一地區較不準確，但仍具參考價值，因此從事變分分析時這些變數均納入一個望佳止步的過程中。

二、變分分析與動力條件 (Numerical Variational Analysis, NVA)

本研究所使用的動力條件是原始方程式，但是和 Lewis (1972) 一樣，平流項仍使用觀測值，本研究所使用的動力條件尚未有人使用過，因此算是一個新的嘗試。本研究的變分原理是

$$\delta J=\delta\iiint[\tilde{\alpha}(fu-\tilde{fu})^2+\tilde{\alpha}(fv-\tilde{fv})^2+\tilde{\beta}(q\pi-\tilde{q\pi})^2+\tilde{\gamma}(\phi-\tilde{\phi})^2$$

$$+\alpha(\frac{\partial u}{\partial t})^2+\alpha(\frac{\partial v}{\partial t})^2]\frac{1}{\sigma^2}dxdyd\theta=0 \tag{4}$$

其中 σ 是 image scale factor, u, v 分別是 x 方向和 y 方向的風速分量，若進行等壓坐標上的分析，ϕ 是 gespotential ($\phi=gz$, g 是重力加速度，z 是高度)，$\theta=-\ln\frac{p}{p_0}$，p_0 是標準大氣壓力，q 是氣體常數，π 是溫度。假如進行等熵垂直坐標上的分析，ϕ 是 Montgomery potential，θ 是位溫，q 是定壓比熱 c_p，$\pi=(\frac{p}{p_0})^{R/c_p}$。$f$ 是科氏參數，靜水方程式可寫爲

$$-\frac{\partial\phi}{\partial\theta}=q\pi \tag{5}$$

因此在等壓坐標和等熵坐標的變分原理在這裏是完全一樣的。不過本文中只從事等壓坐標上的分析。

假如把(5)式代入(4)式再用T代表溫度，R_g 代表氣體常數，則

$$\delta\iiint[\tilde{\alpha}(fu-\tilde{fu})^2+\tilde{\alpha}(fv-\tilde{fv})^2+\tilde{\beta}(-\frac{\partial\phi}{\partial\theta}-R_g\tilde{T})^2$$

$$+\tilde{\gamma}(\phi-\tilde{\phi})^2+\alpha(\frac{\partial u}{\partial t})^2+\alpha(\frac{\partial v}{\partial t})^2]\frac{1}{\sigma^2}dxdyd\theta=0 \tag{6}$$

其中 $\tilde{\alpha}$, $\tilde{\beta}$, $\tilde{\gamma}$ 是觀測權重，代表各觀測值的可靠性。前四項的意義是使眞正值 (u, v, T, ϕ) 與觀測值差的二乘方爲最小，α 是動力權重，若其值很大，代表大氣運動是準定常的 (quasi-steady)，也就是說加

上這二項可以濾去高頻雜波。(6)式各項變數之間並不是互相獨立的，必須滿足若干動力條件。本研究所使用的動力條件是原始方程式系，除了靜水方程式已代入(6)式以外，尚須使用動量方程式

$$\begin{aligned}\frac{\partial u}{\partial t}+\sigma u\frac{\partial u}{\partial x}+\sigma v\frac{\partial u}{\partial y}-fv&=-\sigma\frac{\partial\phi}{\partial x}\\ \frac{\partial v}{\partial t}+\sigma u\frac{\partial v}{\partial x}+\sigma v\frac{\partial v}{\partial y}+fu&=-\sigma\frac{\partial\phi}{\partial y}\end{aligned}\tag{7}$$

當然在(7)式中我們已作了若干假設。(7)式是一個非線型方程式，爲使計算方便，而且仍保留非地轉風的效應，本文跟據 Lewis (1972) 的方法，非線型平流項仍使用觀測值，也就是逐次校正法的分析值，因此(7)式可改寫爲

$$\begin{aligned}\frac{\partial u}{\partial t}&=-\tilde{A}+fv-\sigma\frac{\partial\phi}{\partial x}\\ \frac{\partial v}{\partial t}&=-\tilde{B}-fu-\sigma\frac{\partial\phi}{\partial y}\end{aligned}\tag{8}$$

其中 $\tilde{A}$, $\tilde{B}$ 爲平流項

$$\begin{aligned}\tilde{A}&=\sigma\tilde{u}\frac{\partial\tilde{u}}{\partial x}+\sigma\tilde{v}\frac{\partial\tilde{u}}{\partial y}\\ \tilde{B}&=\sigma\tilde{u}\frac{\partial\tilde{v}}{\partial x}+\sigma\tilde{v}\frac{\partial\tilde{v}}{\partial y}\end{aligned}\tag{9}$$

現在將(8)式代入(6)式得到

$$\begin{aligned}\delta\iiint\Big[&\tilde{\alpha}(fu-f\tilde{u})^2+\tilde{\sigma}(fv-f\tilde{v})^2+\tilde{\beta}\Big(\frac{\partial\phi}{\partial\theta}-R_s\tilde{T}\Big)^2+\tilde{\gamma}(\phi-\tilde{\phi})^2\\ &+\alpha\Big(-\tilde{A}+fv-\sigma\frac{\partial\phi}{\partial x}\Big)^2+\alpha\Big(-\tilde{B}-fu-\sigma\frac{\partial\phi}{\partial y}\Big)\Big]dxdyd\theta\frac{1}{\sigma^2}=0\end{aligned}$$

在(4)，(6)與上式中有 $1/\sigma^2$ 這一係數是代表權重是在地球上決定，而非在地圖上決定的。因此 Euler-Lagrange 方程式是

$$\begin{aligned}&\tilde{\alpha}(fu-f\tilde{u})+\alpha\Big(\tilde{B}+fu+\sigma\frac{\partial\phi}{\partial y}\Big)=0\\ &\tilde{\alpha}(fv-f\tilde{v})-\alpha\Big(\tilde{A}-fv+\sigma\frac{\partial\phi}{\partial x}\Big)=0\\ &\frac{\partial}{\partial x}\Big[\frac{\alpha}{\sigma}\Big(\tilde{A}-fv+\sigma\frac{\partial\phi}{\partial x}\Big)\Big]+\frac{\partial}{\partial y}\Big[\frac{\alpha}{\sigma}\Big(\tilde{B}+fu+\sigma\frac{\partial\phi}{\partial y}\Big)\Big]\\ &\quad+\frac{\partial}{\partial\theta}\Big[\frac{\tilde{\beta}}{\sigma^2}\Big(\frac{\partial\phi}{\partial\theta}-R\tilde{T}\Big)\Big]-\frac{\tilde{\gamma}}{\sigma^2}(\phi-\tilde{\phi})=0\end{aligned}\tag{10}$$

由前二式可得

$$\begin{aligned}fu&=\Big(\tilde{\alpha}f\tilde{u}-\alpha\tilde{B}-\alpha\sigma\frac{\partial\phi}{\partial y}\Big)/(\tilde{\alpha}+\alpha)\\ fv&=\Big(\tilde{\alpha}f\tilde{v}+\alpha\tilde{A}+\alpha\sigma\frac{\partial\phi}{\partial x}\Big)/(\tilde{\alpha}+\alpha)\end{aligned}\tag{11}$$

把(11)式代入（10c）式可以得到一個ϕ的分析方程式：

$$r\left(\frac{\partial^2\phi}{\partial x^2}+\frac{\partial^2\phi}{\partial y^2}\right)+\tilde{\beta}\frac{\partial^2\phi}{\partial\theta^2}-\tilde{\gamma}\,\phi+r\,\frac{\partial}{\partial x}\left(\frac{\tilde{A}-f\tilde{v}}{\sigma}\right)+r\,\frac{\partial}{\partial y}\left(\frac{\tilde{B}+f\tilde{u}}{\sigma}\right)$$

$$+\tilde{\beta}\frac{\partial\,(R_d\tilde{T})}{\partial\theta}+\tilde{\gamma}\,\tilde{\phi}=0,\qquad r=\tilde{\alpha}\alpha\sigma^2/(\tilde{\alpha}+\alpha)\tag{12}$$

自然邊界條件是 $\delta\phi=0$，也就是說ϕ的值在邊界上必須預定，我們使 $\phi=\tilde{\phi}$，也就是ϕ 的值在邊界上不加校正。(12)式是一個二階的橢圓型偏微分方程式，可以用緩和法求解。ϕ 的值求得以後溫度T 可由靜水方程式求出，風速分量 u, v 可由(11) 式求得。由(11)式可知校正後的風速分量 u, v 是觀測風和非地轉風的加權平均。因此校正以後，這些氣象變數不論在水平方向或是垂直方向在力學上均會一致。 由以上的敍述可知這種變分原理能經由動力條件得到分析方程式而同時分析高度、溫度和風， 使其滿足大氣運動的流體力學方程式。

§4. 研究結果

本研究使用民國64年9月21日格林尼治標準時間零時的九個定壓層（850mb, 700mb, 500mb, 400mb, 300mb, 250mb, 200mb, 150mb 與 100mb）的高空天氣資料。當時中度颱風貝蒂在北緯 21.8 度， 東經 129.5度，卽在臺北市東南東方海面930公里處向西北西進行時速22公里，最大風速33m/s，暴風半徑250公里。此外在庫頁島西方有一低壓中心，冷鋒由該處向西南延伸經過日本海到達黃海。 本研究的考察範圍包括整個東亞地區。

首先將天氣資料電碼和測站經緯度打在卡片上，然後完全由計算機進行譯碼， 決定測站和網格點的坐標，進行逐次校正法的客觀分析等工作，最後把逐次校正法得所到的網格點上的高度， 溫度和風當作起始值（卽觀測值 $\tilde{\phi}, \tilde{T}, \tilde{u}, \tilde{v}$）進行變分分析。因此本研究可說是非常接近 operational 了。

本研究使用21×21個網格點，網格點間隔在一千五百萬分之一的地圖上爲 2 公分，也就是說在北緯30度處的格子間隔爲 300 公里。在進行逐次校正分析時，在西太平洋和東南亞等處測站稀少地區，遭遇許多問題，只有增加影響半徑R 來進行分析。表 1 詳列測站上分析值與觀測值差的 rms（root mean square）值。由表中可知溫度的分析大致令人滿意，其值均在1.64度以下。風的rms值最大接近 6m/s，因爲風的觀測值本來誤差就是最大，至於高度的 rms 值最大處在 100mb，達到 47.63公尺。這些變數 rms 的值顯得偏高，其原因是天氣資料中的錯誤未完全修正， 同時在進行分析時曾使用濾波器以濾除短波也會增加 rms 值。逐次校正分析所得的高度場分別在圖 3（850mb），圖 7（700mb），圖 13（500mb），圖 19（300mb），圖25（200mb）。主觀分析的高度場分別在圖2（850mb），圖6（700mb），圖 12（500mb），圖18（300mb）與圖24（200mb），由這些圖可見由這兩種分析的結果其高度場的趨勢大致一樣，但是由客觀分析所得的高度場上低壓不够低，如850mb和700mb的低壓和700mb與500mb 的颱風中心，前者是因爲修勻的關係，後者是因爲颱風中心附近資料缺乏。此外在700mb與500mb 的客觀分析圖右上角（卽在堪察加半島東南方）高度場的趨勢與主觀分析不一樣，這是因爲在堪察加半島東南方有一高壓（在 850mb 主觀分析圖可以看出來，見圖2）在700mb 與 500mb 的主觀分析並未出現，由於當地資料缺乏，甚難判定熟是熟非。

在溫度分析方面，逐次分析所得的溫度場分別在圖5（850mb），圖 10（700mb），圖16（ 500mb），圖22（300mb）與圖27（200mb）。主觀析分的溫度場分別在圖4（850mb），圖9（700mb），圖 15（500mb），圖21（300mb），圖26（200mb）。 由這些圖比較可知這兩種分析的結果其溫度場也大致一樣

，由客觀分析所得的溫度場其等溫線較爲平滑，這是因爲在進行分析時曾使用濾波器把短波濾除了。溫度場的情形也和高度場的情形相似，暖區溫度不够高，冷區溫度不够低。風場也曾進行分析，最先使用零的初次估計值，後來用地轉風的初次估計值，結果發現由這兩種估計值所得的分析場並不一樣，尤其是在測站稀少地區和颱風中心附近相差更多，當然用地轉風的初次估計值結果較爲合理，也比較能與高度場在力學上一致。

完成逐次校正法的客觀分析之後，繼續進行變分分析。從事變分分析時只進行了三個定壓層的高度，溫度與風（即700 mb, 300mb與200mb），而把850mb和200mb的高度場不變只當作上下邊界值，另外中間三個定壓層的周圍邊界值也不加校正，也就是說用緩和法求解(12)式使邊界值等於觀測值。在進行數值解之前，首先必須決定觀測權重 $\tilde{\alpha}$, $\tilde{\beta}$, $\tilde{\gamma}$ 與動力權重 α。第一次權重決定以後，可由分析方程式(12)式求得新的 ϕ 值，然後由靜水方程式得到校正後的溫度，再由(11)式求得校正後的風速分量，最後決定新的權重，如此類推，重覆計算，經過五次週期之後權重會趨近某一定值。雖然有四個權重，但只有三個互相獨立的權重，譬如 $\tilde{\alpha}/\alpha$, $\tilde{\beta}/\alpha$, $\tilde{\gamma}/\alpha$, 另一個權重可假設爲 1。

第一次的權重採用下列各項：

$$\tilde{\alpha}=\frac{1}{(\bar{f}\times 2)^2} \qquad \tilde{\beta}=\frac{1}{(R_g\times 2)^2}$$
$$\tilde{\gamma}=\frac{1}{(9.8\times 10)^2} \qquad \alpha=\frac{1}{(10^{-4})^2} \tag{13}$$

其中 $\bar{f}$ 是科氏參數的平均值。這種權重的決定也就是假設風速的誤差爲 2 m/s，溫度的誤差爲 2°C，高度的誤差爲 10m，而 $\partial u/\partial t$ 或 $\partial v/\partial t$ 的數量級在大規模大氣運動中爲 10^{-4}m/sec²。觀測權重 $\tilde{\alpha}$, $\tilde{\beta}$, $\tilde{\gamma}$ 代表觀測值的可靠度，若 $(u-\tilde{u})$, $(v-\tilde{v})$, $(T-\tilde{T})$ 與 $(\phi-\tilde{\phi})$ 等項愈趨近於零，亦即誤差很小，則其權重 $\tilde{\alpha}$, $\tilde{\alpha}$, $\tilde{\beta}$, $\tilde{\gamma}$ 應該愈大。由(13)式可以看出，決定第一次權重時我們已假設高度的觀測誤差爲最小，其次是溫度，而風的觀測誤差而爲最大，這和實際的觀測誤差符合。動力權重 α 是由 $\partial u/\partial t$ 或 $\partial v/\partial t$ 的數量級決定，假如動力權重愈大，即 $\partial u/\partial t$ 與 $\partial v/\partial t$ 愈小，即大氣的運動趨向於定常的。第二次以後的權重由新的校正值與原來的觀測值決定，即

$$\tilde{\alpha}=2K/\sum[(fu-f\tilde{u})^2+(fv-f\tilde{v})^2]$$

$$\tilde{\beta}=K/\sum(T-\tilde{T})^2$$

$$\tilde{\gamma}=K/\sum(\phi-\tilde{\phi})^2$$

$$\alpha=\frac{K}{\sum[(\frac{\partial u}{\partial t})^2+(\frac{\partial v}{\partial t})^2]/2}$$

其中 $\sum$ 代表內部所有 K 個網格點括弧內值之和。這樣的權重實際代表校正值與觀測值差的平方的平均之倒數。這樣決定權重有使校正值趨近於觀測值的趨向。本研究首先根據上述的方法進行數值實驗，結果發現 $\partial u/\partial t$ 與 $\partial v/\partial t$ 的平均值愈來愈小，雖然會收斂但已小至 10^{-20}m/sec²（見表二），也就是說大氣運動已是定常的了，當然這與大氣的實際運動不合，而且三個權重比 $\tilde{\alpha}/\alpha$, $\tilde{\beta}/\alpha$, $\tilde{\gamma}/\alpha$ 也愈來愈小，與第一

次的假設值相差太多。第二次實驗在5個計算週期中把動力權重α值固定不變，結果 $\partial u/\partial t$ 與$\partial v/\partial t$ 的平均值只降至 1.3×10^{-3}m/sec^2, $\tilde{\beta}/\alpha$ 與 $\tilde{\gamma}/\alpha$ 的值逐漸收斂到假設值，可是 $\tilde{\alpha}/\alpha$ 仍無法接近原來的假設值，這表示 $\tilde{\alpha}$ 的假設值(13)式選擇過高；也就是說風速的觀測誤差比 2m/s 大。第三次實驗固定 $\tilde{\alpha}$的值，經過五個週期的計算以後 $\tilde{\alpha}/\alpha$, $\tilde{\beta}/\alpha$, $\tilde{\gamma}/\alpha$ 仍不能收斂，而且 $z-\tilde{z}$ 的平均值增加到 100m，也就是說高度場完全與原來的高度場不一樣了。因此由三種數值實驗的結果，只有把 α 固定後所得的分析場比較合理，以下討論的就是第二種實驗的結果。

由變分分析所得的高度場分別在圖8(700mb) 圖14 (500mb) 和圖20 (300mb) 。這些高度場與逐次校正法的趨勢大致一樣，但由於使用觀測溫度和風來進行校正，變分分析的高度場已在水平方向和垂直方向與風和溫度保持一種準地轉和靜水的平衡，此外也具有大氣大規模運動的準定常特性。溫度的分析在圖11 (700mb) ，圖17 (500mb) 與圖23 (300mb) 。溫度場的分析完全由高度經由靜水方程式決定的。觀測高度，溫度與風經由分析方程式(12)式校正了高度場，同時也校正了溫度場。溫度場的校正比較明顯。由圖11可以看出，變分分析的溫度場與主觀分析溫度較接近，即圖下方的三個暖區出現，而在逐次校正分析的溫度場 (圖11) 較不顯著。其他二層的溫度場也與逐次分析的溫度有少許差異。

§5. 結　　語

本研究使用客觀分析法來分析九個定壓層的高度、溫度和風速分量，然後再用變分分析校正這些變數值，使其在水平方向與垂直方向能滿足大氣大規模運動的特性，諸如靜水平衡，準地轉平衡和準定常運動。本研究所用的天氣資料事先並未做極端值檢定與靜水檢定，人爲的錯誤也未加完全除去，雖然在逐次校正法分析時能把錯誤改正，但百密一疏可以造成一點分析上的錯誤，而且也浪費了不少的時間與人力。最近欣聞氣象單位正在進行天氣資料自動處理 (Kuo and Hu 1975) ，對正確天氣資料的取得將會方便不少，本研究進行的逐次校正法與變分分析法的結果將會更加正確。氣象單位也正在從事用數值方法來預報天氣，若完成客觀分析以後，再用變分分析來校正變數值，將會改良預報的精度。加上變分分析只要再福傳程式中再加上一個副程式即可，本研究在變分分析中只用了兩分鐘計算時間，當然若分析更多層的天氣資料，所需的計算時間也會更多。因此本研究可以實際使用於數值預報方面。此外我國研究數值預報通常採用主觀分析法而且只利用高度值而不使用觀測溫度與風，著者深感可在主觀分析之後，再加上變分分析，這樣所得的變數值比較代表性，問題是從事風的主觀分析比較不易而且費時。

在進行逐次校正法的分析時似須在初次估計值與權重方面再加研究，在權重方面採用 McFarland 權重 (McFarland 1975) 以增進分析的準確性和節省計算時間。此外在變分分析方面應使權重與緯度有關，因爲在中緯度斜壓區域高度的觀測值比較準確，而在低緯度正壓區域風的觀測值比較準確，因此這些權重至少應該是緯度的函數，這樣方能分析出一個能眞正代表天氣運動的變數場。

本研究中尚未使用連續方程式作爲動力條件，若加上連續方程式會使分析方程式變得更爲複雜。但相信仍能解出。

由於近年人造衛星以及其他遙感儀器所測得的天氣資料大都爲溫度與風，因此變分分析更爲重要，尤其在地面測站稀少地區可使用人造衛星所測得風向和溫度來重建高度場，以改進預報的精度，此外變分分析也可進行四維資料同化。

以上所敍述的三點可作爲本研究的新方向。

§6. 致　　謝

本研究是在國家科學委員會 NSC-65M 0202 02(01)「東亞地區天氣資料變分客觀分析之研究」專題

計劃補助下完成的。本研究所使用的天氣資料由中央氣象局和空軍氣象聯隊氣象中心提供，此外張德青從事大部份的程式上機工作，黃火金從事繪圖工作，對上述的機關和個人，深表謝意。

Reference

Barnes, S. L., 1973: Mesoscale objective map analysis using weighted time series observations. *NOAA Tech. Memo. ERL NSSL-62,* 60pp.

Bergthorssen, P. and B. R. Döös, 1955: Numerical weather map analysis. *Tellus,* **2,** 329-340.

Bleck, R., 1975: An economical approach to the use of wind data in optimum interopalation of geo- and Montgomery potential fields. *Mon. Wea. Rev.,* **103,** 807-816.

Bushby, F. H. and V. M. Huckle, 1956: Objective analysis in numerical forecasting. *Quart. J. Roy. Meteor. Soc.,* **82,** 232-247.

Cressman, G. P., 1959: An operational objective analysis scheme. *Mon. Wea. Rev.,* **87,** 367-374.

Groll, A., 1975: On the initialization problem—a variational adjustment method. *Mon. Wea. Rev.,* **103,** 1089-1103.

Inman, R. L., 1970: Papers on operational objective analysis schemes at NSSFC. *NOAA Tech. Memo. ERL NSSL-51,* 91pp.

Kuo, W. L. and C. Y. Hu, 1975: A design of computer system for weather prediction. (in Chinese) *Meteorological Bulletin,* Central Weather Bureau, Taipei, Taiwan, Vol. **21,** No. 2, 18-24.

Lewis, J. M., 1972: An operational upper air analysis using the variational method. *FNWC Tech. Note No. 72-3,* 50pp., also in *Tellus,* **24,** 514-530.

McDonell, J. E., 1962: On the objective analysis system used at the National Meteorological Center. *NMC-TM No.* **23,** National Meteorological Center, Washington, D. C., 32 pp.

McFarland, M. J., 1975: Variational optimization analysis of temperature and moisture advection in a severe storm environment. *WEAT Report No. 16,* University of Oklahoma, Norman, Oklahoma, 86pp.

Ritchie, A. A., 1975: A variational optimization analysis approach to continuous data assimilation. Ph. D. dissertation, University of Oklahoma, Norman, Oklahoma, 98pp.

Sasaki, Y., 1958: An objective analysis based on the variational method. *J. Meteor. Soc. Japan,* **36,** 77-88.

Sasaki, Y., 1969a: Numerical variational method of analysis and prediction. *Proc. WMO/IUGG Symposium on Numerical Weather Prediction,* Tokyo, Japan, Nov. 26-Dec. 4, 1968, Japan Meteor. Agnecy, Japan, VII 23-25.

Sasaki, Y., 1969b: Proposed inclusion of time variation terms, observational and theorectical, in numerical variational objective analysis. *J. Meteor. Soc. Japan,* **47,** 115-124.

Sasaki, Y., 1970a: Some basic formalisms in numerical variational analysis. *Mon. Wea.*

Rev., **98**, 875-883.

Sasaki, Y., 1970b: Numerical variational analysis formulated under the constraints as determined by long wave equations and a low pass filter. *Mon. Wea. Rev.* **98**, 884-898.

Sasaki, Y., 1970c: Numerical variational analysis with weak constraints and application to surface analysis of severe storm gust. *Mon. Wea. Rev.*, **98**, 899-910.

Sasaki, Y., 1976: Variational design of finite difference scheme for initial value problem of an integral constraint. *J. Comp. Phys.*, **21**, 270-278.

Sheets, R. C., 1973a: Analysis of Hurricane Debbie modification results using the variational optimization approach. *Mon. Wea. Rev.*, **101**, 663-684.

Sheets, R. C., 1973b: Analysis of STORMFURY data using the variational optimization approach. *NOAA Tech. Rept. ERL-264 WMPO-1*, 92pp.

Shuman, F. G. 1957: Numerical method in weather prediction: II. Smoothing and filtering. *Mon. Wea. Rev.*, **85**, 357-361.

Stephens, J. J., 1970: Variational initialization with the balance equation. *J. Appl. Meteor.*, **9**, 732-739.

Stephens, J. J., 1971: On the definable scale reduction by simultaneous observations *J. Appl. Meteor.*, **10**, 23-25.

P	Z	T	u	v
850mb	12.14m	1.32°C	2.27m/s	2.79m/s
700	12.37	1.23	3.47	3.02
500	12.25	0.96	2.33	2.34
400	20.90	1.64	3.55	2.94
300	26.81	1.71	4.23	4.32
250	43.30	1.23	5.92	3.31
200	26.61	1.19	4.06	3.15
150	31.13	1.40	3.78	2.58
100	47.63	1.53	3.39	1.98

表一：各種氣象變數逐次校正分析值與觀測值之 rms (root mean square)

Cycle	A	B	C	D	$\tilde{\alpha}/\alpha$	$\tilde{\beta}/\alpha$	$\tilde{\gamma}/\alpha$
1	2. m/s	2. °C	10.m	$1.\times10^{-4}$m/s^2	5.3×10^{-1}	$3.\times10^{-14}$	$1.\times10^{-12}$
2	7.9	2.9	41.	2.3×10^{-5}	9.2×10^{-6}	7.5×10^{-18}	3.2×10^{-17}
3	12.	2.2	27.	4.5×10^{-11}	1.6×10^{-15}	5.3×10^{-27}	3.0×10^{-26}
4	13.	1.8	14.	4.7×10^{-20}	1.6×10^{-33}	8.0×10^{-45}	1.2×10^{-43}
5	13.	1.9	8.5	3.8×10^{-20}	1.0×10^{-33}	5.0×10^{-45}	2.1×10^{-43}

表二：權重 $\tilde{\alpha}$, $\tilde{\beta}$, $\tilde{\gamma}$, α 不固定時五個週期的 A, B, C, D, $\tilde{\alpha}/\alpha$, $\tilde{\beta}/\alpha$, $\tilde{\gamma}/\alpha$之值，其中

$$A=\{\sum[(u-\tilde{u})^2+(v-\tilde{v})^2]/2\}^{1/2}/\sqrt{K}$$

$$B=\{\sum(T-\tilde{T})^2\}^{1/2}/\sqrt{K}$$

$$C=\{\sum(z-\tilde{z})^2\}^{1/2}/\sqrt{K}$$

$$D=\{\sum[(\frac{\partial u}{\partial t})^2+(\frac{\partial v}{\partial t})^2]/2\}^{1/2}/\sqrt{K}$$

Cycle	A	B	C	D	$\tilde{\alpha}/\alpha$	$\tilde{\beta}/\alpha$	$\tilde{\gamma}/\alpha$
1	2.	2.	10.	$1.\times10^{-4}$	5.3×10^{-1}	$3.\times10^{-14}$	1.0×10^{-12}
2	7.9	2.9	41.	2.3×10^{-6}	1.8×10^{-2}	$3.\times10^{-14}$	6.3×10^{-14}
3	6.	1.2	22.	8.1×10^{-8}	7.8×10^{-3}	$3.\times10^{-14}$	2.1×10^{-13}
4	6.5	1.8	12.	1.8×10^{-8}	7.2×10^{-3}	$3.\times10^{-14}$	6.9×10^{-13}
5	6.5	1.9	6.9	1.3×10^{-3}	7.0×10^{-3}	$3.\times10^{-14}$	2.2×10^{-12}

表三：同表二，但 α 值不變。

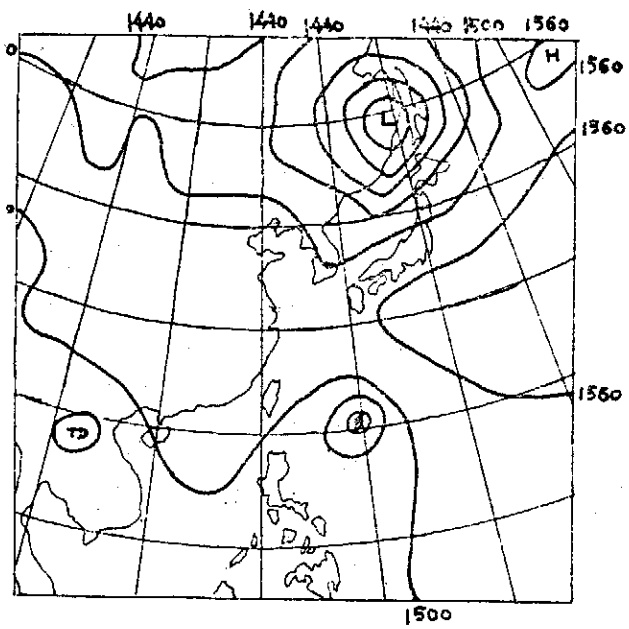

圖2. 850mb 主觀分析高度場

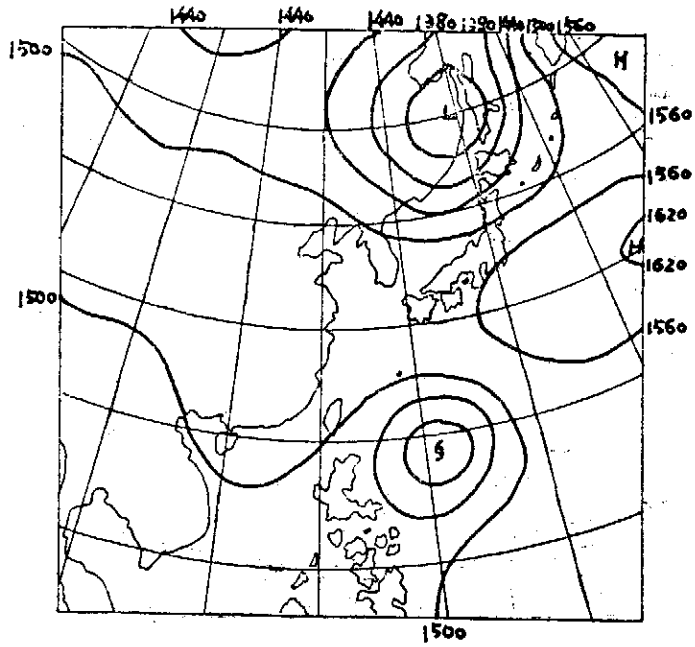

圖3. 850mb 逐次校正分析高度場

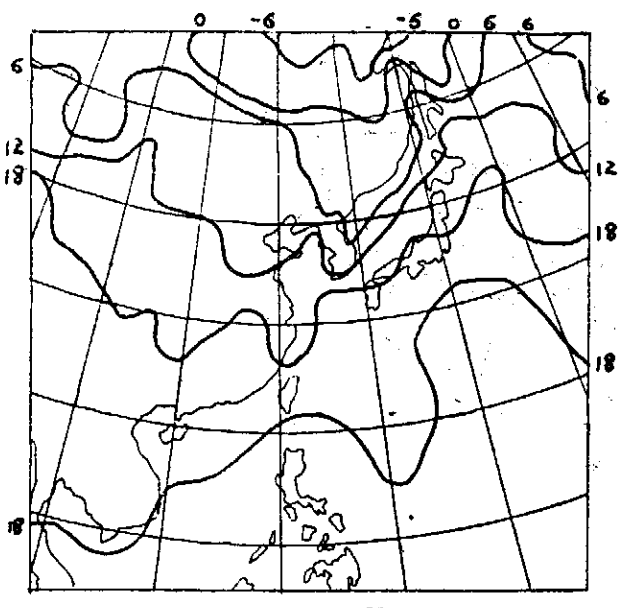

圖4. 850mb 主觀分析溫度場

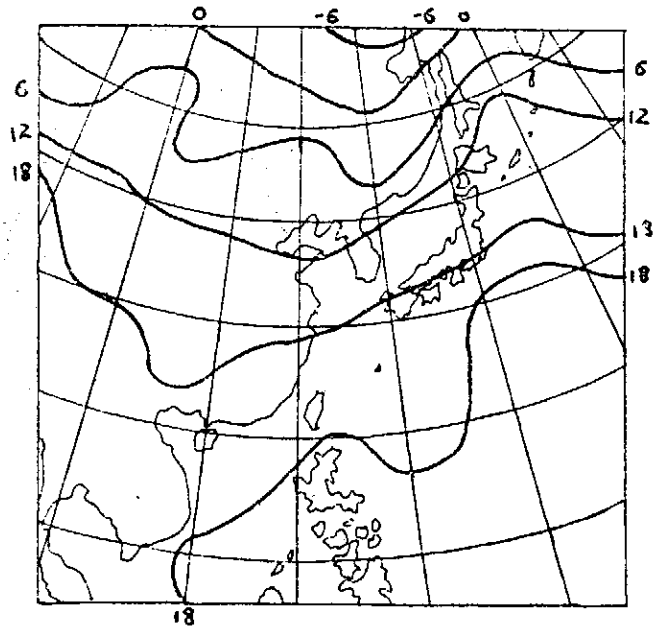

圖5. 850mb 逐次校正分析溫度場

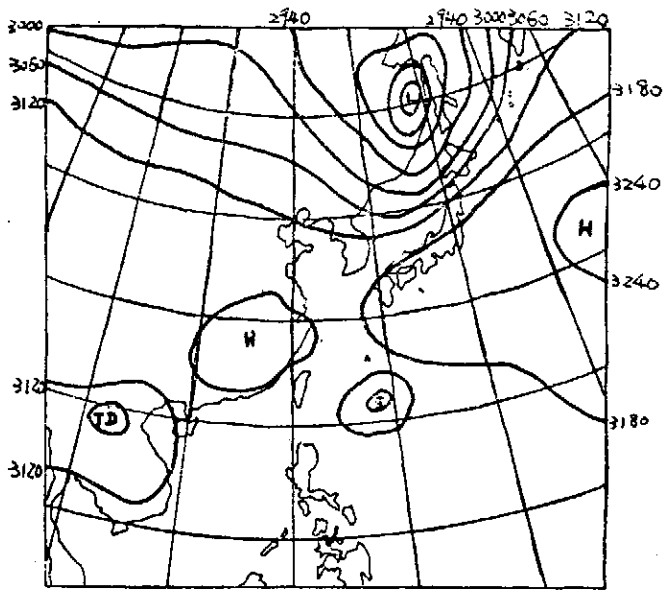

圖6.　700mb 主觀分析高度場

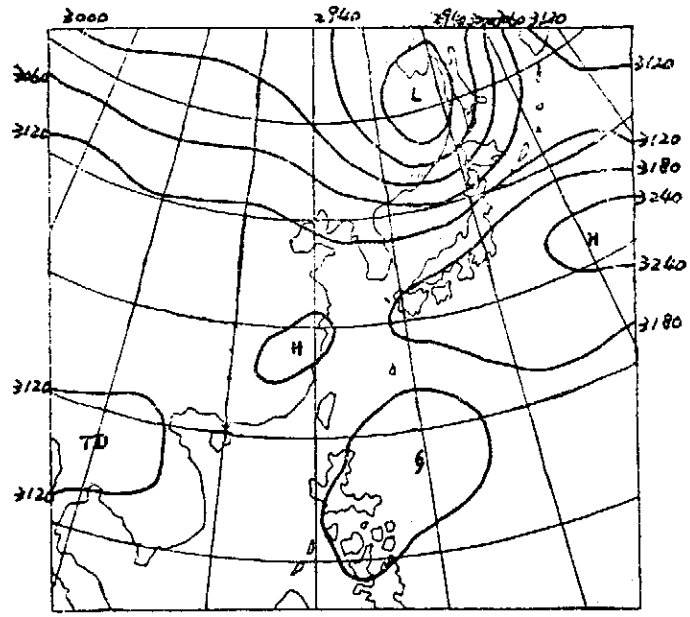

圖7.　700mb 逐次校正分析高度場

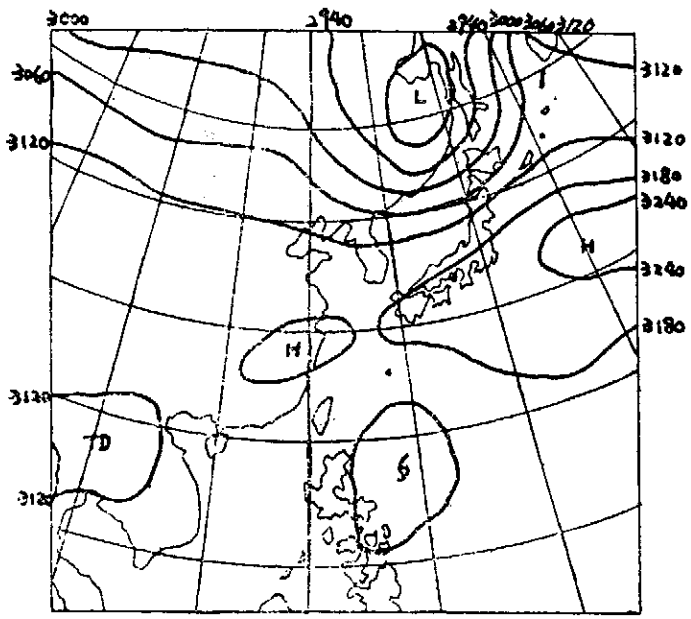

圖8.　700mb 變分分析高度場

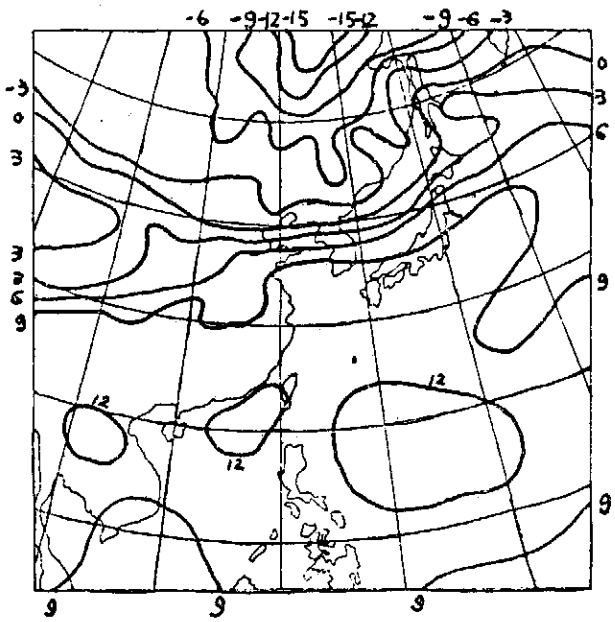

圖9. 700mb 主觀分析溫度場

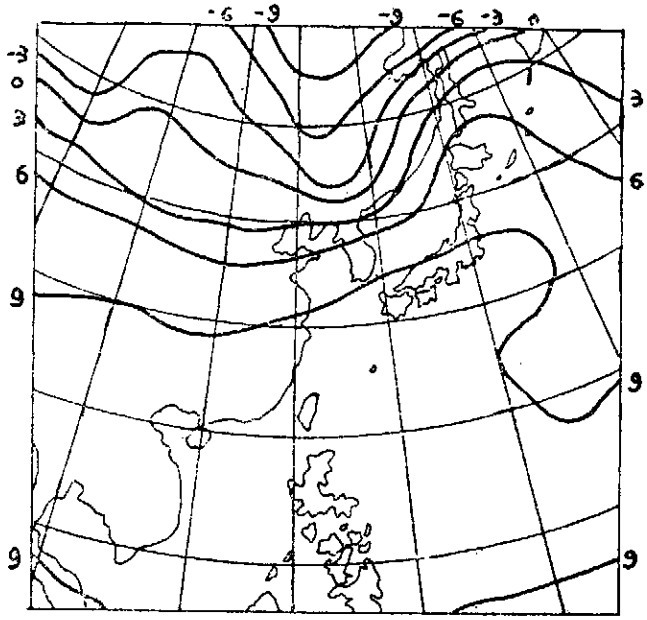

圖10. 700mb 逐次校正分析溫度場

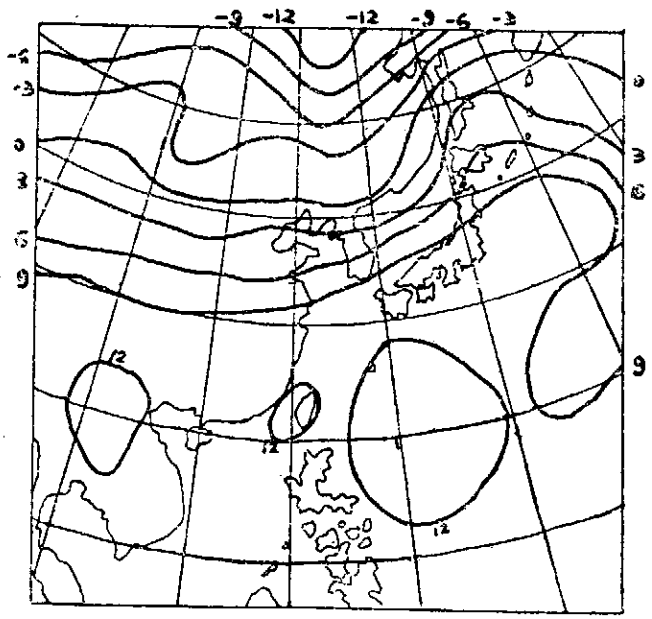

圖11. 700mb 變分分析溫度場

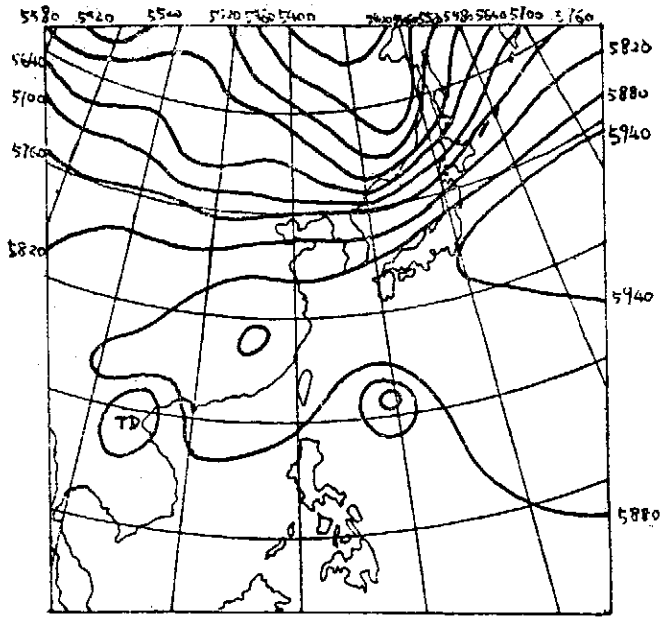

圖12.　500mb 主觀分析高度場

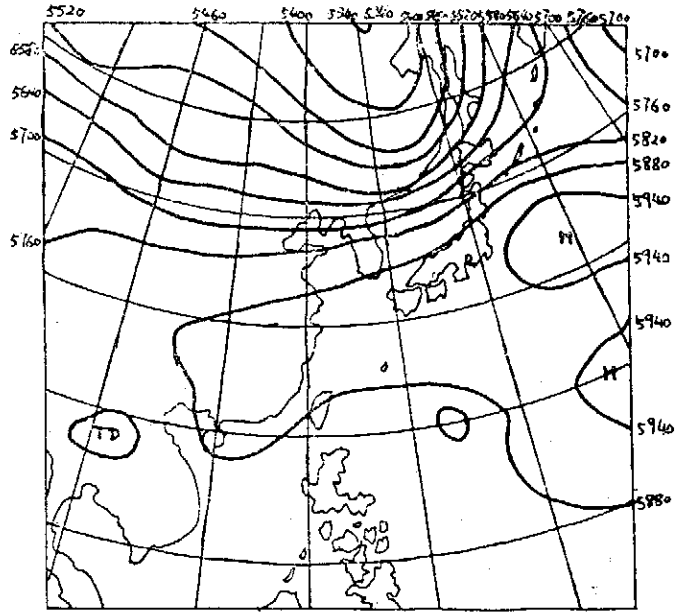

圖13.　500mb 逐次校正分析高度場

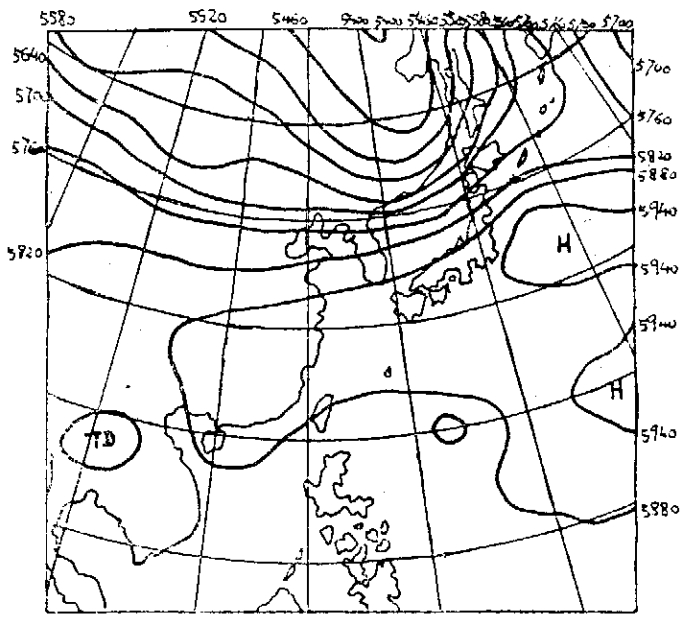

圖14.　500mb 變分分析高度場

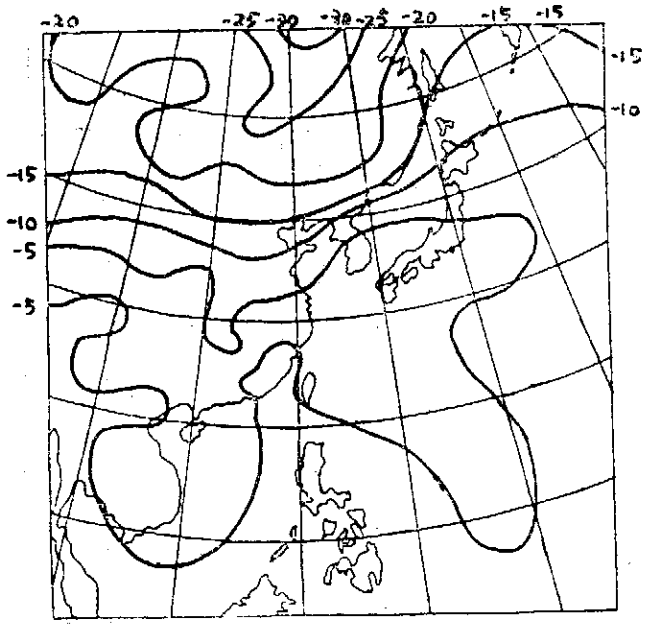

圖15. 500mb 主觀分析溫度場

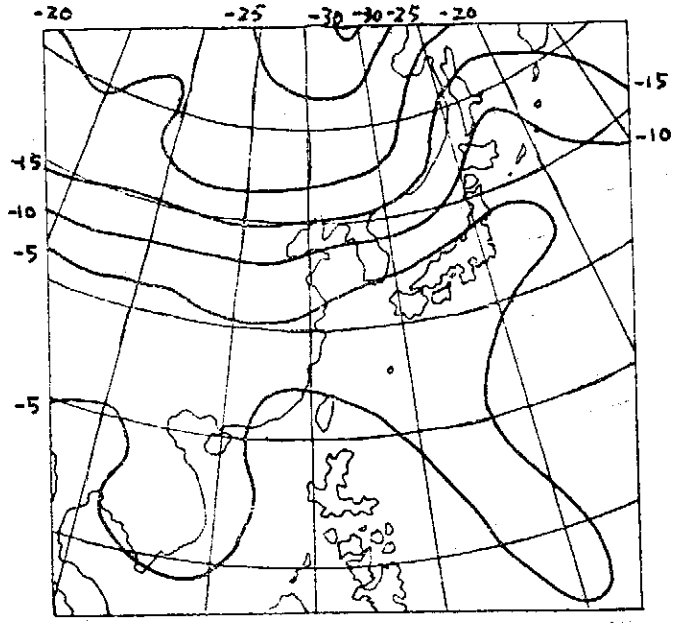

圖16. 500mb 逐次校正分溫析度場

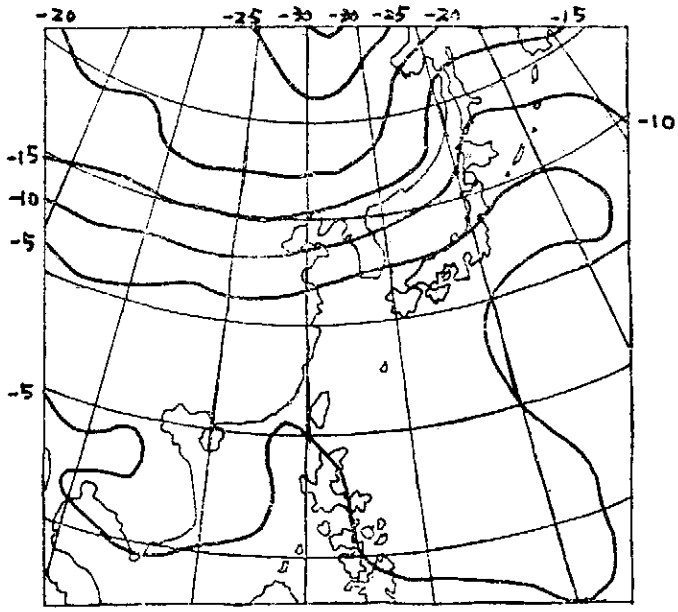

圖17. 500mb 變分分析溫度場

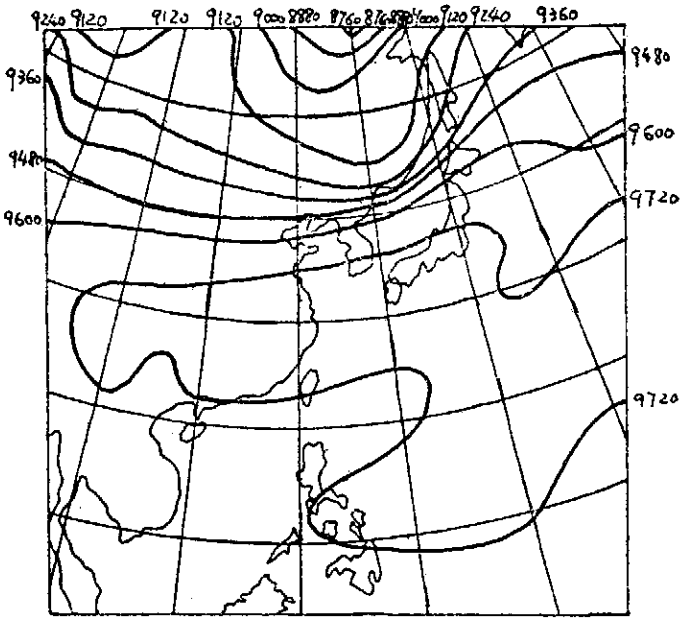

圖18. 300mb 主觀分析高度場

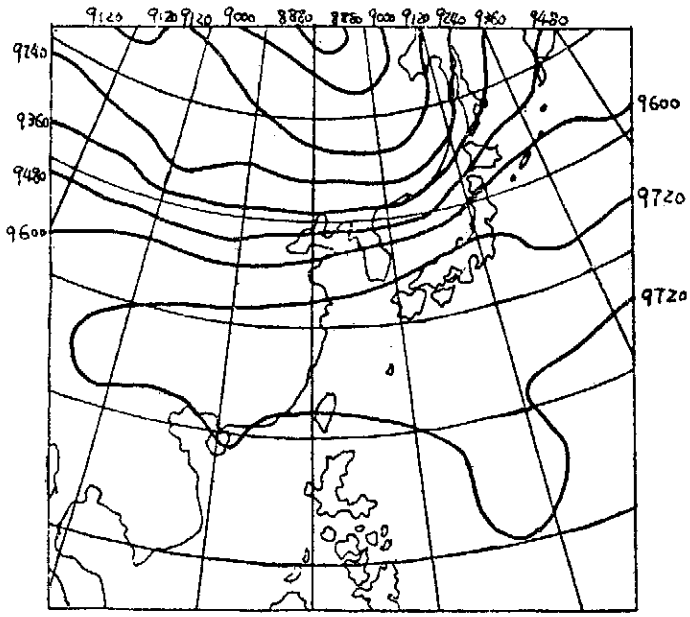

圖19. 300mb 逐次校正分析高度場

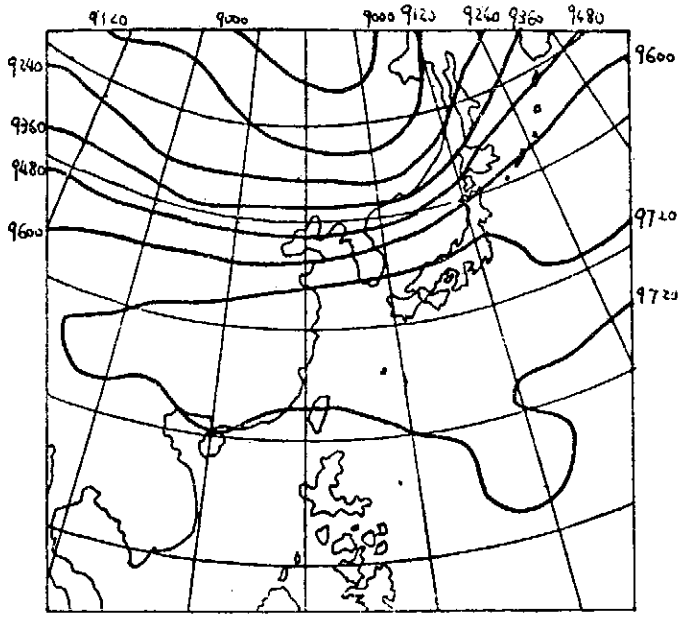

圖20. 300mb 變分分析高度場

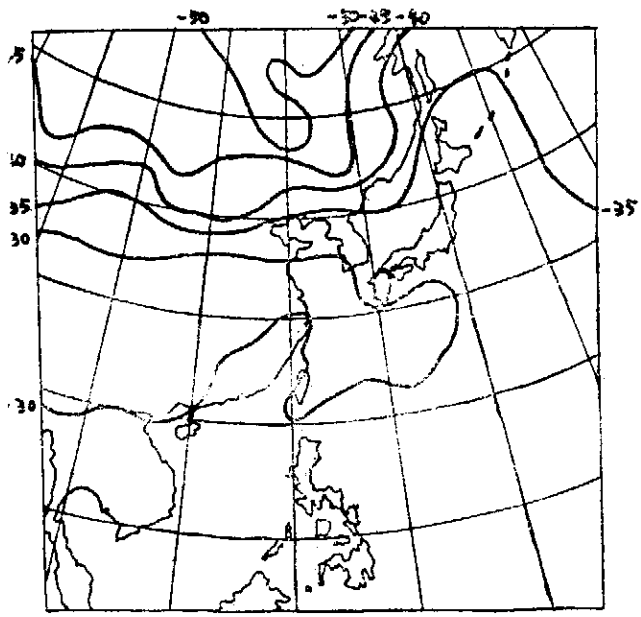

圖21　300mb 主觀分析溫度場

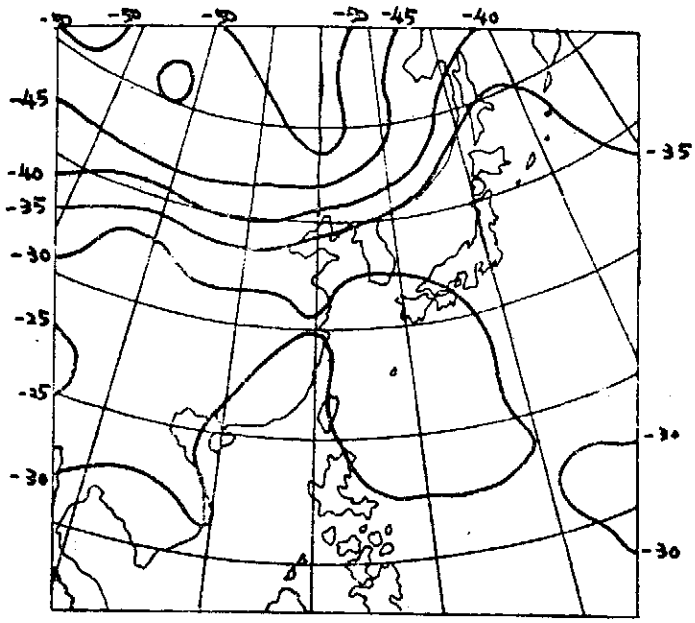

圖22　300mb 逐次校正分析溫度場

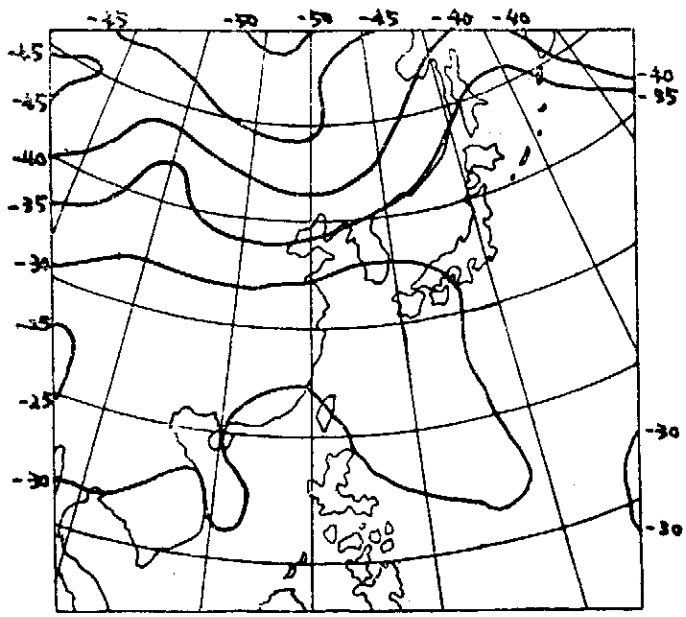

圖23　300mb 變分分析溫度場

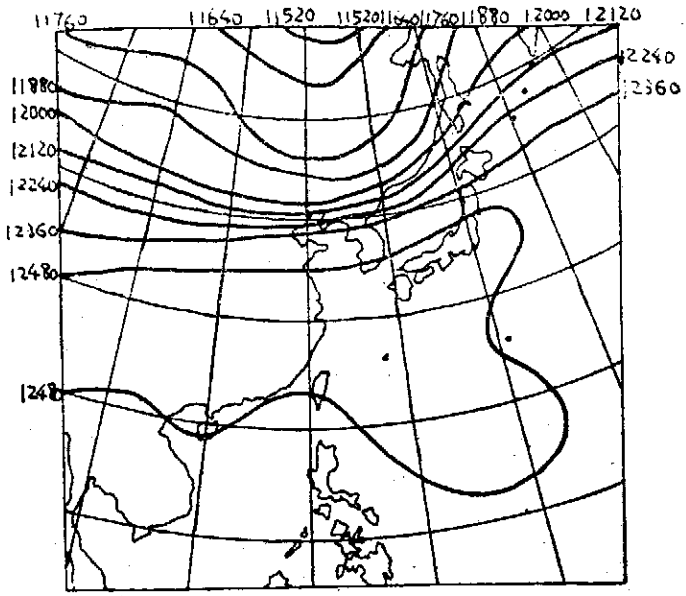

圖24　200mb 主觀分析高度場

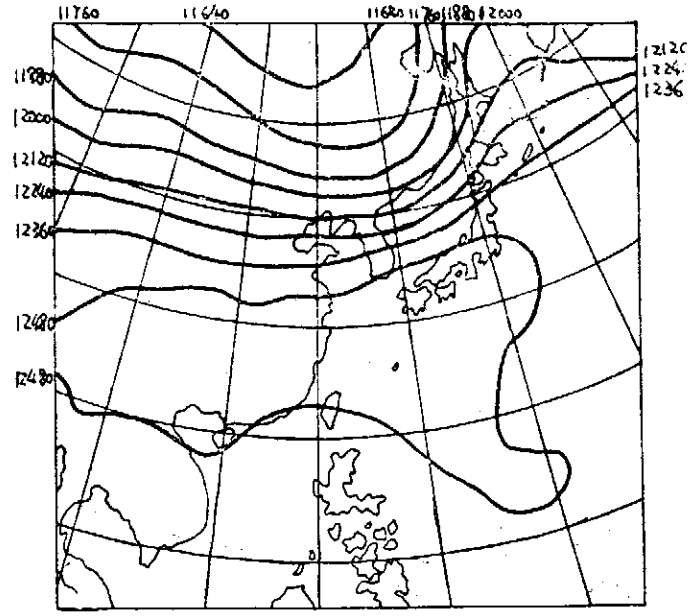

圖25　200mb 逐次校正分析高度場

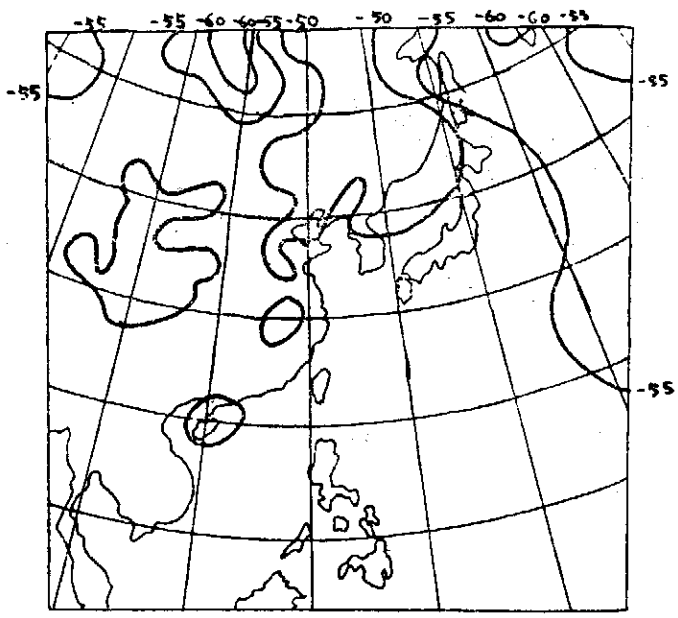

圖26　200mb 主觀分析溫度場

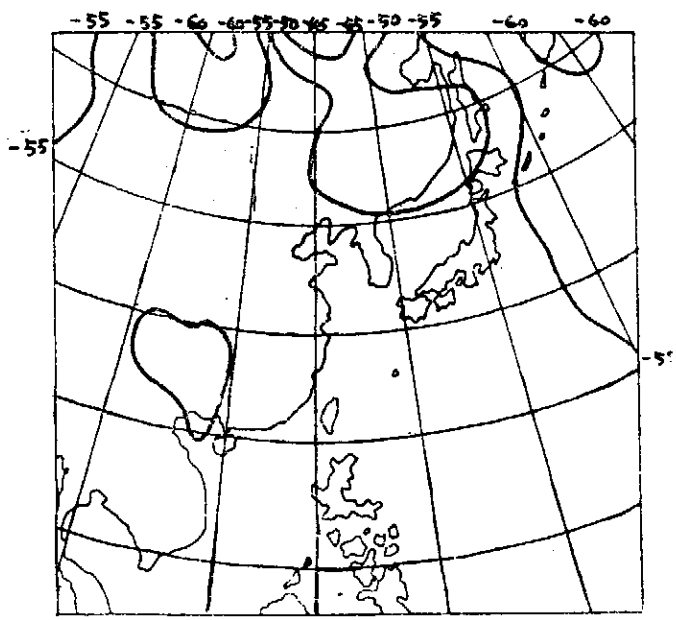

圖27　200mb 逐次校正分析溫度場

Annual Report of the Institute of Physis, Academia Sinica, Vol. 6, 1976

The Variational Optimization of Wind Field for the Estimation of Vertical Velocity

Wen-Jey Liang[1]

Department of Meteorology, University of Oklahoma
Norman, Oklahoma

Abstract

A variational optimization scheme of wind field is developed for the correction of vertical velocity field using kinematic method. The errors which appear in the vertical velocity field are classified as systematic errors and random errors. The systematic errors are suppressed by the use of two strong constraints, i.e., the integrated continuity equation and the global boundary condition. The random errors are filtered by including a low-pass filter simultaneously in the variational formulation that the filtered field still satisfies above constraints. The upper boundary condition of the vertical velocity field is considered in terms of the spatial distribution of upward and downward motion. NASA AVE II data are utilized to verify the scheme. Results show that the magnitudes and general patterns of vertical velocity field are in good agreement with the synoptic weather system and radar reports.

I. INTRODUCTION

A current important problem in meteorology is the estimation of the distribution of vertical velocity in the atmosphere. Because of its smallness, the routine observation of vertical velocity is not available. It is commonly computed from the horizontal wind velocity, the pressure distribution, or the temperature distribution utilizing the continuity equation (the kinematic method), the omega equation, or the adiabatic equation, respectively. Although each method has its inherent advantages and disadvantages, kinematic method is worthist to mention in many situations because of its mathematical simplicity and the fact that hydrostatic balance is the only assumption. However, errors in the wind observations as well as in the computed horizontal divergence often tend to accumulate through the vertical integration that there is little confidence in the use of computed vertical velocity without considerable corrections.

The errors which appear in the vertical velocity field by the use of kinematic method can be classified as "systematic errors" and "random errors". The systematic errors occur primarily because of inconsistencies

[1] Present affiliation: National Taiwan University, and Institute of Physices Academica Sinica, Taipei, Taiwan, Republic of China.

between the observed field and the dynamical model considered. The random errors may be introduced because of inaccuracies of measurements, spatial irregularity of observation points, and by interpolation of values from stations to grid points. Many methods (e. g. Lateef 1967, Kung 1974) have been proposed to correct errors. In this paper, Sasaki's variational optimization approach is utilized. This method provides an important advantage by incorporating dynamic, kinematic, statistical, and other conditions in data management. Consequently, systemmatic errors as well as random errors can be suppressed such that the optimized data are consistent with the dynamical model considered.

In variational formulation, the upper boundary condition on the vertical velocity at the top of the convective layer should be prescribed in order to solve the associated Euler-Lagrange equations. But this condition is unknown. McGinley (1973) assumed that it was zero everywhere without consideration of the fact that in a region of severe convection the vertical velocity is not necessarily zero at an arbitrary level near the cloud tops. Indeed, if the local change of pressure is negligible, over a very large region the average vertical velocity should be zero to ensure conservation of mass. The integral constraint which requires the mean vertical velocity at the top over a large area to be a predetermined value (usually zero) is called the global boundary condition. This condition have been utilized in O'Brien's (1970) adjustment scheme to correct the vertical velocity obtained from kinematic method. However, because the area mean of the vertical velocity at top is usually small, the correction is quite small at most grid points. Furthermore, since the correction is a constant over a horizontal plane (or constant pressure surface), it does not change the vertical velocity patterns. This is desirable only when the vertical velocity patterns obtained from the kinematic method are highly reliable. Indeed, McGinley's top boundary condition is an extreme case of O'Brien's, and is too arbitrary, especially in the vicinity of severe convective system. It is pratically and theoretically valuable to reformulate the variational problem such that the vertical velocity at top can be realistically simulated and the errors can be reasonably corrected.

In the following sections, a variational optimization scheme is developed in which systematic errors are suppressed by the use of two strong conditions, i. e., the integrated continuity equation and the global boundary condition; the random errors are filtered by the use of a low-pass filter. Although the random errors can be suppressed by utilizing varied filters,

the filtering should be incorporated simultaneously in the variational formulation to ensure that the filtered fields satisfy all constraints. Additionally, it can be shown that O'Brien's and McGinley's methods are two special cases of this scheme.

II. VARIATIONAL FORMULATION

The functional is defined as

$$I=\int_x\int_y\int_p\{(u-\bar{u})^2+(v-\bar{v})^2+\bar{\alpha}^2(\omega_t-\bar{\omega})^2+\bar{\beta}^2(\nabla\omega_t\cdot\nabla\omega_t)^2\}dp\ dy\ dx. \quad (1)$$

Here, two strong constraints are utilized:

$$\omega_t=\omega_s-\int_{p_s}^{p_t}\nabla\cdot\vec{v}\ dp, \quad (2)$$

$$\int_x\int_y\omega_t\ dx\ dy=0, \quad (3)$$

where $\bar{u}$, u, $\bar{v}$, and v are observed and optimized wind components along the x and y directions, respectively, ω_t is the optimized p velocity at the top of the domain, $\bar{\alpha}$ and $\bar{\beta}$ are specified parameters, p_s and p_t are pressures at the surface and at the top of atmosphere, respectively, and

$$\bar{\omega}_t=\omega_s-\int_{p_s}^{p_t}\nabla\cdot\bar{\vec{v}}\ dp, \quad (4)$$

$$\omega_s=\bar{\vec{v}}_s\cdot\nabla p_s, \quad (5)$$

where $\bar{\vec{v}}_s$ is the observed surface wind and ∇ is a two dimensional differential operator,

$$\nabla\equiv\left(\frac{\partial}{\partial x},\frac{\partial}{\partial y}\right).$$

Let us take the variation of the functional I and set it to zero, i. e.,

$$\delta I=2\int_x\int_y\int_p\{[(u-\bar{u})-\frac{\partial\lambda_1}{\partial x}]\delta u+[(v-\bar{v})-\frac{\partial\lambda_1}{\partial y}]\delta v+[\bar{\alpha}^2(\omega_t-\bar{\omega}_t)+\frac{\lambda_1}{p_t-p_s}+\lambda_2-\bar{\beta}^2\nabla^2\omega_t]\ \delta\omega_t\}\,dp\ dy\ dx+\int_y\int_p[\lambda_1\delta u]_{x=x_1}^{x=x_2}\ dp\ dy+\int_x\int_p[\lambda_1\delta v]_{y=y_1}^{y=y_2}dp\ dx+\int_y\int_p[\bar{\beta}^2\frac{\partial\omega_t}{\partial x}]_{x=x_1}^{x=x_2}\ dp\ dy+\int_x\int_p[\bar{\beta}^2\frac{\partial\omega_t}{\partial y}]_{y=y_1}^{y=y_2}\ dp\ dx=0, \quad (6)$$

where x_1 and x_2 are the boundary values of x corresponding to the value of y and p held constant in the x-integration, y_1 and y_2 are the boundary values of y corresponding to the value of x and p held constant in the y-integration, ∇^2 is a two dimensional Laplacian operator, and λ_1 and λ_2 are Lagrange multipliers associated with two strong constraints (2) and (3), respectively. Then the associated Euler-Lagrange equestions are:

$$u=\tilde{u}+\frac{\partial\lambda_1}{\partial x}, \tag{7}$$

$$v=\tilde{v}+\frac{\partial\lambda_1}{\partial y}, \tag{8}$$

$$\tilde{\beta}^2\nabla^2\omega_t-\tilde{\alpha}^2\omega_t+\frac{\lambda_1}{p_t-p_t}=\lambda_2-\tilde{\alpha}^2\tilde{\omega}_t \tag{9}$$

For the elimination of the last four terms in (6), there are several choices of boundary conditions associated with Lagrange multiplier λ_1, the derivatives of ω_t, and the variations of u, v, and ω_t. In this study, the associated boundary conditions are:

$$\lambda_1=0, \tag{10}$$

$$\vec{n}\cdot\nabla\omega_t=0, \tag{11}$$

where $\vec{n}$ is an unit normal vector along the boundary.

In order to better understand the physical meaning of this formulation and the associated boundary conditions, let us define the correction velocity, $\vec{v}^*$ s

$$\vec{v}^*=\vec{v}-\tilde{\vec{v}}, \tag{12}$$

where $\vec{v}=(u, v)$, $\tilde{\vec{v}}=(\tilde{u}, \tilde{v})$, and $\vec{v}^*=(u^*, v^*)$. Substitution of (12) into (1), (7), and (8) leads to

$$I=\int_x\int_y\int_p\{\vec{v}^*\cdot\vec{v}^*+\tilde{\alpha}^2\omega_t^{*2}+\tilde{\beta}^2(\nabla\omega_t\cdot\nabla\omega_t)\}\,dp\,dy\,dx, \tag{13}$$

and

$$\vec{v}^*=\nabla\lambda_1, \tag{14}$$

where $\omega_t^*=\omega_t-\tilde{\omega}_t$. Eq. (14) shows that the Lagrange multiplier λ_1 is the correction velocity potential; i. e., the correction velocity field is irrotational. The first two terms in (13) are the weighted correction kinetic energy of the region considered, and $\tilde{\alpha}^2$ is the weighting factor. The third term in (13) is a weak constraint, i. e.,

$$|\nabla\omega_t| \approx 0. \tag{15}$$

Indeed, $|\nabla\omega_t|$ is a part of the horizontal vorticity associated with ω_t. It reflects the spatial distribution of areas of upward and downward motion. In terms of the vertical correction velocity ω_t^*, (15) can be written as

$$|\nabla\omega_t^* + \nabla\tilde{\omega}_t| \approx 0, \tag{16}$$

or

$$\left(\frac{\partial\omega_t^*}{\partial x} + \frac{\partial\tilde{\omega}_t}{\partial x}\right)^2 + \left(\frac{\partial\omega_t^*}{\partial y} + \frac{\partial\tilde{\omega}_t}{\partial y}\right)^2 \approx 0.$$

Since the horizontal gradient of the vertical velocity $|\nabla\omega_t|$ is zero only when

$$\frac{\partial\omega_t^*}{\partial x} = -\frac{\partial\tilde{\omega}_t}{\partial x},$$

and

$$\frac{\partial\omega_t^*}{\partial y} = -\frac{\partial\tilde{\omega}_t}{\partial y},$$

(16) indicates that (15) is satisfied by introducing a horizontal vorticity $|\nabla\omega_t|$ opposite to the original horizontal vorticity associated with $\nabla\tilde{\omega}_t$. Since the horizontal vorticity indicates the spatial distribution of upward and downward motion, any reduction of the horizontal vorticity suppresses the vertical motion. In other words, this procedure smooths the vertical motion field. The parameter $\tilde{\beta}$ is selected to accomplish this purpose. In this study, the value of $\tilde{\beta}$ is assigned to suppress the amplitude of waves whose wave length is less than the distance between adjacent maxima in the large-scale ω field.

The boundary condition (10) implies

$$\vec{v}_t^* = \frac{\partial\lambda_1}{\partial s} = 0,$$

along the boundary. Indeed, it is the no-slip boundary condition for the correction velocity field. This condition ensures that the optimization does not change the circulation of the region considered and is consistent with an irrotational correction velocity field. Furthermore, since ω_t is unknown, the boundary condition (11) permits ω_t to be free on the boundary to allow a wide range of possible ω_t patterns.

Eqs. (2), (3), (7), (8), and (9) are five equations for the five unknowns: u, v, ω_t, λ_1 and λ_2. Their solutions, and associated response functions are discussed in the following sections.

III. SOLUTIONS OF EULER-LAGRANGE EQUESTIONS

Eqs. (2), (3), (7), (7), (8), and (9) are five equations for five unknowns: u, v, ω_t, λ_1, and λ_2. Substituting (7) and (8) into (2), we get

$$\omega_t=\tilde{\omega}_t+(p_t-\bar{p}_t)\ \nabla^2\lambda_1. \tag{17}$$

The substitution of (17) into (9) leads

$$\tilde{\beta}^2\nabla^2\left[(p_t-\bar{p}_t)\ \nabla^2\lambda_1\right]-\tilde{\alpha}^2(p_t-\bar{p}_t)\nabla^2\lambda_1+\frac{\lambda_1}{p_t-\bar{p}_t}=\lambda_2-\tilde{\beta}^2\nabla^2\tilde{\omega}_t \tag{18}$$

From Gauss' theorem and the boundary condition (11), we have

$$\begin{aligned}\overline{\nabla^2\omega_t}&\equiv\int_x\int_y(\nabla^2\omega_t)\ dx\ dy/\int_x\int_y dx\ dy\\&=\int_{C_0}(n\cdot\nabla\omega_t)\ ds/\int_x\int_y dx\ dy\\&=0,\end{aligned}$$

where C_0 is the boundary of the area considered, and $(^-)$ is an area-average operator. After applying the area-average operator to (9), we get

$$\lambda_2=\tilde{\alpha}^2\bar{\tilde{\omega}}_t+\overline{\left(\frac{\lambda_1}{p_t-\bar{p}_t}\right)}, \tag{19}$$

where the strong constraint (3) has been utilized.

Eqs. (18) and (19) contain two unknowns: λ_1 and λ_2. Solutions can be obtained by an iterative technique. Fortunately, because the equations are linear and λ_2 is constant, the solutions can be determined without using an iterative procedure. In order to clarify the procedures utilized to obtain solutions, let us define a linear differential operator L as:

$$L\equiv\tilde{\beta}^2\nabla^2(p_t-\bar{p}_t)\nabla^2-\tilde{\alpha}^2(p_t-\bar{p}_t)\nabla^2+\frac{1}{p_t-\bar{p}_t}.$$

Then, (18) can be rewritten as

$$\lambda_1=L^{-1}(\lambda_2-\tilde{\beta}^2\nabla^2\tilde{\omega}_t) \tag{20}$$

where L^{-1} is the inverse operator of L.

Setting

$$\lambda_1=\lambda_b+\phi, \tag{21}$$

where

$$\lambda_b=L^{-1}(-\tilde{\beta}^2\nabla^2\tilde{\omega}_t) \tag{22}$$

and the boundary values of λ_b and ϕ are chosen to be zero, then, (19) and (20) become

$$\phi = L^{-1}(\lambda_2), \tag{23}$$

$$\lambda_2 = C + \left(\overline{\frac{\phi}{p_s - p_t}}\right), \tag{24}$$

where

$$C = \bar{\alpha}^2 \bar{\omega}_t + \left(\overline{\frac{\lambda_b}{p_s - p_t}}\right)$$

From (22), λ_b can be solved by using a relaxation method. After ϕ and λ_2 are determined from (23) and (24), the complete solution is obtained from (21). Eqs. (22) and (23) show that λ_b is a part of the solution of λ_1 which corresponds to the curvature of the $\bar{\omega}_t$-field, and ϕ is the other part of the solution of λ_1 which corresponds to the mean value of $\bar{\omega}_t$. These properties will be discussed in detail later.

In order to employ iterative procedures to solve for ϕ and λ_2, let us rewrite (23) and (24) as

$$\phi^{(k)} = L^{-1}(\lambda_2{}^{(k)}), \tag{25}$$

$$\lambda_2{}^{(k)} = C + \left[\overline{\frac{\phi^{(k-1)}}{p_s - p_t}}\right], \tag{26}$$

where (k) indicates the k-th iteration. Let zero be the initial guess for the solution of ϕ, and define

$$\left[\overline{\frac{L^{-1}(C)}{p_s - p_t}}\right] \equiv aC,$$

i. e.,

$$a \equiv \frac{\left[\overline{\frac{L^{-1}(C)}{p_s - p_t}}\right]}{C}.$$

Then, (25) and (26) become

$$\lambda^{1(n)} = C \sum_{k=0}^{n} a^k, \tag{27}$$

$$\phi^{(n)} = \phi^{(0)} \sum_{k=0}^{n} a^k, \tag{28}$$

and

$$\phi^{(0)} \equiv L^{-1}(C).$$

The derivation of (27) and (28) are mainly based on the facts that the operator L is linear and λ_2 is constant. It is obvious that if $|a| < 1$, the iteration procedure is convergent provided C and $\phi^{(0)}$ are bounded. Since a is a function of $\bar{\alpha}$ and $\bar{\beta}$, a diagram can be constructed to determine the

convergent and divergent region in $(\bar{\alpha},\bar{\beta})$ space. Convergence of the iterative procedure has been investigated for several cases. If the variables are nondimensionalized by suitable scales (e. g. the scale for the vertical p velocity should be 10^{-3}mb sec^{-1}, and the mass convergence scale should be 10^{-5} sec^{-1}, etc.), all tested cases show that the iteration procedure is convergent (rapidly in most cases) for a wide range of values of $\bar{\alpha}$ and $\bar{\beta}$.

In the convergence region, the solution of (27) and (28) is

$$\lambda_2=\lambda_2^{(\infty)}=\frac{C}{1-a},$$

$$\phi=\phi^{(\infty)}=\frac{\phi^{(0)}}{1-a}, \tag{29}$$

and the complete solution of (18) and (19) is obtained by use of (21).

Following the same concepts utilized in obtaining solutions to (21), ω_i is written as

$$\omega_i=\omega_i^{b}+\omega_i^{\phi} \tag{30}$$

where ω_i^{b} corresponds to λ_b and ω_i^{ϕ} corresponds to ϕ. Referring to (17), ω_i^{b} and ω_i^{ϕ} may be chosen as

$$\omega_i^{b}=\bar{\omega}_i+(p_s-p_i)\nabla^2\lambda_b, \tag{31}$$

$$\omega_i^{\phi}=(p_s-p_i)\Delta^2\phi, \tag{32}$$

and the associated boundary conditions are

$$\vec{n}\cdot\nabla\omega_i^{b}=\vec{n}\cdot\nabla\omega_i^{\phi}=0., \tag{33}$$

Boundary conditions different from (33) may be posed, although we prefer (33) because they are simple and are consistent with (11). According (31) and (32), ω_i^{b} and ω_i^{ϕ} can be determined from λ_b and ϕ, and then ω_i can be obtained from (30).

IV. RESPONSE FUNCTIONS

In order to better understand how to choose suitable values for $\bar{\alpha}$ and $\bar{\beta}$, the associated response function has to be found. Let us assume that

$$p_s-p_i=p_0+p',$$

$$p'=\sum_{k=1}^{\infty}\varepsilon^k p_k,$$

where ε is a small parameter, p_0 is the mean value over the whole region, and p' is the fluctuation of (p_s-p_i) from p_0. Since the ratio of p' to p_0 is smaller than 0.1 and is less than 0.02 at most grid points, p' is treated as a

small pertrurbation. The differential operator L can be expanded as:

$$L=(\tilde{\beta}^2 p_0\nabla^4-\tilde{\alpha}^2 p_0\nabla^2+\frac{1}{p_0})+\{\tilde{\beta}^2\nabla^2 p'\nabla^2-\tilde{\alpha}^2 p'\nabla^2+\frac{1}{p_0}\sum_{k=0}^{\infty}\left(-\frac{p'}{p_0}\right)^k\}=L_0+0(\varepsilon),$$

where

$$L_0\equiv\tilde{\beta}^2 p_0\nabla^4-\tilde{\alpha}^2 p_0\nabla^2+\frac{1}{p_0},$$

and 0 (ε) indicates the order of magnitude of ε (less than 0.1 in this study). To the zeroth order approximation, (22) and (23) become

$$\lambda_b=L_0^{-1}(-\tilde{\beta}^2\nabla^2\tilde{\omega}_t) \tag{34}$$
$$\phi=L_0^{-1}(\lambda_2).$$

The solution of ϕ is simply

$$\phi=p_0\lambda_2\,. \tag{35}$$

From Fourier transformation (FT) theory, any function $\lambda(x, y)$ and its Fourier transform $C(m, n)$ are represented as

$$\lambda(x, y)=FT^{-1}(C(m, n))=\sum_{n=-\infty}^{\infty}\sum_{m=-\infty}^{\infty}C(m, n)e^{i(mx+ny)} \tag{36}$$

$$C(m, n)=FT(\lambda(x,y))=\frac{1}{L_xL_y}\int_{\frac{-L_y}{2}}^{\frac{L_y}{2}}\int_{\frac{-L_x}{2}}^{\frac{L_x}{2}}\lambda(x, y)e^{-i(mx+ny)}\,dx\,dy \tag{37}$$

where m, L_x, n and L_y are the wave numbers and the width of the domain along the direction of x and y, respectively. Utilizing (36) and (37), (34) becomes

$$\gamma^b\equiv\frac{C^b(m,\ n)}{\tilde{C}_w(m,\ n)}$$

$$=\frac{\tilde{\beta}^2k^2}{(\tilde{\beta}^2k^2+\tilde{\alpha}^2)k^2p_0+\frac{1}{p_0}}$$

where $k^2=m^2+n^2$,

$C^b(m,n)$ is the Fourier transform of λ_b, and $\tilde{C}_w(m,n)$ is the Fourier transform of $\tilde{\omega}_t$. Similarly, from (31), we have

$$\gamma_w^b\equiv\frac{C_w^b\ (m,n)}{\tilde{C}_w\ (m,\ n)}$$

$$=1-\frac{p_0\tilde{\beta}^2k^4}{(\tilde{\beta}^2k^2+\tilde{\alpha}^2)kp_0-\frac{1}{p_0}},$$

where $C_m^b\ (m, n)$ is the Fourier transform of ω_t^b, and $C_m^\phi\ (m, n)$ is the Fourier transform of ω_t^ϕ.

In spite of the value of $\tilde{\alpha}$, γ_m^b approaches 1 and γ^b approaches zero as $\tilde{\beta}$ approaches zero for any m, and n. It implies that $C_m^b\ (m,\ n)$ approaches $\tilde{C}_m(m,n)$ and λ_b approaches zero i. e., no filtering of the ω_t^bfield. It is always true even if p' is not negligibly small. On the other hand, as $\tilde{\beta}$ becomes very large, we have

$$\gamma^b\approx\frac{1}{p_0k^2},$$

and

$$\gamma_m^b\approx 0.$$

The above equations show that the yalues of γ^b are dominated by long waves as $\tilde{\beta}$ becomes large. It also implies that $\omega_b{}'$ approaches zero as $\tilde{\beta}$ approaches infinity.

Since λ^2 is a constant, the combination of (32) and (35) implies

$$\omega_t^\phi=0,$$

identically. The above equation indicates that when p' is small, most of the adjustment of the vertical velocity (or mass convergence) is due to the $\omega_b{}'$ part. It can be shown that when $\tilde{\beta}$ is zero, the adjustment is very small, provided a reasonable value of $\tilde{\alpha}$ (e. g., $\tilde{\alpha}=0.1$) is utilized.

IV. SPECIAL CASES

Case a. If $\tilde{\alpha}$ and $\tilde{\beta}$ are both zero, (9) reduces to

$$\lambda_1=\lambda_2\ (p_s-p_t).$$

If above equation is substituted into (7) and (8), and the results are substituted into (2), we get

$$\omega_t=\tilde{\omega}_t+(p_s-p_t)\lambda_2\nabla^2(p_s-p_t) \tag{38}$$

Then, the substitution of (38) into (3) leads to

$$\lambda_2=-\frac{\tilde{\omega}_t}{[(\overline{p_s-p_t})\overline{\nabla^2(p_s-p_t)}]}$$

Eq. (38) implies that if (p_s-p_t) is a constant, ω_t is equal to $\tilde{\omega}_t$. In this case, the adjustment of $\tilde{\omega}_t$ is impossible. In other words, the horizontal curvature of the (p_s-p_t) field is the only mechanism to adjust the observation field such that the continuity equation and the global upper boundary condition of vertical p-velocity are satisfied.

Case b. If $\tilde{\beta}$ is zero and $\tilde{\alpha}$ is very large, (22) becomes

$$\nabla^2\lambda_b=0$$

Because λ_b is zero along the boundary, the solution of the above equation is simply

$$\lambda_b=0,$$

identically, and (18) and (17) may be written as

$$\nabla^2\lambda_1=-\frac{\lambda_2}{\tilde{\alpha}^2(p_s-p_t)} \tag{39}$$

$$\omega_t=\tilde{\omega}_t-\lambda_2/\tilde{\alpha}^2$$

The above two equations imply

$$\lambda_2=\tilde{\alpha}^2\overline{\tilde{\omega}_t} \tag{40}$$

Since

$$\omega=\omega_s-\int_{p_s}^{p}\nabla\cdot\vec{v}\,dp,$$

and

$$\tilde{\omega}=\omega_s-\int_{p_s}^{p}\nabla\cdot\tilde{\vec{v}}\,dp,$$

we have

$$\begin{aligned}\omega-\tilde{\omega}&=-\int_{p_s}^{p}(\nabla\cdot\vec{v}-\nabla\cdot\tilde{\vec{v}})\,dp\\&=-\int_{p_s}^{p}\nabla^2\lambda_1\,dp\\&=-\left(\frac{p_s-p}{p_s-p_t}\right)\overline{\tilde{\omega}_t}\end{aligned} \tag{41}$$

(41) is the differential form of O'Brien's formulation (1970). Because the correction velocity field is irrotational, the optimized wind field can be determined after the correction velocity potential is determined from (39)

and (40).

Case c. If $\bar{\beta}$ approaches infinity, then for any bound $\bar{\alpha}$, (22) and (31) imply

$$\nabla^2\omega_i^b=0,$$

provided ω_i^b and λ_b are bounded. Substitution of the boundary condition (33) leads to

$$\omega_i^b=\text{constant}. \tag{42}$$

Combination of (31) and (42) yields

$$\nabla^2\lambda_b=-\frac{\bar{\omega}_i}{p_s-p_i}+\frac{\text{constant}}{p_s-p_i}.$$

Furthermore, from (23) we have

$$\nabla^2[(p_s-p_i)\nabla^2\phi]=0,$$

or

$$\nabla^2\omega_i=0,$$

by the use of (32). From the boundary condition (33), we have

$$\omega_i^\phi=\text{constant}, \tag{43}$$

or

$$\nabla^2\phi=\frac{\text{constant}}{p_s-p_i}$$

Substitution of (42) and (43) into (30) leads to $\omega_i=$constant. Then, applying the strong constraint (3), we get $\omega_i=0$, identically. Therefore, Eq. (17) reduce to

$$\nabla^2\lambda_1=-\frac{\bar{\omega}_i}{p_s-p_i}.$$

The above equation is exactly McGinley's formulation (1973).

VI. TESTS

a. Objective analysis

In order to investigate the plausibility and applicability of the variational scheme, NASA Atmospheric Variability Experiment (AVE II) data are utilized and the results are discussed in this section. However, because the scheme requires an objective analysis to interpolate values of wind to regularly spaced grid points from irregularly spaced observation points, an objective analysis method is described at first. The weighting function utilized in the objective analysis should account for the observational resolution and real patterns of the data to avoid any unnecessary errors. Because the large-scale

data field is anisotropic and nonhomogeneous, any isotropic or homogeneous weighting function will distort the data field and the unrealistic patterns may occur (McFarland, 1974). In this study, Inman's (1970) elliptic weighting function and Barnes' exponential weighting function (Barnes, 1973) are combined to produce

$$W(r,k) = exp\{-\frac{\alpha^2-(\alpha^2-1)\cos^2\theta}{\alpha^2 k^2} r^2 - \frac{t^2}{\nu}\}, \tag{44}$$

where

$$k^2 = -\frac{b^2}{\ln W_b}$$

r is the distance between the grid point and the observation point, b is the length of the minor axis of an ellipse of constant weight, θ is the angle between the wind direction and the direction from the grid point to the observation point, W_b is the weight when r is equal to b and θ is 90 deg, t is the time difference from a reference time, ν is a constant and α is the ratio of the length of major axis to that of the minor axis b of an ellipse of constant weight. In this study, α is chosen as

$$\alpha = a\frac{V}{V_{max}} \tag{45}$$

where V is the wind speed at the observation point, V_{max} is the maximum value of the observed wind, and a is a specified constant.

After the computation of the weighting function from (44) at each grid point, the value of a quantity X_{ij} at the grid point (i, j) is assigned as

$$X_{ij} = \frac{\sum^m W(r_m,k)X_m}{\sum^m W(r_m,k)}, \tag{46}$$

where X_m is the value of the quantity X at the m-th observation point.

In order to better describe the meteorological fields near a frontal zone, the interpolation scheme is utilized twice. In the vicinity of a front, the stations whose winds make a large angle with the wind at a grid point may be separated from the grid point by the front. After the first conventional interpolation, the wind is assigned at each grid point and the angle between the wind at a station and the wind at a grid point can be determined. During the second interpolation, any stations whose wind make an angle with the wind at a grid point greater than 90 degrees are not utilized in determining the analysis at the grid point. This procedure tends to conserve discontinuities, and is valuable especially near frontal zones.

b. Tests of optimization scheme. Data are from the second NASA Atmospheric Variability Experiment (AVE II). There were fifty-four

rawinsonde stations participating in the AVE II Pilot Experiment. Soundings were made at three-hour intervals at each station beginning at 1200 GMT 11 May 1974, and ending at 1200 GMT 12 May 1974. The data were obtained during a period when convective activity was present, large horizontal temperature gradients were evident and rapid changes in weather patterns were occurring. The data area is over the eastern United States east of approximately 105° W longitude. Radar data were obtained from eleven stations located near the center of the observational area, and as much data as possible were collected from the NIMBUS 5, NOAA-3, ATS-3, and DMSP (DAPP) satellites.

The synoptic situation of 2100 GMT 11 May 1974 is shown in Figs. 1-6. There is a cold front across the central part of the country and a warm front extends through the northern states. Three lows and two precipitation areas appear on the map at the analysis time. Also, there is a deep trough in the upper levels extending from north to south across the central United States.

The grid system is shown in Fig. 7; the polar stereographic projection is utilized. The standard latitude and the standard longitude are 60°N and 100°W, respectively. The 11 by 13 computation grid is oriented so that the y-axis is perpendicular to the standard longitude. The map scale is 1:15,000,000, the upper-left-hand corner grid point is located at $x=12.6$ in and $y=0.97$ in (the origin is at the North pole), and the grid interval is 190.5km on the image plane.

The interpolation scheme is described in part a. The parameters a, k and ν in (45) and (44) are $\sqrt{8}$, 0.9772, and 2, respectively. During the second interpolation, the weighting function W_2 is assigned as $W_2=W_1\cos\phi$, where ϕ is the angle between the wind at observation stations and the wind at grid points, and W_1 is the weighting function of the first interpolation determined from (44). After interpolation of wind velocity to grid points, mass divergence are computed utilizing a fourth-order finite-difference approximation. The vertical p velocity, $\bar{\omega}$, is determined at each grid point by integration of the continuity equation from the surface; its surface value is determined from (5). Results are shown in Figs. 8-14. The values of $\bar{\omega}$ at the surface are very small (10^{-5}mb $\sec^{-1}$); the patterns reflect the synoptic situation and orographic lifting. Because of the accumulative errors in the divergence fields, the $\bar{\omega}$-fields at higher levels are highly unrealistic, both in pattern and in

magnitude. For example, the $\tilde{\omega}$ patterns don't clearly reveal the areas of upward and downward motion associated with the two troughs in the upper levels, and the magnitudes of the $\tilde{\omega}$ values are incredibly large, especially at the 100-mb level.

Before the optimization of the wind field, let us investigate several numerical examples of the response function shown in Fig. 15. Generally speaking, for synoptic-scale systems, errors in the velocity field are of the order of 10 percent and errors in the $\tilde{\omega}$ field may be ten times larger. In other words,the reliability of the velocity field may be ten times larger than that of the $\tilde{\omega}$ field, and, therefore, $\tilde{\alpha}$ may be chosen as 0.1 in the optimization scheme. Since the wavelength of resolvable waves is about 600 km and the width of the area considered is about 2,000km, waves whose wave number is less then three should be suppressed. Also, for the synoptic situation under study, the distance between adjacent extrema in the vertical motion field is between 700 and 1,000km. Therefore, the most important waves are those of wave number one or two, and the value of is chosen as 0.3 in this study.

The optimization of the wind field is performed and the results are shown in Figs. 16-21. From 500mb up to the 100-mb level, the optimized ω fields clearly reveal a major trough across the central United States and a minor trough across the southwestern portion of the country. To the east of the major trough, strong upward motion exists and to the west of the major trough strong downward motion is evident in the optimized ω fields. Also, there is a small area of upward motion associated with the minor trough in the southwestern United States. All these features were ambiguous before the optimization was accomplished. Also, the values of ω are reduced to reasonable magnitudes by the optimization. Compared to the National Weather Service radar chart for 2035 GMT 11 May 1974, the area of upward motion coincides with the region of deep convection.

VII. CONCLUSIONS

The main objective of this paper is to develope a variational optimization scheme of wind field to correct vertical velocity field using kinematic method. The errors which appear in the vertical velocity field are classified as systematic errors and random errors. The systematic errors are suppressed by the use of two strong constraints, i.e., the integrated continuity equation

and the global boundary condition, and the random errors are filtered by including a low-pass filter simutaneously in the variational formulation that the filtered field still satisfies above constraints. The most important feature of this scheme is that the unknown upper boundary values of the ω field become solvable by consideration of spatial distribution of upward and downward motions. Also, because the functional includes the velocity field and the ω field, the procedure insures that both fields are optimized. Each condition and procedure is physically and mathematically understandable; therefore, the scheme can be assumed to be realistic with a high degree of confidence.

NASA AVE II data are utilized to verify this scheme. Results show that the upward motion prevails over the area of surface cyclone (to the east of upper trough) with the maximum intensity of 10 μb sec^{-1} at 400mb level to the northeast of surface center, and the downward motion prevails in the area of surface unticyclone to the west of upper trough with the maximum intensity of -6 μb sec^{-1} at 400mb level to the east of surface center. Also, there is a weak upward motion over the area to the east of a minor trough with the maximum intensity of 1 μb sec^{-1} at 500 mb level. The magnitudes and general patterns are in good agreement with the synoptic weather maps and radar reports.

The scheme developed in this study is quite general that it may be utilized to analize various weather systems. The test of the applicability of this scheme in meso-scale weather system with severe convection may be interesting in the future.

ACKNOWLEDGMENTS. This research was supported by the George C. Marshall Space Flight Center, Contract NAS8-31333, and was directed by Dr. Rex L. Inman. Support was also received from the National Science Council, Republic of China.

I wish to express my deep gratitude and appreciationto Dr. Rex L. Inman for his constant support, encouragement, assistance and convincing suggestion. I also wish to thank Dr. Y. K. Sasaki, Dr. J. S. Fein, Dr. J. F. Kimpel, Dr. E. F. Blick and Dr. M. Jischke for their encouragement and helpful suggestions. Appreciation must be extended to my fellow graduate students, Adrian Ritchie, Richard Hodur, Walter L. F. Chang, Main Hutcheson, and Alvina Hutcheson for reading the manuscript and offering helpful discussion. I wish to thank Jo Ann Oberst for her expert typing of the manuscript.

REFERENCES

Barnes, S. L., 1973: Mesoscale objective map analysis using weighted time-series observations. NOAA Technical Memor andum ERL, NSSL-62.

Inman, R. L., 1970: Papers on operational objective analysis schemes at the National Severe Storms Forecast Center. NOAA Technical Memoran dum ERLTM-NSSL 51.

Kung, E. C., 1973: Note on design of an optimized computation scheme for kinematic vertical motion field. Mon. wea. Rev., **101**, 685-690.

Lateef, M. A., 1967: Vertical motion, divergence, and vorticity in the troposphere over the Caribbearn, August 3-5, 1963. Mon. Wea. Rev., **95**, 778-790.

McFarland, M. J., 1974: Variational optimization analysis of temperature and moisture advection in a severe storm environment. Ph. D. Dissertation, Dept. of Meteor., University of Oklahoma.

McGinley, J. A., 1973: Environmental energy fields associate with severe storms. M. S. Thesis, Dept. of Meteor., University of Oklahoma.

O'Brien, J. J., 1970: Alternative solutions to the classical vertical velocity problem. J. Appl. Meteor., **9**, 197-203.

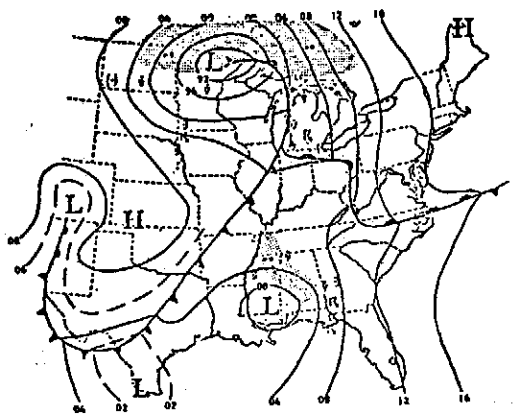

Fig. 1. Surface chart for 2100 GMT 11 May 1974. Isobars are drawn at 4mb intervals.

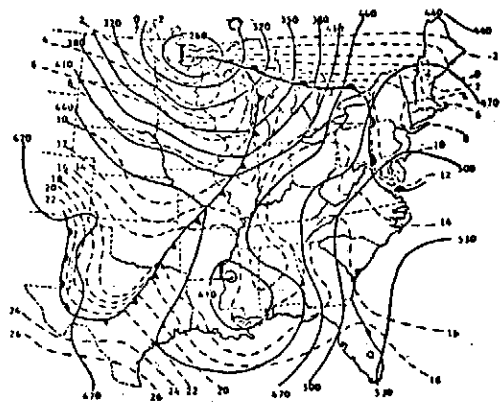

Fig 2. 850mb chart for 2100 GMT 11 May 1974. Height(solid) contours are drawn at 30m intervals. Isotherms (dashed) are constructed at 2°C intervals.

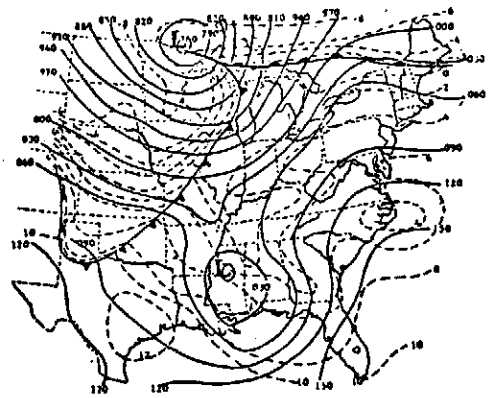

Fig. 3. Same as 2 except for 700mb.

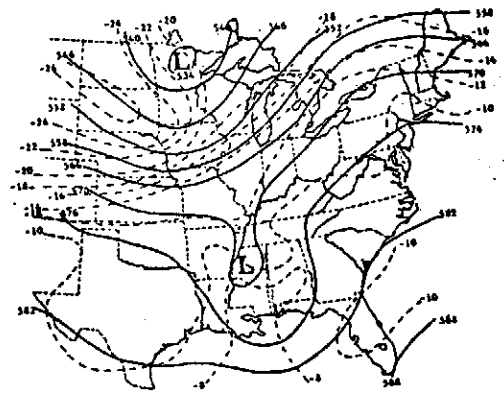

Fig. 4. Same as Fig. 2 except for 500mb with contours drawn at 60m intervals.

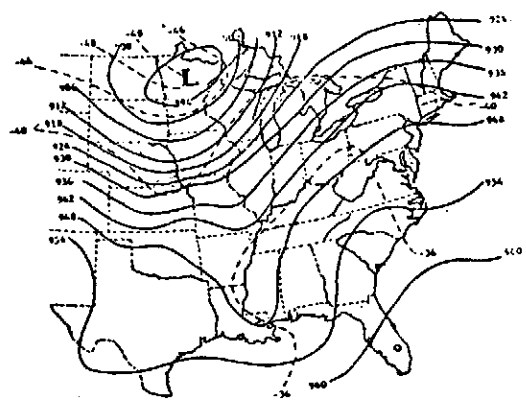

Fig. 5. Same as Fig. 2 except for 300mb with contours drawn at 120m intervals and isotherms constructed at 4°C intervals.

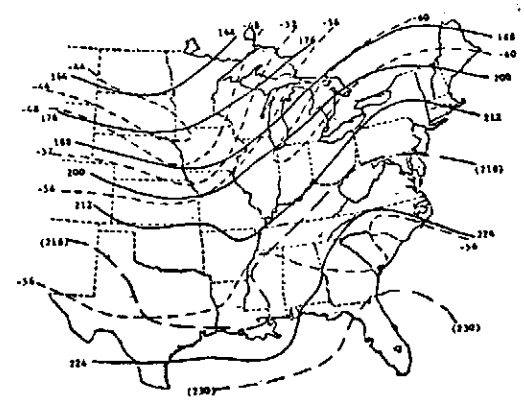

Fig. 6. Same as Fig. 2 except for 200mb with contours drawn at 120m intervals and isotherms constructed at 4°C intervals.

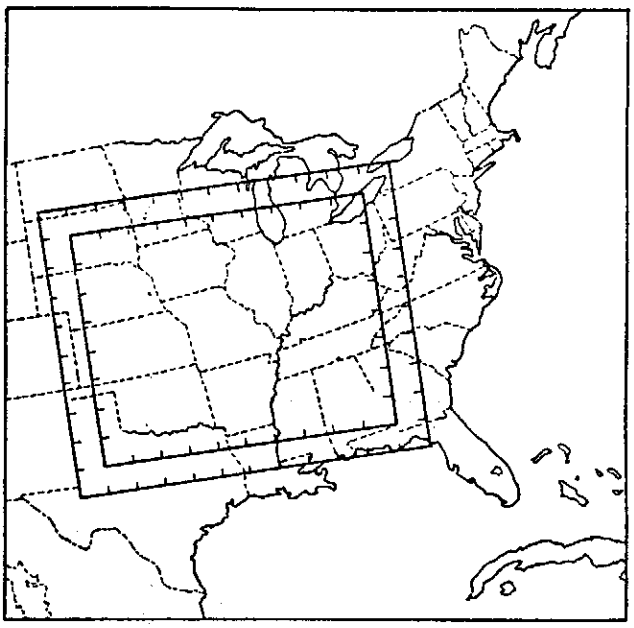

Fig. 7. Data grid and interior working grid.

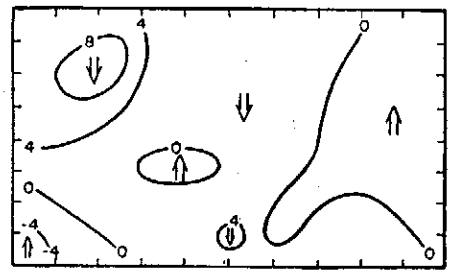

Fig. 8. Vertical velocity, $\omega=dp/dt$, at surface before optimization. Isolines are drawn at intervals of 0.4μb sec^{-1}. Positive values refer to decent; negative values refer to ascent.

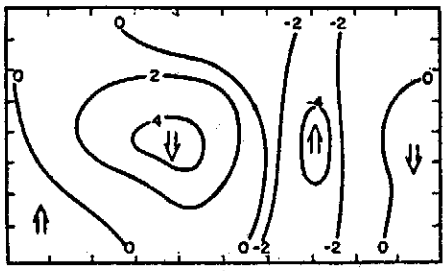

Fig. 9. Same as Fig. 8. except for 800mb with isolines drawn at intervals of 2 μb sec^{-1}.

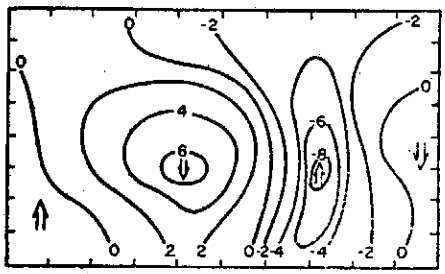

Fig. 10. Same as Fig. 9. except for 700mb with isolines drawn at intervals of 2 μb sec^{-1}.

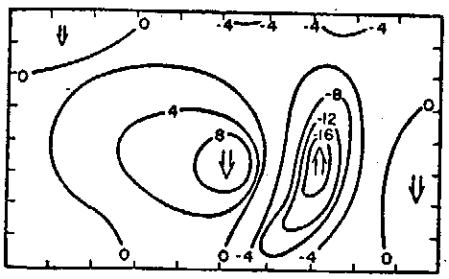

Fig. 11. Same as Fig. 8. except for 500mb.

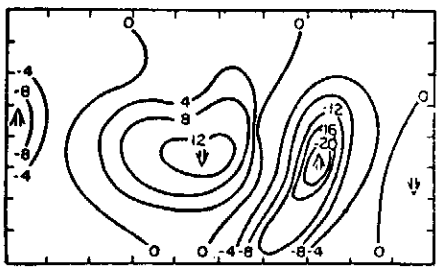

Fig. 12. Same as Fig. 11. except for 300mb.

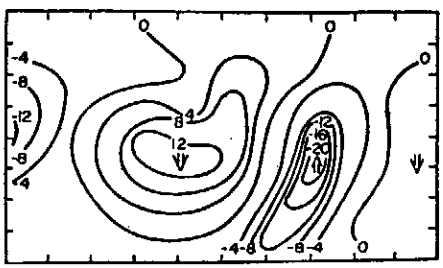

Fig. 13. Same as Fig. 11. except for 200m .

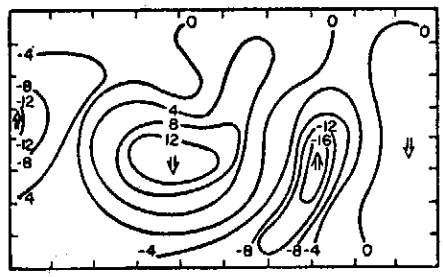

Fig. 14. Same as Fig. 11. except for 100mb.

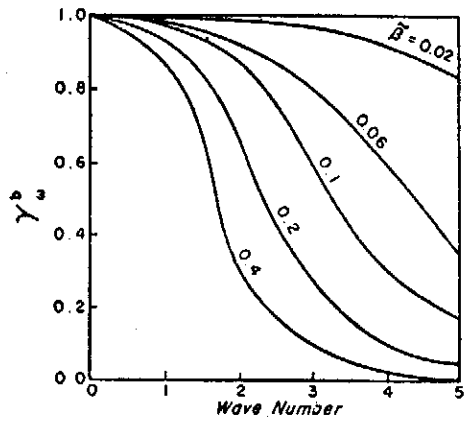

Fig. 15. The response function for $\tilde{\alpha}$=0.1.

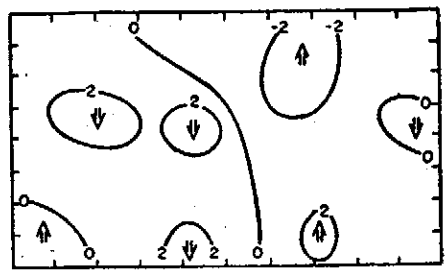

Fig. 16. Optimized vertical velocity, omega, at 800mb with isolines drawn at intervals of 0.2μb sec^{-1}.

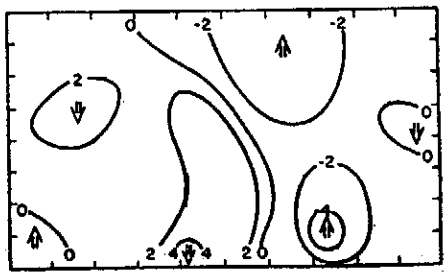

Fig. 17. Same as Fig 16. except for 700mb with isolines drawn at intervals of 2 μb sec^{-1}.

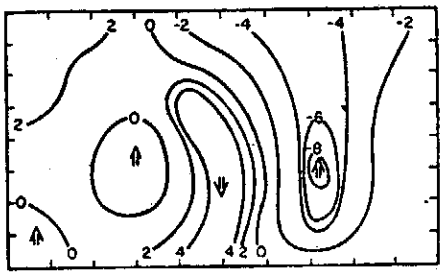

Fig. 18. Same as Fig. 17 except for 500mb.

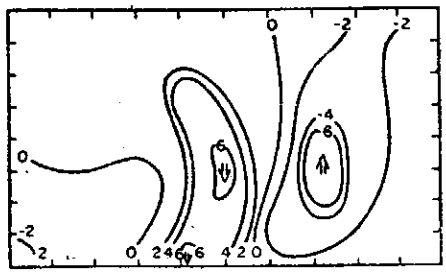

Fig. 19. Same as Fig. 17. except for 300mb.

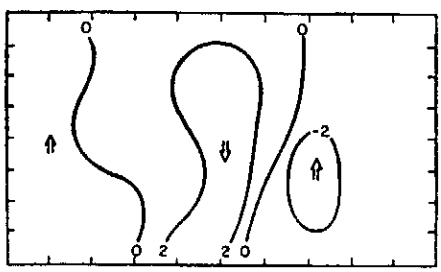

Fig. 20. Same as Fig. 17. except for 200mb.

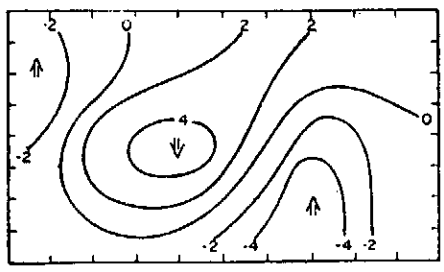

Fig. 21. Same as Fig. 16. except for 100mb with isolines drawn at intervals of 0.02μb sec^{-1}.

Annual Report of the Institute of Physis, Academia Sinica, Vol. 6, 1976

The Diagnostic Analysis and Modifications of Kuo's Parameterization of Cumulus Convection In Middle Latitudes

Wen-Jey Liang*

Department of Meteorology, University of Oklahoma
Norman, Oklahoma, U. S. A.

Abstract

In this study, the applicability of Kuo's parameterization of cumulus convection in the middle latitudes is examined, and a modification of his theory is developed. An evaluation of Kuo's scheme is performed to reveal physical insight into the involved mechanisms through a combination of the large-scale heat and moisture budgets and Kuo's formulation of the latent heat released. In order to improve upon the treatment of the interaction of deep convection with the environment, modifications consisting of considerations of the large-scale moisture supply and of the vertical transport of moisture and of dry static energy inside the cloud are made. Also, a two-layer cloud ensemble model is combined with the modified scheme. An examination of the modified scheme is performed by combining the large-scale heat and moisture budgets, and the modified formulation of the latent heat released. The modified parameterization procedures are compared with Kuo's original scheme, and the results of tests of both schemes are discussed.

I. INTRODUCTION

Over many regions in the middle latitudes as well as in the tropics, cumulus convection plays an important role in vertical transport of heat, moisture and horizontal momentum, especially in the warm season (Palmen and Newton, 1969). In these regions, a large portion of the annual precipitation is derived from convective showers and thunderstorms; these storms also account for the greatest weather damage in many areas. Convective systems also are of particular interest because they manifest perhaps the most obvious interaction between disturbances of large and small (or medium) scales. However, because of insufficient resolution of the present observational network, this mechanism must be parameterized in terms of large-scale variables. In the past decade, many parameterizations of cumulus convection have been developed. Each scheme has served surprisingly well

* Present affiliation: National Taiwan University, and Institute of Physics, Academia Sinica, Taipei, Taiwan, R.O.C.

in the particular numerical model in which it has been employed. However, because many investigators believe that cumulus convection is a dominant mechanism in the tropics (Riehl and Malkus 1958), most procedures have been developed for this region. We hardly can expect these schemes to fit our needs in middle latitudes without some modifications.

Currently, two types of cumulus parameterizations are used. One, based on the hypothesis of convective adjustment (Manabe et al., 1965), is utilized in general circulation models and synoptic-scale prediction models. The idea of convective adjustment is based on the assumption that thermal convection develops when the lapse rate of temperature exceeds a certain neutral value. The other, based on the hypothesis of penetrative convection (Ooyama, 1964; Kuo, 1965; Arakawa, 1969), is also utilized in general circulation models; but the scheme is primarily applied to the study of the deveopment of tropical cyclones (Yamasaki, 1968; Ooyama, 1969). Penetrative convection is assumed to occur when cumulus clouds penetrate deeply into an unsaturated atmosphere in areas of low level mass convergence. Although both types of cumulus parameterization have practical significance, the latter appears to be more feasible for our purpose, because the hypothesis of penetrative convection is pertinent for middlelatitude deep convective systems and it can be used to simulate cloud ensembles after some modifications are made. From the simulation of such an ensemble, one can obtain a great deal of information on the statistical properties of the cloud clusters and a deeper understanding of the dynamical mechanisms involved.

Based on the hypothesis of penetrative convection, the parameterization procedure consists of two significant mechanisms involved in the interaction between convection and the environment: 1) adiabatic warming due to the downward motion of the environmental air which compensates for the upward motion inside convective elements, 2) lateral mixing of cloud substance into the environment. Among such parameterization schemes, those developed by Kuo (1965, 1974) and Arakawa (1969, 1974) are two of the most representative. Kuo's scheme is based on a non-steady deep cumulus model; the temperature of environment, and the large-scale low-level convergence of moisture are the key indicators. Arakawa's scheme is based on the concept of a balance of the vertical mass transport in the clouds and the environment. Although several authors, such as Ooyama (1971) and Fraedrich (1973, 1974), have developed a theoretical framework to include these mechanisms and to discuss the

relationship between these schemes, some confusion still exists (e. g., Ceselski, 1974). It has been stated that Kuo has neglected the heating by adiabatic compression of the slowly descending environment. Also, the reality of the horizontal mixing process involved in his scheme has been questioned. Recently, Kuo (1974) tried to clarify those misunderstandings; however, it is believed that if in Kuo's formulation the terms which account for departures from the area mean, as well as the precipitation terms, are examined carefully, a better explanation can be given.

Kuo's scheme is applicable in those situations where a deep conditionally unstable layer and large-scale low-level convergence are in existence. The former condition makes it possible for huge cumuli to penetrate into the upper troposphere and the lower stratosphere, while the latter condition provides a lifting mechanism to trigger the convective instability. Therefore, in some situations, although the computed fractional area of coverage may be near unity, only shallow or even no clouds may develop. Investigations of moisture convergence and its relationship to severe storm occurrence (e. g., Sasaki 1973) indicate that unstable conditions, downward momentum transport, and other factors, which may be important to thunderstorm outbreaks, are implicitly shown in the moisture convergence patterns. Because we believe that large-scale moisture convergence in a conditionally unstable region is a key mechanism in the development of deep convection, we would like to examine the applicability of Kuo's scheme and to modify it so that the scheme becomes dynamically and practically plausible.

II. GOVERNING EQUATIONS FOR EVALUATING CUMULUS PARAMETERIZATION SCHEMES

Described in the following paragraphs is a procedure for examining and evaluating the mechanisms involved in Kuo's (1965) parameterization scheme and in the modified scheme to be specified later. The method is based on the concept that utilization of an accurate expression for the latent heat released by cumulus should lead to good evaluations of other characteristics of the cloud ensemble. It will be shown below that when Q_c, the latent heat released by cumulus, is expressed in terms of certain cloud ensemble properties, the cloud ensemble properties may be determined from the large-scale budget equations if the time derivatives of dry static energy and mixing ratio in the environment is specified. In other words the cloud

ensemble properties computed from this procedure should directly reflect the quality of the expression, for the latent heat released, which is utilized in the parameterization scheme. Furthermore, if the large-scale budgets and the parameterization scheme are both perfect, the latent heat released, as computed from the parameterization scheme and as determined using the evaluation procedure, should be exactly the same. In the following discussion, any quantity, except the vertical velocity, in the environment is approximated by the area-mean value of that quantity (for more detail, see Appendix A).

First, let us define the dry static energy s and the moist static energy h as

$$s \equiv c_p T + gz, \text{ and}$$

$$h \equiv c_p T + gz + Lq,$$

where T is temperature, z is height, q is mixing ratio, c_p is the specific heat of dry air, and g is the acceleration of gravity. From (A.2) and (A. 3), the heat and moisture equations for the large-scale motion can be written as

$$Q_1 - Q_R \equiv \frac{d\bar{s}}{dt} - Q_R = Q_C + \frac{\partial}{\partial p}[M_C(s_c - \bar{s})], \tag{1}$$

$$-Q_2 \equiv L\frac{d\bar{q}}{dt} = -Q_C + L\frac{\partial}{\partial p}[M_C(q_c - \bar{q})], \tag{2}$$

where s_c, q_c, $\bar{s}$ and $\bar{q}$ are dry static energies and mixing rations in the cloud and in the environment, respectively, Q_R is the heating rate by radiation, L is the latent heat of condensation, p is pressure, Q_C is the latent heat released by subgrid scale convection and M_C is the cloud mass flux dedefined as $M_C = -\sigma\omega_c$, where σ is the fractional area covered by the clouds, and ω_c is the pressure velocity inside the clouds.

Also, the saturation moist static energy of the environment, $\bar{h}^*$, is

$$\bar{h}^* \doteq \bar{C}_p^* T + g\bar{z} + L\bar{q}^* \equiv \bar{h}^*,$$

where $\bar{q}^*$ is the saturation mixing ratio at temperature $\bar{T}$.
Then, after Arakawa (1969), we have

$$s_c = \bar{s} + \frac{1}{1+\gamma}(h_c - \bar{h}^*), \tag{3}$$

$$q_c = \bar{q}^* + \frac{\gamma}{(1+\gamma)L}(h_c - \bar{h}^*), \tag{4}$$

where $\gamma \equiv \frac{L}{C_p}\left(\frac{\partial \bar{q}^*_s}{\partial \bar{T}}\right)_p$.

If Q_c is expressed in terms of the other variables, combination of (1)–(4) gives four equations for the four unknowns, s_c, q_c, M_c, and h_c. They can be solved provided that the observed large-scale heat and moisture budgets over the area considered are known. The associated boundary conditions are (Yanai et al. 1973):

$$\frac{\Delta p}{g}(Q_1 - Q_R) = S_S - \frac{M_{cb}}{g}(s_{cb} - \bar{s}_b),$$

$$-\frac{\Delta p}{g}Q_2 = LE_s - \frac{M_{cb}}{g}L(q_{cb} - \bar{q}_b),$$

$$S_S/LE_S = C_p(T_s - \bar{T}_0)/[L(\bar{q}_s - \bar{q}_0)],$$

where the subscript b denotes values at cloud base and $\bar{T}_S$, $\bar{T}_0$, $\bar{q}_s$, and $\bar{q}_0$ are the temperatures and mixing ratios at the surface and at a level above which is representative of the surface boundary layer. Let us define Y as $-\overline{\omega' h'}$. Then, adding (1) and (2) and integrating the resultant equation, we get

$$Y(p) = \int_{p_t}^{p}(Q_1 - Q_2 - Q_R)\,dp,$$

$$= M_c(h_c - \bar{h}), \text{ if } p \leq p_b, \tag{5}$$

where p_t is the pressure at the top of atmosphere (100mb in this study): $Y(p_t)$ is assumed to be zero. Utilizing (5), the boundary conditions are explicitly expressed as

$$M_{cb} = \frac{a_1 - (1+\gamma_b)a_2}{\bar{h}_b^* - \bar{h}_b}, \tag{6}$$

$$h_{cb} = \bar{h}_b + \frac{a_1}{M_{cb}}, \tag{7}$$

where

$$a_1 = g(S_S + LE_S) - \Delta p(Q_1 - Q_R - Q_2),$$

$$a_2 = gS_S - \Delta p(Q_1 - Q_R),$$

and

$$S_s+LE_s=Y(p_s),$$

where p_s is surface pressure.

III. AN EXAMINATION OF KUO'S EXPRESSION FOR THE RELEASE OF LATENT HEAT BY CUMULUS

Following Kuo (1965) Q_c is specified as

$$Q_c=B(s_c-\bar{s})$$

which is (A.13), where

$$B=(1-b)\frac{\sigma}{\tau}=\frac{M_L}{M_t}(1-b) \tag{8}$$

Substitution of (A. 12) and (A. 10) into the expression for B leads to

$$B=\frac{1}{M_t}\int_0^{p_s}Q_2\frac{dp}{g}$$

Because b is computed from the local time change of $\bar{q}$, from the parameterization point of view b is unknown and must be specified experimentally. In order to avoid additional error introduced from the specification of values of b, in this study b is computed from $\partial\bar{q}/\partial t$ according to (A. 12). The same values of b are used in the computation of the release of latent heat in the parameterization schemes. The cloud base is assumed to be at the lifted condensation level representative of the surface layer, and the top of cloud is assumed to be at a level where the temperature of the clouds is equal to that of the environment.

After elimination of s_c, q_c and h_c from (1)—(4), an ordinary nonlinear differential equation is obtained:

$$\frac{dU}{dp}=F-G/U, \tag{9}$$

where

$$U=M_c\left(\frac{\bar{h}-h^*}{1+\gamma}\right)$$

$$F=Q_1-Q_R-\frac{B(\bar{h}-h^*)}{1+\gamma}-\frac{\partial}{\partial p}\left(\frac{Y}{1+\gamma}\right),$$

and $$G=\frac{BY}{(1+\gamma)^2}(\bar{h}-\bar{h}^*),$$

where Y is determined from (5) as a function of Q_1, Q_2, and Q_R, and b is defined by (A. 12).

Eq. (9) can be reduced to Abel's equation of the first kind if B is prescribed, and can be solved analytically if the ratio of the two coefficients, G and F, is constant, or it can be solved numerically even if the coefficients are variable. M_c is determined from solutions of (9). Then, according to (5) h_c can be determined by

$$h_c=\frac{Y}{M_c}+\bar{h}.$$

Next s_c and q_c are computed utilizing (3) and (4), respectively, and T_c is determined by

$$T_c=\frac{s_c-\bar{s}}{C_p}+\bar{T}.$$

Finally, Q_c may be calculated from (A. 13).

Employing the procedures described in the preceding paragraphs, calculations of M_c, h_c, T_c, q_c, Q_c, and heights of cloud tops have been made utilizing NASA AVE II data. Results of these calculations show that although radar charts prepared by the National Weather Service (2035 GMT 11 May 1974) show that the cloud tops were at about 275mb in the vicinity of the test area, the computed cloud tops are at 556mb. M_c computed from (9) is unrealistically large. For example, the values are about an order of magnitude larger than those calculated by Lewis (1975) for a thunderstorm system in central Oklahoma. Also, the latent heat released is about an order of magnitude smaller than required by the large-scale budget equations. All results show that the properties of the cloud ensemble, computed on the basis of Kuo's expression for the latent heat released, are questionable.

In his tropical prediction model, Krishnamurti (1969) treated the terms which account for departures from the area mean (i. e. vertical diffusion terms) and the precipitation terms, separately. The precipitation terms were computed utilizing an extension of Kuo's scheme, and the vertical diffusion terms were computed utilizing eddy exchange coefficients; the results seem satisfactory. However, other problems still exist. Reed and Recker (1971)

found evidence, in a composite Pacific tropical wave, of a heating maximum centered near 400mb. As mentioned by Ceselski (1974), Kuo's scheme will yield an upper tropospheric heating maximum only if unrealistically deep and hot clouds are assumed. Clouds that include entrainment and extend only to 200mb or below will generally have maximum $(\bar{T}_c - \bar{T})$ in the lower troposphere (Ceselski, 1973). This is particularly true if the disturbance in question is relatively warm in the upper troposphere, as is often the case.

Recently, Edmon and Vincent (1975) have employed Kuo's scheme, as well as the modified scheme by Krishnamurti, to calculate the latent heat released in a case involving the interaction of tropical storm Candy with an intensifying extratropical baroclinic frontal system (0000–1200GMT 25 June 1968). Comparisons between the convective latent heat released and actual precipitation rates show, in general, that Kuo's scheme and Krishnamurti's scheme fail. They state that there was very little convective latent heat released in the computational region, even though there were widespread thunderstorms during the analysis periods. Therefore, it is necessary to modify Kuo's formulation so that the modified scheme may be applied in middle latitudes.

IV. MODIFIED PARAMETERIZATION OF CUMULUS CONVECTION

Before discussing any modifications, a few statements about the cloud ensemble model proposed in this study are appropriate. Here we assume that the hydro-thermodynamic fluid properties in area σ are the same as those of the environment before the clouds form. Later, clouds form and the whole area σ is covered by clouds, and the hydro-thermodynamic fluid properties in σ are changed from values typical of the environment. During the formation period, entrainment and detrainment, condensation, evaporation, and induced subsidence in the environment may occur. The formation period can be divided into two stages; in the first stage moisture is supplied to the cloud and in the second stage condensation occurs. The conservation law for water vapor implies that there are two sources of water vapor available to produce clouds in a layer. One is the large-scale moisture spupply (i. e., the apparent moisture sink) through the lateral boundaries, and the other is vertical moisture convergence inside the cloud across the upper and lower boundaries of the layer. In other words, during the first stage, for the modified scheme, the rate of increase of mixing ratio in a layer in the cloudy

region is formulated as

$$B_q = \frac{Q_2}{L} + \frac{\partial}{\partial p}(M_c q_c). \tag{10}$$

The second term on the right-hand-side of (10) allows the low level moisture convergence to produce a high level release of latent heat. If (10) is integrated from the top of atmosphere down to the surface, we have

$$\frac{1}{g}\int_{p_t}^{p_s} B_q \, dp = -\frac{1}{g}\int_{p_t}^{p_s} \frac{\partial \bar{q}}{\partial t} dp - \frac{1}{g}\int_{p_t}^{p_s} s \nabla \cdot \vec{q}\vec{V} dp + E,$$
$$= (1-b)\, M_L.$$

The above expression is the same as that used by Kuo to determine the rate at which moisture is supplied to form clouds. During the condensation stage, a part of the moisture supplied to the cloudy region is utilized to increase the mixing ratio from $\bar{q}$ to q_c, and the other part is condensed and latent heat is released. Since the moisture required to produce a unit mass of cloud air (i. e., to increase the mixing ratio and temperature from $\bar{q}$, $\bar{T}$ to q_c, T_c) in a layer of thickness δp is $\frac{\delta p}{gL}(h_c - h)$, for the modified scheme, the production rate of cloudy air in a layer is expressed as

$$B = \begin{cases} \dfrac{B_q}{(h_c - \bar{h})/L} & \text{if } B_q > 0 \\ 0 & \text{if } B_q \leq 0. \end{cases}$$

On the other hand, the conservation law of energy implies that the latent heat released in a layer can be divided into two parts. One part is utilized to heat the air inside the cloud in that layer from $\bar{T}$ to T_c and the other part is transported to adjacent layers by the vertical motion in the cloudy region. Therefore, for the modified scheme, the latent heat released is formulated as

$$Q_c = B(s_c - \bar{s}) - \frac{\partial}{\partial p}(M_c s_c), \tag{11}$$

where $-\frac{\partial}{\partial p}(M_c s_c)$ is the vertical divergence of dry static energy in the cloudy region. The latent heat released is zero if Q_c is negative; the level where Q_c is zero is assumed to be the top of clouds. In other words, the

latent heat released is assumed to be zero at the cloud top. If M_c in (11) is zero, and B is replaced by $(1-b)M_L/M_t$, (11) is reduced to Kuo's expression for the latent heat relcased. As shown by Fraedrich (1973), Kuo did not account for the vertical mass flux inside the cloud. Comparison of (11) with (A. 13) indicates that a significant modification is that the effect of cloud mass flux on the latent heat released is included in the modified formulation.

A comparison of the modified scheme with the cloud ensemble model proposed by Yanai et al. (1973), may clarify the physical processes allowed in the modified scheme. According to Yanai (1973), if the cloud ensemble is assumed to be in quasi-equilibrium with the large-scale forcing mechanism (Arakawa and Schubert, 1974), the budget equation for heat inside the clouds may be written as

$$\frac{\partial}{\partial p}(M_c s_c)+\sum_i \varepsilon_i \bar{s}-\sum_i D_i s_{ci}+LC=0, \tag{12}$$

where ε_i, D_i and s_{ci} are entrainment, detrainment and dry static energy of the *i-th* cloud, respectively, and C is the condensation inside the clouds. Since

$$Q_c=L\ (C-e), \tag{13}$$

where e is the rate of evaporation of liquid water detrained from the clouds, combination of (11), (12) and (13) implies

$$B(s_c-\bar{s})=-\sum_i \varepsilon_i \bar{s}+\sum_i D_i s_{ci}-Le. \tag{14}$$

Eq. (14) shows that entrainment, detrainment, and evaporation are parameterized in terms of the temperature difference between the cloud and the environment and the production rate of cloud air. Furthermore, substitution of (11) into (1) leads to

$$Q_1-Q_R=-M_c\frac{\partial \bar{s}}{\partial p}-\bar{s}\frac{\partial M_c}{\partial p}+B(s_c-\bar{s}).$$

The above equation shows that the apparent heat source for the large-scale motion field, in addition to Q_R, consists of an adiabatic warming due to downward motion outside the clouds which compensates upward motion (positive M_c) inside the clouds, a cooling due to the vertical mass divergence outside the clouds which compensates the vecrtial mass convergene inside the clouds, and a warming directly due to the increasing dry static energy

inside the clouds.

For the modified parameterization scheme, in order to determine the latent heat released utilizing (11), the cloud mass flux M_c has to be determined first. A simple two-layer model, which consists of a primary and a detrainment layer, is suggested to accomplish this purpose. Except near the cloud top where a strong detrainment layer exists due to the strong negative buoyancy above the cloud top, the vertical mass convergence inside the cloud in the primary layer is assumed to be proportional to the mass convergence of the large-scale motion and to the fractional increment of moisture inside the clouds; i. e.,

$$\frac{\partial}{\partial p}M_c=\lambda M_c, \text{ where} \tag{15}$$

$$\lambda=-K_1\nabla\cdot\vec{V}+K_2\left(\frac{q_c-\overline{q}}{q_c}\right). \tag{16}$$

Indeed, (15) is similar to the conventional entrainment model.

In the detrainment layer near the top of the cloud, the cloud ensemble model is described by the following three equations:

$$0=-D+\frac{\partial}{\partial p}M_c, \tag{17}$$

$$0=-Ds_c+\frac{\partial}{\partial p}(s_cM_c)+LC, \tag{18}$$

$$0=-Dq_c+\frac{\partial}{\partial p}(q_cM_c)-C. \tag{19}$$

The latent heat released is specified as

$$Q_c=-\frac{\partial}{\partial p}(s_cM_c)+Ds_c=LC. \tag{20}$$

Eqs. (17), (18), and (19) are similar to those of the cloud ensemble model proposed by Yanai et al. (1973) except that here entrainment is assumed to be negligible compared to detrainment. Eq. (20) shows that production of cloud air is neglected. Evaporation also is neglected because the liquid water content of the clouds is very small at high levels. The solutions of (17), (18), and(19) are

$$\frac{\partial M_c}{\partial p}=D, \tag{21}$$

$$LC=-M_c\frac{\partial}{\partial p}s_c, \text{ and} \tag{22}$$

$$\frac{\partial}{\partial p}h_c=0. \tag{23}$$

Eqs. (21), (22), and (23) are three equations for four unknowns, T_c, M_c, C, and D. In this section, one more equation is introduced by assuming that the detrainment, D, is constant in the layer such that the cloud mass flux M_c is zero at the top of the clouds; i. e.,

$$D=\frac{M^*_c}{\Delta p},$$

where Δp is the depth of the detrainment layer, and M^*_c is the cloud mass flux at the bottom of the detrainment layer.

In order to make sure that the modified parameterization scheme is reasonable, the procedures described in section II will be utilized; results of this investigation will be discussed in next section. Also, the modified scheme will be compared to Kuo's (1965) scheme.

IV. TESTS OF THE PARAMETERIZATION OF CUMULUS CONVECTION

In the following paragraphs, Kuo's scheme and the modified scheme are examined by utilizing the procedures discussed in Chapter II Eq. (1)—(4) along with the associated boundary conditions are used in this examination. Since these four equations contain five unknowns, s_c, q_c, h, M_c and Q_c, an additional equation must be obtained from the formulation of latent heat released. Different formulations of Q_c provide different solutions. When Kuo's scheme is examined, Q_c is formulated according to (A. 13), and when the modified scheme is investigated, Q_c is formulated according to (11). The solutions include the latent heat released, the height of the cloud tops, and four bulk properties of the cloud ensemble, s_c, q_c, h_c and M_c. These bulk properties, the latent heat released, and the height of the cloud tops reveal physical insights of the mechanisms involved in each parameterization scheme.

After the evaluation procedure is completed, the latent heat released by cumuli will be determined directly, utilizing both parameterization schemes. The computed latent heat released will be compared to the observations, i. e., to the precipitation which is required by the large-scale budgets, and to the solutions obtained by utilizing the evaluation procedures specified in the preceding rections.

The Diagnostic Analysis and Modifications of Kuo's Parameterization of Cumulus Convection In Middle Latitudes

All data are from the second NASA Atmospheric Variability Experiment, (AVE II) except for the radiation data. There were fifty-four rawinsonde stations participating in the AVE II Pilot Experiment as shown in Fig. 1. Soundings were made at three-hour intervals at each station beginning at 1200 GMT 11 May 1974, and ending at 1200 GMT 12 May 1974. The data were obtained during a period when convective activity was present, large horizontal temperature gradients were evident and rapid changes in weather patterns were occurring. The data area is over the eastern United States east of approximately 105°W longitude. Radar data were obtained from eleven stations located near the center of the observational area, and as much data as possible were collected from the NIMBUS 5, NOAA-3, ATS-3, and DMSP (DAPP) satellites.

The radiation climatological data are from Rodger's results (1967), which are available in the region 0−70N, 1000−10mb, and for the months of January, April, July and October. Because the AVE II pilot experiment was held in May, an average of the data for April and July will be utilized in this research.

The synoptic situation of 2100 GMT 11 May 1974 is shown in Figs. 2 and 3. We choose this particular time because a deep conditionally unstable layer exists over a wide area of the southern United States. There is a cold front across the central part of the country and a warm front extends through the northern states. Three lows and two precipitation areas appear on the map at the analysis time. Also, there is a deep trough in the upper levels extending from north to south across the central United States.

The grid system is shown in Fig. 4; the polar stereographic projection is utilized. The standard latitude and the standard longitude are 60°N and 100°W, respectively. The 11 by 13 computational grid is oriented so that the y-axis is perpendicular to the standard longitude. The map scale is 1:15,000,000, the upper-left-hand corner grid point is located at $x=12.6$ in and $y=0.97$ in (the origin is at the North pole), and the grid interval is 190.5km on the image plane.

The schemes for the interpolation of each field variables from stations to grid point and the optimization of wind velocity are exactly the same as those in Liang 1976; the values for each paramter in these schemes are also the same.

The tests are performed at grid point (8, 9) where a deep unstable layer

exists from the lifted condensation level of the surface layer up to the 100-mb level. The horizontal diffusion terms $\overline{\nabla\cdot\vec{V}'s'}$ and $\overline{\nabla\cdot\vec{V}'q'}$ are computed by the use of nonlinear horizontal diffusion coefficients similar to those used by Smagorinsky et al. (1965) and Manabe et al. (1965); i. e.,

$$\overline{\nabla\cdot\vec{V}'s'} = \nabla\cdot(K_s \nabla \bar{s})$$

$$\overline{\nabla\cdot\vec{V}'q'} = \nabla\cdot(K_q \nabla \bar{q}),$$

$$K_q = K_s = \frac{1}{2}k_0^2\Delta^2(D_1^2+D_2^2)^{1/2},$$

where

$$D_1 = \frac{\partial \bar{u}}{\partial x} - \frac{\partial \bar{v}}{\partial y},$$

$$D_2 = \frac{\partial \bar{v}}{\partial x} + \frac{\partial \bar{u}}{\partial y},$$

k_0 is the Karman constant (0.4 in this study), and Δ is the grid length. The results show that values of these horizontal diffusion terms are one or two orders of magnitude smaller than those of the apparent heat source, Q_1, and the apparant moisture sink, Q_2. The local time changes of the dry static energy and the mixing ratio are determined from observations at 1800 GMT and at 2400 GMT 11 May 1974. Results show that. these two terms are not negligible. The divergence field and the ω field are optimized according to the procedures described tn Liang 1976, and are shown in Figs. 5 and 6. The lifted condensation level is computed according to Inman's approximate formula (1969). The temperature $\bar{T}$, the mixing ratio $\bar{q}$, the dry static energy $\bar{s}$, the moist static energy $\bar{h}$, the saturation moist static energy $\bar{h}^*$, th apparent heat source $\bar{Q}_1$, the apparent moisture sink $\bar{Q}_2$, the radiation $\bar{Q}_R$, and the derived vertical eddy heat flux Y are shown in Figs. 7-11. Because of the large horizontal gradients of moisture and temperature in the middle latitudes, the apparent heat source, the apparent moisture sink, and the derived vertical eddy heat flux are about three to five times larger than those of the tropics as determined by Yanai et al. (1973).

In order to obtain a better comparison between the observations and the results computed from the parameterization schemes, the required precipitation is determined from the large-scale heat and moisture budgets as follows. Let

us assume that the vertical eddy heat flux and the vertical eddy moisture flux is zero at the cloud tops, i.e.,

$$M_c(s_c-\overline{s})_{p=p_t}=0,$$

$$M_c(q_c-\overline{q})_{p=p_t}=0.$$

Then, integration of (1) leads to

$$\frac{1}{g}\int_{p_t}^{p_s}(Q_1-Q_R)dp=LP_0+S_s, \tag{24}$$

where P_0 is the total precipitation inside the clouds, and S_s is the rate of transport of sensible heat from the surface. Since the observed tops of clouds are near 275 mb, computations based on the large-scale heat and moisture budgets indicate that the required P_0 is 0.08 in hr^{-1}. This amount of precipation is reasonable compared with observations from the National Weather Service radar charts (2035 GMT 11 May 1974) and Service A teletype reports.

In the evaluation of Kuo's parameterization scheme M_c is determined from (9) and B is specified by (10). Because the production rate of cloud air, B, depends on M_c, the equations are nonlinear integral-differential equations. A Runge-Kutta method and an iterative technique are utilized to solve the set of equations. The solutions are shown in Figs. 12-15 From these results and (24) the precipitation rate is 0.00966 in hr^{-1}, and the cloud top is at 556 mb. Compared to observations, the computed precipitation is one order of magnitude smaller than that observed, and the top of the cloud is about 300 mb lower. Furthermore, the cloud mass flux M_c and the residual mass flux in the environment, $\tilde{M}$, are unrealistically large. These unsatisfactory results may be understood by the following discussion.

Let us rewrite (1) and (2) as follows:

$$Q_c=Q_1-Q_R-\frac{\partial}{\partial p}[M_c(s_c-\overline{s})] \tag{25}$$

$$Q_c/L=Q_2/L+\frac{\partial}{\partial p}[M_c(q_c-\overline{q})]. \tag{26}$$

The first two terms on the right-hand-side of (25) indicate that a part of the latent heat released in a layer is utilized to heat the atmosphere in that layer, and the third term denotes that the other part of the latent heat released is utilized to heat the air in the adjacent layers by means, of the vertical motion inside the clouds. The first term on the right hand-side of (26) indicates that a part of the precipitation in a layer comes from

condensation of water vapor in that layer, and the second term shows that the other part of the precipitation comes from the moisture of adjacent layers by means of the vertical motion in the clouds. In other words, latent heat is released as condensation occurs and the dry static energy in a layer is increased. At the same time the vertical eddy flux terms account for the redistribution of moisture and dry static energy. However, because of large horizontal gradients of temperature and moisture in the middle latitudes, the apparent heat source, Q_1, and the apparent moisture sink, Q_2, are very large and $(s_c-\bar{s})$ and $(q_c-\bar{q})$ are very small. The vertical eddy flux terms may transport the required energy and moisture only when the vertical mass divergence (or convergence) inside the cloud, $\frac{\partial M_c}{\partial p}$, is extremely strong. In other words, the cloud mass flux must increase rapidly with height. According to (3) and (5), the cloud temperature can be expressed in terms of M_c, Y, and large-scale variables as

$$T_c=\bar{T}+\frac{1}{C_p(1+\gamma)}\left[\frac{Y}{M_c}-L(\bar{q}^*-\bar{q})\right].$$

From the above equation, it can be seen that as M_c increases the cloud temperature decreases. When M_c is sufficiently large that

$$M_c>\frac{L}{Y}(\bar{q}^*-\bar{q})$$

the cloud temperature will be less than that of the environment. In other words, the rapid increase of M_c with height decreases the cloud temperature and, therefore, suppresses the vertical development of the cloud. This phenomena is verified by the low tops of clouds and the large cloud mass flux in the solutions of the examination of Kuo's scheme. The discussions indicate that a suitable modified scheme should consist of a better mechanism to transport energy and moisture vertically.

The equations and associated boundary conditions utilized in testing the modified parameterization scheme are the same as those used in testing Kuo's scheme except that the latent heat released is formulated according to (11). The equations are nonlinear ordinary differential equations, and a Runge-Kutta method is utilized to solve them. The solutions are shown in Figs. 16-18. From these calculations and (24), the precipitation rate is 0.075 in hr^{-1}, the tops of clouds are at 260 mb, ahd the maximum latent heat released is at 450 mb. These results agree evry well with the observed values.

In order to better explain the improvement of the modified scheme, let us decompose the total latent heat released, as given by (11), into three components as shown below:

$$Q_c = Q_2 \frac{s_c - \bar{s}}{(h_c - \bar{h})} + \frac{L(s_c - s)}{h_c - \bar{h}} \frac{\partial}{\partial p} (M_c q_c) - \frac{\partial}{\partial p} (s_c M_c) .$$

Each term on the right-hand-side of the above equation is evaluated and the results are plotted in Fig. 19. The first component is due to the large-scale moisture convergence, the second is due to the vertical transport of moisture inside the cloud, and the third represents the vertical divergence of the dry static energy. These three components are nearly equal in magnitude. Therefore, the latent heat released in a layer may not be confined to that layer; the vertical transport of released latent heat is a significant mechanism involved in cumulus convection. Because of the third term, the maximum of the latent heat released is at the 450-mb level. In order to gain insight of the physical meaning of this component, let us consider a special case. If the apparent heat source, Q_1, is negative such that the rate of increase of moisture in a layer inside the cloud, B_q, is zero, i. e.,

$$Q_2/L = -\frac{\partial}{\partial p} (M_c q_c), \tag{27}$$

and (11) becomes.

$$Q_c = -\frac{\partial}{\partial p} (M_c s_c). \tag{28}$$

In this situation, although the production rate of cloud air is zero, latent heat is still being released because of the nonzero vertical mass flux inside the clouds. The cloud acts as a machine which pumps the moisture and the dry static energy from the lower levels up to higher levels or vice versa. Also, because the freezing process may occur at the upper levels, the maximum latent heat released may be at the higher levels.

So far, examination of the modified scheme by the use of the large-scale budget equations shows that the modified formulation of latent heat released can better simulate the physical mechanisms involved in the release of latent heat. However, from the parameterization point of view, the cloud mass flux, M_c, and the cloud temperature have to be determined first in order to utilize the modified scheme to compute the release of latent heat. In this section, M_c is computed according to (15) and (16). Utilizing 1000 mb as the pressure scale and 10^{-4} sec^{-1} as the velocity divergence scale, these two

equations can be nondimensionalized, and the dimensionless values of K_1 and K_2 are specified to be 0.18.

Following Kuo, the temperature of the cloud is regarded as the temperature of the moist adiabat through the condensation level representative of the surface layer. Calculations of Q_c and M_c are shown in Figs. 17 and 20. Also, for the modified scheme, the precipitation rate is 0.0822 in hr^{-1}, the cloud tops are at 220 mb, and the maximum of the latent heat released is at 400 mb. Compared to the observations, the deviations are only a few percent.

The latent heat released by Kuo's original scheme is shown in Fig. 17. Ie is about the same amount as accounted for by the first component of tht modified formulation. As mentioned by Ceselski (1973) the. maximum latent heat released, computed from Kuo's scheme, is often in the lower troposphere this is verified in Fig. 17.

VI. CONCLUSIONS

The main objectives of this study are to evaluate the applicability of Kuo's parameterization of latent heat released in middle latitudes and to develope a modification of his theory. The evaluation is performed through the combination of the large-scale heat and moisture budgets and the formulation of the latent heat released. The results show that the precipitation rate computed from Kuo's scheme is one order of magnitude smaller than that observed and the top of the cloud is about 300 mb lower in middle latitudes. Further analysis indicates that Kuo's scheme does not consist of a suitable mechanism to transport energy and moisture vertically.

In order to improve Kuo's scheme upon the treatment of the interaction of deep convection with the environment, modified scheme consists of considerations of the large-scale moisture supply and of the vertical transport of moisture and of dry static energy inside the cloud. Also, a two-layer cloud ensemble model is combined with the modified scheme. The evaluation of the modified scheme is performed by combining the large-scale heat and moisture budgets, and the modified formulation of the latent heat released. The results show that the precipitation rate and the top of clouds computed from modified scheme agree well with the observed values. The theoretical analysis indicates that the latent heat released of modified scheme consists of three components. The first component is due to the large-scale moisture convergence, the second is due to the vertical transport of moisture inside the cloud, and the third represents the vertical divergence of the dry static energy. These three

components are nearly equal in magnitude. Therefore, the latent heat released in a layer may not be confined to that layer; the vertical transport of released latent heat is a significant mechanism involved in cumulus convection. Furthermore, because of the vertical transport of the moisture inside the clouds, latent heat still may be released even the production rate of cloud air is zero. The cloud may act as a machine which pumps the moisture and the dry static energy from the lower levels up to higher levels or vice versa.

The comparison of original and modified Kuo's scheme concludes that the most important of the modified parameterization scheme is that it models physically realistic processes which may be verified by examination of the large-scale heat and moisture budget equations. Another significant feature is that the modified scheme is consistent with a variable cloud ensemble model which may be time dependent or static, and may or may not account for entrainment, detrainment, and/or evaporation. If large-scale moisture convergence above the cloud base is neglected and cloud mass flux is assumed to be constant with height., the latent heat released in the modified scheme becomes proportional to the cloud mass flux at the cloud base and is similar to that proposed by Ooyama (1969) in his numerical simulation of the life cycle of tropical cyclones. Furthermore, the vertical distribution of the latent heat released, computed from the modified scheme, has a maximum value at the 400-mb level which is physically understandable and is verified by observations (Reed and Recker, 1971). These features are not present in Kuo's scheme.

Although results obtained with the modified scheme are very encouraging, they are still far from perfect. For example, the two-layer model which is utilized to determine the cloud mass flux should be improved. Extensions of this study probably should be focused on the following subjects.

(a) Improved treatment of evaporative downdraft cooling. This may be the biggest defect of current versions of all parameterization models. The downdraft cooling is a very effective mechanism to transport the horizontal momentum of upper levels downward and increases the low level mass convergence around the cloudy area. The low-level mass convergence induced by downdraft cooling can not be observed by the present observational network and should be parameterized in terms of large-scale variables and bulk properties of a cloud ensemble. This may be performed by dividing the cloudy area into downward and upward regions (Asai and Kasahara, 1967); the

interaction between these two regions and between cloudy regions and the environment may be revealed by consideration of two sets of cloud ensemble equations. Combination of considerations of downdraft cooling and of the spectral distribution of cloud properties is a very challenging problem for future research.

(b) Improved treatment of the sub-cloud layer. It is evident that accurate determinations of the mass flux, temperature, and moisture content at cloud base are very necessary for accurate computations of latent heat released and of bulk properties of the cloud ensemble. However, because of the poor understanding of atmospheric turbulence, estimates of the flux of heat, momentum, mass, and moisture into the cloud base from the planetary boundary layer are still highly uncertain. Variational optimization of thermodynamic properties and of the wind field may be utilized to improve the realiability of the computations by employing a planetary boundary layer model. A feasible model should be consistent with the large-scale motion field above the palnetary boundary layer such that the derived eddy heat flux, Y, is nearly zero at the top of atmosphere (or at the tops of the clouds).

(c) Inclusion of the spectral distribution of cloud Properties. The clouds may be divided into continuous or discrete categories according to the heights of the cloud tops; it may be assumed that the cloud bases are the same. Since the cloud properties are different for different categories, the latent heat released should be different for different clouds. In order to find the cloud properties and the latent heat released, the spectra of the cloud population should be found first. This may be the key problem for further research.

(d) Improved treatment of radiation term. The radiation term in this study is computed from Rodgers' climatological data. Indeed, clouds can change the radiation dramatically. Some tests show that clouds in an overcast situation change the radiational cooling by one order of magnitude. However, better radiation results depend on better cloud information, and the cloud information is unknown in the convection parameterization problem. In order to solve this problem, combination of the parameterization of cumulus convection and a radiation model may be necessary.

(e) Incorporation of scheme into a numerical prediction model. After applying the modified parameterization scheme in a diagnostic sense on several data sets, necessary modifications should be determined in order that

the scheme may be incorporated into a regional numerical forecast model such as Kreitzberg's (1974). The scheme should then be inserted into the fo ecast model and tested on real cases.

ACKNOWLEDGMENTS. This research was supported by the George C. Marshall Space Flight Center, Contract NAS 8-31333, and was directed by Dr. Rex L. Inman. Support was also received from the National Science Council, Republic of China.

I wish to express my deep gratitude and appreciation to Dr. Rex L. Inman for his constant support, encouragement, assistance and convincing suggestions. I also wish to thank Dr. Y. K. Sasaki, Dr. J. S. Fein, Dr. J. F. Kimpel, Dr. E. Blick and Dr. M. Jischke for their encouragement and helpful suggestions. Appreciation must be extended to my fellow graduate students, Adrian Ritchie, Richard Hodur, Walter L. F. Chang, Main Hutcheson, and Alvina Hutcheson for reading the manuscript and offering helpful discussion. I wish to thank Jo Ann Oberst for her expert typing of the manuscript.

BIBLIOGRAPHY

Arakawa, A., 1969: Parameterization of cumulus convection. Proc. WMO/IUGG Symp. Numerical Prediction, Tokyo, IV 8, 1-6.

_____, and W. H. Schubert, 1974: Interaction of a cumulus cloud ensemble with the large-scale environment, Part I. J. Atmos. Sci., 31, 674-701.

Asai, T. and A. Kasahara, 1967: A theoretical study of the compensating downward motions associated with cumulus clouds. J. Atmos. Sci., 24, 487-496.

Ceselski, B. F., 1973: A comparison of cumulus Parameterization techniques. Tellus, 25, 459-478.

_____, 1974: Cumulus convection in weak and strong tropical disturbances. J. Atmos. Sci., 31, 1241-1255.

Edmore, H. J. and D. G. Vincent, 1975: An application of Kuo's Parameterization scheme of convective latent heat release to a middle latitudes cyclone system. Mon. Wea. Rev., (in Press).

Fraedrich, J., 1973: On the parameterization of cumulus convection by lateral mixing and compensating subsidence. Part I. J. Atmos. Sci, 29, 240-243.

_____, 1974: Dynamic and thermodynamic aspects of the Parameterization

of cumulus convection. Part II. J. Atmos. Sci., 31, 1838-1849.

Hudson, H. R., 1971: On the relationship between horizontal moisture convergence and convective cloud formation. J. Appl. Meteor., 10, 755-762.

Inman, R. L., 1969: Computation of temperature at the lifted condensation level. J. Appl. Meteor., 8, 155-158.

Krishnamurti, T. N., 1969: An experiment in numerical prediction in the equatorial latitudes. Quart. J. Roy. Meteor. Soc., 95, 594-620.

Kreitzberg, C. W., D. J. Perkey, and J. E. Pinkerton, 1974: Mesoscale modeling and forecasting research. Final report, Dept. of Physics and Atmospheric Science, Drexel University.

Kuo, H. L., 1965: On the formation and intensification of tropical cyclones through latent heat release by cumulus convection. J. Atmos. Sci., 22, 40-63.

_____, 1974: Further studies of the parameterization of the influence of cumulus convection of large-scale flow. J. Atmos. Sci., 31, 1232-1240.

Liang, W. J. 1976: The variational optimization of wind field for the estimation of vertical velocity. Annual Report of the Institute of physics, Academia Sinica, 6, 179-198.

Manabe, S., J. Smagorinsky, and R. F. Strickler, 1965: Simulated climatology of a general circulation model with a hydrologic cycle. Mon. Wea Rev., 93, No. 12, 769-798.

_____: Physical climatology of a general circulation model with a hydrologic cycle. Mon. Wea. Rev., 93, 769-798.

Miller, R. C., 1972: Notes on analysis and severe storm forecasting procedures of the air force global weather central. M.A.C. United States Air Force.

Newman, W. R., 1971: The relationship between horizontal moisture convergence and severe storm occurrences. M.S. Thesis, Dept. of Meteor., University of Oklahoma.

Ooyama, K., 1964: A dynamical model for the study of tropical cyclone development. Geofisica Intern. (Mexico), 127-198.

_____, 1969: Numerical simulation of the life cycle of tropical cyclones. J. Atmos. Sci., 26, 3-40.

_____, 1971: A theory on parameterization of cumulus convection, J. Meteor. Soc. Japan, 49, (special issue), 744-756.

Palmen, E., and C. W. Newton, 1969: Atmospheric Circulation Systems. Academic press, New York, 391-422.

Reed, R. J., and E. E. Recker, 1971: Structure and properties of synoptic-scale wave disturbances in the equatorial western Pacific. J. Atmos. Sci., 28, 1117-1133.

Riehl, H., and J. S. Malkus, 1958: On the heat balance of the equatorial trough zone. Geophysica, 6, 503-538.

Rodgers, C. D., 1967: The radiative heat budget of the troposphere and lower stratosphere. Report No. A2, Department of Meteorology, Massachusetts Inst. of Technology.

Sasaki, Y., 1973: Final report of investigation of an operational scheme of analysis and short range prediction of local severe weather. The University of Oklahoma Research Inst.

Smagorinsky, J., S. Manabe, and J. L. Holloway, 1965: Numerical results from a nine-level general circulation model of the atmosphere. Mon. Wea. Rev., 93, 727-768.

Yamasaki, M., 1968: Numerical simulation of tropical cyclone development with the use of primitive equations. J. Meteor. Soc. Japan, 46, No. 3, 202-294.

Yanai, M., 1971: A review of recent studies of tropical meteorology relevant to the planning of GATE. WMO Publ., 2, Annex I. 1-43.

_____, S. Eskensen and J. Chu, 1973: Determination of bulk properties of tropical cloud clusters from large-scale heat and moisture qudgets. J. Atmos. Sci., 30, 611-627.

APPENDIX A

KUO'S PARAMETERIZATION SCHEME

The large-scale flow variables are interpolated to the grid points of a horizontal grid system with grid length $\Delta x=\Delta y=\Delta$. The value of the large-scale flow variable X_{ij} at any grid point can then be taken as representing the average of X over the area $A=\Delta^2$ centered at this point, while the actual value of X is given by the sum of the aver-age value and the departure. i. e.,

$$X=\bar{X}+X' \quad , \quad \bar{X}=\frac{1}{A}\int_A X dA \quad , \quad \bar{X}'=0. \tag{A.1}$$

The grid area A is chosen to be much larger than the area occupied by a single cumulus cloud and its surrounding descending region such that a large number of clouds are included in A.

The equations for the potential temperature θ, the water vapor mixing ratio q, and the horizontal velocity $\vec{V}$ of the large-scale system can be written in (x,y,p,t) coordinates as shown below. The equation for energy conservation is

$$\frac{d\bar{\theta}}{dt} - Q_R - \frac{L\pi}{C_P}\bar{C}_L = \frac{L\pi}{C_P}\bar{C}_1 - \frac{\partial}{\partial p}\overline{\omega'\theta'} - \nabla\cdot\overline{\vec{V}'\theta'}, \qquad \text{(A. 2)}$$

Also, the equations expressing conservation of moisture and momentum are

$$\frac{d\bar{q}}{dt} + \bar{C}_L - T_q = -\bar{C}_1 - \frac{\partial}{\partial p}\overline{\omega' q'} - \nabla\cdot\overline{\vec{V}' q'}, \qquad \text{(A.3)}$$

$$\frac{d\vec{\bar{V}}}{dt} + f\vec{k}\times\vec{\bar{V}} + \nabla\bar{\phi} - \vec{F} = \frac{\overline{\omega'\partial\vec{V}'}}{\partial p} - \overline{\vec{V}'\cdot\nabla\vec{V}'}, \qquad \text{(A. 4)}$$

respectively, where C_L and C_1 are the condensation rates produced by the large-scale motions and by the subgrid-scale convective motions, respectively, L is the latent heat of condensation, Q_R is the heating rate by radiation and turbulent diffusion, T_q and $\vec{F}$ are the rates of turbulence diffusion of moisture and momentum, respectively, d/dt is $\partial/\partial + \vec{V}\cdot\Delta + \omega\frac{\partial}{\partial p'}$ and $\pi = (p/_l)^R C_p$. The other symbols have their usual meanings.

Assuming that at any given moment the active clouds, including their strongly descending parts, occupy the fractional area σ, while their environments occupy the fractional area $(1-\sigma)$, and denoting the flow variables in the active cloud regions by a subscript c and those in the surrounding regions by a subscript d, we then have

$$\bar{X} = (1-\sigma)X_d + \sigma X_c, \qquad \text{(A.5)}$$

where X stands for either ω, $\vec{V}$, θ, *or* q. Also, by means of algebraic manipulations we obtain

$$\overline{\omega' X'} = \frac{\sigma}{1-\sigma}(\omega_c - \bar{\omega})(X_c - \bar{X}). \qquad \text{(A.6)}$$

Since $\sigma \ll 1$, $\omega_c < < \bar{\omega}$, *we get*

$$\overline{\omega' X'} \doteq -\sigma\omega_c(\bar{X}-X_c),$$

$$\equiv M_c(\bar{X}-X_c) \qquad \text{(A.7)}$$

$$\doteq M_c(X_d - X_c) \quad , \quad if \ X_d \doteq X.$$

Deep cumulus towers and cumulonimbi appear to be associated with a deep conditionally unstable layer and the presence of large-scale convergence (Riehl 1950, Riehl and Malkus 1961). The former of these two conditions make it possible for huge cumuli to penetrate into the upper troposphere and the lower stratosphere, while the latter condition provides a general lifting mechanism to trigger the convective instability. These two conditions can be represented as follows:

$$\begin{aligned} &H_1 H_2 \Delta \bar{\theta}_e > K_1 \\ &-\bar{\tau}\bar{\omega}_m > K_2 \ (p_s - p^*) \end{aligned} \qquad \text{(A.8)}$$

where $\Delta \bar{\theta}_e$ is the maximum difference of the equivalent potential temperature in the conditionally unstable layer, H_1 is the depth of this layer, H_2 the height difference between the level where θ_e is a minimum and the level above when θ_e is equal to its maximum value below, $\bar{\tau}$ is the period of the large-scale flow, $P_s - P^*$ is the lift needed for the surface air at the level p, to become saturated, $\bar{\omega}_m$ the maximum low-level p-velocity, and K_1 and K_2 are critical values of instability and low-level convergence, respectively, which ensure that deep convergence will develop. Kuo used the net convergence of moisture into the vertical column of air of unit cross section produced by the large-scale flow and by evaporation from the ground as one fundamental parameter. Let this quantity be M_L; then,

$$M_L = -\frac{1}{g}\int_0^{p^*} (\nabla \cdot \bar{\vec{V}}\bar{q}) \, dp + \bar{\rho}_o C_D \bar{V}_o (\bar{q}_s - \bar{q}_o) \ , \qquad \text{(A.9)}$$

where subscripts s and o indicate values at the surface and at a nearby higher level, respectively, and C_D is the drag coefficient.

The amount of moisture needed to create a deep cumulus of area σ and pressure depth $p_b - p_t$ with temperature T_c and saturation mixing ratio $q_c(T_c)$ is

$$\sigma M_t = \frac{\sigma}{g}\int_{p_t}^{p_b} \left[\frac{C_p}{L}(T_c - \bar{T}) + (q_c - \bar{q})\right] dp. \qquad \text{(A,10)}$$

This is supplied by the large-scale convergence of moisture in time τ. Hence,

$$\sigma = \frac{\tau M_L}{M_t} \qquad \text{(A.11)}$$

where τ is the half-life of the cloud (approximately 30 minutes).

Let's assume that a fraction (1-b) of the total convergence of moisture M_L is condensed and either precipitated out as rain or was carried away, while the remaining fraction b of M_L is stored in the air to increase the humidity (including the influence of evaporation of condensed water). That is to say, we have

$$bM_L=\frac{1}{g}\int_0^{p_0}\frac{\partial\overline{q}}{\partial t}dp\ . \tag{A.12}$$

Now, according to Kuo (1965), the rate of the release of latent heat Q_a is

$$Q_a=\frac{\sigma}{\tau}C_p(T_a-\overline{T})(1-b) \tag{A.13}$$

Also, according to Kuo (1974), the vertical velocity ω_c is approxmated as

$$\omega_c=-\frac{\theta_c-\overline{\theta}}{\tau(\partial\theta_e/\partial p)_{ef}}, \tag{A.14}$$

where $(\partial\theta_e/\partial p)_{ef}=\partial\overline{\theta}/\partial p+\frac{L}{C_p}(\partial q_c/\partial p)$.

Kuo suggested that the temperature T_c of the cloud can be taken as the temperature T_{es} of the moist adiabat through the condensation level of the representative surface air, as a first approximation.

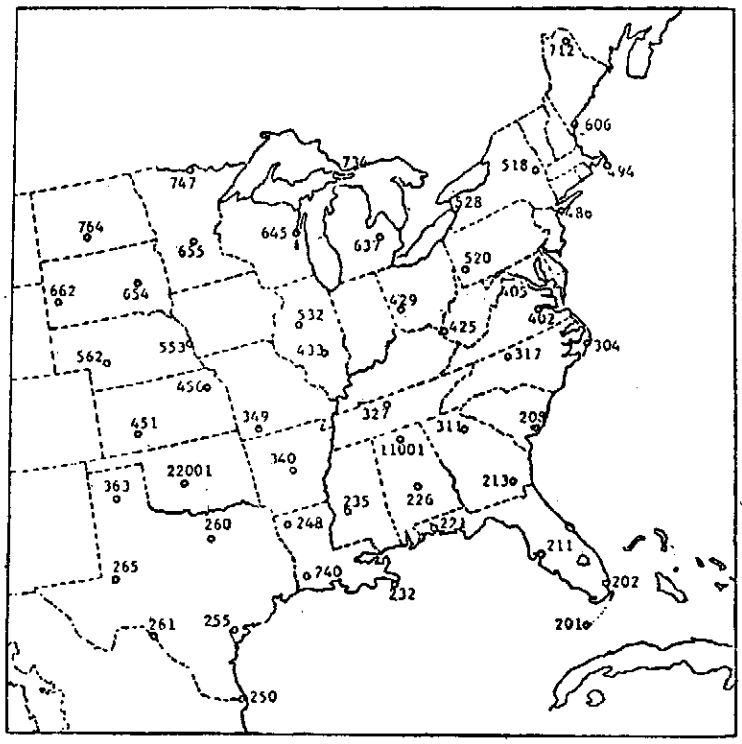

Fig. 1. Rawinsonde stations for AVE II Pilot Experiment.

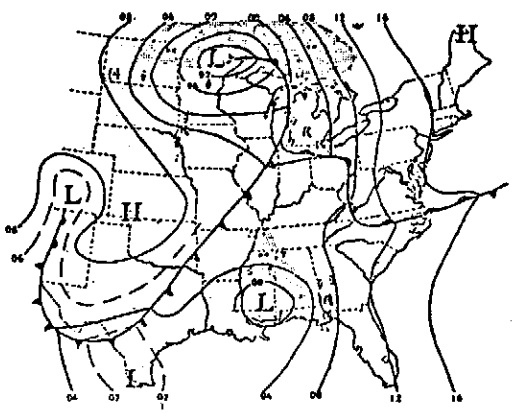

Fig. 2. Surface chart for 2100 GMT 11 May 1974. Isobars are drawn at 4 mb intervals.

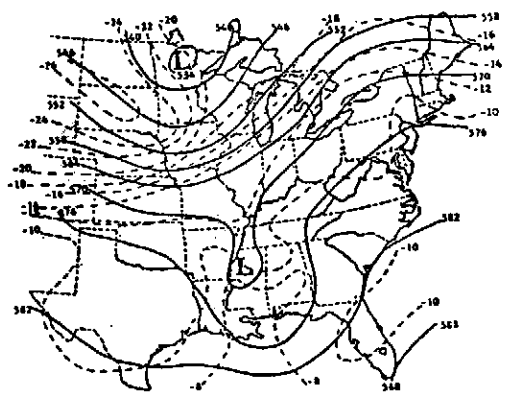

Fig. 3. 500 mb chart for 2100 GMT 11 May 1974. Height (solid) contours are drawn at 60 m intervals. Isotherms (dashed) are constructed at 2°C intervals.

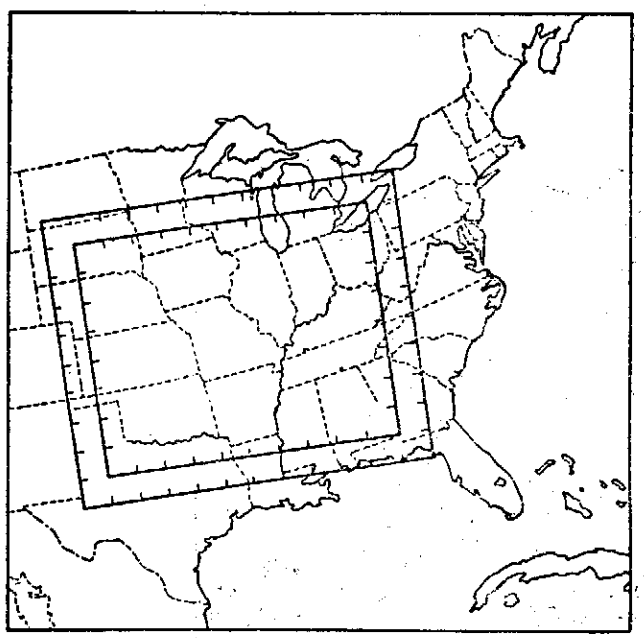

Fig. 4. Data grid and interior working grid.

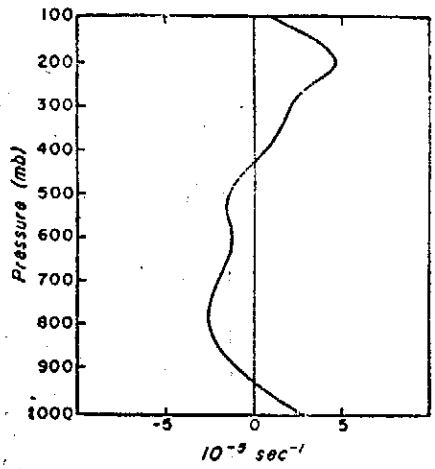

Fig. 5. Horizontal divergence at test point.

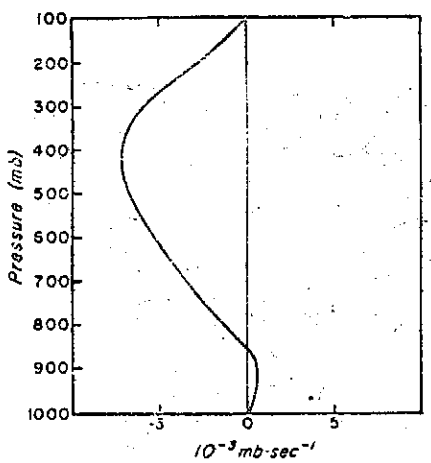

Fig. 6. Vertical velocity, $\omega = \frac{dp}{dt}$, at test point.

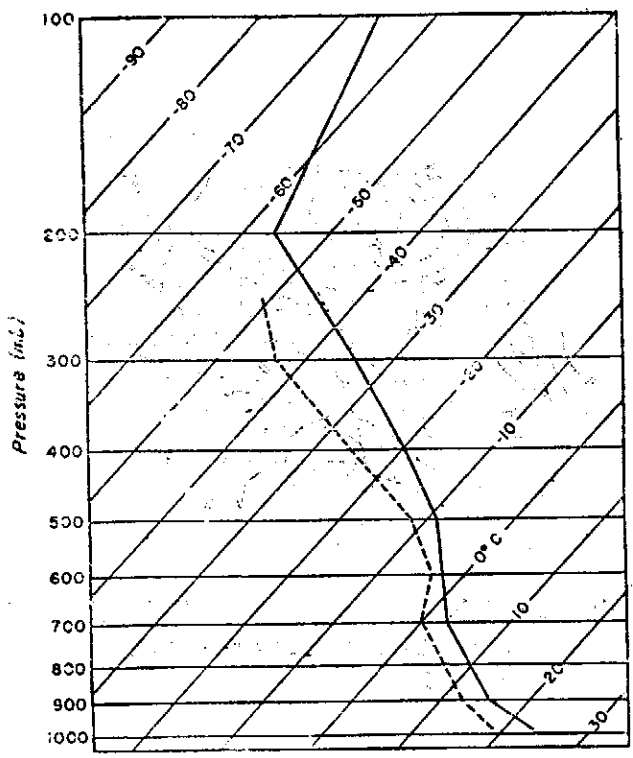

Fig. 7. Observed temperature and dew-point temperature at test point.

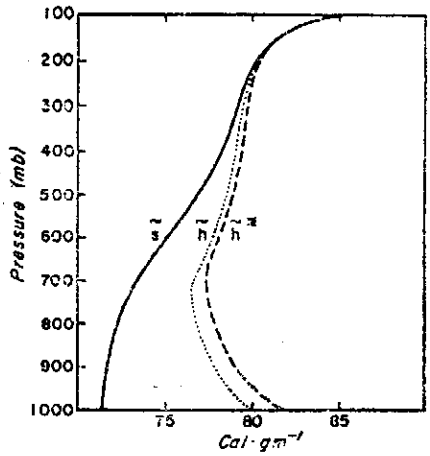

Fig. 8. The dry static energy, s (solid), moist static energy, h (dotted), and saturation moist static energy, h* (dashed), of environment.

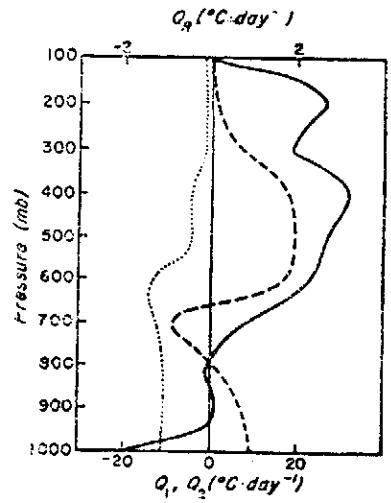

Fig. 9. The apparent heat source, Q_1 (solid), the apparent moist sink, Q_2 (dashed), and the radiational heating from Rodger's results (1967), Q_R (dotted).

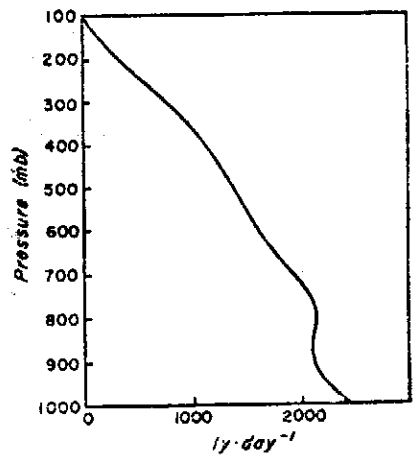

Fig. 10. The derived vertical eddy heat flux, Y.

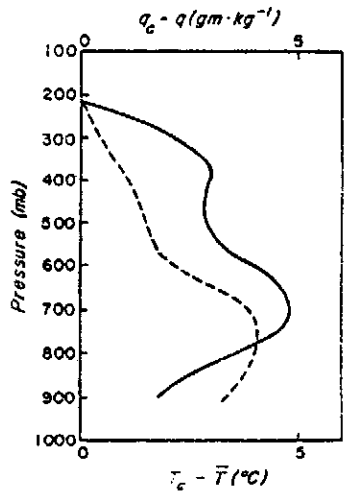

Fig. 11. The excess temperature, $T_C-\overline{T}$ (solid), and the excess mixing ratio, $q_C-\overline{q}$ (dashed), computed from the moist adiabat through the lifted condensation level representative of the surface layer.

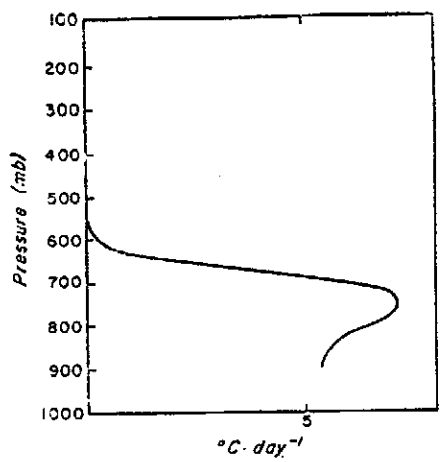

Fig. 12. Released latent heat, computed from large-scale budgets and Kuo's formulation.

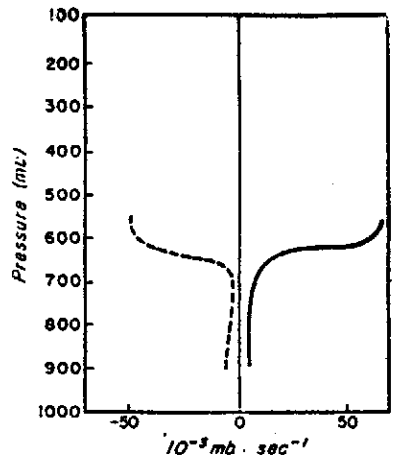

Fig. 13. Cumulative mass flux distribution within clouds, M_c (solid), and the corresponding environmental mass flux, $\bar{M}$ (dashed), computed from the large-scale budgets and Kuo's formulation of the latent heat released by subgrid-scale convection.

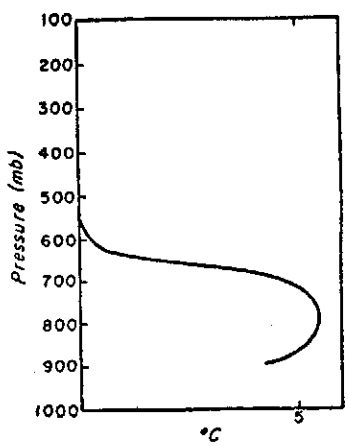

Fig. 14. The excess temperature, $T_c-\bar{T}$, computed from the large-scale budgets and Kuo's formulation of the latent heat released by subgrid-scale convection.

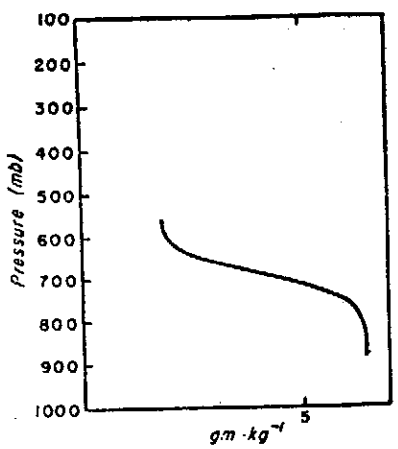

Fig. 15. The excess mixing ratio $q_c-\bar{q}$, computed from the large-scale budgets and Kuo's formulation of the latent heat released by subgrid-scale convection.

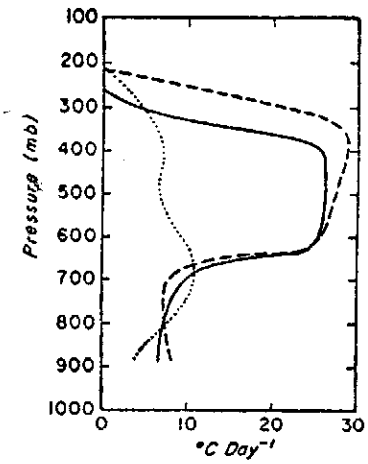

Fig. 16. Cumulative mass flux distribution within clouds, M_c (solid), and the corresponding environmental mass flux, M (dashed), computed from the large-scale budgets and theeat released by subgrid-scale convection.

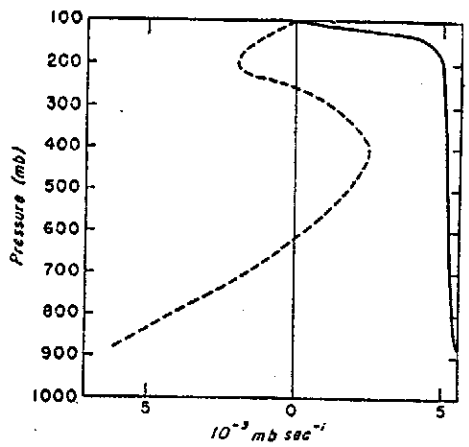

Fig. 17. The latent heat released by subgrid-scale convection, computed from (a) Kuo's scheme (dotted), (b) the modified scheme (dashed), and (c) the large-scale budgets and the modified formulation (solid).

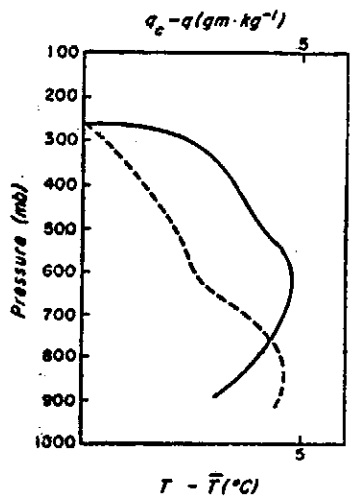

Fig. 18. The excess temperature, $T_c-\bar{T}$ (solid), and the excess mixing ratio, $q_c-\bar{q}$ (dashed), computed from the large-scale budgets and the modified formulation of latent heat released.

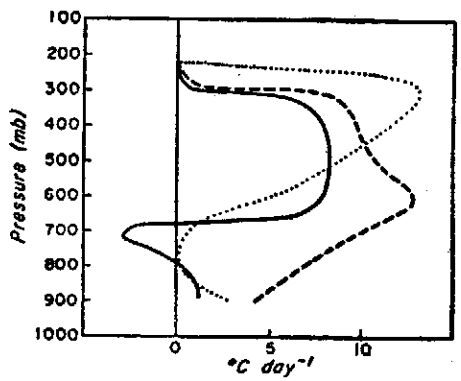

Fig. 19. The first (solid), the second (dashed), and the third (dotted) components of the expression for the latent heat released, computed from modified scheme

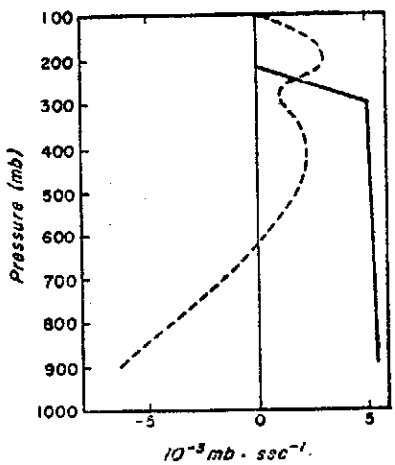

Fig. 20. Cumulative mass flux distribution within clouds, M_c (solid), and the corresponding environmental mass flux, $\tilde{M}$ (dashed), computed from the modified scheme.

Annual Report of the Institute of Physis, Academia Sinica, Vol. 6, 1976

有限區域原始方程式模式之初步探討

(On the preliminary study of a limited-area primitive equation model)

蕭錫璋 (C. J. Shiau) 汪群從 (C. T. Wang)

Institute of Physics, Academia Sinica, Nankang, Taiwan,
The Repulic of China

摘 要

本文對有限區域原始方程式模式之邊界條件作初步的探討。在 (x, y, p, t) 坐標上，將大氣分作 300mb, 500mb, 700mb, 900mb 四層。初始資料僅爲主觀分析之高度場、海面溫度及 600mb, 800mb 之溫度露點差。經計算發現，參考 Hawkins 方法所得的初值化場 300mb ，500mb ，及太平洋高壓皆向東退縮，而 300mb 尤甚。在原始方程式模式 24 小時的計算，颱風走向偏東北與實際路徑西北方向有所偏差。若改用參考日本氣象廳平衡方程式的解法，雖能使天氣型態 (pattern) 不再有大變化，但是 300mb 往往在計算 6～12 小時，自右邊邊界附近開始有擾動發生，隨時間增加向場內發展。由於運算範圍小，雖試過多種不同的邊界條件，例如固定邊界條件 (fixed B. C.) 會使波在邊界上反射，致使能量不斷累積，擾動逐漸增大。自由滑動邊界條件 (free slip B. C.) 及絕熱光滑邊界條件 (insulated slippery B. C.) 雖能有限地考慮邊界的變化，但不能完全控制邊界的問題。若加入一層「多孔海棉」邊界條件 (porous sponge B. C.) 則雖能吸收部份反射波，亦未能有效地解決邊界問題，而認爲邊界條件確爲計算成敗的重要關鍵之一。又由於擾動現象僅出現於 300mb，其他三層計算至 24 小時，仍有合理的型態，故再對初始資料作進一步探討。利用調和波分析 (Harmonic analysis) ，檢視各層高度場的振幅與波數關係，發現 300mb 的初始高度場，雖經 9 點 smooth 及 balance eq. 處理，仍有較大振幅之高頻波。又檢視實際天氣圖，在擾動發生處附近即日本與華北一帶，有一强風帶 (Jet stream) 存在，風速高達 80～90 knots，其南及北風速皆小。此種短波未經完全濾除，也是造成擾動的重要原因之一。故邊界條件及初始資料是吾人計算困難的所在。

1. 引 言

用原始方程式模式作數值天氣分析能探討各種天氣的基本現象，所以近年各氣象學者多使用原始方程式模式來探討大氣現象。但是這種未經濾波的方程組，往往受到各種雜波，例如重力波、內重力波 (internal gravitive wave) 的干擾，或非線性計算的不穩定，而使數值計算產生許多困難。所以有許多學者致力於初值化 (initialization) 問題的探討，例如 Shuman (1968), Miyakoda 及 Moyer (1968), Nitta 及 Hovermale (1969), Sundqvist (1975) ，等以平衡方程式模式處理初始場；也有些學者如 Sasaki (1958), Achtemeier (1975) 等用變分客觀分析法 (variational objective analysis method) 處理初始場。國內亦有多人開始分析初始資料場，如胡仲英 (1975) ，鄧施人 (1975) 等的客觀分析，以及曾忠一 (1976) 的變分客觀分析之研究。本文僅將主觀讀取的高度場資料以平衡方程式模式完成初值化處理。

原始方程式模式的邊界條件非常重要，稍有不妥，很容易使雜波被邊界反射回計算場內，累積能量，而使擾動不斷發展。對於邊界問題，許多學者爲避免邊界條件的困難，大多採用全球或半球作爲運算範圍，例如Shuman (1968) Yamasaki (1968) 等，也有以有限區域爲運算範圍的，例如Miller (1969,1972) 及Williamson and Browning (1974) 等。

中研院物理所大氣物理組曾對東南亞有限區域的大氣運動用不同的模式，作過一系列的探討 (Ann. Rep. Inst. Phys., Academia Sinica 1971～1975)，現在進一步藉原始方程式模式來作探討。因限於國內電子計算機的容量 (memory space) 及使用經費，且爲探討邊界條件及初始狀態對此模式之影響，故先以有限區域爲運算範圍，對原始方程式模式作初步之探討。

2. 數學物理模式

潛熱 (latent heat) 及感覺熱 (sensible heat) 對熱帶天氣系統的發展和維持，影響重大。本文所設計的模式爲四層，非絕熱有限區域原始方程式模式。爲簡化起見，暫不考慮地形及摩擦阻力。在 (x, y, p, t) 坐標上的控制方程式爲運動方程式、熱力方程式、連續方程式、流體靜力方程式和狀態方程式。它們分別如下：

$$\frac{\partial u}{\partial t}=-u\frac{\partial u}{\partial x}-v\frac{\partial u}{\partial y}-\omega\frac{\partial u}{\partial p}+fv-\frac{\partial \phi}{\partial x} \tag{2.1}$$

$$\frac{\partial v}{\partial t}=-u\frac{\partial v}{\partial x}-v\frac{\partial v}{\partial y}-\omega\frac{\partial v}{\partial p}-fu-\frac{\partial \phi}{\partial y} \tag{2.2}$$

$$\frac{\partial \theta}{\partial t}=-u\frac{\partial \theta}{\partial x}-v\frac{\partial \theta}{\partial y}-\omega\frac{\partial \theta}{\partial p}+\frac{\theta}{C_pT}\frac{d(Q-\bar{Q})}{dt} \tag{2.3}$$

$$\frac{\partial u}{\partial x}+\frac{\partial v}{\partial y}+\frac{\partial \omega}{\partial p}=0 \tag{2.4}$$

$$\frac{\partial \phi}{\partial p}=-\frac{RT}{p}=-\frac{R}{p}\left(\frac{P_{1000}}{p}\right)^{R/C_p} \tag{2.5}$$

其中 $u, v, \theta, \omega, \phi$ 爲未知數。u, v 爲風在 x, y 方向上的速度分量；$\omega\equiv\frac{dp}{dt}$ 爲垂直運動速度，$\theta\equiv T\left(\frac{P_{1000}}{p}\right)^{R/C_p}$ 爲相當位溫；Q 爲熱能；R 爲氣體常數；p爲壓力；P_{1000} 爲1000毫巴處之壓力 C_p 表示等壓比熱；$\bar{Q}$表示在空間爲常數之輻射冷却 (staff members, 1965)。

加熱率 $\frac{dQ}{dt}$ 包括潛熱釋放率 $\frac{dQ_L}{dt}$ 及可感熱變化率 $\frac{dQ_s}{td}$，曾在本所期刊上 (Ann. Rep. Inst. Phys. Academia Sinica, 1973, 1974) 有詳盡的敍述，在此僅略述其要：

$$\frac{dQ}{dt}=\frac{dQ_L}{dt}-\frac{dQ_s}{dt} \tag{2.6}$$

$$\begin{aligned}&\frac{dQ_L}{dt}=-0.06\ C_p\omega\ \Delta S \qquad \text{當}\quad \omega<0\\ &\quad=0 \qquad\qquad\qquad\quad \text{當}\quad \omega\geq 0 \text{ 或 } p\leq 700\text{mb}\\ &\text{而}\quad 1\geq\Delta S=1-\frac{T-T_d}{\Delta T'}\geq 0\end{aligned} \tag{2.7}$$

其中 T_d 表示露點溫度；$\Delta T'=7.5°K$ 爲一經驗常數。

$$\frac{dQ_s}{dt}=A|V_{1000}|(T_{sea}-T_{1000})\left(\frac{p}{P_{1000}}\right)^2$$
$$A=0.001 \quad \text{當} \quad T_{sea}>T_{1000}$$
$$=0.0001 \quad \text{當} \quad T_{sea}<T_{1000} \tag{2.8}$$
$$|V_{1000}|\cong 0.7|V_{900}|=0.7\,(u_{900}^2+v_{900}^2)^{0.5}$$

由〔(2.2) 式對 x 微分〕減去〔(2.1) 式對 y 微分〕，經幅度分析 (scale analysis) 得到

$$\nabla^2\phi=f\left(\frac{\partial v}{\partial x}-\frac{\partial u}{\partial y}\right)-u\frac{\partial f}{\partial y}+2J(u,v) \tag{2.9}$$

利用此式，可由 u, v 求得 ϕ 值。

3. 初始資料之處理 (Initialization: Balancing the initial data)

大氣中大幅度的運動 (large-scale motion) 是準平衡狀態的 (Quasi-balanced state)，要達到完全的平衡並不可能，事實上也不存在，尤其是在摩擦阻力大和熱效應大的地方。除此而外，觀測資料的不準確及未經過濾的雜波存在，會造成擾動的增大而破壞整個流體場之計算。所以在計算之前必須校正原始資料，使儘可能接近平衡狀態。欲達近乎平衡狀態，本文所用的方程式有平衡方程式 (balance eq.)，Omega 方程式，流體靜力方程式和連續方程式。計算的步驟與汪 (1974,1975) 大致相同，僅平衡方程式今爲非線性者，略述如下：

(1)由於沒有風場分析資料，僅有高度場資料，風的旋轉部份 (rotational part) 是由流線函數 (stream function) ψ 求得。所用的公式爲平衡方程式，

$$f\nabla^2\psi-u\frac{\partial f}{\partial y}+2(\psi_{xx}\psi_{yy}-\psi_{xy}^2)=\nabla^2\phi \tag{3.1}$$

其中 f 爲科氏參數 (coriolis parameter)。欲得有意義之解 (3.1) 式必須爲橢圓型態 (elliptic type) 且天氣場中絕對渦旋度 η 不能小於零 (Hawkins, 1972) 即：

$$\eta=\left[\left(\frac{\partial^2\psi}{\partial x^2}-\frac{\partial^2\psi}{\partial y^2}\right)+4\left(\frac{\partial^2\psi}{\partial x\partial y}\right)^2+2\nabla^2\phi T+f^2-2\nabla f\cdot\nabla\psi\right]^{\frac{1}{2}}\geq 0 \tag{3.1.A}$$

首先逐點檢查經 9 點 smooth 後高度場的 $[2\nabla^2\phi+f^2]_{ijk}$ 值，確使它大於零，避免平衡方程式中可能有的虛數解 (imaginary solution)。若某點 $[\quad]_{ijk}$ 之值小於零，則令該點此值爲零，且其鄰近四點之值都減小 $0.25|[\quad]_{ijk}|$。如此逐點檢查，至各點都合乎上述條件爲止。由此調整 $[\quad]_{ijk}$ 值，可求得初始流線場 ψ 及初始平衡高度場 (initial balanced geopotential height) ϕ 值。(以下簡稱此法爲 A法)。爲使經此處理得的天氣場與原來天氣型態差異不致太大，參考日本氣象廳之做法 (Shiau, 1975)，爲使 (3.1) 式得解，必須滿足

$$\nabla^2\phi+\frac{1}{2}f^2-\nabla f\cdot\nabla\psi>0 \tag{3.1.B}$$

條件。逐點檢查檢查經 9 點 smooth 後的高度場，且令初始流線場 $\psi^\circ\equiv\frac{\phi^\circ}{f}$；$\phi^\circ$ 爲經 9 點 smooth 後的重力位高度；f 爲在此區域中 f 之平均值。若某點 (i,j) 不合乎 (3. 1. B) 之條件，就調整高度場，在該點高度場上增加 $\frac{1}{8}(\nabla^2\phi+\frac{1}{2}f^2-\nabla f\cdot\nabla\psi)$，直至合乎要求爲止，如此逐點檢驗，調整了高度場後，由此平衡高度場經 (3.1) 式 Iteration 求得流線場。經 Iteration n+1 次當 $|\psi^{n+1}-\psi^n|\leq\varepsilon$ 時，ε 爲一任意小之正數，才承認 ψ^{n+1} 之值。但此 Iteration 之次數最多不得超過12次 (以下簡稱此法爲B法)。300mb 做到12次，其他三層不到12次就達到要求。由此顯示 300mb 高度場尚未達到平衡狀態，(若强自使之平衡，可能是造成其型態變化 (太平洋高壓向東退縮) 的原因之一。

(2)溫度場由厚度經流體靜力方程式計算而得：

$$\frac{\partial \phi}{\partial p}=-\frac{RT}{p} \tag{3.2}$$

$$\theta \equiv T\left(\frac{P_{1000}}{p}\right)^{R/C_p}$$

(3)風的發散部份 (divergent parts of wind) χ 由連續方程式求得，

$$\nabla^2\chi=-\frac{\partial \omega}{\partial p} \tag{3.3}$$

假設ω之初值爲零，ω及 χ 的邊界值爲零。Iteration $n+1$次，至 $|\chi^{n+1}-\chi^n|\leq 10^2 \sec^{-1}$，求得 χ 值。再計算風場 u, v，

$$u=-\frac{\partial \psi}{\partial y}+\frac{\partial \chi}{\partial x} \tag{3.4}$$

$$v=\frac{\partial \psi}{\partial x}+\frac{\partial \chi}{\partial y} \tag{3.5}$$

(4)垂直速度由 Omega 方程式求得：

$$\nabla^2\sigma^*\omega+f^2\frac{\partial^2\omega}{\partial p^2}=-\nabla^2\left[J\left(\psi,\frac{\partial \phi}{\partial p}\right)+\nabla\chi\cdot\nabla\frac{\partial \phi}{\partial p}+\frac{R}{C_p p}\cdot\frac{dQ_s}{dt}\right]$$

$$+\frac{\partial}{\partial p}\left[-\frac{\partial}{\partial t}\nabla f\cdot\nabla\psi+fJ(\psi,\eta)+f\nabla x\cdot\nabla f\right] \tag{3.6}$$

其中 $\sigma^*=\sigma-0.06\Delta S\cdot\frac{R}{p}\geq 0.2\bar{\sigma}$ 當 $\omega<0$ 或 $p>500$mb

$=\sigma\geq 0.2\bar{\sigma}$ 當 $\omega\geq 0$ 或 $p\leq 500$mb (3.7)

σ爲靜力穩定度 (static stability)，可由下式及 (4.1) 式求得，

$$\sigma=-\frac{1}{\rho\theta}\frac{\partial \theta}{\partial p}$$

$$=\frac{\partial^2\phi}{\partial p^2}+\left(1+\frac{R}{C_p}\right)\cdot\frac{1}{p}\frac{\partial \phi}{\partial p} \tag{3.8}$$

$$\rho=\frac{p}{RT}\ (\text{空氣密度})$$

又 (3.6) 式中η表示絕對渦旋度 (absolute vorticity)。此式中假設ω的邊界值爲零。Iteration $n+1$次 至 $|\omega^{n+1}-\omega^n|\leq 10^{-3}$mb/sec。若不合乎此要求則上述(1)至(4)步驟重覆，直至達到此條件爲止。而得到一組近乎平衡狀態的原始值 $u^{t=t_0}$, $v^{t=t_0}$, $\theta^{t=t_0}$, $\phi^{t=t_0}$, $\omega^{t=t_0}$。

4. 數值計算過程及邊界條件

本文所採用的運算範圍在水平面爲 $(NX-1)\cdot(NY-1)$; $NX=20$, $NY=14$，的有限區域網格。各網格點間之距離 $d=332.5$ 公里。網格點中心在 125°E, 29°N，即 $(i=10,\ j=8)$ 之格點。(見圖一) 解上述 (2.1) 式至 (2.5) 式時，u, v, θ, ϕ 四變數置於各格點上，ω置於格點中央 (見圖二)。垂直方向上分作四層，在計算值，在 300mb, 500mb, 700mb, 900mb 計算 u, v, θ, ϕ 值，在 200mb, 400mb 600mb, 800mb 上計算 ω, $\frac{\partial u}{\partial p}$, $\frac{\partial v}{\partial p}$ 之值，並假設ω, $\frac{\partial u}{\partial p}$, $\frac{\partial v}{\partial p}$ 在 200mb 及 1000mb 邊界值都爲零 (見圖三)。

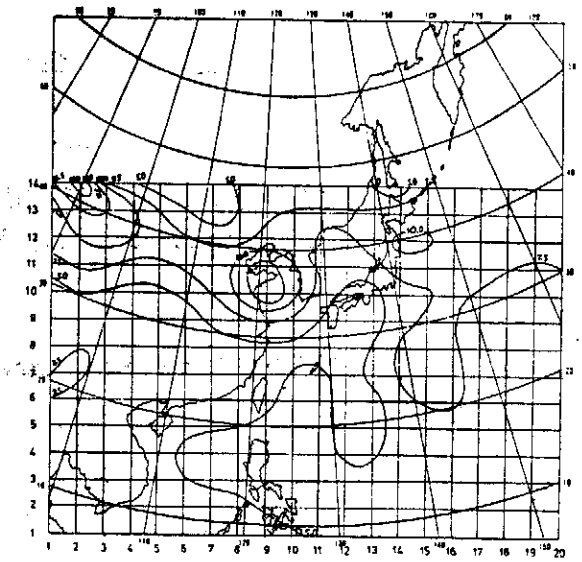

Fig 1. Computation domain & T-T_d field at 800 mb.

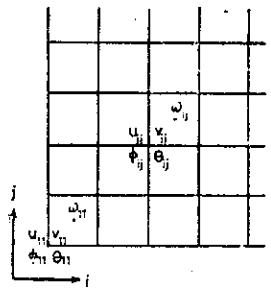

Fig. 2. Horizontal grid structure for finite differencing.

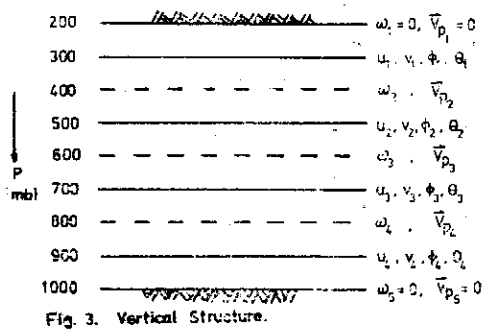

Fig. 3. Vertical Structure.

其中 900mb 的重力位高度場 ϕ_{900} 由內插求得，內插公式爲

$$\phi = A + B\ln p + c(\ln p)^2 \tag{4.1}$$

式中 A, B, C 爲常數，由 850mb, 700mb,500mb 三層高度場資料求得。

(2.1) 式至 (2.5) 式及 (2.9) 式可改寫爲定差方程式，分別如下 (Miller, 1969; Shuman, 1957)

$$\overline{u_t}^{xy} = -\overline{m}^{xy}\left[\overline{u}^{xy}\overline{u}_x^{xy} + \overline{v}^{xy}\overline{u}_y^{xy} + \overline{\phi}_x^{xy}\right] - \overline{\omega}^{p}\ \overline{u_p}^{xyp} + \overline{f}^{xy}\,\overline{v}^{xy} \tag{4.2}$$

$$\overline{v_t}^{xy} = -\overline{m}^{xy}\left[\overline{u}^{xy}\overline{v_x}^{xy} + \overline{v}^{xy}\overline{v_y}^{xy} + \overline{\phi_y}^{xy}\right] - \overline{\omega}^{p}\ \overline{v_p}^{xyp} - \overline{f}^{xy}\overline{u}^{xy} \tag{4.3}$$

$$\overline{\theta_t}^{xy} = -\overline{m}^{xy}\left[\overline{u}^{xy}\overline{\theta_x}^{xy} + \overline{v}^{xy}\overline{\theta_y}^{xy}\right] - \overline{\omega}^{p}\ \overline{\theta_p}^{xyp} + \frac{1}{C_p}\left(\frac{P_{1000}}{p}\right)^{R/C_p}\left(\overline{\frac{dQ}{dt}}^{xyp} - \overline{\frac{dQ}{dt}}^{xyp}\right) \tag{4.4}$$

$$\overline{m}^{xy}\left(\overline{u}^{xp}\overline{v}_x^{yp}\right)^{xy} = -\overline{\omega}_p^{xy} \tag{4.5}$$

$$\overline{\phi_p}^{xyp} = -\frac{R}{p}\left(\frac{P_{1000}}{p}\right)^{-R/C_p}\overline{\theta}^{xyp} \tag{4.6}$$

$$\frac{m^2}{d^2}\overline{\nabla^2\phi}^{xyp} = \overline{f}^{xy}\left(\overline{v}_x^{y} - \overline{u}_y^{x}\right) - \overline{f}_y^{x}\ \overline{u}^{xy} + \frac{2\overline{m}^2}{4d^2}\overline{\mathrm{J}(u,v)}^{xyp} \tag{4.7}$$

其中

$$A^{yyxx} = \frac{1}{16}\left(A_{i+1,j+1} + A_{i+1,j-1} + A_{i-1,j+1} + A_{i-1,j-1}\right) + \frac{1}{8}\left(A_{i+1,j} + A_{i-1,j} + A_{i,j+1} + A_{i,j-1}\right) + \frac{1}{4}A_{ij} \tag{4.8}$$

$$\overline{A_x}^{xyy} = \frac{1}{8\Delta x}\left(A_{i+1,j+1} + A_{i-1,j-1} - A_{i-1,j+1} - A_{i-1,j-1}\right) + \frac{1}{4\Delta x}\left(A_{i+1,j} - A_{i-1,j}\right) \tag{4.9}$$

$$\overline{A_y}^{xyy} = \frac{1}{8\Delta y}\left(A_{i+1,j+1} + A_{i-1,j+1} - A_{i+1,j-1} - A_{i-1,j-1}\right) + \frac{1}{4\Delta y}\left(A_{i,j+1} - A_{i,j-1}\right) \tag{4.10}$$

$$\bar{\omega}^{xy}=\frac{1}{4}(\omega_{i,j}+\omega_{i-1,j}+\omega_{i,j-1}+\omega_{i-1,j-1}) \tag{4.11}$$

$$u_{P_k}=\frac{1}{2\Delta p}(u_{k+1}-u_{k-1})\ ,\ v_{P_k}=\frac{1}{2\Delta p}(v_{k+1}-v_{k-1})\ ,\ \theta_{P_k}=\frac{1}{\Delta p}(\theta_k-\theta_{k-1}) \tag{4.12}$$

$$\omega_{pp}=\frac{1}{(\Delta p)^2}(\omega_{k+1}+\omega_{k-1}-2\omega_k) \tag{4.13}$$

註脚 t 表示對時間之偏微分，其餘註脚 x, y, p 表示對空間水平及垂直方向之偏微分，$\bar{A}$ 表示平均值 。 **J** 表示 Jacobian operator，採用 Arakawa 的方法，使渦旋度平方 (the square vorticity) 及動能守恒。 (Arakaw, 1971)

使用經初值化的初始值，其計算步驟爲：

(1)經 (4.2) 式， (4.3) 式， (4.4) 式分別可計算 $\bar{u}_i^t$, $\bar{v}_i^t$, $\bar{\theta}_i^t$ 值，再對時間積分 (time advancement)，求得下一時刻的風及相當位溫值，分別爲 $u^{t=t_0+\Delta t}$, $v^{t=t_0+\Delta t}$, $\theta^{t=t_0+\Delta t}$

(2)由 (4.7) 式，代入 $u^{t=t_0+\Delta t}$,$v^{t=t_0+\Delta t}$ 求得 $\phi^{t=t_0+\Delta t}$。

(3)由 (4.5) 式，代入 $u^{t=t_0+\Delta t}$,$v^{t=t_0+\Delta t}$ 求得 $\omega^{t=t_0+\Delta t}$。

(4)第(1)步驟至第(3)步驟重覆若干次，至 $t=24$ 小時止。

5. 時間積分 (Time advancement)

本文用兩種時間積分法，時間間隔 Δt 爲6分鐘。

(1)當 $t=0$ 時用 forward time advancement $\quad h^{t+1}=h^t+\Delta t(\frac{\partial h}{\partial t})^t$

當 $t>0$時用 centered time advancement $\quad h^{t+1}=h^{t-1}+\Delta t(\frac{\partial h}{\partial t})^t$ (5.1)

(2) Euler-backward time advancement，其計算方法爲

$$h^*=h^t+\Delta t(\frac{\partial h}{\partial t})^t$$

$$h^{t+1}=h^t+\Delta t(\frac{\partial h}{\partial t})^* \tag{5.2}$$

其中 h^t 爲任一變數在 t 時刻之值，h^* 爲一推測值 (tentative value)

6. 個案討論 (Case Study)

本文所用的天氣資料是 1971 年 9 月 22 日 0000 Z (Bess 颱風即將登陸臺灣的前一天)，海面溫度 600mb, 800mb溫度露點差 (見圖一) 及850mb, 700mb, 500mb, 300mb 高度場 (raw data，見圖四) 經內插得 900mb 高度場，再經 9 點 smooth 後的高度場如圖四。由平衡方程式模式初值化後得到此模式之初始高度場 (見圖六)。以四層原始方程式模式，探討 24 小時的大氣運動。在固定的邊界條件下以 forward and centered time advancement 作時間積分，由 A 法處理所得的初始資料， 300mb 及 500mb 太平洋高壓有顯著東退縮小，計算12小時及24小時的結果 (見圖七) 無擾動，但颱風受太平洋高壓導引氣流的影響向東發展。在實際天氣中， 此颱風走向爲西北。若改用 B 法處理所得的初始資料 300mb 及 500mb 太平洋高壓型態沒有大變化，但以 forward and centered 時間積分計算 6~12 小時左右，300mb 高度場右上角邊界處開始出現擾動，並隨時間增加向左發展 (見圖八)。爲消除此現象，吾人首先考慮改用具有抑制擾動性質的 Euler-backward time advancement 計算 24小時結果與前法大致相同

（見圖九），但前法較後法約省一半的時間，以中山科學研究院 CDC CYBER 72 的電子計算機做24小時的預測計算，費時約800秒。

又試用不同的邊界條件（都用 Euler-backward time advancement）。

(1)固定的邊界條件（fixed boundary condition）

假設各變數在邊界上不隨時間改變，即

$$\frac{\partial u}{\partial t}=\frac{\partial v}{\partial t}=\frac{\partial \phi}{\partial t}=\frac{\partial \theta}{\partial t}=\frac{\partial \omega}{\partial t}=\omega=0 \qquad (6.1)$$

計算 6 小時左右，300mb 高度場右上角邊界處出現一擾動，且隨時間增加而發展，其24小時的結果如圖九。此種固定邊界條件係將邊界視爲一剛體（rigid body），波動遇到邊界均被反射，無法穿過，致使雜波能量累積，造成上述擾動。

(2)自由滑動邊界條件（free slip boundary condition）

假設流體在邊界上能自由滑動（汪，1971；大氣物理組同仁，1972）則

$$\begin{aligned}
&\phi_{\text{邊界外一層}}=2\phi_{\text{邊界}}-\phi_{\text{邊界內一層}}\\
&\theta_{\text{邊界外一層}}=2\theta_{\text{邊界}}-\theta_{\text{邊界內一層}}\\
&(V_{normal})_{\text{邊界外一層}}=2(V_{normal})_{\text{邊界}}-(V_{normal})_{\text{邊界內一層}}\\
&(V_{tangent})_{\text{邊界外一層}}=(V_{tangent})_{\text{邊界內一層}}
\end{aligned} \qquad (6.3)$$

雖能有限地考慮邊界的變化，但不能減小 300mb 之擾動，計算 6 小時左右，300mb 邊界上出現擾動。

(3)絕熱光滑邊界條件（Insulated and slippery boundary condition）

假設運算範圍爲一絕熱系統，在運算範圍的側向邊界上無熱之傳送，且邊界爲光滑的，則

$$\begin{aligned}
&\theta_{\text{邊界外一層}}=\theta_{\text{邊界內一層}}\\
&\phi_{\text{邊界外一層}}=2\phi_{\text{邊界}}-\phi_{\text{邊界內一層}}\\
&(V_{tangent})_{\text{邊界外一層}}=(V_{tangent})_{\text{邊界內一層}}\\
&(V_{normal})_{\text{邊界外一層}}=-(V_{normal})_{\text{邊界內一層}}
\end{aligned} \qquad (6.4)$$

也只能有限地考慮邊界的變化，不能減小 300mb 之擾動，計算 6 小時左右，300mb 邊界上出現擾動。

(2)(3)條件加入「多孔海棉」邊界條件 $W_{ij}=0.5$（詳見(4)），亦未能有顯著之改善。（見圖十，十一）。

(4)「多孔海棉」邊界條件（"porous sponge" boundary condition）

欲避免波在邊界反射，吾人加入「多孔海棉」邊界條件（Perkey & Kreitz, 1976）。假設 A^t_{ij}爲邊界上 (i,j) 格點在 t 時刻之值，則下一時刻之值 A^{t+1}_{ij}爲：

$$A^{t+1}_{ij}=A^t_{ij}+W_{ij}\left(\frac{\partial A_{ij}}{\partial t}\right)\Delta t \quad ; \quad 0\le W_{ij}\le 1 \qquad (6.2)$$

其中 W_{ij} 表示邊界上 (i,j) 格點上之權重係數（weighting coeff.）。

當波動接近邊界時，在邊界上的 W_{ij} 能將其相速度（phase velocity）減至爲零，而避免波之反射。

當 $W_{ij}=0$ 時，表示固定邊界條件。

當 $W_{ij}=1$ 時，表示邊界條件隨時間完全變化。

當 $0<W_{ij}<1$時，表示使變數在邊界上的時間變量（tendency value)減小，能減少波在邊界之反射。

故阻止擾動波反射的程度由 W_{ij} 值決定。吾人曾試用下列三種權重係數：

(i) $W_{ij}=0.35$ (i,j)=邊界上的格點

計算 6 小時，300mb 右上角邊界附近仍出現擾動。

(ii) 考慮兩層「多孔海棉」邊界

$W_{ij}=0.6$ (i,j)=邊界上的格點

$W_{ij}=0.9$ (i,j)=邊界內一層的格點

計算6小時，亦未能完全阻止 300mb 邊界之反射波。

(iii) 由於本文運算範圍較小，仍只用一層「多孔海棉」邊界，選用

$W_{ij}=0.5$ (i,j)=邊界上的格點

計算6小時的結果已有顯著改善，未見擾動現象，至小12時後略有小擾動，但情況也較上述者輕微。24小時的計算結果如圖十二所示。除500mb有擾動發生外，其他各層均有合理的流型（flow pattern）。

由上述計算24小時，除300mb擾動隨時間增加而發展外，其他三層尚有合理的流型(flow pattern)。(5)由於擾動僅出現於 300mb，故吾人對這組天氣資料作調和波分析（harmonic analysis），分析各層高度場波之振幅與波數關係。計檢視原始資料，9點 smooth 及 balance 後的高度場。對各層網格系統每行 j 作一次分析，j 共14行，其 $j=1$ 及 $j=14$ 兩行因在邊界外一層，故無論 smooth 或 balance均未對其處理，仍與原始資料相同。

經分析發現，就這組資料一般而言 850mb, 700mb, 500mb 都以波數1的振幅最大居大多數，約佔10行。高頻波振幅都很小，有類似指數下降之曲線，換言之即長波顯著。這正是大幅度現象氣象波的特性。而 300mb 振幅最大出現在波數爲1，2，3的行數各有5、6、3行，且高頻波的振幅也較大。就此組天氣資料而言，300mb 較短波顯著（見圖十三）。又由1971年9月22日 0000Z 實際天氣圖看來，300mb 約在 35°N，華北及日本一帶，風速很强，達80～90 knots 以上，其北、其南風速都小。而高空噴射氣流（upper jet stream）出現在 300mb～250mb 之間，爲一蜿流，在喜馬拉亞山被截分二支，北面一支恰通過華北、日本一帶，寬度約 300公里左右。是一種短波現象。由調和波分析，吾人可見在 $j=9$～11，振幅與波數之曲線呈鋸齒狀，且短波振幅很大，經9點 smooth 及 balance 後，曲線稍微平滑，振幅也略爲減小，但仍比 500mb 及 700mb 的大。在原始方程式模式計算時，擾動現象即在此帶發生，與短波干擾有關。

由調和波分析可見，9點 smooth 的結果使較高頻波之振幅減小。高度場經9點 smooth 後再經平衡方程式處理，又使較高頻波之振幅減小。對於同一層高度場資料言，大體上低緯度的波振幅較高緯度者爲大，此與能量之分布有關。（與季節也有關係，夏季所有的天氣現象多發生於低緯度，且東風波盛行，故低緯度波之振幅較大。）

7. 結論與建議

限於計算機容量及使用經費，吾人首先對有限區域原始方程式模式作初步探討，發現利用A法處理，由於所作的限制較嚴，爲使天氣場達到平衡狀態，所得的初始資料有些流型（flow pattern）產生變化，如太平洋高壓在 300mb 有顯著退縮，500mb 亦略有退縮，但不似 300mb 嚴重，導致有限區域原始方程式24小時的計算，颱風環流向東發展，與實際路徑有所偏差。而用B法處理，限制較寬，所得的初始資料，各層高度場的型態沒有重大改變。經此模式計算，發現 300mb 高度場，往往在計算6～12小時左右，出現擾動。首先將時間積分方法由 forward and centered time advancement 改爲 Euler-buckward time advancement，24小時的結果大致相同，而前者較後者約省一半時間。

又在 Euler-backward time advancement 下，試用多種邊界條件；固定邊界條件會使波在邊界反射，累積能量，而使擾動不斷發展；自由滑動邊界條件及絕熱光滑邊界條件也僅能有限地考慮邊界的變化，而當加入一種「多孔海棉」邊界條件，由於運算範圍小，此種邊界不能太厚，只設計一層，故僅能阻止部份波的反射，亦未能有效地抑制擾動之發展。

由於此種擾動僅在 300mb 出現，故以調和波分析法檢視各層高度場（承梁文傑先生指導，胡仲英先生幫助，特此致謝），在網格系統上，各緯向的波數與振幅關係。發現除 300mb 外，其他三層大多以波數 1 的振幅最大居絕大多數，且高頻波振幅小，唯 300mb，短波較顯著，在計算時，加上邊界的影響，出現擾動，故邊界條件及初始資料是計算遭遇困難的重要因素。

欲避免這些困難，吾人建議：

(1)邊界的選取最好避免地形複雜，或天氣現象擾動强烈之處。

(2)運算範圍不宜太小，若採用半球或全球爲運算範圍，可簡化邊界問題，且適於作短期或較長時間之預報。吾人將以北半球爲運算範圍，由北半球準地轉模式（Q.G.M.）每小時供給有限區域原始方程式模式之邊界條件（updating B. C.），來探討原始方程式模式。若計算機容量及使用經費許可，將擴大以北半球原始方程式模式繼續探討。（承林永哲教授及陳泰然教授指導，特此致謝）

(3)初始資料只用高度場，似嫌不够，應加入風及溫度之校正，或改用可靠的風場資料。

(4)原始資料做初值化之前應經過嚴密的檢定及校正。例如統計檢定（statistical check），儀器結冰點檢定（Icing check），靜力穩定度檢定（static stability check）及流體靜力檢定（hydrostatic check），（胡仲英, 1975）；或由熱力風的關係，加入溫度和風的關係，使天氣資料能達到垂直一致性（vertical consistency）（Lewis 1972）。這也是吾人將改進的一點。

8. 誌　　謝

本文承梁文傑教授、林永哲教授、陳泰然教授及胡仲英先生的熱心指導、幫助及寶貴建議，深致謝意。又獲行政院國家科學委員會之補助，克以完成，特此申謝。

參 考 資 料

Achtmeier, G. L., 1975: On the initialization problem: A variational adjustment method. Mon. Wea. Rev., **103**, 1089-1103.

Haltiner, G. J., 1971: Numerical Weather Prediction. Wiley, New York, 317pp.

Hawkins, H. F., 1972: Development of a seven-level, balanced, diagnostic model and its application to three disparate tropical disturbances. NOAA Tech. Memo. ERL NHRL-98, 207pp.

Lewis, J. M., 1972: An operational upper air analysis using the variational method. Tech. Note, No. 72-3, Fleet Numerical Weather Central, Monterey California, May, 50pp.

Miller, B. I., 1969: Experiment in forecasting hurricane development with real data. ESSA Tech. Memo. ERLTM-NHRL **85**, Apr., 28pp.

_____,1972: Numerical prediction of tropical weather systems. Mon. Wea. Rev., **100**, 825-835.

Miyakoda, K., and R. M. Moyer, 1968: A method of initialization for dynamical weather forecasting. Tellus, **20**, 115-130.

Nitta, T. and J.B. Hovermale, 1969: A technique for objective analysis and initalization for the primitive forecast equations. Mon. Wea. Rev., **97**, 652-658.

Perkey, D. J., and C. W. Kreitzberg, 1976: A time-dependent lateral boundary scheme

for the limited area primitive equation models. Mon. Wea. Rev., **104**, 744-755.

Shiau, C. J., 1975: A typhoon movement study by balance barotropic model. Ann. Rep. Inst. Phys., Academia Sinica, **5**, 323-343.

Shuman, F. G., and J. B. Hovermale, 1968: An operational six-layer primitive equation model. J. Appl. Meteor., **7**, 525-547.

Staff Members of Electronic Computation Center, 1965: 72-hr baroclinic forecast by the diabatic quasi-geostrophic model. J. Metor. Soc. Japan, **43**, 246.

Sundqvist, H., 1975: Initialization for models using sigma as the vertical coordinate. J. Appl. Meteor., **14**, 153-158.

Wang, C. T, 1971: Drop-water impact. Ann. Rep. Inst, Phys., Academia Sinica, **1**, 107.

_____1975: Numerical Study of a simplified balanced model, Atmos. Sci., The Meteor. Soc. of the Republic of China, **2**, 51-58.

大氣物理組同仁，1972-1974：大氣及颱風模型（Ⅰ），（Ⅱ），（Ⅲ），中研究物理所集刊，**2, 3, 4.**

胡仲英，1975：預報電腦化之研究與設計，氣象學報第21卷，第2期。

曾忠一，1976：東亞地區天氣資料變分客觀分析之研究，中研院物理所集刊，本卷。

鄧施人，1975：資料輸入與客觀分析修正之研究，氣象預報與分析，第64期，32-36.。

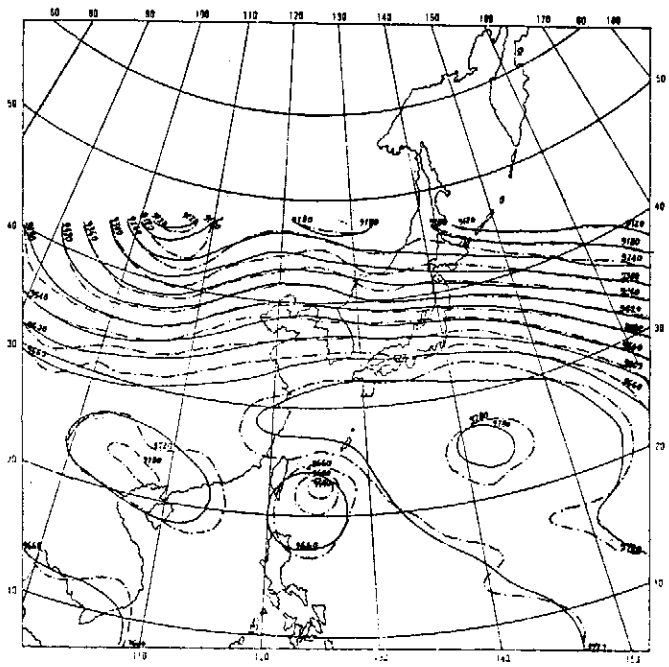

Fig. 4.1 Geopotential height field (ϕ/g m) at 300 mb
—•—•— raw data
———— 9-point smoothed data

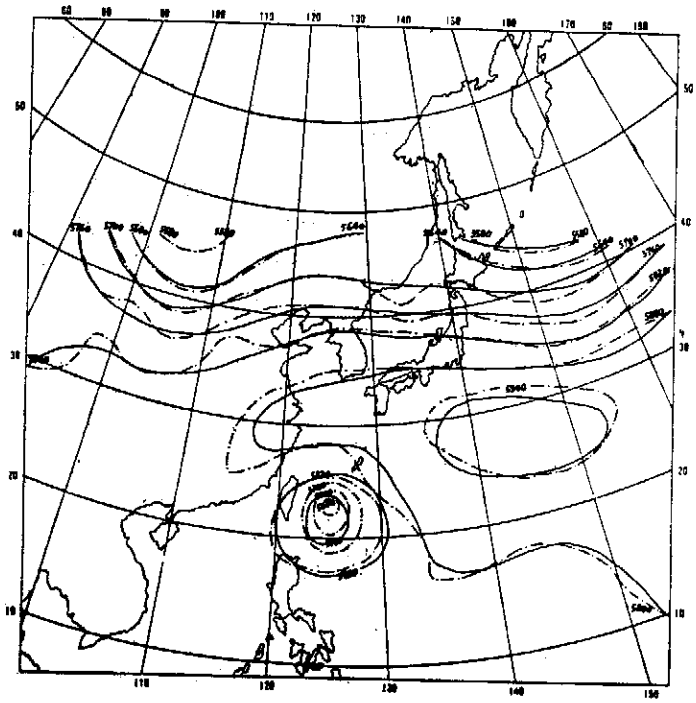

Fig 4.2 Geopotential height field (ϕ/g m) at 500 mb
••——••——•• raw data
———————— 9-point smoothed data

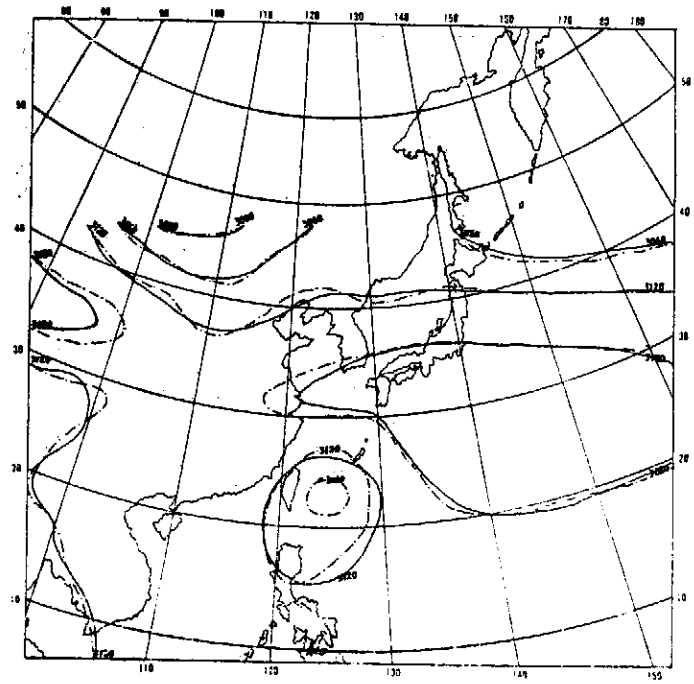

Fig. 4.3 Geopotential height field (ϕ/g m) at 700 mb
••——••——•• raw data
———————— 9-point smoothed data

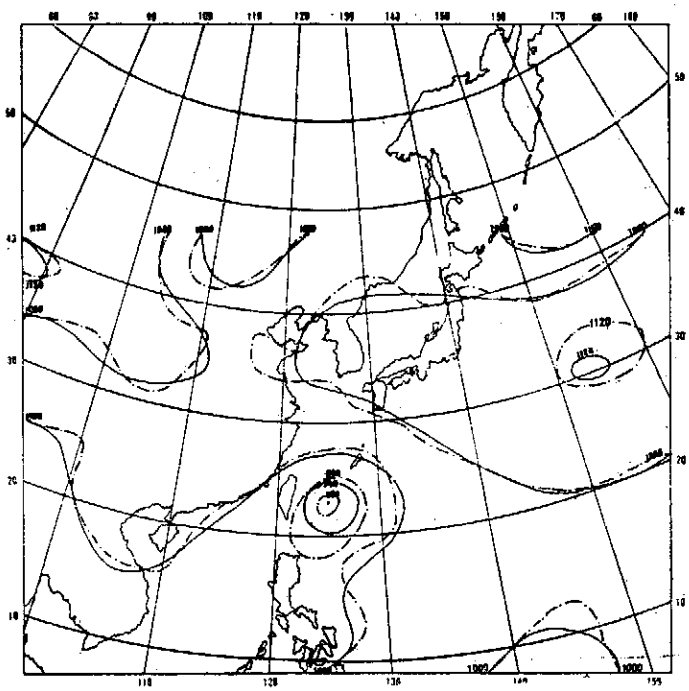

Fig. 4.4 Geopotential height field (ϕ/g m) at 900 mb
••——••——•• raw data
———————— 9-point smoothed data

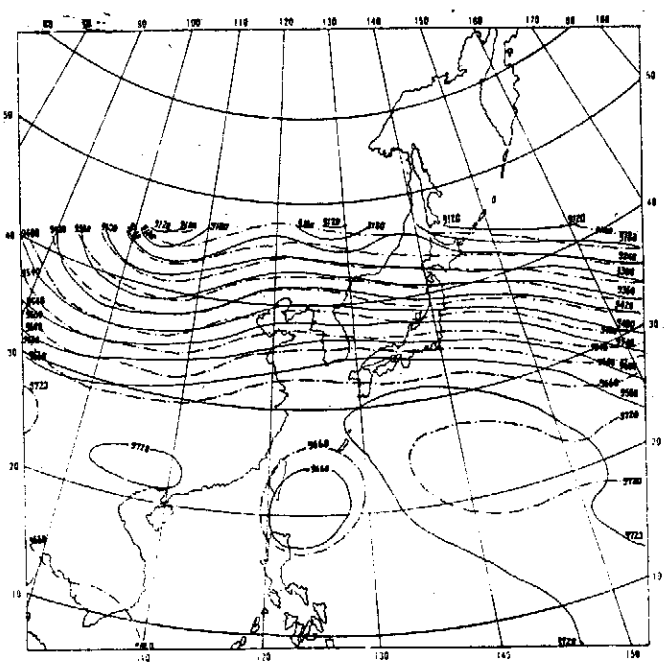

Fig. 5.1 Balanced geopotential height field (ϕ/g m) at 300 mb
••——••——•• treated by method A
———————— treated by method B

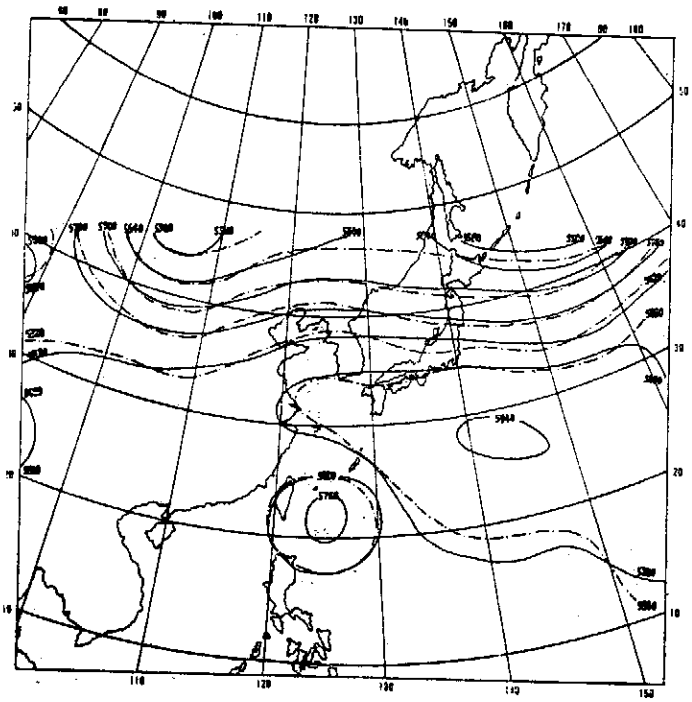

Fig. 5.2 Balanced geopotential height field (ϕ/g m) at 500 mb
••——••——•• treated by method A
——————— treated by method B

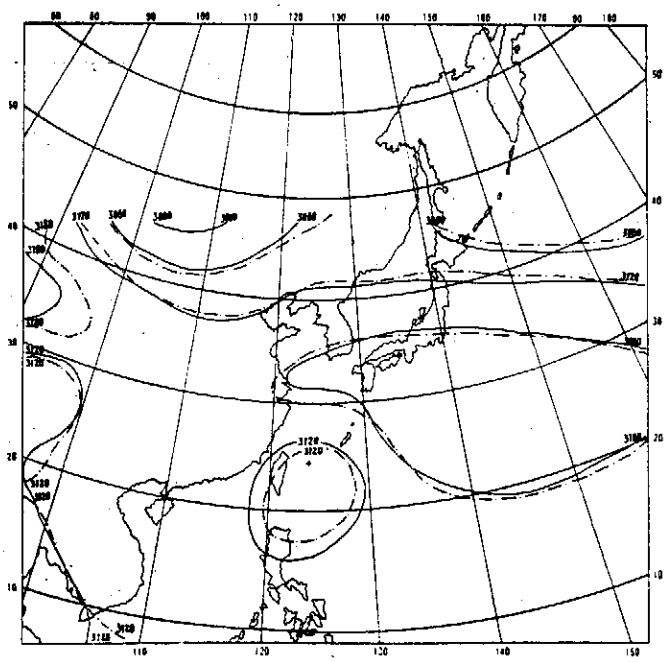

Fig. 5.3 Balanced geopotential height field (ϕ/g m) at 700 mb
••——••——•• treated by method A
——————— treated by method B

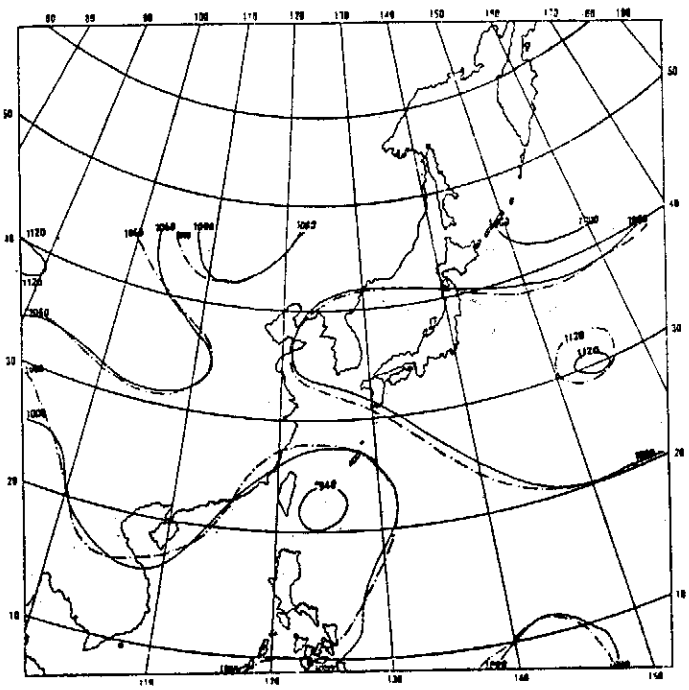

Fig. 5.4 Balanced geopotential height field (ϕ/g m) at 900 mb
•• —— •• —— •• treated by method A
———————— treated by method B

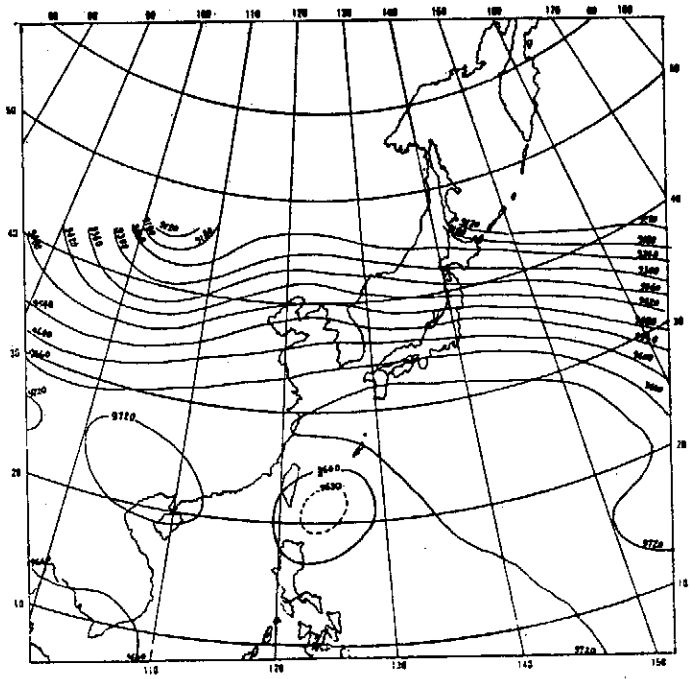

Fig. 6.1 Geopotential height field (ϕ/g m) after initialization at 300mb

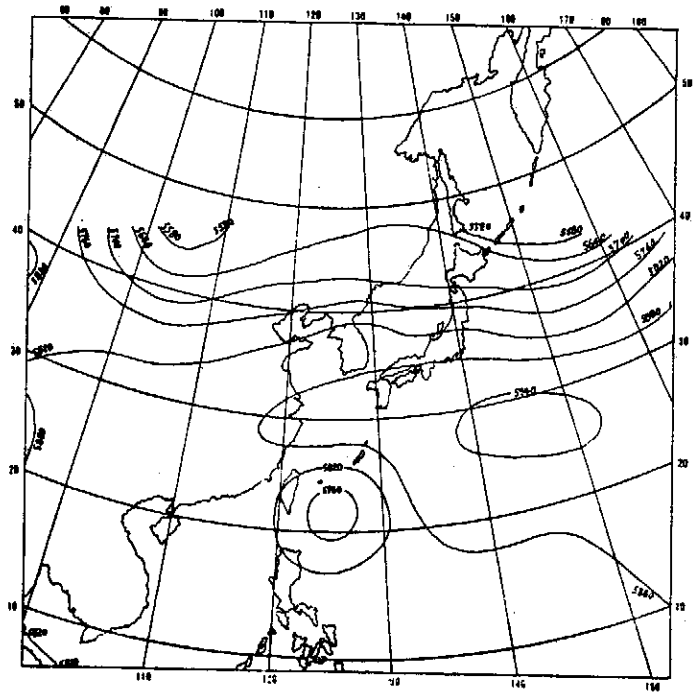

Fig. 6.2 Geopotential height field (ϕ/g m) after initialization at 500 mb

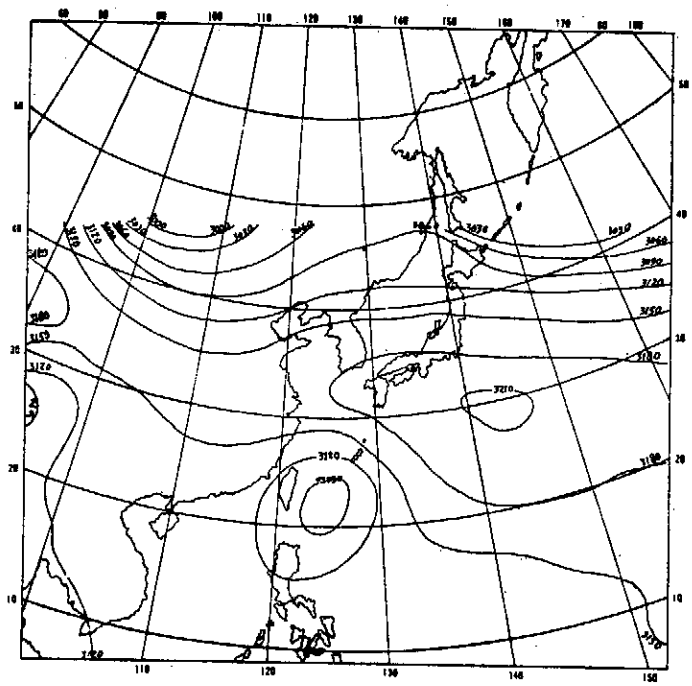

Fig. 6.3 Geopotential height field (ϕ/g m) after initialization at 700 mb

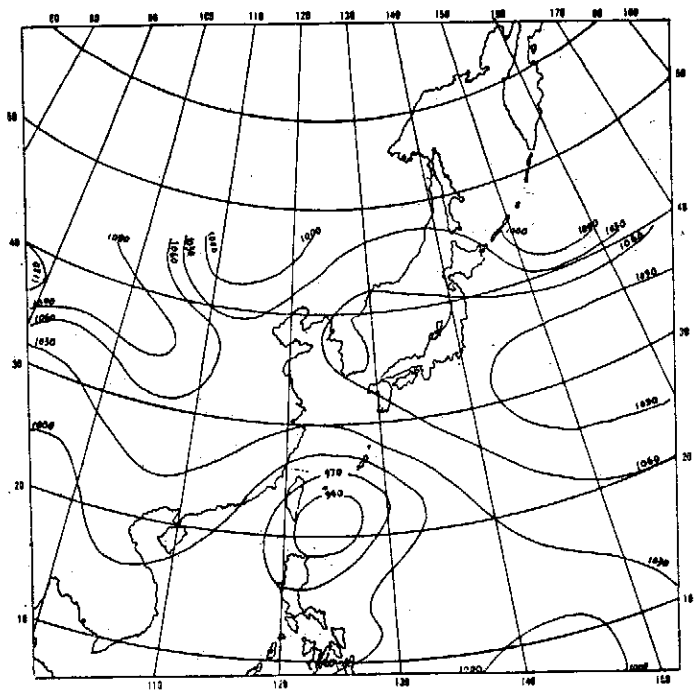

Fig. 6.4 Geopotential height field (ϕ/g m) after initialization at 900 mb

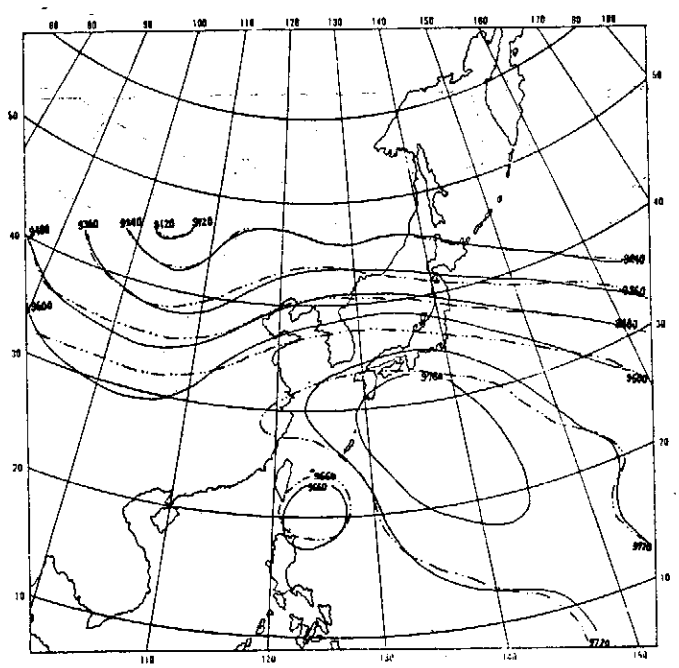

Fig. 7.1 Geopotential height field (ϕ/g m) at 300 mb
Treated by method A, under fixed B.C.
Forward & centered time advancement
••——••——•• T=12-hour
———————— T=24-hour

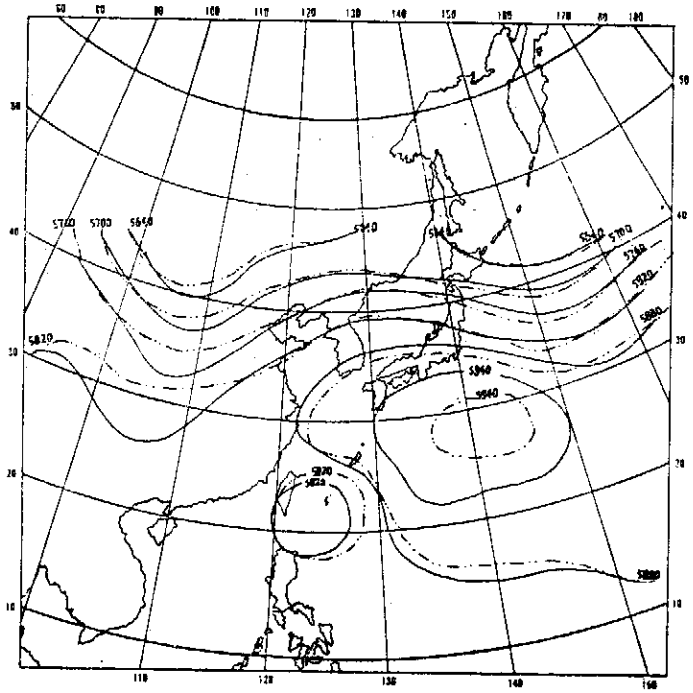

Fig. 7.2 Geopotential height field (ϕ/g m) at 500 mb
Treated by method A, under fixed B.C.
Forward & centered time advancement
••——••——•• T=12-hour
———————— T=24-hour

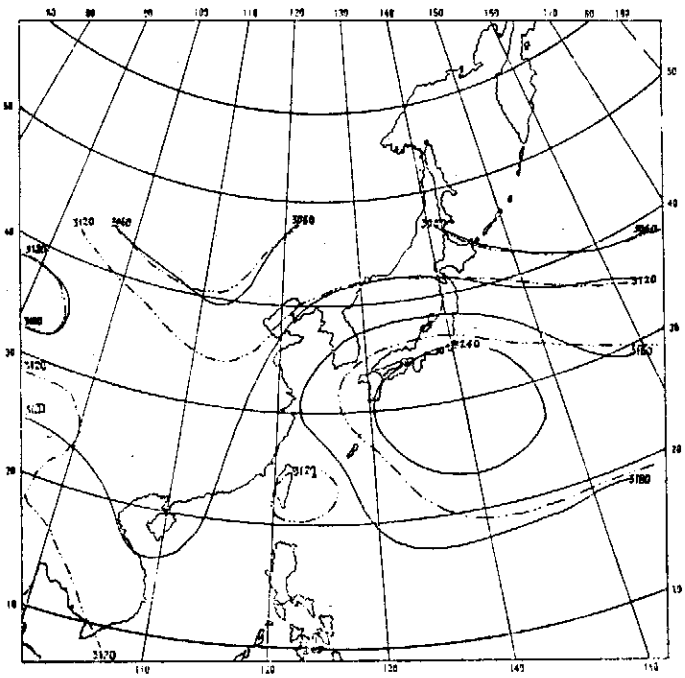

Fig. 7.3 Geopotential height field (ϕ/g m) at 700 mb
Treated by method A, under fixed B.C.
Forward & centered time advancement
••——••——•• T=12-hour
———————— T=24-hour

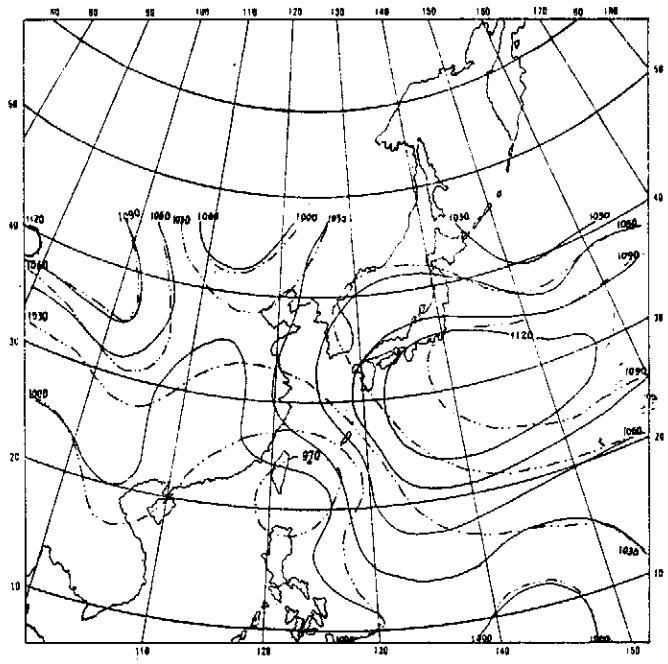

Fig. 7.4 Geopotential height field (ϕ/g m) at 900 mb
Treated by method A, under fixed B.C.
Forward & centered time advancement
••——••——•• T=12-hour
———————— T=24-hour

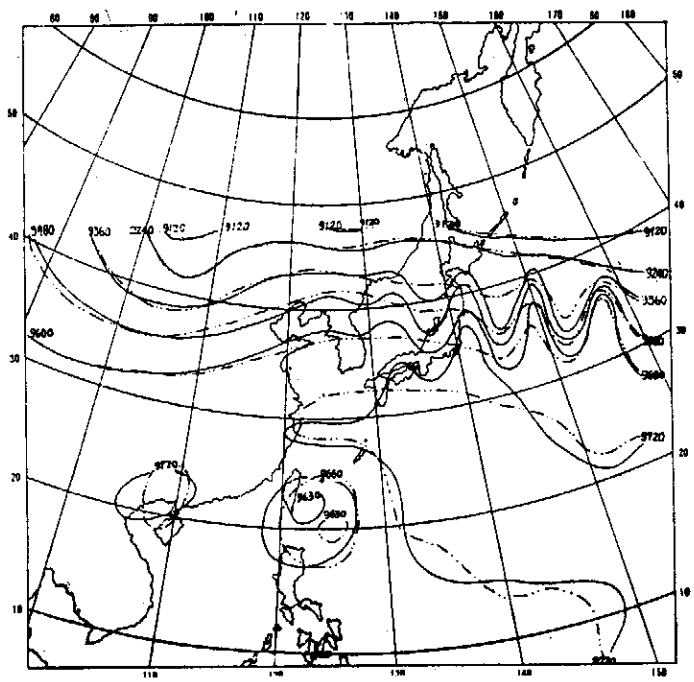

Fig. 8.1 Geopotential height field (ϕ/g m) at 300 mb
Treated by method B, under fixed B.C.
Forward & centered time advancement
••——••——•• T=12-hour
———————— T=24-hour

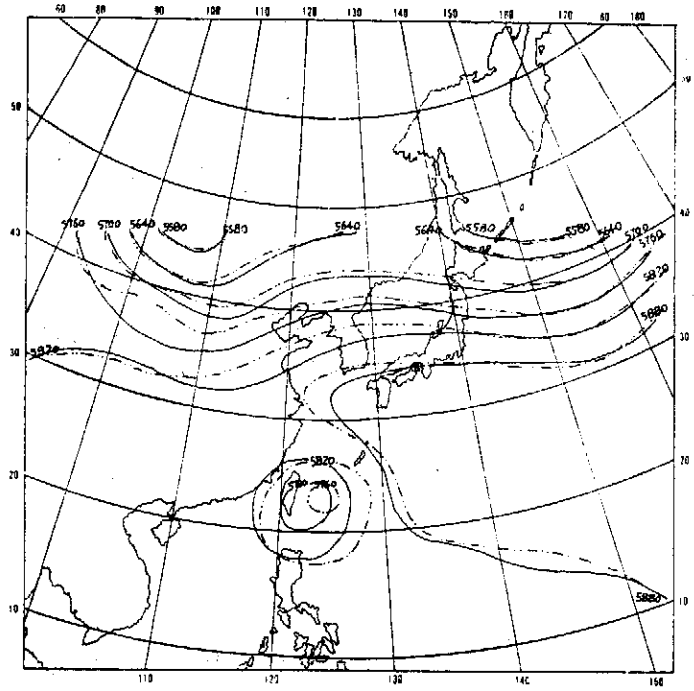

Fig. 8.2 Geopotential height field (ϕ/g m) at 500 mb
Treated by method B, under fixed B.C.
Forward & centered time advancement
••——••——•• T=12-hour
———————— T=24-hour

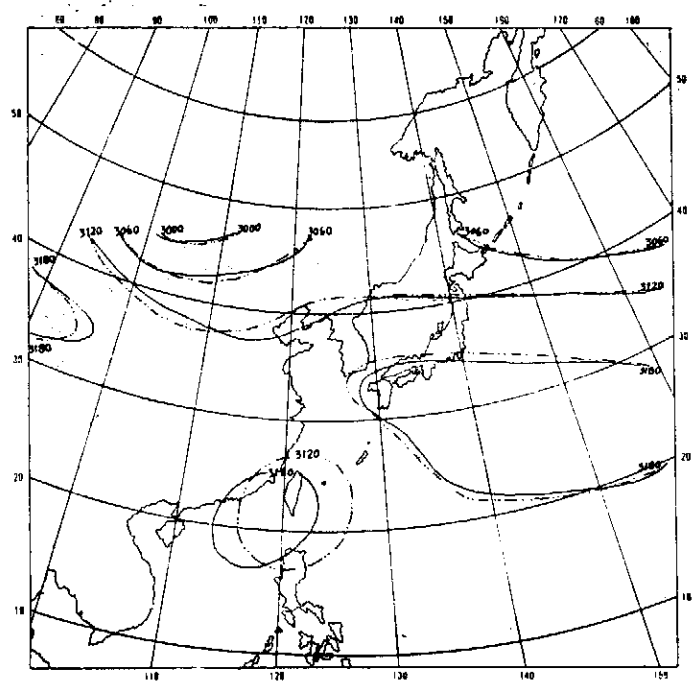

Fig. 8.3 Geopotential height field (ϕ/g m) at 700 mb
Treated by method B, under fixed B.C.
Forward & centered time advancement
••——••——•• T=12-hour
———————— T=24-hour

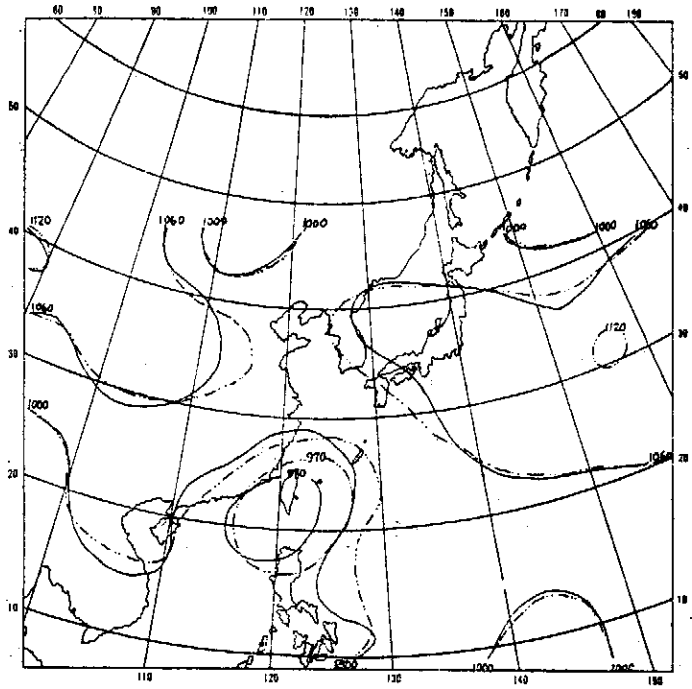

Fig. 8.4 Geopotential height field (ϕ/g m) at 900 mb
Treated by method B, under fixed B.C.
Forward & centered time advancement
••——••——•• T=12-hour
———————— T=24-hour

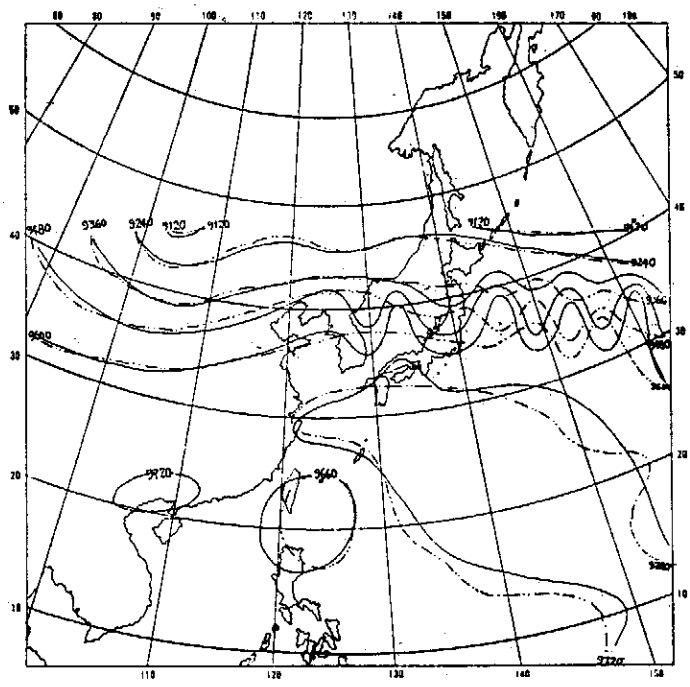

Fig. 9.1 Geopotential height field (ϕ/g m) at 300 mb
Treated by method B, under fixed B.C.
Euler-backward time advancement
••——••——•• T=12-hour
———————— T=24-hour

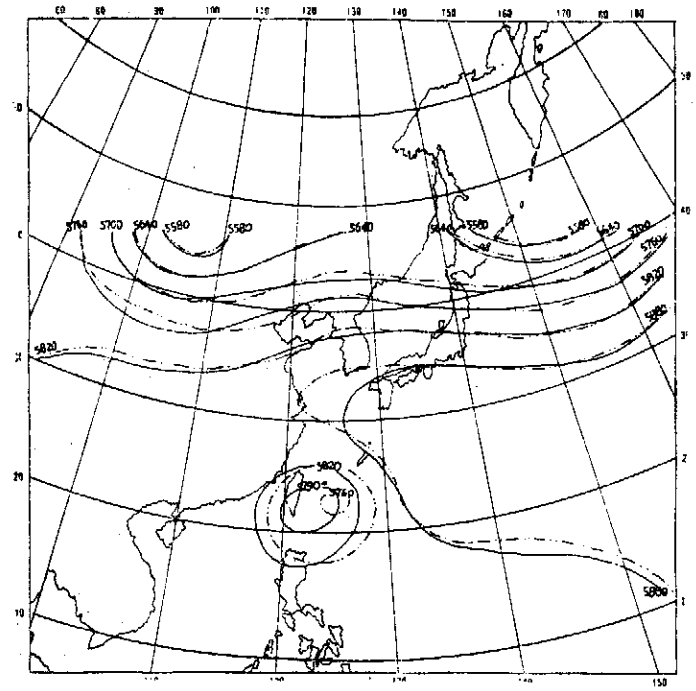

Fig. 9.2 Geopotential height field (ϕ/g m) at 500 mb
Treated by method B, under fixed B.C.
Euler-backward time advancement
••——••——•• T=12-hour
———————— T=24-hour

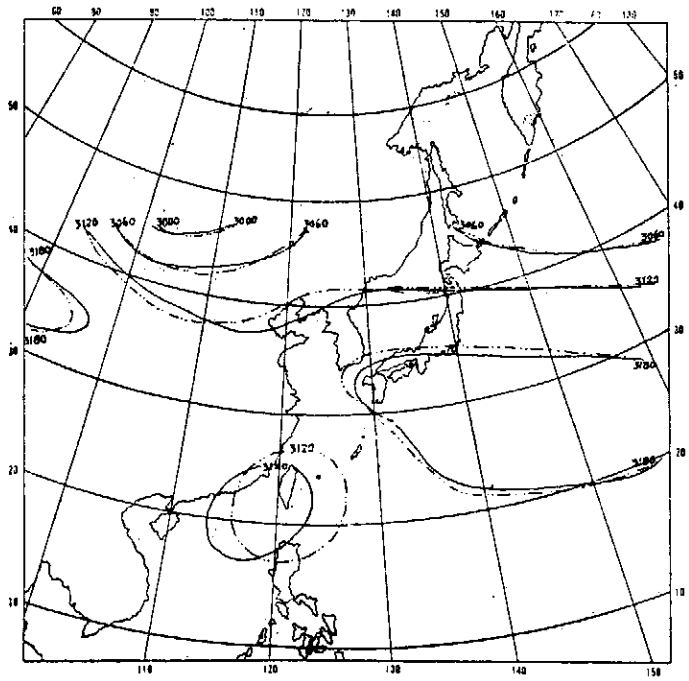

Fig. 9.3 Geopotential height field (ϕ/g m) at 700 mb
Treated by method B, under fixed B.C.
Euler-backward time advancement
••——••——•• T=12-hour
———————— T=24-hour

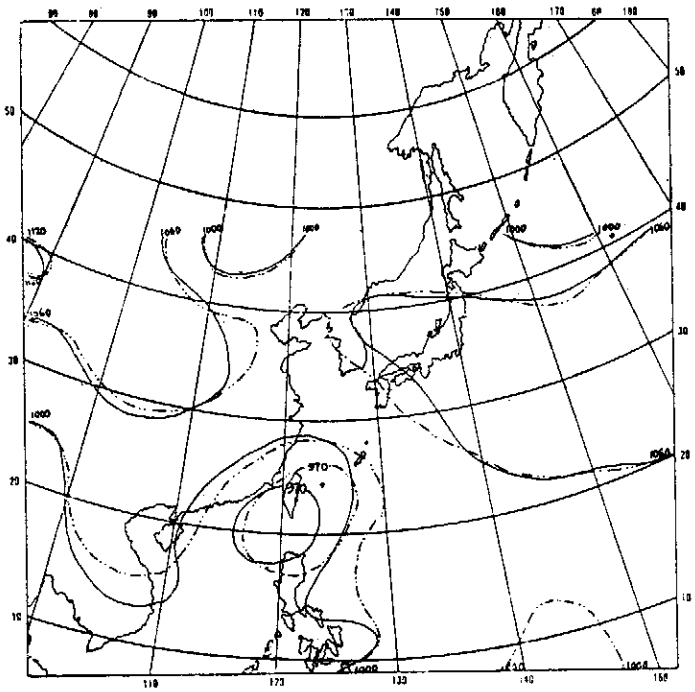

Fig. 9.4 Geopotential height field (ϕ/g m) at 900 mb
Treated by method B, under fixed B.C.
Euler-backward time advancement
••——••——•• T=12-hour
———————— T=24-hour

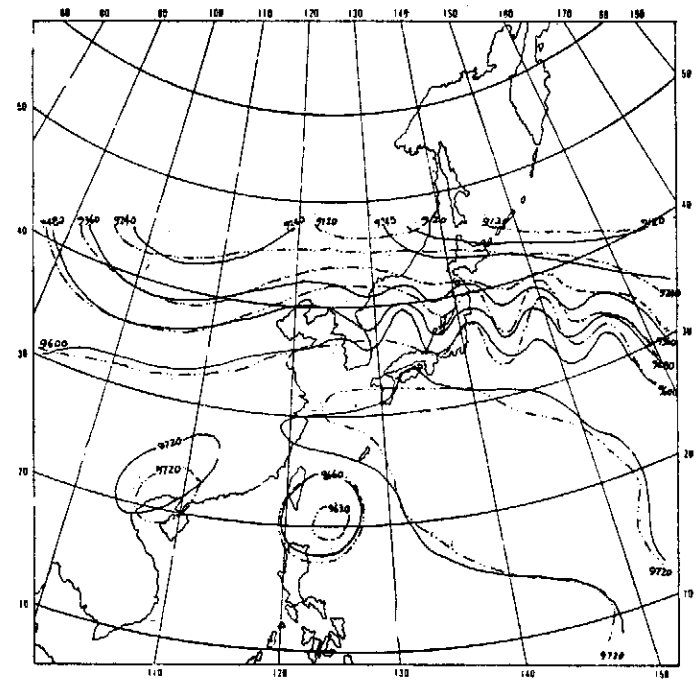

Fig. 10.1 Geopotential height field (ϕ/g m) at 300 mb
Treated by method B, under free slip B.C.
Euler-backward time advancement
••——••——••T=12-hour
———————— T=24-hour

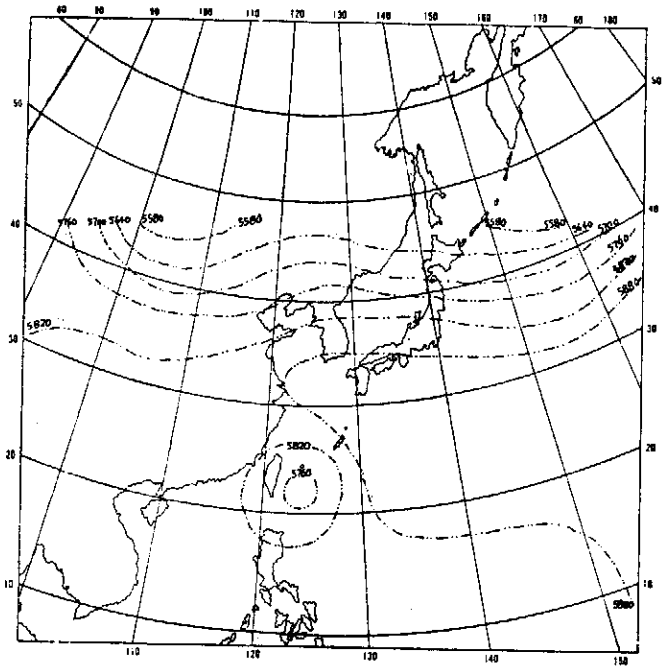

Fig. 10.2 Geopotential height field (ϕ/g m) at 500 mb
Treated by method B, under free slip B.C.
Euler-backward time advancement
••——••——•• T=24-hour
———————— T=12-hour

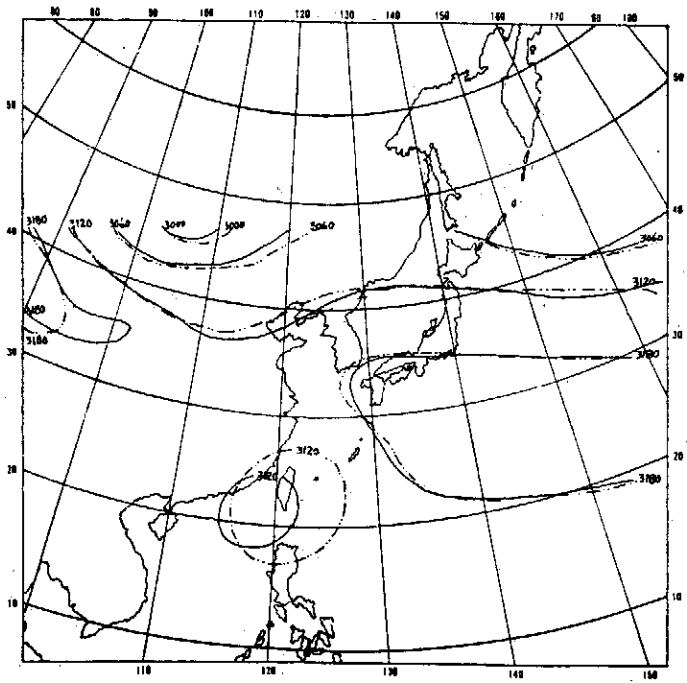

Fig 10.3 Geopotentiial height field (ϕ/g m) at 700 mb
Treated by method B, under free slip B.C.
Euler-backward time advancement
••——••——•• T=12-hour
———————— T=24-hour

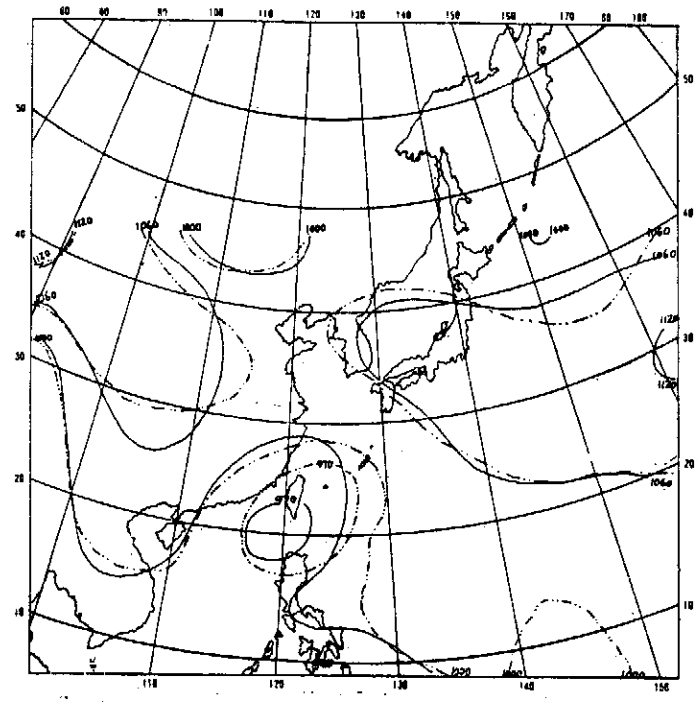

Fig. 10.4 Geopotential height field (ϕ/g m) at 900 mb
Treated by method B, under free slip B.C.
Euler-backward time advancement
••——••——•• T=12-hour
———— T=24-hour

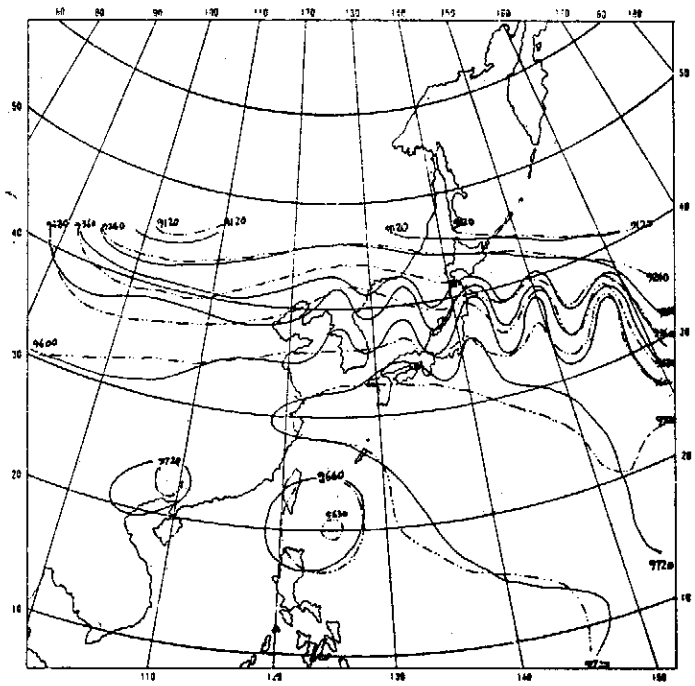

Fig. 11.1 Geopotential height field (ϕ/g. m) at 300 mb
Treated by method B, under insulated & Slippery B.C.
Euler-backward time advancement
••——••——•• T=12-hour
———— T=24-hour

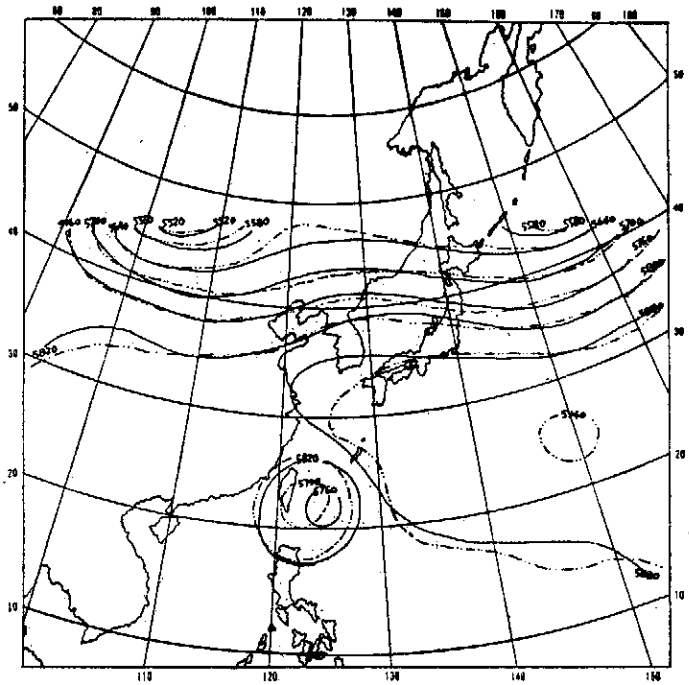

Fig. 11.2 Geopotential height field (ϕ/g m) at 500 mb
Treated by method B, under insulated & Slippery B.C.
Euler-backward time advancement
••——••——•• T=12-hour
———————— T=24-hour

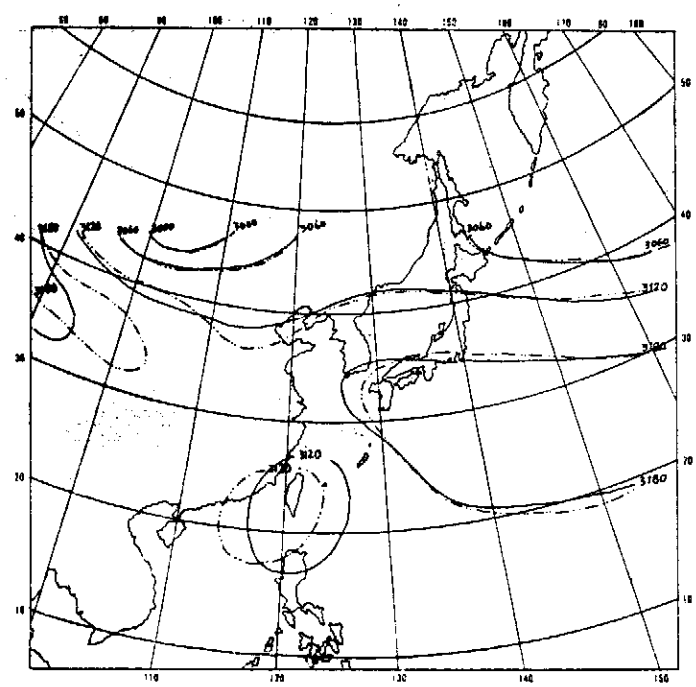

Fig. 11.3 Geopotential height field (ϕ/g m) at 700 mb
Treated by method B, under insulated & Slippery B.C.
Euler-backward time advancement
••——••——•• T=12-hour
———————— T=24-hour

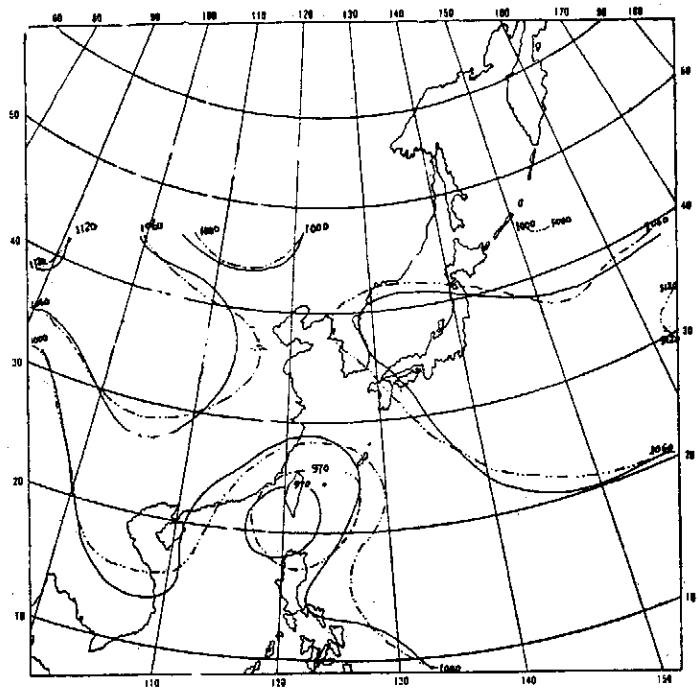

Fig. 11.4 Geopotential height field (ϕ/g m) at 900 mb
Treated by method B, under insulated & Slippery B.C.
Euler-backward time advancement
••——••——•• T=12-hour
———————— T=24-hour

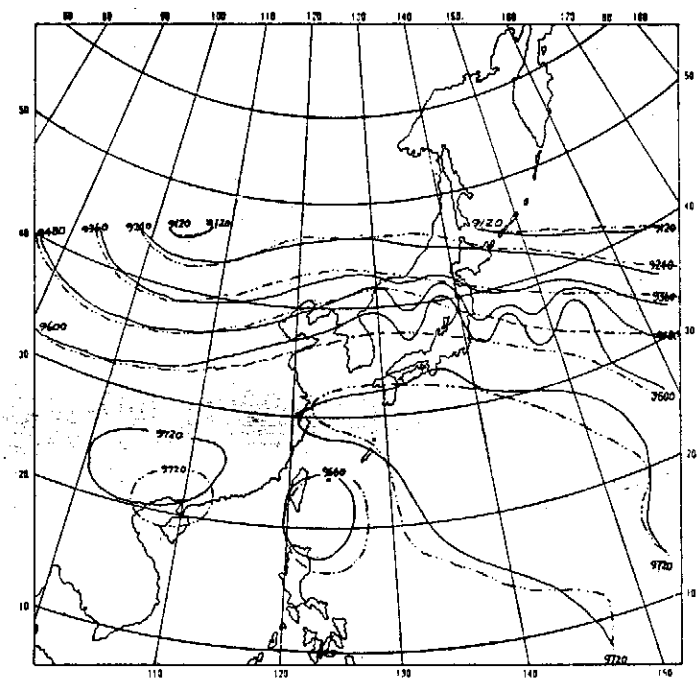

Fig. 12.1 Geopotential height field (ϕ/g m) at 300 mb
Treated by method B, under porous sponge B.C. (W_{fj}=0.5)
Euler-backward time advancement
••——••——•• T=12hour
———————— T=24-hour

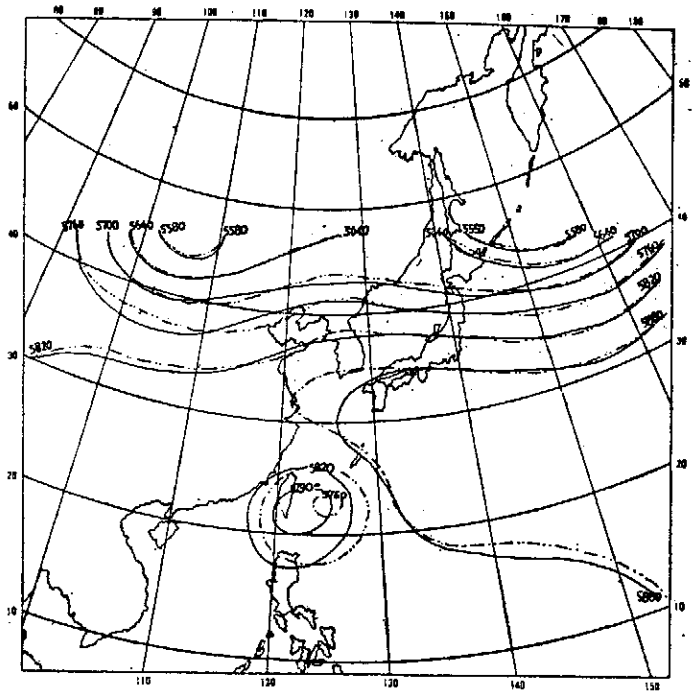

Fig. 12.2 Geopotential height field (ϕ/g m) at 500 mb
Treated by method B, under porous sponge B.C. (W_{ij} =0.5)
Euler-backward time advancement
••——••——•• T=12hour
———————— T=24-hour

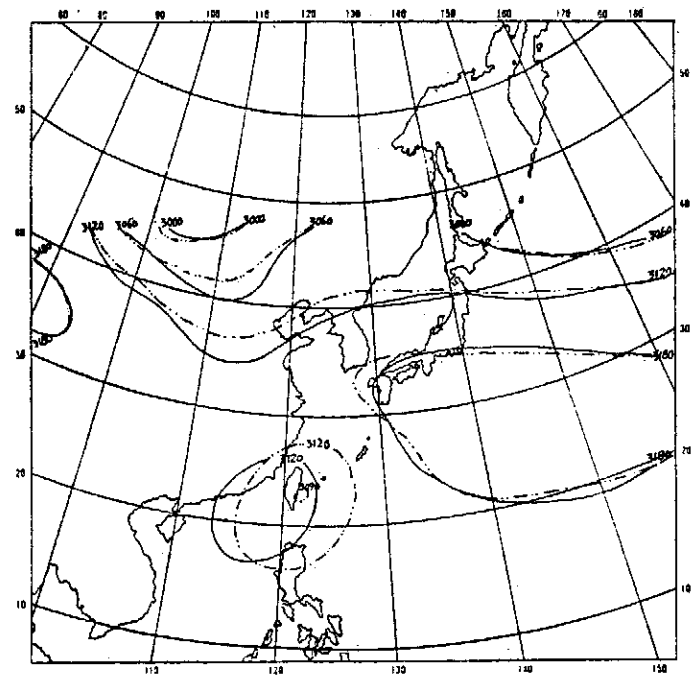

Fig. 12.3 Geopotential height field (ϕ/g m) at 700 mb
Treated by method B, under porous sponge B.C. (W_{ij}=0.5)
Euler-backward time advancement
••——••——•• T=12 hour
———————— T=24-hour

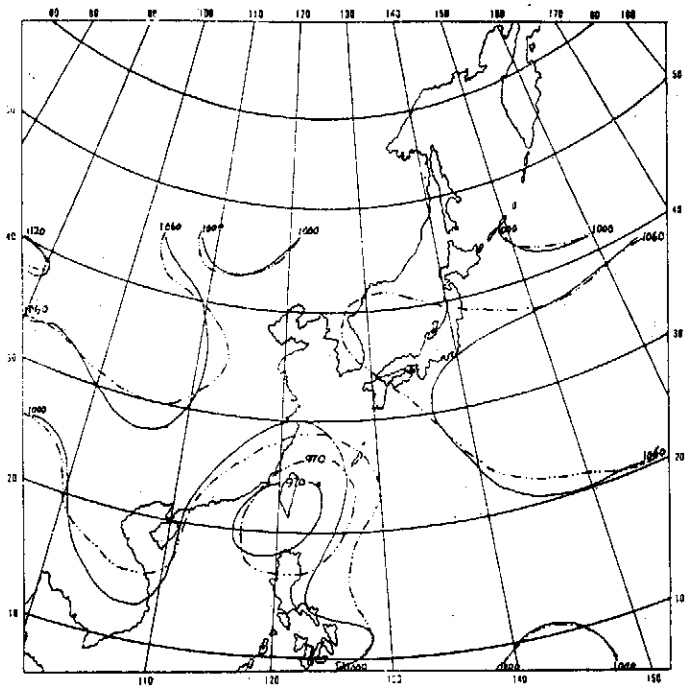

Fig. 12.4 Geopotential height field (ϕ/g m) at 900 mb
Treated by method B, under porous sponge B.C. (W_{ij}=0.5)
Euler-backward time advancement
••——••——•• T=12 hour
———————— T=24-hour

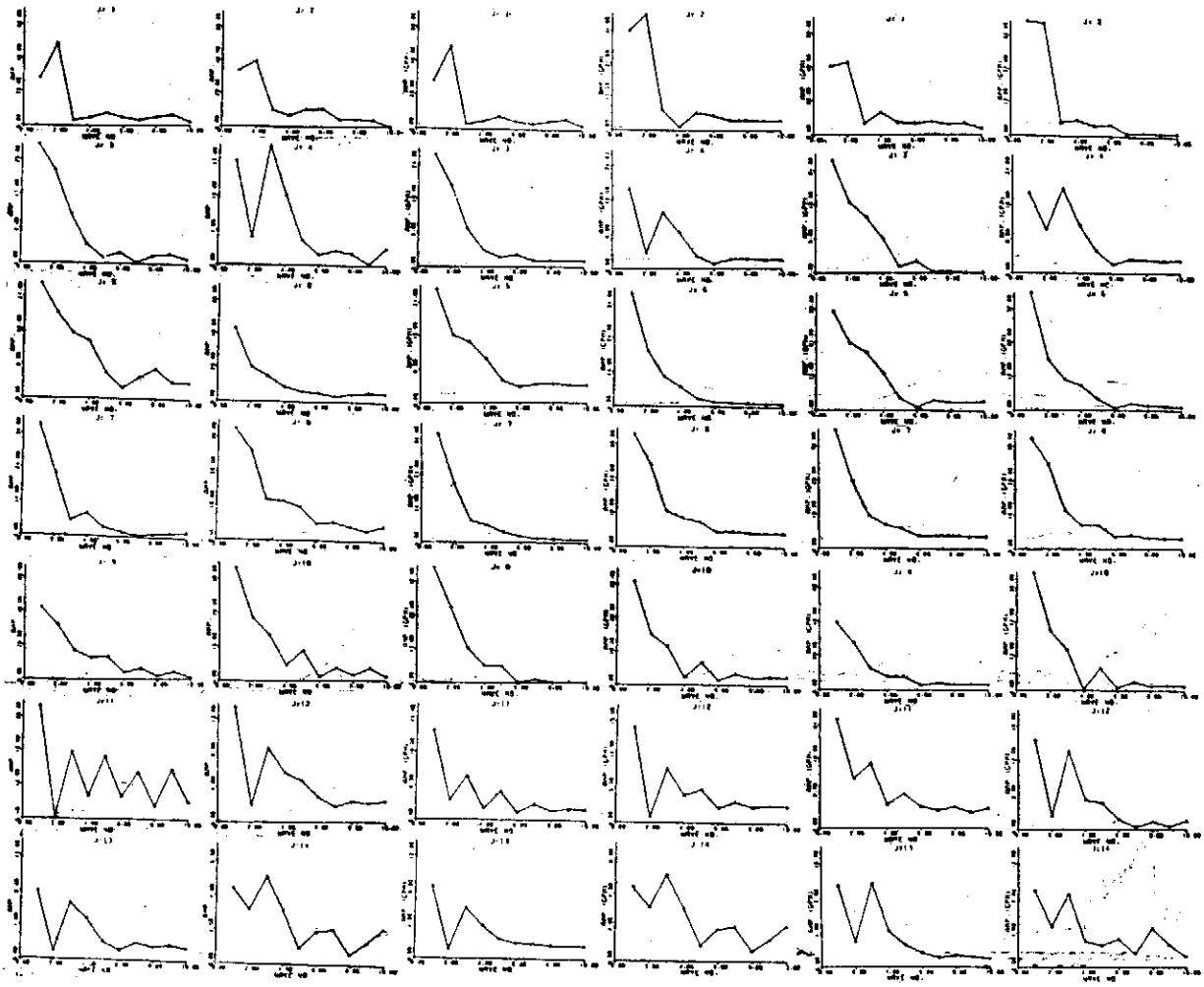

(a) (b) (c)

Fig. 13.1 Harmonic wave analysis at 850 mb (a) raw data (b) 9-point smooth data (c) balanced data

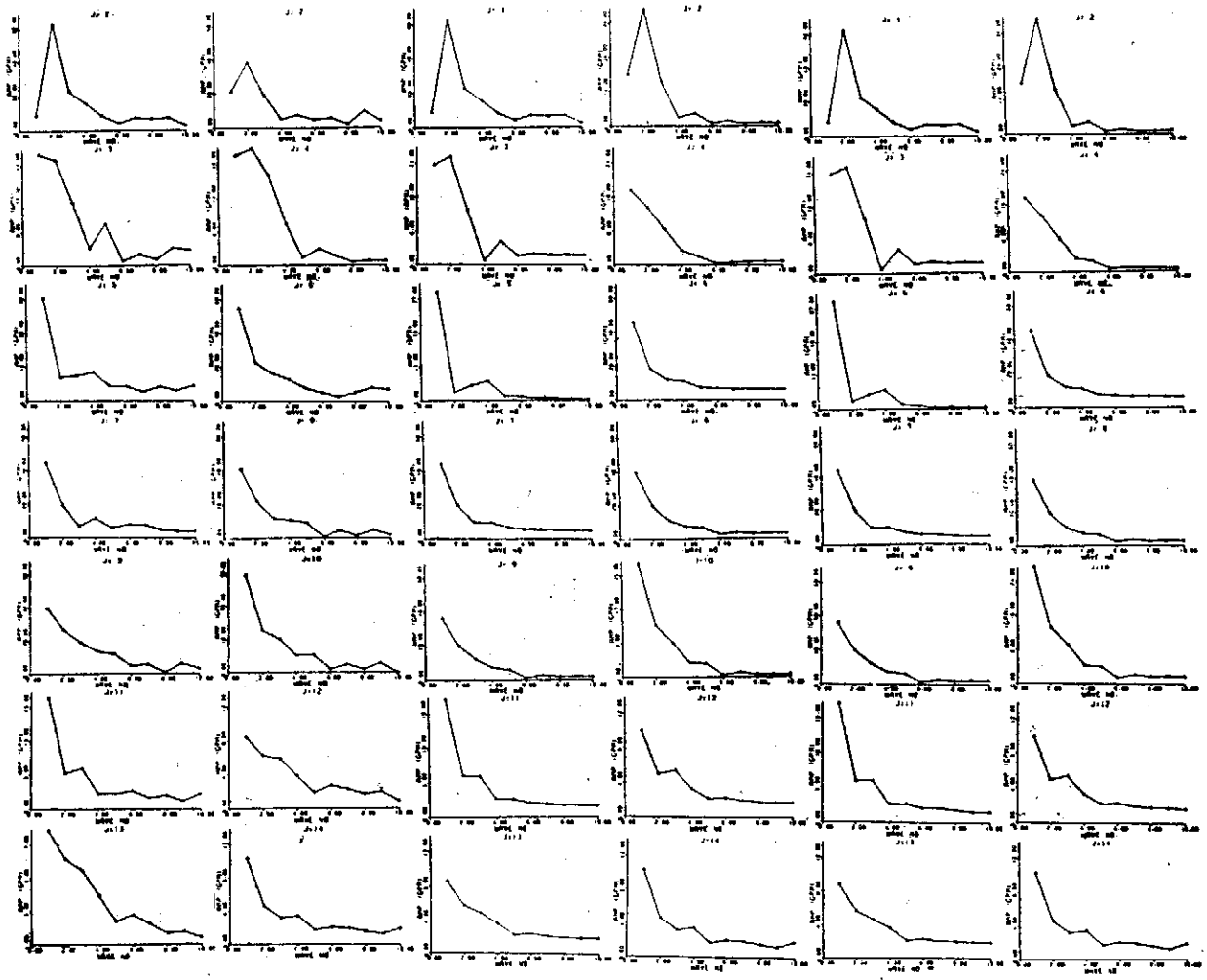

(a) (d) (c)

Fig. 13.2 Harmonic wave analysis at 700 mb (a) raw data (b) 9-point smooth data (c) balanced data

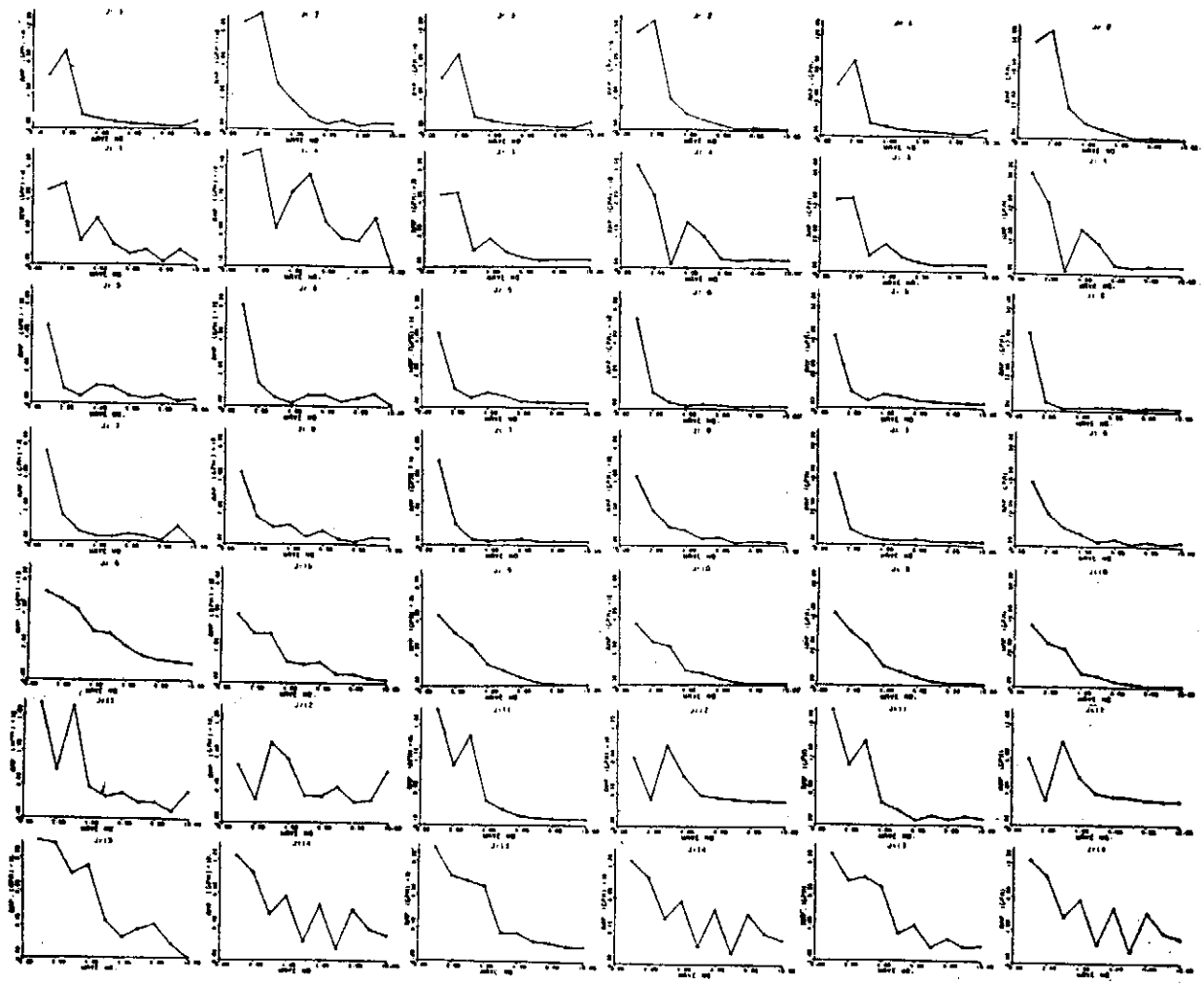

(a) (b) (c)

Fig. 13.3 Harmonic wave analysis at 500 mb (a) raw data (b) 9-point smooth data (c) balanced data

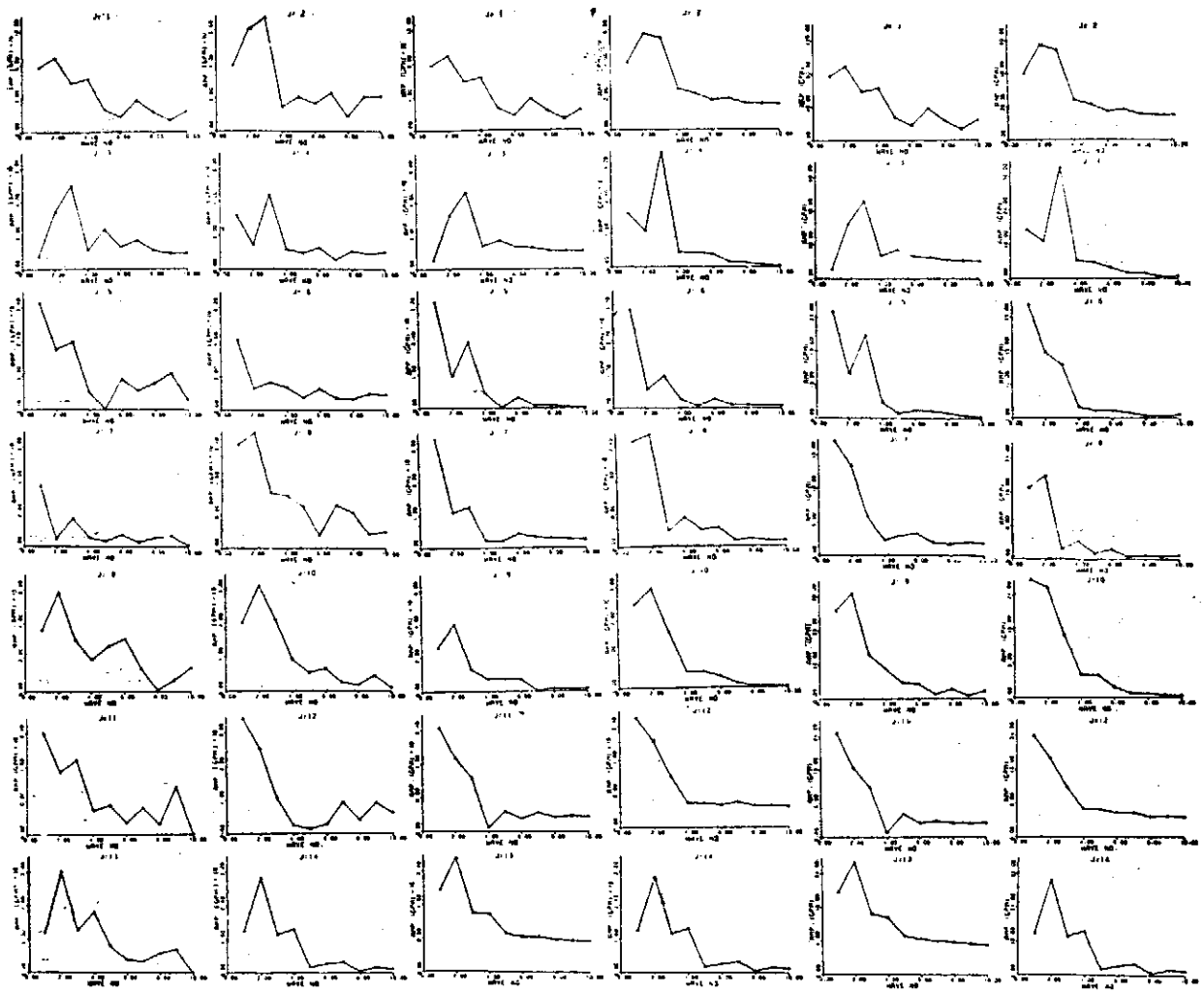

(a) (b) (c)

Fig. 13.4 Harmonic wave analysis at 300 mb (a) raw data (b) 9-point smooth data (c) balanced data

Annual Report of the Institute of Physis, Academia Sinica, Vol. 6, 1976

Still Water Resistance of a Single-Step Planing Hull*

C. T. Wang & C. Y. Lu

Abstact

By modifying Blount & Fox's equations for stepless planing hull, governing equations are derived to analyse still water characteristics of single-step planing hull. Experimental results from free trim and heave tests of a three feet model with different step positions, step heights, and loading conditions confirm the analytical solutions.

The present study thus presents an analytical model for selecting desired step position as well as for studying still water resistance and trim behavior of various step position, step height, loading condition and L.C.G. position of a single-step planing hull.

* This paper has been appeared in NTU-INA-Tech.Rept. 49, June 1976; Also SNAMEC, 24, 1, 1976.

Experimental Study of a 27800 LTDW Bulk Carrier*

C. T. Wang & C. L. Huang

Abstact

A modified INA practice for model-ship correlation is introduced and found to predict ship performance successfully.

For the 27800 dwt bulk carrier studied, at full load condition, the original ship (ship A) is able to cruise around 15 kts at MCR 11200×122. The modified ship with an improper designed bulbous bow and a new propeller (ship B) can only cruise around 14.5 kts at MCR 11500×150, and is found useless. Ship C with a new bulbous bow designed by INA could reduce part of the breaking and ship generated waves, and could reduce ship A resistance by more than 10% at design speed of 15 kts.

* This paper has ben appeared in NTU-INA-Tech. Rept. 53, June 1976.

Analytic Solutions of the Falkner-Skan Equation When $\beta=-1$ and $\gamma=0$*

H. T. Yang and L. C. Chien†

Abstact

Two types of unique analytic solution are presented for the Falkner Skan equation $f'''(\eta)+ff''+\beta(1-(f')^2)=0$ when $\beta=-1$, subject to the boundary conditions $f(0)=\gamma, f'(0)=0$, $f'(\infty)=1$. For $\gamma\leqq\sqrt{2}, f''(0)=\sqrt{\gamma^2-2}$, the solution is given in terms of exponential and error functions, with $f'(\eta)$ in a dominantly exponential asymptotic approach to unity. For $0\leqq\gamma\leqq\sqrt{2}$, $f''(0)=0$, the solution is given in terms of confluent hypergeometric functions, with an algebraic approach from above. As γ increases continuously from zero, the solution goes over continuously from an algebraic to a dominantly exponential approach through $\gamma=\sqrt{2}$.

* This paper has been published in SIAM J. Appl. Math Vol. 29 (1975)558—569.

† On leave supported by National Science Council, from the Institute of Physics, Academia Sinica, Taiwan, China.

Theoretical Study of Two-Dimensional, Incompressible, Turbulent, Curved-Wall Jets*

George Mon* and Hsien-Ping Pao**

Abstact

A theoretical study of the effects of the surface curvature on the flow field of a two-dimensional, incompressible, turbulent jet has been made. By using a perturbation technique, the governing equations for the flow have been obtained and solved numerically. The perturbation parameter, $\varepsilon(x)$, has been found to be $x/(R_0\, x^m)$, where x is the coordinate along the surface, R_0 is a constant related to the radius of curvature, and mis the surface curvature parameter. We have flow similarity for a curved-wall jet when $m=1$, and for the flow of a plane wall jet when $R_0\to\infty$.

In comparison with a straight wall, the theoretical results show that a convex surface decreases the velocity of the jet near the surface, displaces the position of the maximum velocity away from the surface and increases the growth rate of the jet width and the rate of decay of the maximum velocity.

* Research Mechanical Engineer, Harry Diamond Laboratories, Washington, D.C. Member, ASME

** Professor, Dept. of Aerospace and Atmospheric Science, The Catholic University of America, Washington, D.C.

† This paper has been appeared in Memorial Volume to President Chiang Kai-Shek, Academia Sinica, Taipei, Taiwan, ROC, April, 1976, p. 193

Annual Report of the Institute of Physics, Academia Sinica, Vol. 6, 1976

The Effects of Mountains on a Typhoon Vortex as Identified by Laboratory Experiments*

Hsien-Ping Pao

The Catholic University fo America, Washingion, D.C. 20064

(*Manuscript received* 20 *March* 1976, *in revised form* 31 *Marɔh* 1976)

Abstact

In this study laboratory experiments were performed by introducing an essentially two-dimensional concentrated vortex which interacts with a two-dimensional elliptical barrier resembling the general shape of the island of Taiwan. Comparisons are made between the experimental results and field data. It is found that the general behavior and the accompanying surface flow patterns of a typhoon vortex, when interacting with the mountainous island of Taiwan, can be reasonably simulated in the laboratory. In the case of deflected flows, the typhoon vortex resembles a two-dimensional vortex past an equivalent two-dimensional mountain barrier and its pathline seems to be not sensitive to the typhoon strength. It is suggested that laboratory modeling may provide a reliable and effective way for predicting the movement of a typhoon vortex when it is in the vicinity of the island.

* This paper has been appeared in Atmospheric Science, The Meteo. Soc. of ROC, Vol. 3, May 1976, p. 55.

On Vortex Trails over Ocean Islands*

Hsien-Ping Pao and Timothy W. Kao

The Catholic University of America, Washington, D. C. 20064

Abstact

In this study some experimental results are given to demonstrate that the density stratification is the main reason for the appearance of cloud vortex trails over ocean islands. Evidences are given that the similarity of these vortex trails to von Kàrmàn streets may not go beyond the general streak-line pattern. The experimental results reveal the three-dimensional vortex shedding structure when a sphere is towed at a constant velocity through a stratified fluid. It is found that for small or moderate stratification and Reynolds numbers in the range from 10^3 to 10^4 the vortex is shed three-dimensionally. The stratification however quickly and effectively inhibits the vertical motion and the initially turbulent wake collapses and reveals the vertically oriented portion of the vortex structure, reminiscent of the two-dimensional vortex street behind a circular cylinder when viewed from above. Considerable insights are given concerning the vortex shedding and its structure in the wake of a three-dimensional body.

* This paper has been appeared in Atmospheric Science, The Meteo. Soc. of ROC, Vol. 3, May, 1976, p. 28

Annual Report of the Institute of Physics, Academia Sinica, Vol. 6, 1976

Hydrodynamic Instability of Stoke's Second Problem*

Robert R. Hwang and C. J. Chen

Abstact

The stability of a small disturbance in a flow near a plate executing a linear harmonic oscillation is examined. The partial differential equation governing the evolution of distur.ance with respect to time and space is solved by Kantorovich weighted residual method subjected to three different initial disturbance profiles. It is found that the flow is inherently unstable even when the modified Reynolds number, $N_R=\sqrt{\frac{2}{f\nu}}U_0$, ($U_0$, maximum velocity; f, frequency; and ν, kinematic viscosity) is small. The velocity disturbances with wave number of 15 to 19 per a length of $\sqrt{\frac{2\nu}{f}}$ is most susceptible of amplification. The time, normalized by the frequency, t_e, for which disturbulence kinetic energy will amplify by a factor of 10^m over its initial value is given approximately $t_e=(100\ m)\ N_R^{-1.85}$.

* Contributed Paper of the 14th International Congress of Theoretical and Applied Mechanics Deft, the Netherlands, 1976.

二次元紊性熱噴流擴散之分析

黃　榮　鑑*

摘　要

本文以數值分析的方法探討有關紊性熱噴流排除後在近域的擴散情形，並以實驗的數據加以印證數值分析所得的預測結果。數值模式是直接由紊流平均量的動量及熱能量偏微分方程分析而得。爲了方程式的閉合問題，對於紊流動量傳遞是以紊流動能及流場混合長度的關係式設立一紊流模式表示之。紊流動能及混合長度直接由紊流傳遞的偏微分方程式求出。本文所討論者僅限於，水平二次元不可壓縮流體的情況。

*中央研究院物理研究所、臺灣大學水資源研究小組

本文已發表於工程月刊 Engineering Journal vol. 49, No. 8, August, 1976

Annual Report of the Institute of Physics, Academia Sinica, Vol. 6, 1976

臺中港設置風車之研究*

黃榮鑑　簡又新　劉通敏

摘　要

以理論分析及風洞實驗的方法探討風車的特性。對水平軸式風車，根據 Glaueret 氏的風車理論，採用波音公司 FX 60—126 型翼形剖面，變化四個影響性能的參數—設計翼端速度比，葉片數、疏密度（或弦長比）及葉片形狀；在直立軸式風車以改變弦長比爲主製成不同的風車模型在風洞中作實驗分析並與理論所得結果相比較，以對風車的性能特性係數即功率、扭矩及阻力作一系列的探討，尋找出其最高效率的模式。同時，實驗在風洞中由於風車的吸收風能，風車尾端的流場變化及風速降低情形，以供臺中港設置風車的參考。

*臺中港務局委託研究報告（民國六十五年八月）